ANALYSIS, ASSESSMENT AND OPTIMIZATION OF INTEGRATED SOLAR ENERGY SYSTEMS FOR MULTIGENERATION

by

Rami El-Emam

A Thesis submitted in Partial Fulfillment

of the Requirement for the Degree of

Doctor of Philosophy

in

Mechanical Engineering

Faculty of Engineering and Applied Science

University of Ontario Institute of Technology

December 2014

Abstract

The extensive usage of fossil fuel in most of human activities has led to the undesirable effects on the environment starting from global warming and greenhouse effects to the climate changes, acid rain and others. Renewable energy is at the core of most of recent research activities to overcome these environmental challenges. Being an integral part of other renewable resources, solar energy utilization aims to occupy more portion of the world energy framework. Integrated energy systems for multigeneration produces several useful products using the same energy input. Electrical power generation, fresh water, space heating and cooling and domestic hot water are the major commodities that furnish our life activities. Hydrogen is another useful product taken into consideration. The proposed systems in this work cover all these products as a step for achieving a sustainable and environmentally benign community. These systems pose great potential for global warming mitigation. In the work presented, different multigeneration energy systems based on solar energy are introduced. Comprehensive thermodynamic, environmental and economic analyses for the proposed multigeneration energy systems are the main goals of this thesis study. Thermodynamic analyses are based on energy and exergy, associated with the efficiencies of overall and system components performances. For a better understanding of the systems performances and the potential of more improvement in their performances, exergoeconomic and environmental analyses and system optimization are performed. Solar dish based integrated system considering biomass-SOFC as alternative for solar unavailability is the first studied system. The system performance is assessed during solar availability and considering the performance of a 24-hours operation. The second system is based on solar parabolic trough providing concentrated heat to an organic Rankine cycle. The system is integrated with electrolyzer for hydrogen production, a reverse osmosis water desalination unit and absorption chiller system and providing domestic hot water. The third main system is based on heliostat solar system integrated with steam turbine for multigeneration purposes. The system produces cooling, heating, fresh water and hydrogen through electrolysis.

Keywords: Multigeneration, Integrated Energy Systems, Solar Energy, Exergy, Exergoeconomic, Optimization.

Acknowledgment

I would like to express my deepest appreciation and sincerest gratitude to my supervisor, Dr. Ibrahim Dincer, for his continuous support and patient guidance throughout my research work. He provided me with the motivation and supervision that helped me to overcome all the challenges I faced during my PhD research.

I am so thankful to Dr. Calin Zamfirescu for his endless support and help. I would like also to thank the examining committee members, Dr. Tony Mazza, Dr. Greg F. Naterer, Dr. Anatoli Chkrebtii and Dr. Martin Agelin-Chaab for their precious feedbacks and comments which has helped improve my thesis.

My appreciation and deep thanks to all my friends and colleagues in Dr. Dincer Research Group at the Clean Energy Research Laboratory (CERL) and ACE3030 at the Automotive Centre of Excellence at UOIT, and in Turkey, with whom I shared big part of my academic and social life during the last four years.

I would also like to thank all staff members of the Faculty of Engineering and Applied Science, University Library, Graduate Studies, Teaching and Learning Centre and Student Learning Centre. Especial thanks to Svetlana Novak, Reem Ali, Nadia Morel, Olga Bulakh and Joel Stewart for all the support I needed, and to Dr. Hossam Kishawy for his kind encouragement and guidance since my first day at UOIT. I would like to thank my friends Janette Hogerwaard and Joanne Goyette for their assistance in editing my thesis.

Special thanks and love go to my wife, Dina, and my son, Kareem, for their sacrifice, their continuous encouragement and for joining my academic journey with all its ups and downs. This work wouldn't have been accomplished without their efforts and unwavering support. Most importantly, I would like to register my greatest gratitude to my mother, Nagwa, my father, Salah, and my lovely sister, Nada, for being with me with their prayers, love and thoughts for all my life.

TABLE OF CONTENTS

LIST OF FIGURES

LIST OF TABLES

NOMENCLATURE

A	Area, m^2
Ar	Archimedes number
Bo	Bond number
c	Unit cost of exergy, $/kJ
c_p	Specific heat at constant pressure, kJ/kg K
$\dot{C}$	Cost rate, $/h
d	Diameter, m
D_{eff}	Effective gas diffusion factor, m^2/s
D_g	Diffusion coefficient, m^2/s
E	Energy, kJ
E_{act}	Activation energy, kJ/mol
ex	Specific exergy, kJ/kg
$\overline{ex}^{ch}$	Specific chemical exergy, kJ/kmol
$\dot{E}x$	Exergy rate, kW
$\dot{E}x_d$	Exergy destruction rate, kW
Ex_R	Exergy destruction ratio, %
f	Exergoeconomic factor, %
F	Faraday constant
G	Gibbs free energy, kJ
Gr	Grashof number
h	Specific enthalpy, kJ/kg
h_s	Sand heat transfer coefficient, $kW/m^2.K$
h^f	Enthalpy of formation, kJ/kg.K
H	Height, m
i_o	Exchange current density, A/cm^2
i_s	Limiting current density, A/cm^2
IP	Improvement potential, kW
j	Current density, A/m^2
K	Equilibrium constant
l	Length, m
m	Mass, kg
$\dot{m}$	Mass flow rate, kg/s
MW	Molecular weight, kg/kmol
n	Number of moles
$\dot{n}$	Molar flow rate, mole/s
P	Pressure, kPa
Pr	Prandtl number

$(\Delta P/P)$	Pressure loss coefficient
$\dot{Q}$	Heat flow rate, kW
r_c	Pressure ratio
r_m	Annual membrane replacement factor, %
r_n	Plant recovery ratio, %
R	Gas constant, kJ/kg K
s	Specific entropy, kJ/kg.K
$\dot{S}_{gen}$	Entropy generation rate, kW/K
SI	Sustainability index
T	Temperature, °C, K
t	Time, s
u	Specific internal energy, kJ/kg
U	Internal energy
U_L	Overall heat transfer coefficient, W/m^2K
U_f	Fuel utilization factor, %
U_O	Oxygen utilization factor, %
V	Volume, m^3
$\dot{V}$	Volumetric flow rate, m^3/s
V_B	Bubble velocity, m/s
V_{act}	Activation losses, V
V_{con}	Concentration losses, V
V_e	Superficial emulsion gas velocity, m/s
V_f	Fluidization velocity, m/s
V_{mf}	Minimum fluidization velocity, m/s
V_{ohm}	Ohmic over potential, V
υ	Specific volume, m^3/kg
$\dot{W}$	Work, kW
y	Molar fraction
y_D	Exergy destruction percentage, %
$\dot{Z}$	Capital cost, $

Greek Letters

β	Temperature ratio
ϒ	Specific heat ratio
ε	Heat exchanger effectiveness, %
π	Osmotic pressure, kPa
ρ	Density, kg/m^3
η	Energy efficiency
σ	Surface tension, N/m
τ	Annual operating hours, h

ψ	Exergy efficiency
ω	Moisture content, %

Subscripts

o	Ambiant conditions
cv	Control volume
cd	Condenser
cf	Cooling fluid
cr	Critical
cw	Cooling water
ev	Evaporator
Exp	Expander
ex	Exergy
f	Fuel
HE	Heat exchanger
hf	Hot fluid
in	Inlet
L	Liquid
OF	Organic fluid
out	Exit
P	Product
V	Vapor
Q	Thermal energy
s	Surface
w	Work

Acronyms

AFC	Alkaline Fuel Cell
BCHP	Building Cooling, Heating and Power
CELF	Constant Escalation Levelization Factor
CHP	Combined Heat and power
CPV	Concentrated Photovoltaic
CRF	Capital Recovery Factor
DSWH	Domestic Solar Water Heater
HFC	Heliostat Field Collector
HHV	Higher Heating Value, kJ/kg
HRSG	Heat Recovery Steam Generator
HTF	Heat Transfer Fluid
LHV	Lower Heating Value, kJ/kg
MCFC	Molten Carbonate Fuel Cell

O&M	Operation and maintenance
PAFC	Phosphoric Acid Fuel Cell
PDC	Parabolic Dish Collector
PEC	Purchased Equipment Cost
PEM	Proton Exchange Membrane
PTC	Parabolic Trough Collector
PV	Photovoltaic
RO	Reverse Osmosis
SOFC	Solid Oxide Fuel Cell
SWIP	Seawater Intake and Pretreatment
SWRO	Seawater Reverse Osmosis
TCI	Total Capital Investment

Chapter 1

INTRODUCTION

1.1 OVERVIEW AND OUTLOOK FOR ENERGY DEMANDS

The advances of human civilization and technological advancement during the last century are directly related to the huge and unprecedented increase in the energy consumption. Electrical power generation industry to transportation, all mainly depend on the depleted hydrocarbon fossil fuel. The extensive use of fossil fuel in most of our activities causes severe changes to our environment. Global warming, ozone depletion and greenhouse effect are some of the environmental threats to our life on the planet that are mainly caused because of the unwise consumption of our depleting fossil fuel. These phenomena are wreaking havoc with the natural system of our environment and affect the lives of the entire creature on the earth.

A former Saudi Arabian oil minister said that the Stone Age did not end for the lack of stone, and the Oil Age will end long before the world runs out of oil (Kemp, 2005). Although renewable energy was known since the beginning of the last century, it was brought into sharp focus after the 1973 oil crisis. However the interest in renewable alternatives again dwindled following the stabilization in oil prices, it became clear and imperative that relentless efforts should be places on tapping renewable resources of energy following the concerns of energy security, climate change and human development (Kishore, 2009).

Oil and gas are expected to continue to be a main source of fuel through the next two decades as shown in Figures 1.1 and 1.2, and considering the increasing rate of energy demand, the liquid fuels are the slowest growing source of energy. But with the dramatic increase in greenhouse gas emissions, it becomes not a choice to work on finding more efficient energy systems with integrating other clean energy resources. Renewable alternatives are the fastest growing energy sources in the world.

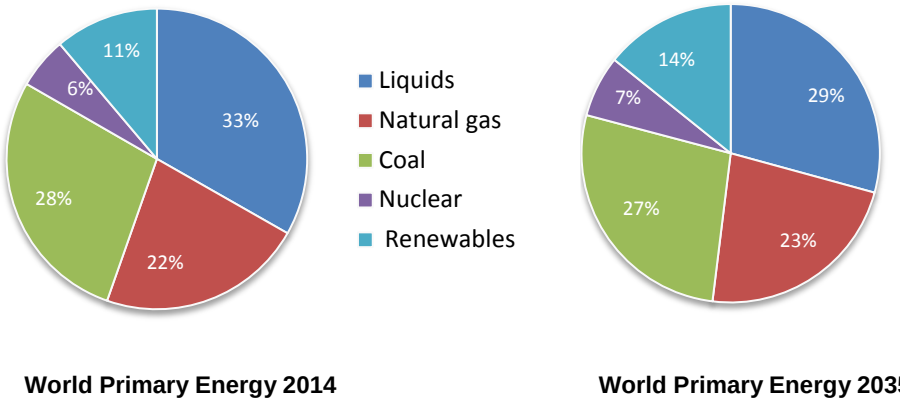

Figure 1.1 World primary energy demand at 2014 and the expected demand at 2035, data from (EIA, 2013)

In many countries, the governments' incentives are to increase the usage of renewable alternatives. The 1.6% per year increasing rate of energy demand, as well as the concerns about the fossil fuels environmental impacts and their increasing prices improves the outlook of increasing the usage of renewable sources of energy.

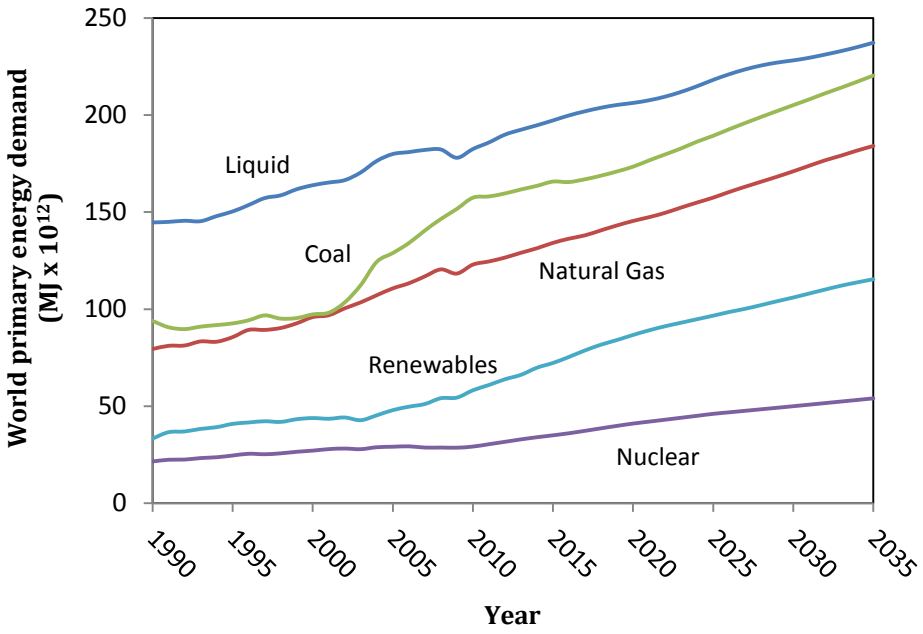

Figure 1.2 World primary energy demand by fuel type, data from (EIA, 2013)

As it has been for the past decades, electricity is expected to be the fastest growing form of energy for use. For the next twenty five years, the annual rise in the net electricity generation is estimated to be 2.3%. It is expected that world energy consumption will increase by about 40% between 2006 and 2030. The growth in the electricity generation is mainly the developing countries where the standards of living rises, infrastructures and population is relatively high (EIA, 2013).

From Figure 1.3, it is clear that coal continues to be the most used fuel for power generation. However, its share decreases as the renewable alternatives, natural gas and nuclear power are expected to advance during the projection area. In the near future, energy cost most likely will be attached to the carbon dioxide emissions through carbon credits and taxes, so researchers and policymakers are more concerned now with the several available alternatives with no or relatively low level of emissions to displace the existing electricity generation systems.

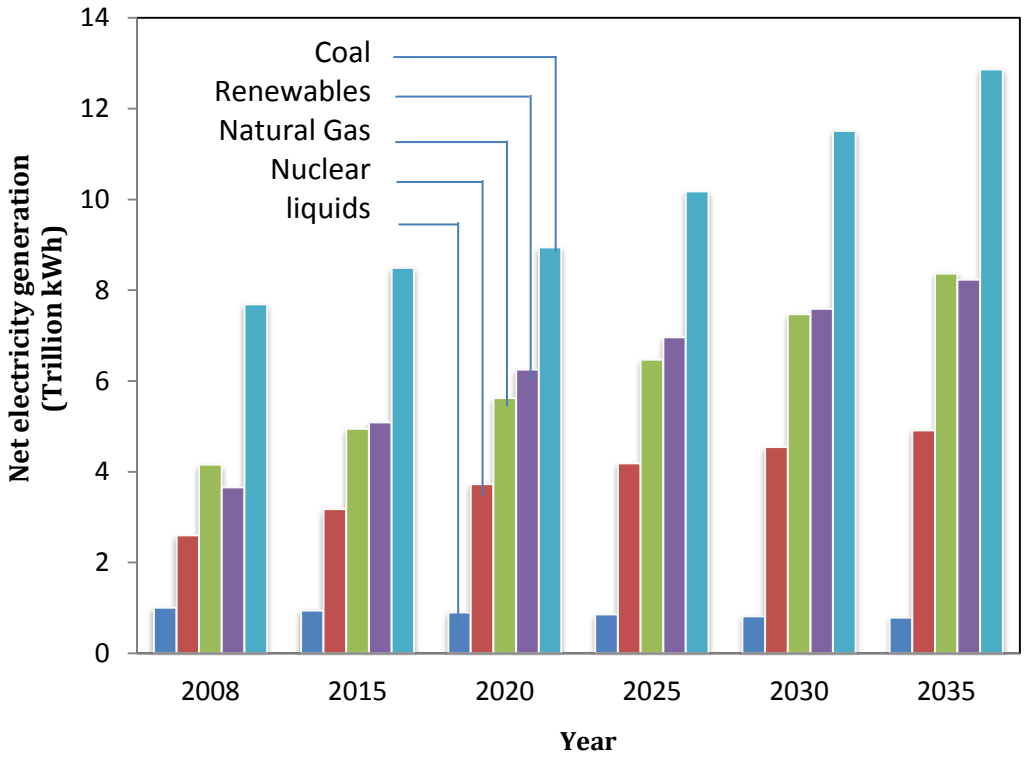

Figure 1.3 World net electricity generation by fuel type, data from (EIA, 2013)

Weizsacker et al. (1998) stated that twice of the current prosperity must be achieved for the next five decades with half the energy and resources demand. Sustainability, industrial ecology and other environmental and societal concerns and regulations all over the world are driving the development and improvement of energy production alternatives. A significant reduction in the fossil fuel consumed per unit energy can be achieved by increasing of renewable energy utilization efficiency, which leads to reduction in greenhouse gas emissions.

One of the main sectors of power generation is providing electricity for rural area and for about one third of the world population living in isolated regions and has no access to an electricity utility grid. The best alternative for this sector is the development of systems depending on the local renewable energy resources.

There are different alternatives for fossil fuels to be used for power production. These alternatives include solar energy, wind, hydropower, geothermal and nuclear energy. Being available for large scale utilization, environmentally benign, and cost effectiveness are the main points that support the solar energy to play the main role of power generation for the future.

The amount of solar energy that reaches the earth annually is about ten thousand times more than the annual global mankind primary energy demand (Quaschning, 2005). Solar Energy can be simply used for heating, cooling and day lighting in residential applications (Sen, 2004).

1.2 COGENERATION AND MULTIGENERATION

1.2.1 Cogeneration Energy System

Cogeneration is simply the production of electricity and usable heat in one process, saving a considerable amount of energy. Cogeneration, or combined heat and power (CHP) based systems are of a great interest because of their high efficiency, reduced energy use cost and lower operating cost. These systems provide a reduction of the environmental emissions due to the reduction of the system emissions per unit energy produced. In fact, cogeneration is not a new technology to be used as it has been around early in the preceding century or even before as the first commercial cogeneration based plant was constructed in 1882 in USA by Thomas Edison (DOE, 2003). Cogeneration

systems are often thermal-electrical generation based stations, except for a percentage of the generated heat that is delivered in the form of a useful product. Generally, in fossil fuel based power generation station, the energy content of the used fuel is converted into heat in the form of steam or hot gases, which is transferred into mechanical energy in the form of a rotating shaft. The mechanical energy is then converted into electricity. Normally, 20-45% of the generated heat is converted to electricity, while the rest is wasted as a rejected heat (Dincer and Rosen, 2007). In cogeneration system, part of the generated heat is delivered as a product, e.g., hot water of steam, and consequently, the electricity produced and the waste heat are reduced. The useful product can be also in the form of providing heat for domestic hot water, heating pools, space heating. It also is of a great use for some industrial processes that demand heat at wide range of temperature, e.g., drying, chemical and metal processing and mining. An overall efficiency of more than 65% can be achieved with cogeneration as it overcomes the significant heat losses that detract greatly from the system efficiency. Generally, the source of generated heat in cogeneration systems is fossil fuel combustion; recently, natural gas is widely used. Other sources as renewable energy sources and burning of waste materials can be used as well.

1.2.2 Trigeneration Energy System

Recently, much research has been conducted on a step beyond cogeneration for the production of more useful outputs. In trigeneration energy systems, a common source of energy is used for a simultaneous production of electricity, heat and cooling as the generated heat can drive an adsorption cooling system (Rosen and Dimitriu, 1993). For residential applications, heating might be needed just for winter and cooling for summer. The overall efficiency of trigeneration systems can exceed 80% with the utilization of the waste heat of a prime mover; e.g., gas or steam turbine, Diesel engine or organic Rankine cycle engine (Al-Sulaiman et al., 2010). Such systems are more financially attractive for facilities with large amount of heating and cooling demands, e.g., hospitals, residential buildings, hotels and chemical and food industries as well.

1.2.3 Multigeneration Energy System

Multigeneration energy systems technique is a step further for achieving a sustainable energy trend and to cope with the market and energy demands. Multigeneration energy

systems are mainly multi-useful products systems using the same prime mover. The useful output rages from hot water supply and potable and fresh water production, to space heating/cooling and hydrogen production. Integrating renewable energy sources with multigeneration systems is one of the most attractive trends. It is reasonable to state that the multigeneration systems efficiency is higher than that of trigeneration and cogeneration systems and of less environmental impact. Figure 1.4 shows an example of a multigeneration energy system with the integration of solar energy, for the production of electricity, hot water, air heating/cooling and water desalination unit. Hydrogen production by water electrolyzing is also considered. For optimizing the useful output of a multigeneration energy system, it should be designed flexible enough to meet the demands variations, and energy storage system should be considered as well to store energy at minimal demand periods.

1.2.4 Benefits of Multigeneration Energy Systems

The main merit of multigeneration energy system is the achieved improved efficiency and the reduction of the operating cost. For a conventional power plant, the maximum overall efficiency does not exceed 39% as more than half of the feeding fuel heating value is lost. This limit goes to about 60% for a conventional power plant that produces electricity and heat separately (Kerr, 2008a). However, with the considering the system prime mover waste heat as a useful product and get it utilized may increase the system efficiency to 80% (Kerr, 2008b).

For on-site power production multigeneration systems, one of the main gains is the significant reduction of electrical transmission and distribution units. This reduces the cost and the energy losses as a loss of about 9% due to electricity transmission and distribution from centralized plants to end users occurs (Kerr, 2008b). The reduction of transmission and distribution units also increases the reliability of the system to the point that the chance of grid failure is negligible, this reduces the impacts of some out-of-hand or natural crisis that might affect the grid, as it happened in the USA and Canada in 1998 where five million people were left in darkness due to an ice storm that destroyed the transmission line and towers (Lecomte et al., 1998) or the famous 2003 blackout that cost

the two countries billions of dollars (Levy and Zernike, 2003). Another benefit of these systems is the flexibility of production with varying demands.

The reduction of fuel used for same output of a conventional power plant is a great benefit of the multigeneration energy systems. This reflects directly to a significant reduction of the greenhouse gas emissions which make it a more environmentally benign option, especially if it is integrated with clear renewable resources. With the utilization of multigeneration energy systems, it is expected that an annual reduction of about 950 million ton of carbon dioxide emissions can be achieved within two decades (Kerr, 2008b).

The achieved improvement in thermal efficiency of the multigeneration energy systems with the above stated benefits, make it an attractive field for researchers and engineers to delve into more investigation on possible integration of systems with a maximum useful output. Further assessments on capital and operating costs are also required to be investigated before selecting the multigeneration plants.

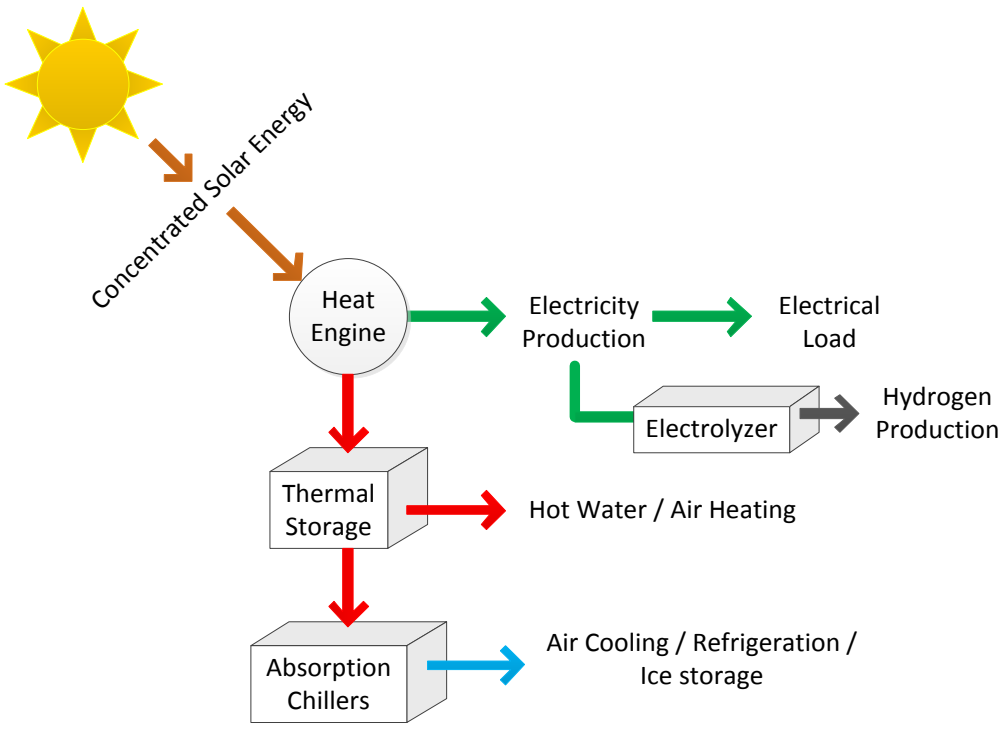

Figure 1.4 Schematic diagram of a typical multigeneration energy system based on solar energy

1.3 PRIME MOVERS

The prime mover is the main component in any energy system and it affects the overall performance and efficiency of the system. Selecting the proper prime mover is the main concern in designing multigeneration energy systems. It mainly depends on the required useful products of the energy system. Thermal, economic and environmental analyses have to be conducted after selecting the prime mover to have a better vision over the feasibility of the selected prime mover for the proposed multigeneration energy system. The characteristics of the prime mover selection are bounded with some guidelines:

- The electricity generation required from the system, considering the efficiency and the possibility of having multi prime mover system. Also the heating and cooling demand should be specified to determine the power to cooling/heating ratios for the system.
- The flexibility to extend the prime mover operating range, e.g., extending the operation as a reheating system in a multi-stage prime mover. Different fuel usage flexibility is also important considering the fuel impacts on the system operation and maintenance cost and its environmental impacts as well.
- The prime mover power density, noise level and emissions are all related to the location and size of the multigeneration energy plant.

1.4 HEAT ENGINE AS A PRIME MOVER

Heat engines are the most well studied and common prime movers to be used in multigeneration systems. They include gas and micro gas turbines, steam turbines as internal combustion engines prime movers. External combustion heat engines, e.g., Stirling engine, are a good candidate as prime mover for multigeneration energy systems. Examples of the heat engines as prime movers are illustrated in the following subsections.

1.4.1 Gas Turbine Engine

Gas turbine is the most common and suitable internal combustion engine to be used in multigeneration energy systems. It operates on the Brayton cycle. Basically, the engine consists of an air compressor, combustor, turbine and generator, and they share the same shaft. The process starts with spinning the turbine shaft by external auxiliary machine to start introducing air to be compressed through the axial compressor, then is mixed with

the gas fuel and passed to the combustion chamber. The mixture is compressed to a point of continuous combustion that drives the turbine blades, increasing the shaft speed. More air and fuel are introduced in turns. The produced rotary mechanical energy is then transferred into electricity through the generator. The hot exhaust residual from the combustion process can be recoverable through a heat recovery steam generator (HRSG) in a multigeneration energy system. The selection of HRSG is based on the gas turbine engine size and it can be used for electricity generation through a steam turbine.

1.4.2 Micro Gas Turbine Engine

Micro gas turbine is one of the most promising technologies for providing power for hybrid vehicles. The principle of operation of the micro gas turbine is on the Brayton cycle. The units ranging from tens to hundreds of kW were developed for small scale distributed power. They are ideal option for distributed generation applications (Scott, 1998). They are also applicable for CHP applications as the waste heat from the engine can be utilized for producing hot water or provide heat for a building space or industrial processes. It can be also used to drive an absorption cooling system in a multigeneration energy system. Even the waste heat from low power units is recoverable and can be used for water and space heating. Modern micro gas turbine engines are of better performance with the advanced components like recuperators and control systems. Micro gas turbines share several advantages with the gas turbine engines as listed below:

- Operates at high power to weight ratio.
- Provides stable and reliable power with low emission levels.
- The rotary motion of the engine results in less vibrations, lower noise level and higher reliability when compared with the stoke-based engines, e.g., the Diesel engines.
- Uses excess air that results in lower emissions
- Complicated liquid cooling systems are not required.
- High potential for hybrid integration with fuel cells.
- Micro gas turbines have flexibility to be stacked in parallel for large loads.

The two major disadvantages of micro gas turbine engines are the high sensitivity to ambient conditions and the requirement of high skilled technicians. The efficiency of

microturbines ranges from 28%-32%, which is relatively low when compared with the efficiency of the conventional reciprocating internal combustion engines that sometimes exceed 38%. The micro gas turbine overall thermal efficiency rises to about 80% when a recuperator is engaged, but the electrical efficiency falls in this case. The waste heat can be utilized through a HRSG to provide domestic hot water and hot water for fan coil heating units in residential applications. A steam ejector refrigeration system can be used for cooling purpose as well.

1.5 FUEL CELL AS A PRIME MOVER

Fuel cell is an electrochemical energy conversion device that produces electricity directly from chemical energy, and the by-products are only water and heat. It is really so convenient to be a prime mover for a multigeneration energy system. It is seen by many pioneers that fuel cell is the solution to a whole range of environmental challenges, such as global warming and harmful levels of local pollutants. It also provides economic benefits due to the high efficiency and flexibility. Fuel cells have several highly attractive characteristics. The efficiency of a fuel cell can be higher than other conventional energy conversion processes and they perform well even at partial loads. Normally, the fuel used is hydrogen. Fuel reformation adds the benefit of fuel flexibility, where hydrocarbon fuels can be used. Furthermore, the lack of moving parts and modular design make the maintenance easy and improve system reliability. Fuel cells are classified according to the nature of the electrolyte. Each type requires particular materials and fuels and is suitable for different applications. There are six main types of fuel cells. Descriptions and characteristics of different fuel cell types are illustrated in Table 1.1.

On-site power generation has a potential of utilizing the fuel cell generated heat as a useful output, resulting in an increase the overall efficiency of the fuel utilization by CHP (Croper, 2004). Small scale CHP fuel cell system, 100 kW up to several MW, is seen to play an important role in electric power generation in developing countries. Future growth in power consumption is expected in these countries. Growth is projected to occur at a rate that will not allow the lengthy process of planning and building large central power stations (Hoogers, 2003). PEMFC or SOFC are good candidates for covering CHP demands of private households or small businesses, in the range of 10 kW.

Table 1.1 Description of different types of fuel cells

		T(°C)	Fuel	DESCRIPTION
Low temperature FC	AFC	50 – 220°C	H_2	One of the most developed technologies used since the 1960s by NASA. Their electrolyte consists of potassium hydroxide KOH at different concentrations. The fuel is pure hydrogen. AFCs are among the most efficient types in generating electricity of about 0.3 to 5 kW at nearly 70% efficiency.
	PAFC	190 – 220°C	H_2	The first to be commercialized. It uses 100% concentrated phosphoric acid H_3PO_4 electrolyte which be well ionic conductor in range 150~220°C. Hence, it can be used for cogeneration. It generates electricity at more than 40% efficiency, for cogeneration applications, it reaches 85%.
	PEMFC	60 – 95°C	H_2	PEMFC uses an electrolyte which is a layer of solid polymer which allows protons to be transported from one half of the cell to the other. It requires a limited operating temperature and an accurate control of fuel humidity. Recent development focuses on operation in 160°C range using new membrane. It can produce electricity at 40 – 50% efficiency.
	DMFC	50 – 120°C	CH_3OH	Initially developed in the early 1990s. It is similar to PEMFC but uses methanol as the fuel. It is used for powering mobile phones and laptops. Methanol delivers hydrogen ions directly to the anode then penetrate through the membrane towards the cathode.
High temperature FC	MCFC	630 – 700°C	H_2, CO	MCFC operates at high temperature where the salt mixture electrolyte melts producing highly ionic carbonate ions (CO_2^{3-}). It exhibits higher efficiency and greater fuel flexibility that make them a good candidate for CHP applications. Designs for units with output of 2 MW to 100 MW are developed. It operates at up to 60% efficiency and it reaches 80% when by-product heat is utilized.
	SOFC	700 – 1000°C	H_2, CO	It's a leading candidate for high-power stationary applications due to the high temperature, where high pressure steam can be generated. It uses a ceramic electrolyte and can be fuelled with a variety of gases. The efficiency of electricity generation is high, about 60% and goes up to 70% when combined with a turbine or hybrid engines.

*data are compiled from Hocevar (2007) and Williams (2011).

1.6 SOLAR ENERGY AS PRIME SOURCE

Entering the new solar age, a vision of solar based electricity generation system had been put in focus by research and development sector, politicians and policymakers as well. Huge efforts are put, technologically and politically, into integrating the renewable energy systems based mainly on solar power, with the existing conventional systems that are in use (Lynn, 2010).

For remote areas and new communities built in desert areas; like in Egypt and new costal extensions, the renewable energy based systems with energy storage technology is the most inspiring options to be utilized. There are limitations of using the regular Diesel generators for such applications. The nature of remote areas increases the difficulties and expenses of fuel supply. Batteries are commonly used for storing energy for certain application in remote areas; however they are not a sustainable alternative as they lose 1-5% of the energy content every hour. They can be only used for short periods of time (Wichert et al., 1999). Hydrogen based systems are a great alternative. There are a wide variety of hydrogen based technologies that can be used for electric power production for remote areas applications. On-site solar based produced hydrogen can be used to fuel heat engines coupled with electricity generators for power production (Patro, 1993; White et al., 2006). Some modifications can be done to the regular fossil fuel internal combustion engines to be run on hydrogen (Henriknen et al., 1979). Hydrogen gas and steam turbine generator are other alternatives (Justi and Bockris, 1987). Hydrogen fuel cell technology is the most recent competitive. It can be integrated with solar photovoltaic to be used as a load-leveling electric system when photovoltaic system is not efficient due to climate and weather conditions (Agbossou et al., 2001).

In this section, the solar harvesting options that can be utilized through the new development trends for deserts, urban and coastal areas are highlighted. Solar based prime movers are also covered. Solar energy can be utilized indirectly; in the form of wind, hydro and tidal power, or in a direct way; in the form of thermal energy or photochemical energy. In the figure below, the available direct utilization of the adopted of solar energy are shown. Photovoltaic technology would seem to be the magical solution at the first glance, however; it is still of high cost, even for mass production. Therefore, it is

reasonable to consider the conventional indirect conversion of solar heat as an intermediate step. Even if this solution appears to be less desirable as it introduces the concept of Carnot with its limitations, but its advantages seem to be worth reconsidering when one compares cost situation with the highest available efficiency of PV. Figure 1.5 shows a schematic of a solar based system for covering the essential demand of residential applications besides hydrogen production.

1.6.1 Thermal-Solar Energy

As it is shown in Figure 1.6, solar thermal energy applications can be classified into two different categories, according to the temperature, to low and high temperature applications. Domestic solar water heating (DSWH) is the most common application for active solar low temperature applications. Table 1.2 gives a view over other applications.

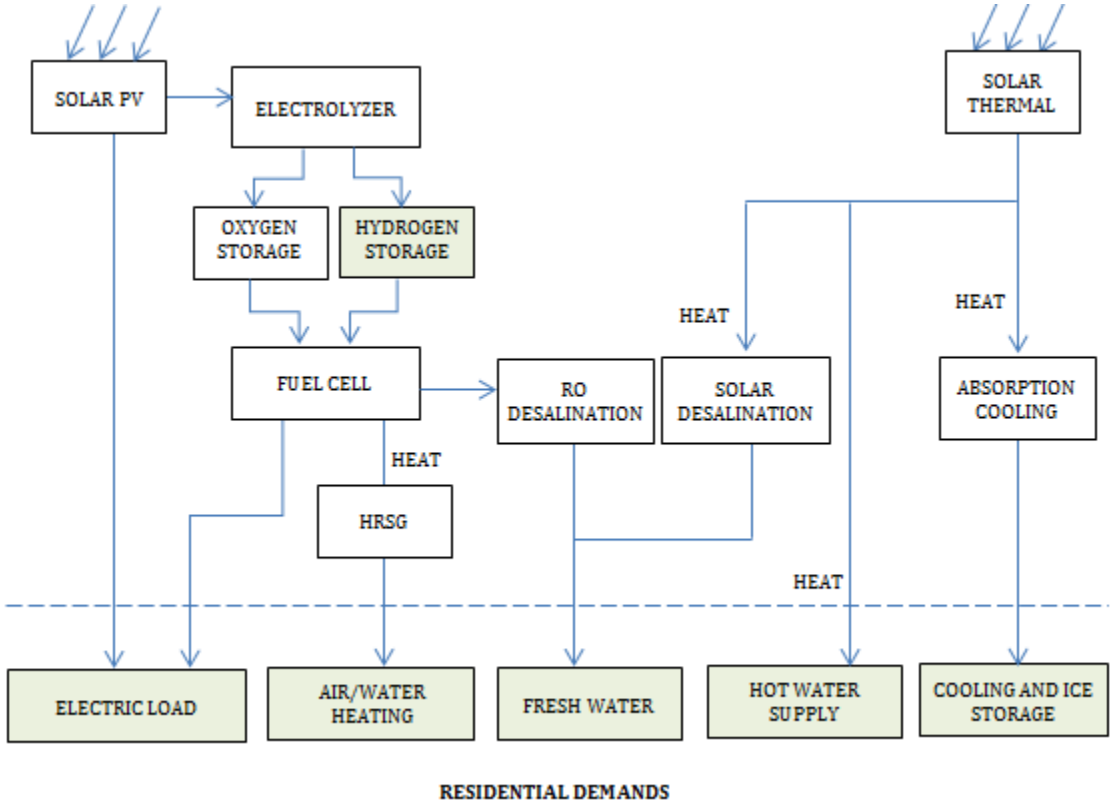

Figure 1.5 Schematic for a solar driven system for hydrogen production and covering residential demands

High temperature solar thermal power applications commonly work on producing steam that is used to drive a conventional steam turbine for electricity production (Patel, 1999; Sorensen, 2011). It has an advantage over the conventional thermal electricity generation systems as it does not need any fossil fuel that contributes in greenhouse gases emissions. However, fossil fuel still can be used as backup when the solar thermal power is not available. In Fact, the environment is the major beneficiary of this clean technology (Justi and Bockris, 1987). The solar concentrator technologies are a promising candidate to be integrated with multigeneration energy systems for electricity and hydrogen production besides other useful products.

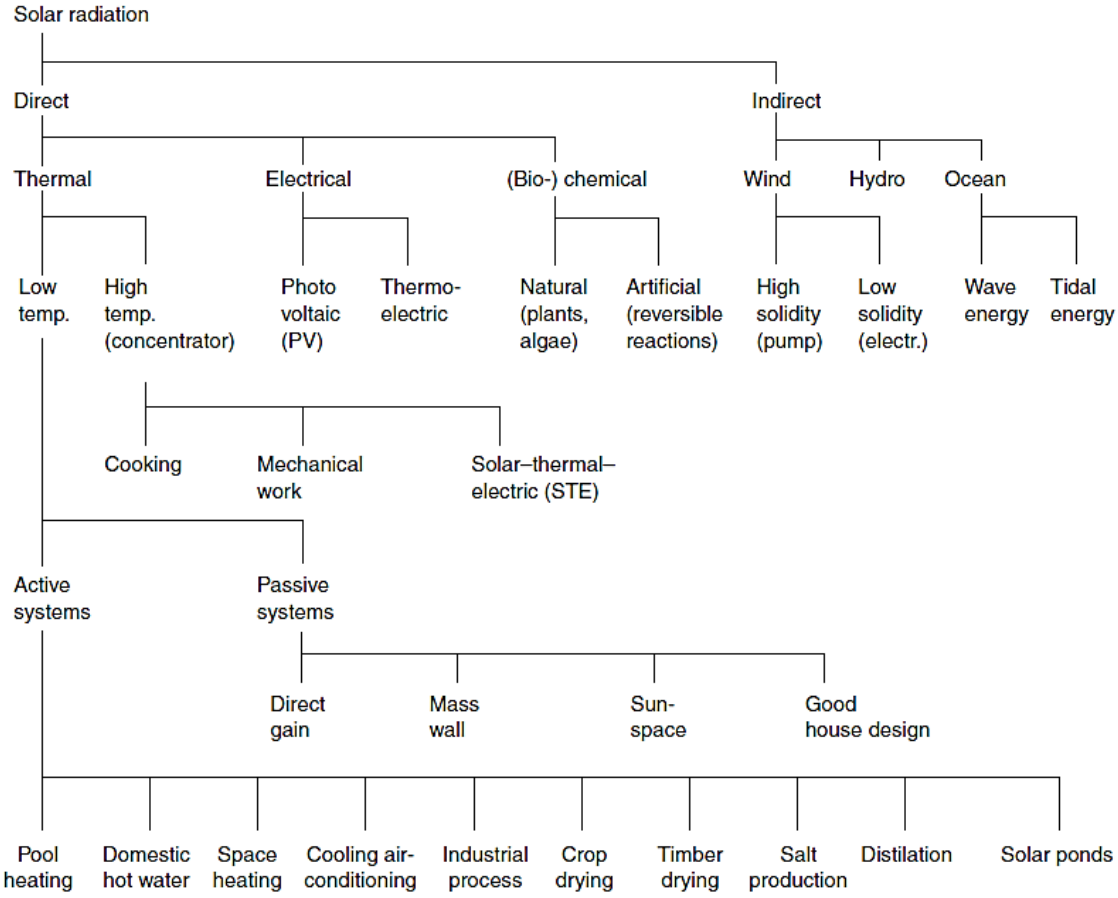

Figure 1.6 Solar energy conversions and technologies (Szokolay, 2004)

The best known technologies for electric power generation from solar thermal energy on large scale are the parabolic trough, parabolic dish and heliostat field collectors (solar power towers) as well as hydrogen production. They have a cohesive relation to urban development and high potentials for desert development, besides the very large scale PV (VLS-PV) and concentrated PV. Energy constituent for urban development in desert regions needs integrated systems of energy; solar energy here can provide energy as a main production and integrated to produce fresh water and other usable products besides electricity generation. Social development is considered one of the most important issues for desert development and the integrated variable types of communities as agricultural, industrial and technological communities.

Table 1.3 shows a comparison between the first three technologies; parabolic trough, parabolic dish and solar heliostat field collectors. A typical solar thermal power system can provide energy at full load for 2000 to 3000 hours annually. Sometimes solar thermal power generation on large scale is considered a land-intensive technology. However, the energy production capability of a solar thermal system is larger than that of conventional ones of the same proportions (Simoes and Farret, 2004).

a. Parabolic trough Concentrator (PTC):

The parabolic solar trough is considered the most commercially matured concentrated solar power technology. It is designed as parabolic long trough-shaped reflectors that work on focusing the sun energy on a pipe running along the mirror focal line. The pipe is likely made of a black metal and its surface is covered with a coating that increases the solar absorbance and lowers the thermal emittance. The pipe is encased in a glass tube for a lower convection heat loss, and vacuum is applied in the space between the metal and glass tubes for more heat loss prevention. The glass tube surface is often coated with an anti-reflective coating for better transmissivity.

The heat transfer fluid (HTF) flowing through the receiver pipe usually an absorbent oil or water. HTF in pipes absorbs the heat reflected off the trough and transfer the thermal energy to water through a heat exchanger to produced high pressure steam (at around 100 bar at temperature up to 400°C) which is used to drive a conventional turbine (Valenzuela et al., 2005).

The parabolic cross sectional design of the trough increases the conversion efficiency. A sun tracker can be provided for large scale systems by including a rotating shaft to allow each group to follow the sun. Yaw controllers can be used for large systems to achieve more precision to a fraction of a degree. The reflectors have to be made of a high reflectance material. Silver is the ideal candidate as a reflector, however; aluminum is preferred as it is cheaper and easier to be protected against the corrosive environmental effects. The reflector's surface has to be kept clean to avoid the efficiency degradation. The maximum optical efficiency of such a system is 70 - 80%. However, about 60% is useful, considering the heat loss in the solar field piping. The optical efficiency is a measure of how much sunlight is reflected into the system (Fanchi, 2004). Parabolic trough plants are commonly used to generate power for providing hot water, steam, air heating and cooling, desalination, industrial processes heating and electricity generation.

b. Parabolic Dish Concentrator (PDC):

The solar dish is the most appropriate alternative for stand-alone applications in remote areas. It is a point-focus collector that can reach a high level of light concentration up to 1000 sun at a temperature of 1500°C. It produces electric power efficiently ranging from few watts to several kW at a high temperature of about 800°C. This system is of a high efficiency because of the high concentration ratios achievable. Several units can be combined for higher power production. Parabolic dish systems are constructed of a mirror array in the shape of large parabolic dish. A two-axis sun tracking system is used to maintain light convergence at the dish focal point. Solar radiation energy is concentrated on a receiver mounted at the dish focal point as heat. The most convenient scheme for power conversion is to mount a heat engine near or at the focal point of individual dishes to absorb the thermal energy from the receiver and use it for electricity production from mechanical work. The other scheme of power conversion is to have a heat transfer fluid connecting the receivers of several dishes and conducting the collected concentrated thermal energy to a central power generation plant. Gas turbine engines, combine gas and steam turbine engines and Stirling engines are the most prevalent candidates to be used with PDC for electricity production. The Stirling engine is applicable for temperature

lower than 950°C, and for a higher temperature, gas turbine and combined cycles work more efficient (Karabulut et al., 2009).

c. Heliostat Field Concentrator/Solar power tower (HFC):

Heliostat field is one of the most recent concentrated solar power technologies to emerge into commercial utility. The HFC are typically designed in large scale, for more than 10 MW to be economically beneficial. They work on capturing and concentrating the solar energy on a field of reception mirrors. Heliostat sun tracking mirrors are distributed in rings around a central tower. The heliostats concentrate the solar thermal energy on a receiver mounted on the tower containing a fluid that most likely is circulating in a closed loop. The fluid can be water, air, molten salt, diluted salt, oil or liquid metal. Each heliostat has a surface area ranging from 50 – 150 m^2 and sits on a two axis tracking mount. The towers typically stand for 75 – 150 m height.

The first heliostat plants incorporated are the one MW plant of the European community that was built near Genoa in 1976 (Justi and Bockris, 1987) and the 10 MW Solar One and Solar Two that were built in Mojave desert in California in 1981 and 1995, respectively. The amount of radiation focused on a single receive of a heliostat plant is as high as 200 – 1000 kW/m^2, and the huge solar flux towards the receiver yields concentration ratios as high as 100 – 1500 sun, which results in operating at a temperature more than 1500°C.

Mounting the receiver on a tall tower helps to decrease the distance between mirrors to avoid shading; however, grounded central receiver has been proposed and studied by mounting a secondary reflector on the tower to reflect the concentrated solar flux to the receiver placed at the ground level (Segal and Epstein, 2000).

The solar tower reflector technology can be integrated with solar reforming of methane by concentrating and reflecting the solar flux onto the solar reformer that rests at the ground level. It can also be integrated with concentrated photovoltaic (CPV). It this proposed design, the solar spectrum is split into thermal and PV-used portions. A HFC-CPV with considering splitting the solar spectrum was studied by Segal et al. (2004).

Table 1.2 Active Solar thermal applications

Domestic Solar Water Heaters (DSWH)	
In its simplest form; water, driven by thermosyphon principle, is heated through solar collector and return to a pre-heat storage tank. The figure shows an indirect heater with a separate solar primary fluid loop. Normally the storage temperature is ~65 °C and the average person uses 100 L of water a day.	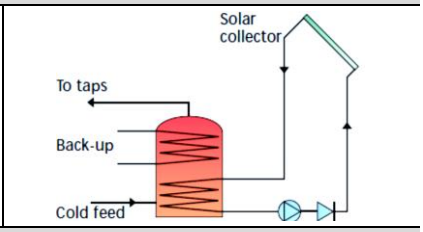
Water Desalination and Distillation	
It is one of the most attractive applications for using solar thermal energy especially in the developing countries that are in lake of fresh water resources. The figure shows a solar still system that is similar to a greenhouse. Solar heat is absorbed by the black basin that contains the sea water to evaporate and condenses on the cold glass walls. Distilled water droplets run down are collected for use.	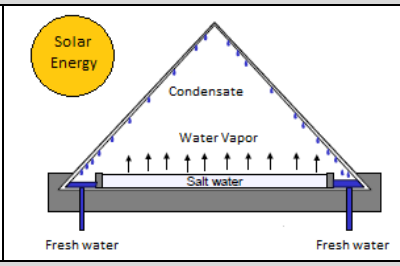
Swimming Pools Heating	
It is one of the ideal applications of solar thermal energy as peak energy availability coincides with peak usage. It can be used for outdoor and indoor pools with direct and indirect solar heating which is similar to the DSWH systems. For a 5°C above ambient temperature, a collector in between 50-80% and 40-60% of the pool surface area is required for outdoor and indoor pools, respectively.	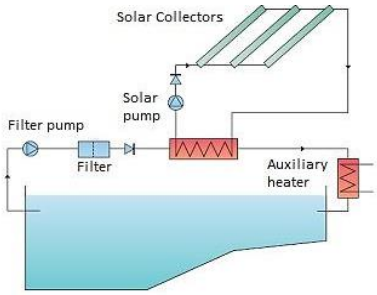
Solar Cooling	
Solar cooling systems are of a great interest as the cooling demand for residential is usually in coincidence with the sunshine availability. In closed absorption and adsorption systems, solar heat is used to regenerate the sorbent. In open systems, a desiccant system provides a cooled and dehumidified air, and solar heat removes water from the desiccant.	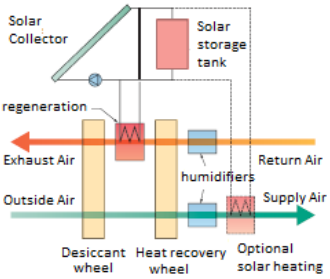
Air Heating	
For domestic heating, a 5 m^2 roof mounted flat plate collectors with a fan can be used to pre-heat the ventilation air which can be drawn from outside or being circulated from the building. For an input air temperature of 6°C, an output of 30°C can be achieved.	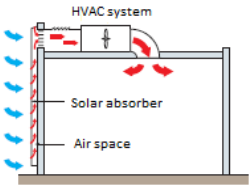
Crops and Products Drying	
This application can be conducted by either exposing the product to the sun, and the product may be covers, or expose the product to a solar heated air bowing through or over the product. It is used for drying grain, fruits, palm, rubber, etc.	

*modified drawings are adopted and processed from Miller (2004) and Rawlings (2009).

Table 1.3 Different solar thermal concentrators' technologies

	Schematic	System Description	Operating Temperature (°C)	Concentration Ratio (sun)	Thermodynamics Efficiency	Figures
Parabolic Trough	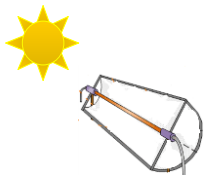	Parabolic sheet made of a reflective material used to concentrate the solar flux and transfer it to a heat transfer fluid flowing in a linear reservoir of a metal pipe.	50 - 400	15 - 45	Low	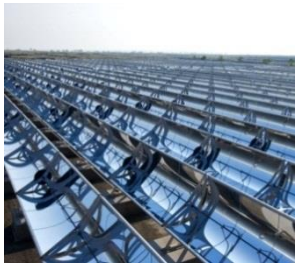
Parabolic Dish	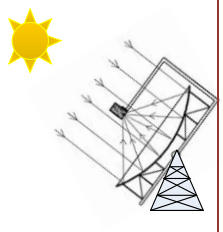	Reflective parabolic dish with a receiver at its focal point, Stirling engine can be mounted at the focal point for direct electricity production.	150 – 1500	100 – 1000	High	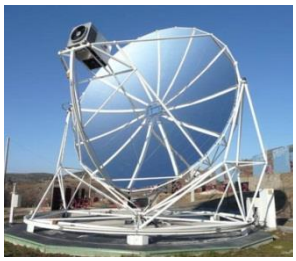
Heliostat Field	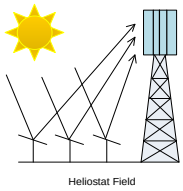	Large heliostat field used to concentrate solar flux over a reservoir mounted on a tower where energy is stored or integrated with a steam power cycle.	300 – 2000	100 – 1500	High	

*Concentration ratio is the aperture area divided by the absorbing receiver area.
*Data are compiled from Kalogirou (2004) and Barlev et al. (2011).

Chapter 2

LITERATURE REVIEW

There have been several research and development studies conducted to investigate the performance and feasibility of cogeneration and trigeneration energy systems. However, very few comprehensive studies have been performed on the performance of multigeneration energy systems. Multigeneration energy systems are mainly distinguished by their prime movers. Review of the available literature is done based on the prime movers used in the studied system. This literature review addresses the up-to-date research works on cogeneration and trigeneration energy systems.

2.1 HEAT ENGINE AS A PRIME MOVER

Several studies were conducted on internal and external combustion engines, micro gas turbine as prime movers for single or multi-prime mover based cogeneration and trigeneration energy systems.

2.1.1 Internal Combustion Engine

Energy analysis was performed in many studies in the literature. Five different schemes of trigeneration systems in supermarkets were studied by Maidment and Tozer (2002) with different absorption chillers. An energy analysis was performed and the results showed that significant primary energy savings were achieved with reduction in carbon dioxide emissions compared to coal and gas powered systems for electricity production. Miguez et al. (2004) conducted performance assessment for a developed tri-generation plant with a reversible heat pump. Porteiro et al. (2004) investigated the same developed system at different modes of operation. They found that the system performance was enhanced. Huangfu el al. (2007b) studied the performance of a micro-scale building CCHP integrated with adsorption chiller system, experimentally. Thermal and economic analyses were performed in several earlier studies. Chicco and Mancarella (2005) introduced energy indicators for assessing the fuel efficiency of a trigeneration integrated energy system. Chicco and Mancarella (2006a) performed comparative study on different

cooling systems. They studied the change in pay-back time for six designs with respect to variation in electricity and of gas prices.

Few studies were conducted on exergy and exergoeconomic analyses of cogeneration and trigeneration energy systems with internal combustion engines as a prime mover. Tracy et al. (2007) thermodynamically studied the effect of splitting the waste heat of a trigeneration system proportionately between heating and cooling systems based on first and second laws of thermodynamics. Huangfu et al. (2007a) studied a micro-scale trigeneration system, integrated with an adsorption chiller cooling system. They performed economic and energy analyses on the system. From the exergy analysis, they showed an improvement of the engine electrical efficiency causes an improvement of the trigeneration system performance.

2.1.2 Gas Turbines and Micro-Gas Turbines

Many studies were performed on gas turbines as a prime mover for cogeneration and trigeneration energy systems. A simple model for different gas turbine was developed by Calva et al. (2005). Their model discussed the design of trigeneration energy systems. Ziher and Poredos (2006) performed economic analysis on a trigeneration system for a hospital building. Steam absorption along with compression cooling system integrated with cold storage facility was proposed for cooling purposes. An exergy analysis was performed on a trigeneration energy system based on a gas turbine by Khaliq and Kumar (2008). They investigated the effect of compressor pressure ratio variation and process heat pressure on first and second law efficiencies and electrical to thermal energy ratio. Further studies were performed by Khaliq (2009) on the same system to include the effect turbine inlet temperature variation, pressure drop percentage of combustion chamber and HRSG and evaporation temperature. The results showed that combustion and steam generation contributes with more than 80% of the system exergy destruction. Cao et al. (2004) carried out exergy and exergoeconomic analyses to investigate the performance of power generation with covering heating and cooling demands of a building. They examined the effect of power load on the system performance, measured in energy and exergy efficiencies and the exergetic costs per unit of power produced. They concluded that the model is economically viable when power load rates are higher than 50%.

Numerous studies on micro turbines as the only prime mover of a cogeneration and trigeneration energy systems were found in the literature. Jaaskelainen and Wallace (2009) conducted energy and economic analyses for a trigeneration system powered by a microturbine of 240 kW. The economic analysis of this system showed that it is not recommended to use the proposed microturbine due to low electricity rates with respect to the natural gas price. Medrano et al. (2006) performed a comparative exergy study of three different trigeneration integrated energy systems. The proposed systems are integrated with a single effect, a double effect and combined single and double effect absorption chillers. They concluded that exergy efficiency variation of the three plants is less than 1%. Liang and Wang (2007) conducted a study on microturbine based trigeneration system. They evaluated the system exergy efficiency considering integration of double effect absorption chiller for cooling. They performed exergetic comparative analysis measured by the exergy efficiency of the proposed system with a system that uses electrical chiller instead. It was found that trigeneration energy system with absorption chiller is of higher exergy efficiency. Several gas turbine plants, based on the well-established closed cycle gas turbine technologies, are in operation for over hundreds of thousand hours. The main advantages of this technology is its adaptability to a wide range of fuels, e.g., gas, oil, coal, solar and nuclear fuels and the possibility to use different working gases, e.g., air, helium, nitrogen, carbon dioxide, argon, neon or their mixtures. Helium is the one of the most suitable working fluids for large closed cycle gas turbine plants. Helium turbines, based on a closed Brayton gas cycle, are also considered proper alternative for efficient power generation for nuclear reactors. Helium is radioactively stable, inert and a non-corrosive gas (Conn and Kuo, 1976; Frutschi, 2005; Horlock, 2002).

In addition, helium gas turbine is a candidate as a multigeneration energy system for different purposes. The heat rejected from the plant is available at high temperature. It can be utilized for combined cooling and heat production, water desalination, process steam and industrial process heat in integrated chemical plants. In early 60's, two helium closed cycle gas turbines were built for power generation and air liquefaction; heat was provided to the gas at 650 - 660^{o}C and 18 - 23 bar through a natural gas furnace. In 1974, a helium gas turbine achieved 30 MW of power production, when the turbine was fed

with helium at 750^{o}C and 27 bar (Frutschi, 2005). Helium turbines are also integrated with nuclear reactors where heat is to be provided through a molten salt blanket or heat exchanger that transmits the heat from the reactor cooling system to the helium turbine plants. Conn et al. (1976) studied a conceptual design of 500 MW helium gas turbine units to be utilized with a nuclear reactor. The operating turbine inlet temperature was set to 870^{o}C at around 68 bar. Solar energy is a good source of heat to helium turbines as well. The low density and high thermal capacity of helium facilitate a more efficient operation of the gas turbine at more compact design of the heat exchangers of the system. Heat can be provided using heliostat solar towers or parabolic dish technology and it can be concentrated to a high pressure helium heater or through a molten salt heat exchanger with storage tank.

Various studies in the literature have been undertaken to investigate the performance of helium gas turbine power plants. No et al. (2007) performed a review study on helium turbines which work with the high temperature gas cooler reactors. A model for calculating the design point performance of the gas turbine plant was developed in this study. Transient analysis software for high temperature cooled reactor helium gas turbine was developed by Wenlong et al. (2012). A review on the helium gas turbine history and the operation experience from different test and power facilities was performed (McDonald, 2012), focusing on the helium turbines powered by the nuclear heat as well. Multi-reheat helium gas turbine was investigated (Zhao and Peterson, 2008) at different turbine inlet temperature values and achieved a thermal efficiency of 39% to 47%, respectively.

The thermodynamic assessment of closed cycle gas turbine plant is performed at different operating conditions at steady and transit operation. A recuperative closed cycle gas turbine of a scramjet was thermodynamically investigated (Qin et al., 2010). They presented a thermal management system for reducing the hydrogen cooling flow and also studied the effect of different operating parameters on the system performance. A Study by Gandhidasan (1993) was performed to study the effects of different pressure ratio on a solar driven closed cycle gas turbine.

2.2 SOLAR ENERGY AS A PRIME SOURCE

Limited research was carried out on multigeneration solar energy driven energy systems. Buck and Fredmann (2007) experimentally studied a trigeneration system based on microturbine and assessed by small solar tower. Their study assessed the economics of using single and double effect absorption chiller which shows a clear enhancement of the system performance and lower operating cost, with respect to single effect absorption chiller. A significant saving in energy and reduction in carbon dioxide emissions are reported by Medrano et al. (2008) when solar thermal collectors were used to support the production of heating and cooling provided by trigeneration integrated energy system operated by an internal combustion engine. There are several recent studies on solar based co-, tri- and multigeneration systems. Cho et al. (2014) conducted a comprehensive review on conventional and unconventional CHP and CCHP systems. Most current studies with their key parameters have been discussed in detail. Al-Sulaiman et al. (2011) modeled a new solar based tri-generation system using exergy analysis. PTSCs are used for the analysis and the system is integrated with an ORC system and absorption chiller, where the maximum tri-generation efficiency has been found to be 20% with thermal energy storage option. Rosiek and Batlles (2013) investigated solar based building cooling, heating and power generation applications (BCHP). An investigation on solar absorption solar geothermic and solar electric compression systems has been conducted. Solar absorption BCHP system has the only energy saving potential. Chua et al. (2014) evaluated the potential of renewable energy based CHP plants on a remote island, depending on the climate and other environmental parameters. Three different schemes for tri-generation is proposed where US$150,000 can be saved by renewable energy based tri-generation application.

A new CCHP plant was proposed by Wang et al. (2012) where a parametric analysis was conducted to analyze the performance of the system working with a transcritical CO_2 cycle using solar energy as the heat input. Meng et al. (2010) conducted a solar based CCHP system with additional input of industrial waste heat, to produce power and refrigeration. Integration performance of the system is reported to be better than traditional CCHP systems. Ozcan and Dincer (2013) conducted a parametric study

for a tri-generation system utilizing the waste heat from the SOFC system and solar energy as the assisting energy source for an integrate ORC system. The proposed plant showed up to 85% efficiency with solar integration and waste heat utilization.

2.3 MULTI-PRIME MOVER SYSTEM

Few studies were conducted considering systems with multi-prime movers. A new integrated trigeneration system with micro gas turbine, SOFC and single effect absorption chiller was proposed by Velumani et al. (2010). The results show that the energy efficiency of system is about 70%. The feasibility of the proposed system was studied through cost analysis. Chung Tse et al. (2011) studied the performance of a trigeneration system based on SOFC and gas turbine for marine applications. It was concluded that an increase of 47% in the generated power was achieved as compared to the power generated for a conventional SOFC and gas turbine with HVAC system.

2.4 COGENERATION AND MULTIGENERATION SYSTEMS

Several studies in the literature investigated the biomass gasification. Schuster et al. (2001) performed an extensive parametric study on a dual steam gasifier for CHP. They studied the effect of the gasification temperature, fluidization agent and water content on the performance of the system. Cohce et al. (2011) performed an efficiency assessment for biomass gasification process for hydrogen production. They presented a simplified model for energy and exergy analysis considering chemical equilibrium. SOFC, among the different types of fuel cells, is the most suitable type to be integrated with biomass gasifiers. The high operating temperature of SOFC, relative tolerance to fuel contaminants, and high energy conversion efficiency make SOFC the suitable candidate to be integrated with biomass gasification technology and to be fed with the produced biogas for clean energy production. Athanasiou et al. (2007) performed energy analysis and optimization study on integrated gasification and SOFC system. Wongchanapai et al. (2012a) investigated the performance of a small scale integrated biomass gasification and SOFC system. They studied the effect of different gasifier and fuel cell operating parameters on the system performance.

Molten carbonate fuel cell (MCFC) technology has great potential for combined heat and power (CHP) applications. Much research showed that for electric power generation, the integration of MCFC systems with gas turbines enhances the overall performance of the integrated system (Rashidi et al., 2008; De Simon et al., 2003). Yoshiba et al. (2004) studied a high efficiency MCFC-GT system in partial load operation with applying a pressure swing air compressor. Varbanov et al. (2005) showed that the efficiency of a MCFC integrated with a gas turbine nearly reaches 70%. Optimization of the lifetime of a biogas fueled MCFC-GT hybrid system with hydrogen production was studied by Nicolin and Verda (2011). There are other studies on portable applications of CHP using MCFC integrated with gas turbine as studied by Specchia et al. (2008). In these studies, thermodynamic analyses based on the first law of thermodynamics were conducted. Applying the second law of thermodynamics, along with the exergy concept, while studying the overall plant performance is very important to know the extent of losses within the thermodynamic system (Akkaya et al., 2008; Rashidi et al., 2009).

Rashidi et al. (2009) performed parametric studies and energy and exergy analysis for a hybrid MCFC-GT system to investigate the fuel cell and the overall system performance. An exergy efficiency of 56.2% was achieved for the overall system performance compared with 57.4% for the overall energy efficiency. An exergy based thermodynamics analysis was performed by Haseli et al. (2008) in the study of the performance of a combined SOFC-GT system for power generation. The energy and exergy efficiencies achieved were 60.6% and 57.9%, respectively. In the recent years, there has been a significant increase in the low-grade heat recovery and renewable energy market. Geothermal energy is considered one of the most reliable and relatively least-expensive source of renewable energy. To utilize this energy, the organic Rankine cycle (ORC) is a promising technology for converting this energy into useful power. ORC also has the benefit of being simple in construction, system components are available, and being of high flexibility and safety (Algieri and Morrone, 2012; Quoilin et al., 2011; Roy et al., 2011; Wei et al., 2007).

ORC is a potential candidate for integrated systems and multigeneration. Considerable research has been conducted to study the performance assessment of the organic Rankine cycle that is based on geothermal and solar energy sources. Researchers

studied the choice of an appropriate working fluid, optimal reinjection condition of the geothermal fluid, the ability of cogeneration and the economic analysis of such a system. One of the main challenges in the study of ORC is the choice of the working fluid and the cycle design to achieve the highest performance (Uehara et al., 1997). Madhawa Hettiarachchi et al. (2007) studied the performance of ORC using different pure working fluids. Karellas and Schuster (2008) simulated the processes of the ORC using normal and supercritical fluids, and studied the variation of the system efficiency in various applications. Badr et al. (1985) studied the characteristics of ideal working fluid for an ORC operating between 120^{o}C and 40^{o}C. A comparative study and optimization analysis was conducted by Shengjun et al. (2011) on subcritical and transcritical geothermal based ORC. They found that among sixteen different working fluids, R125 led to an excellent economic and environmental performance for a transcritical cycle, and R123 gave the highest energy and exergy efficiencies for a supercritical cycle. Tchanche et al. (2010) showed an increase of 7% in the energy efficiency of an ORC integrated with a reverse osmosis desalination system when a regenerator was used. The optimization analysis of ORC is performed based on the heat exchanger area and the exergy destruction in heat exchangers as the main parameter of study in different studies (Franco and Villani, 2009; Madhawa Hettiarachchi et al., 2007; Shengjun et al., 2011). Some research analyzed the geothermal ORC systems economically and exergoeconomically (Heberle et al., 2012; Nafey et al., 2010; Quoilin et al., 2011). They studied the effect of different operating parameters of the ORC and the geothermal fluid conditions on the cost rates associated with the energy and exergy streams through the system.

2.5 MOTIVATION

Multigeneration energy systems are of a great importance and are of high potential to pursue high efficiency output at lower emissions per unit energy used. Besides electricity and hydrogen production, the useful products of such a system include hot water, space heating and cooling and fresh water supply. Integrating renewable energy resources with conventional ones in a multigeneration energy system amplifies its importance, considering the issues that arise with fossil fuel based energy systems, like global warming and the depletion of fossil fuel resources. Multigeneration energy systems are

the most convenient option for providing the demands of rural and new residential applications away from the central grid. These systems are of a great interest of researchers.

From the literature, one can see that there are several researches on the analysis of cogeneration and trigeneration energy systems. However, not enough research has been conducted on multigeneration energy systems, especially, renewable based multigeneration systems. There is a great lack of the studies on multigeneration systems exergy, exergoeconomic and exergoenvironmental analyses.

2.6 OBJECTIVES

The main objective of this work is to propose three novel multigeneration energy systems integrated with solar energy. Energy and exergy analyses will be conducted to find the best performance of the systems. Economic, exergoeconomic and environmental assessments will also be conducted. The objectives of this study can be listed as follows:

a) To develop a comprehensive thermodynamic modeling of the proposed multigeneration system, based on different solar concentrator technologies; with gas turbines and fuel cell as prime movers for electricity and hydrogen production with the supply of domestic hot water and air, also integration of absorption cooling system is considered. Also, it is aimed to perform a model validation for each part of the integrated systems to ensure the correctness of developed code. All mass, energy and entropy balance equations are written for each component of the proposed systems.

b) To apply exergy analyses to each system:
   - Determine the flow exergy of each stream of the systems.
   - Identify exergy destruction rate and exergy efficiency for each component.
   - Calculate the exergy efficiencies and exergy destruction ratios and exergy destruction factors.

c) To conduct exergoeconomic analyses for each system:
   - Calculate of cost of each line of the system.
   - Determine cost of exergy destruction of each component.
   - Estimate of purchase cost of each component.

- Calculate the exergoeconomic factor for each component.

d) To investigate the environmental impact of each system:
   - Evaluate the systems carbon dioxide emissions.
   - Study sustainability index
   - Develop relationships among exergy, economic and environmental impacts.

e) To assess the systems through complete parametric studies:
   - Perform comprehensive parametric studies to investigate the effect of different design and operating parameters on the performance of the system.
   - Study the effects of varying environment condition of the performance assessment of each system studied.

f) To perform an optimization study of the proposed systems to find the best design parameters:
   - Define different objective functions for the system, e.g., exergy efficiency to be maximized and the ones to be minimized as the cost and system emissions.
   - Define the decision variables for each multigeneration integration system.

Chapter 3

SYSTEMS DESCRIPTION

Three novel multigeneration energy systems, based on solar energy, for producing electricity with other useful products, i.e., heat, space cooling, hot water, fresh water and hydrogen, are proposed in the chapter. Detailed description of the proposed integrated systems is provided and it is expected that these systems meet with energy sustainable development requirements. Concentrated solar thermal energy based systems can operate at full rated power using solar energy for 10 to 12 hours during summer days. From 8 am to 4 pm, the solar radiation intensity is high enough to be used as concentrated solar thermal energy for powering the system and provide storage of solar energy if a storage system integrated. From 6 pm to 6 am, the stored energy is utilized to power the integrated system. Another prime mover is to be integrated if solar thermal storage is not considered. There are different options that can also be added as heat backup to the system as biomass or coal gasification for producing a syngas for a SOFC unit, biomass burner or fluidized bed or providing heat through hot exhaust gas of a gas turbine.

3.1 SYSTEM 1: SOLAR PARABOLIC DISH – GAS TURBINE BASED SYSTEM

The solar parabolic dish technology is used to provide a concentrated solar thermal energy as the prime mover of the system presented in Figure 3.1. Electrical power production is provided through a regenerative closed cycle gas turbine with intercooling. Helium is proposed as the working fluid for the gas turbine cycle. An absorption cooling system is integrated to provide space cooling using heat of turbine outlet flow. In this system, biomass gasification-SOFC system is integrated to provide heat source for the closed cycle gas turbine for hydrogen and power production. Steam gasification is applied in this system and syngas produced from the gasification is used to feed a direct reforming SOFC unit for electricity production when solar power is not available. Part of the produced syngas is directed to be more hydrogen enriched using a shift reaction for hydrogen production.

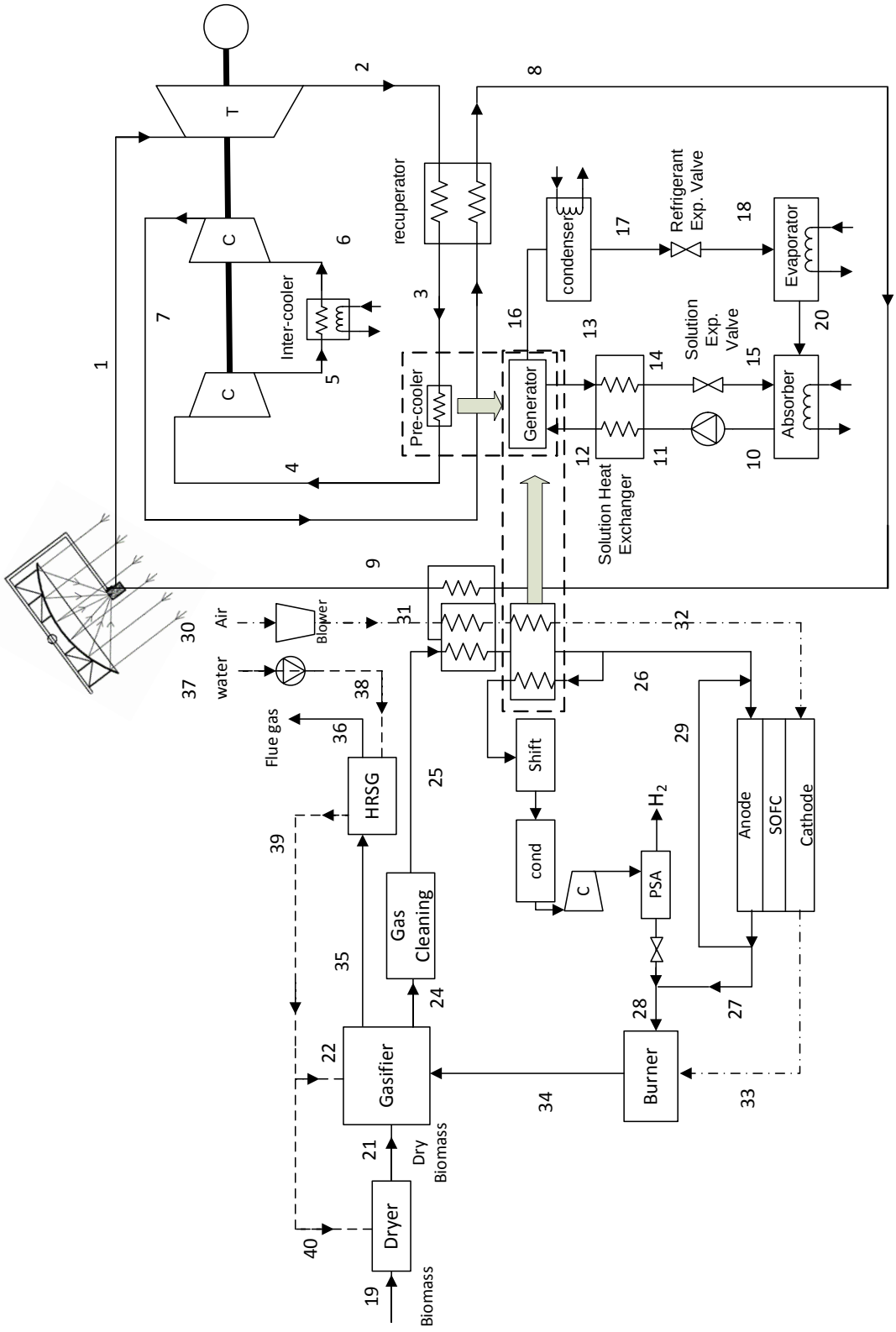

Figure 3.1 Schematic diagram of a multigeneration energy system based on parabolic dish – gas turbine integrated systems with biomass or coal gasification

The integrated system is designed to produce 500 kW of electric power, provided by the solar gas turbine during day time, which is assumed to have available solar power from 7 am to 5 pm. During the rest of the day, the electric power is provided by the SOFC. The gas turbine precooler is utilized to provide heat to a single effect absorption chiller system which is supposed to provide cooling load of 500 kW. The heat to the absorption chillers is provided to the system using the heat from the produced syngas when the solar power is not provided.

Parabolic Solar Dish:

The main heat source of the proposed system is an array of parabolic dish concentrators with focal-mounted heat receivers. It is considered that two axis tracking capability of the dishes are provided so that the receivers orientation is always optimum for a maximum solar radiation intensity.

Closed Cycle Gas Turbine:

The technology of closed cycle gas turbine is now well established and there are several plants have been in operation for over hundreds of thousand hours. It is adapted to a wide range of fuels, e.g., gas, oil, coal, solar and nuclear and of a possibility to use different working gases, e.g., air, helium, nitrogen, carbon dioxide, argon, neon or their mixtures. The heat rejected from the system is available at high temperature and directly and economically is useful for combined cooling and heat production, water desalination, industrial process heat in integrated chemical plants and process steam. Generally, it is agreed that helium is the most useful working fluid for larger closed cycle gas turbine plants (50-100 MWe) and indeed a necessity in nuclear plants. In this system, helium gas turbine is used with the solar thermal system. After being heated, the working fluid expands through the gas turbine unit. The low pressure exhaust gas from the turbine enters a heat transfer recuperator to heat the cooler working fluid. The cooled working fluid leaving the recuperator is directed to another heat exchanger that works as a pre-cooler before the compressor. The working fluid is further cooled in the pre-cooler and the heat is transferred to the generator of an absorption cooling system. Two stage compressions with inter-cooler used to raise the working fluid pressure to its highest

value in the cycle. The working fluid then is heated by the turbine exhaust through the recuperator before it goes to the main heat source.

Biomass Gasification – SOFC:

One of the most promising alternatives of multigeneration energy systems is integrated gasification and solid oxide fuel cell (SOFC) technology. This technology is more attractive as an alternative when utilizing indigenous biomass driven fuel for the gasification process. Biomass can be considered green and renewable source of sustainable hydrogen production rich gas through gasification process (Toonssen et al., 2008).

Gasification of biomass works on producing a biogas with higher heating value and better hydrogen to carbon ratio. This results in less greenhouse gas emissions when the fuel is used. Also removal of sulfur is a great benefit of this process where limestone is to be added to capture it preventing the formation of sulfur oxides. Also nitrogen oxides are minimized as the temperature is relatively low compared with other combustion processes. Fluidized bed gasifiers are widely used for converting biomass into energy, which also has great potential to be integrated with other energy conversion systems for more useful products and enhancing the overall performance of the system.

Numerous studies are performed on biomass gasification applications and their potential use for cogeneration and for hydrogen production. Abuadala and Dincer (2012) conducted a review study on the potential of hydrogen production through biomass gasification. They performed some parametric studies to investigate the operating conditions of gasification on the system performance. An extensive parametric study is conducted by Schuster et al. (2001) on a dual steam gasifier for combined heat and power (CHP) generation. They investigated effects of gasification temperature, fluidization agent and water content on the performance of the system. Song et al. (2013) carried out a thermodynamic assessment based on exergy efficiency for biomass steam gasification process. They considered interconnected fluidized bed in their analysis.

SOFC is considered the most suitable for integration with biomass gasifiers. This is assisted by its relatively high operating temperature, high energy conversion efficiency, and relative insensitivity tolerance to fuel contaminants. Thermodynamic and

optimization analyses are conducted by Athanasiou et al. (2007) to study the performance of integrated gasification and SOFC system. Fryda et al. (2008) performed exergy analysis on an integrated biomass gasification and SOFC with heat pipes for CHP. They reported overall exergy efficiency of 34%. Wongchanapai et al. (2012a) investigated the effect of different operating parameters on the performance of a small scale integrated biomass gasification and SOFC system. An electric efficiency of 58.2% is reported by Bang-Møller et al. (2011) for a biomass-gasification, SOFC and micro gas-turbine integrated system. Bang-Møller et al. (2013) investigated the potential of increasing electric efficiency of a two-stage biomass gasification and SOFC integrated system.

The syngas produced through the biomass gasification process, after being cleaned and sulfur removed, is cooled down providing heat to the closed gas turbine cycle and is used as a fuel for a SOFC unit. Steam gasification is used to facilitate the production of hydrogen rich syngas to be used for hydrogen production when the solar radiation is available. Air is provided to the fuel cell unit and to a combustion chamber for burning the fuel cell hot exhaust gas for providing the required heat to the system.

Absorption Cooling System:

Absorption refrigeration is essentially vapor compression system in which the mechanical compressor is replaced by a thermally activated system. In an absorption system, a secondary fluid, absorbent, is used to absorb the refrigerant, which is the primary fluid, after the refrigerant leaves the evaporator. The vaporized refrigerant is then converted back to liquid in the absorber. Cooling water is used to absorb the heat released in the absorption process. The absorbent and refrigerant solution is then pumped to the generator where heat is supplied. The refrigerant volatilizes and is separated from the absorbent through distillation. The primary fluid is then directed to the condenser and then to the evaporator after being expanded. The absorbent returns back to the absorber.

The absorption systems are excellent for waste heat utilization. The most common absorption systems are ammonia water and water lithium bromide. A typical absorption machine, according to ASHRAE Handbook, requires about 9 kg of steam for 3.5 kW (1 ton) refrigeration effect at about 7°C.

3.2 SYSTEM 2: SOLAR PARABOLIC TROUGH– ORGANIC RANKINE CYCLE BASED SYSTEM

This multigeneration energy system is based on concentrated solar thermal energy using parabolic trough technology with a solar thermal energy storage system. Figure 3.2 shows a schematic diagram for the proposed integrated system. Electricity is provided by an organic Rankine cycle. Domestic water heating and an absorption cooling system are integrated with the system. Part of the produced turbine power is provided to power an electrolyzer for hydrogen production. Turbine work partially covers electrolyzer and RO system demands. Fresh water is provided by RO desalination system power by the produced electric power.

Solar Parabolic Trough:

Solar parabolic trough concentrators are the most mature technology among other concentrated solar thermal energy. This technology is utilized in large power plants for electric power generation, since 1980s. In the proposed system, a parabolic solar trough assessed with a two tank storage system is utilized to provide heat to an organic Rankine cycle. It is considered that the system perform steady by providing solar heat during solar radiation availability counted as 12 hours including the storage time, and the heat is provided from the molten salts in the tanks to the heat transfer fluid of the solar trough system during the rest of the day when the solar radiation is unavailable. The working fluid used with the solar trough is Therminol-66 which is commercial thermal oil with operating temperature ranging from 0°C to 345°C.

Organic Rankine Cycle:

During last decade, the interest in low grade heat recovery has been growing fast, due to the concern over energy shortage and global warming. ORC is considered the most widely low heat source temperature based system. It involves same components as conventional steam power plant. Utilizing an organic fluid as a working fluid for the system means lower boiling temperature compared with water and allows for evaporation at lower temperature values. The selection of the working fluid for solar powered ORC depends on many criteria of which the maximum temperature of the cycle is the most

important. In the proposed system, a regenerative organic Rankine system performing with n-octane is considered. It had a high critical temperature of 296°C and is commonly used with ORC.

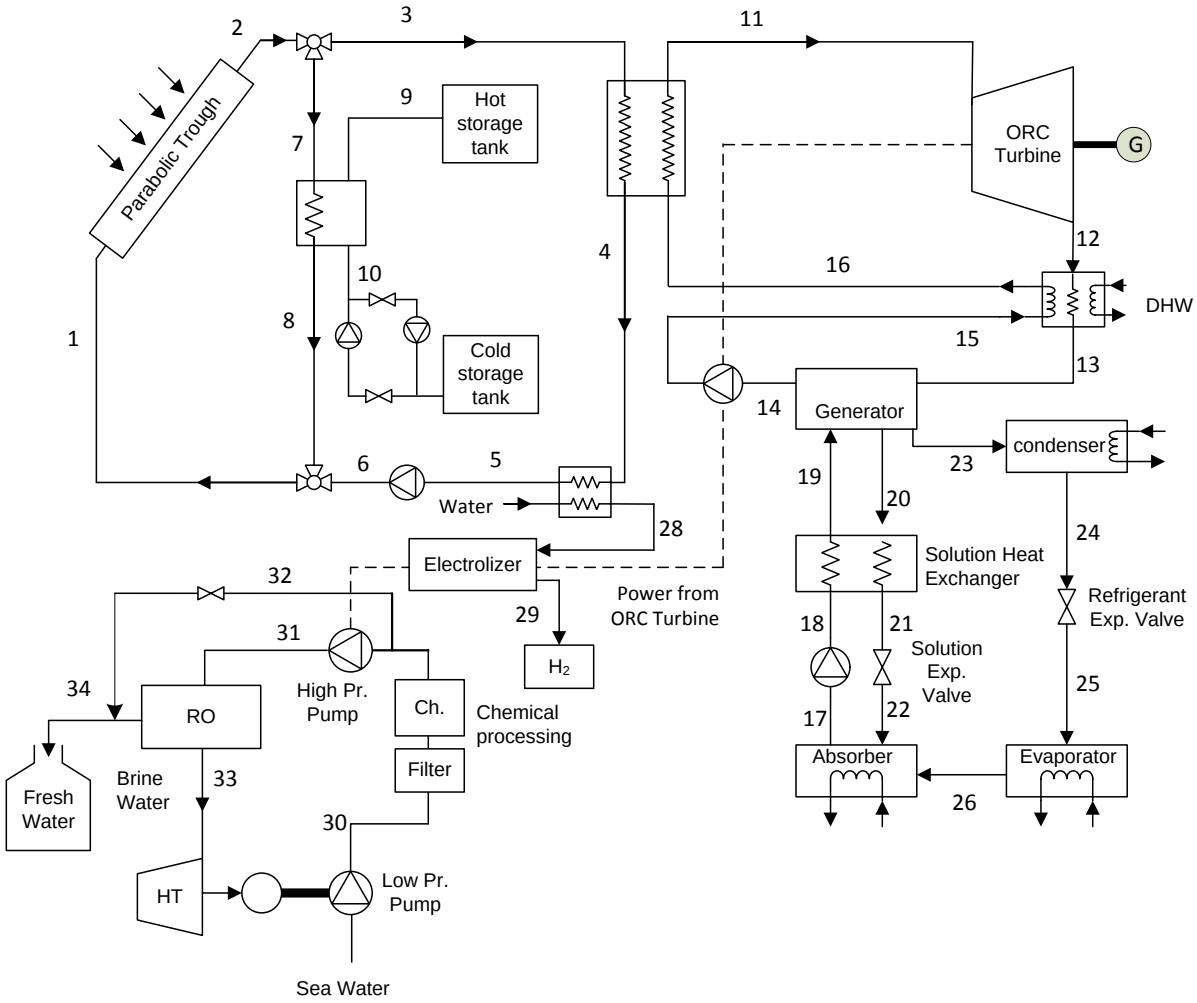

Figure 3.2 Schematic diagram of a multigeneration energy system based on solar parabolic trough – organic Rankine cycle

PEM Electrolyzer:

Hydrogen production is of great importance to mitigate global warming problem and for achieving sustainable development. Hydrogen is considered as energy carrier generated from other energy sources. Nowadays, hydrogen generation from reforming process of hydrocarbon is an economically viable process. However, this method is not an environmentally benign technology considering its life cycle assessment. Hydrogen can

also be generated, by using solar energy, through photocatalysis, thermochemical and hybrid thermochemical cycles, or conventional electrolysis. The required thermal and electric power energy can be also provided from nuclear power plants. Currently, photocatalysis process, thermochemical and hybrid thermochemical cycles for hydrogen production are operating at very low efficiencies to be considered as viable alternatives, compared with water electrolysis. For large scale production, electrolysis is considered the most promising alternative.

The major electrolysis alternatives are: alkaline electrolysis, using electrolyte of aqueous potassium hydroxide; and proton exchange membrane PEM which is used in this system. This electrolyzer is powered by electricity supply from the turbine. All required energy, heat and water are provided to the electrolyzer during the reaction from the turbine exhaust gas and from the distilled water. Produced hydrogen leaves the electrolyzer to be stored. Oxygen can be stored or supplied for medical or other applications such as oxy-fuel combustion, however; it is not considered in the proposed system.

Reverse Osmosis Seawater Desalination:

RO desalination represents about 42% of the world wide desalination capacity. This is a membrane separation technology. During this process water is recovered from a saline solution, which has a pressure higher than the solution osmotic pressure. The membrane only allows water to pass through after it filters out salt ions from the solution. Removing dissolved gasses can be handled in post treatment process, as well as water pH stabilization which is done by adding calcium or sodium salts. The osmotic pressure of seawater is around 2.5 MPa which results in an operating pressure of 5.4 to about 8 MPa for RO system. For brackish water this range drops to 1.5 to 2.5 MPa. For large scale plants, the energy required for seawater desalination is as low as 9 kJ/kg product. In the system that is described, Pelton turbine is utilized for energy recovery from the system brine rejected. The proposed RO system operates with a bypass from the fed water to the product for producing the required salinity of the final produced water. The RO system is comprehensively analyzed and discussed.

3.3 SYSTEM 3: SOLAR HELIOSTAT – STEAM TURBINE BASED SYSTEM

Figure 3.3 shows a schematic of a heliostat solar tower based integrated system. A reheat steam cycle is integrated with the system for power production. Steam is generated using the heat absorbed by a molten salt in the solar tower. The steam leaving the high pressure pump is used to provide heating to water up to 80°C, which is the operating temperature of the PEM electrolyzer which is utilized for hydrogen production. It also provides heating power to the electrolyzer if needed, based on the operation condition. Part of the expanded steam from the high pressure turbine is directed to an absorption cooling system generator after proving heat for producing domestic hot water. Both lines are then pumped to the steam generator. The system is designed to provide at 4 MW of net power and produce 90 kg/s of fresh water and providing hydrogen at rate of 1.25 kg/h.

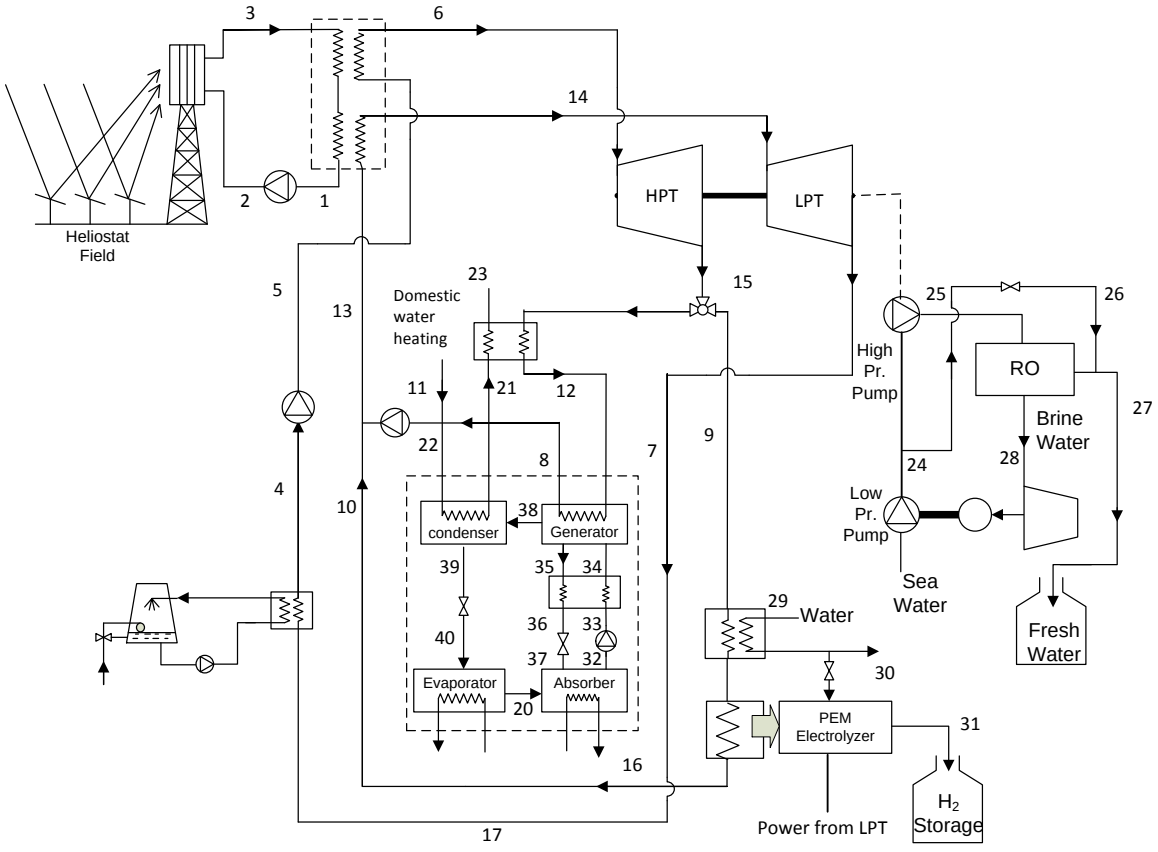

Figure 3.3 Schematic diagram of a multigeneration energy system based on solar heliostat – steam turbine

Chapter 4

MODELS DEVELOPMENT AND ANALYSES

The thermodynamics analyses of the proposed systems are based on energy and exergy concepts. Economic analyses based on exergoeconomic concepts are also applied to the developed models. The systems performances are also described by the energy and exergy efficiencies and sustainability indexes. In this chapter, the basic concepts and the analyses procedure and equation used are described and explained.

4.1 BASIC THERMODYNAMICS CONSERVATION CONCEPTS

In this section, the mass, energy, entropy and exergy balance equation applied to a control volume that exchanges heat, work and mass with the surrounding environment will be discussed.

4.1.1 Conservation of Mass

For any system, the general form of conservation of mass through the control volume can be written as follows:

$$\frac{dm_{cv}}{dt} = \sum \dot{m}_{in} - \sum \dot{m}_{out} \quad (4.1)$$

where m is the mass and $\dot{m}$ is mass flow rate. The subscripts *cv*, indicates the control volume, *in* and *out* are inlet and outlet streams, respectively.

4.1.2 Conservation of Energy

The energy conservation can be formulated based the first law of thermodynamics, applied on control volume as follows:

$$dE = \delta Q - \delta W \quad (4.2)$$

where Q represents heat and W is the work that the system exchange with the environment in the process from initial state 1 to final state 2, while E refers to all energy forms, e.g, internal, kinetic and potential energy, that the system has at each indicated

state. The energy balance equation in a general transient form can be defined as follows (Cengel and Boles, 2011):

$$\frac{dE_{cv}}{dt} = \dot{Q}_{cv} - \dot{W}_{cv} + \sum \dot{m}_{in}\left(h + \frac{V^2}{2} + gz\right)_{in} - \sum \dot{m}_{out}\left(h + \frac{V^2}{2} + gz\right)_{out} \quad (4.3)$$

where E ,$\dot{Q}$ and $\dot{W}$ are the energy, heat transfer rate and the power exchange through the system control volume, respectively, and h is specific enthalpy, V is velocity, z and g are elevation and the gravitational acceleration, respectively.

4.1.3 Entropy Balance and Entropy Generation

From the second law of thermodynamics, the entropy generation associated with the processes that the systems go through can be described as stated in the following general equation:

$$\frac{dS_{cv}}{dt} = \sum \dot{m}_{in} s_{in} - \sum \dot{m}_{out} s_{out} + \sum \frac{\dot{Q}_{cv}}{T} + \dot{S}_{gen} \quad (4.4)$$

where s stands for specific entropy and $\dot{S}_{gen}$ is the entropy generation.

4.1.4 Exergy Analysis

Exergy can be defined as the maximum work that can be extracted from a system interacting with a reference environment (Dincer and Rosen, 2013). The main aim of applying exergy analysis is to evaluate quantitatively the causes of thermodynamics imperfection and indicating the possible thermodynamics improvements of the process under consideration, with considering the economic analysis as well (Szargut et al., 1988). Exergy balance has the fundamental difference from the energy balance that exergy is exempt from the law of conservation. Exergy balance can be defined as a statement of law of degradation of energy. It provides a description of the irretrievable loss of exergy in the system that occurs due to processes irreversibilities (Kotas, 1995). The exergy balance equation for any system can be described, in general form, as follows:

$$\frac{dEx_{CV}}{dt} = \sum \dot{E}x_Q - \sum \dot{E}x_w + \sum_{in} \dot{E}x_{flow} - \sum_{out} \dot{E}x_{flow} - \dot{E}x_d \quad (4.5)$$

where $\dot{E}x_Q$ represents the exergy transfer rate with the heat energy exchange across the system control volume. $\dot{E}x_w$ refers to the exergy transfer rate by the boundary or shaft work applied on or done by the system. The term $\dot{E}x_{flow}$ represents the exergy transfer

rate with flow transfer through the system. The exergy destruction, which describes the system irreversibility, is shown in the equation as $\dot{E}x_d$. These terms are described in turn, below.

Exergy Associated with Heat Transfer:

For the heat transfer rate $\dot{Q}$ which occurs at a control surface with boundary temperature T_b, the maximum rate of conversion from thermal energy to useful work, which describes the thermal exergy flow, can be sated as follows (Moran et al., 2011):

$$\dot{E}x_Q = \left(1 - \frac{T_o}{T_b}\right)\dot{Q} \qquad (4.6)$$

where $(1 - T_o/T_b)$ is defined as the dimensionless exergetic temperature term. This term reflects Carnot efficiency which is working between environmental temperature at T_o and the temperature T_b of the surface at which the heat transfer occurs.

Exergy Associated with Work:

Work equivalent of a given form of energy is a measure of its exergy (Kotas, 1995). From this definition, it can be stated that exergy transfer with shaft or boundary work equals to work. In the same way, exergy transfer rate is specified by work transfer rate. The following equation represents the exergy transfer rate associated with work, considering boundary work:

$$\dot{E}x_w = \dot{W}_{cv} + P_o\frac{dV_{cv}}{dt} \qquad (4.7)$$

where P_o is the dead state pressure.

Exergy Associated with a steady stream:

Exergy of a flow of matter can be defined according to Kotas (1995), as the maximum amount of work obtainable when the flow is brought from its initial state to the dead state during a process of interaction with the surrounding environment. Exergy transfer by flow streams can be expressed as follows, in terms of flow specific exergy:

$$\sum_{in}\dot{E}x_{flow} - \sum_{out}\dot{E}x_{flow} = \sum_{in}\dot{m}_i ex_i - \sum_{out}\dot{m}_i ex_i \qquad (4.8)$$

Flow exergy is composed of four components; physical exergy, ex^{ph}, chemical exergy, ex^{ch}, kinetic exergy, ex^{ke} and potential exergy, ex^{pe} as follows:

$$ex_{\text{flow}} = ex^{ph} + ex^{ch} + ex^{ke} + ex^{pe} \quad (4.9)$$

The kinetic and potential components of exergy, as they appear in the previous equation, are negligible during the analyses done in this work, as the changes in velocities and elevations across the systems components are small when compared to the values of the other terms.

The physical exergy is the specific flow exergy portion caused by physical processes that involve thermal interaction with the surrounding environment of the system, to bring the flow from its initial condition to dead state. Specific physical exergy can be calculated as follows:

$$ex^{ph} = (h - h_{\text{o}}) - T_0(s - s_{\text{o}}) \quad (4.10)$$

where h and h_{o} are the enthalpy values, and s and s_{o} are the entropy values at the defined and the reference environment states, respectively.

Chemical exergy is the specific flow exergy portion caused by processes involving heat transfer and exchange of substances only with the surrounding environment to bring the substance to dead state (Kotas, 1995). Chemical exergy for a gaseous mixture can be calculated using the following equation, considering ideal gas assumption (Moran et al., 2011):

$$ex_{mix}^{ch} = \sum y_i ex_i^{ch} + RT_o \sum y_i \ln y_i \quad (4.11)$$

where y_i is the mole fraction of component *i* in the gas mixture.

For solid fuels, chemical exergy can be estimated based on as follows (Kotas, 1995):

$$ex_{fuel}^{ch} = \left(LHV + w.h_{fg}\right)\varphi_{dry} + 9{,}417s \quad (4.12)$$

where *LHV* is net calorific value of the fuel, *w* is moisture content, and h_{fg} is latent heat of water at T_o. Sulphur mass fraction in the fuel is represented by *s*. Chemical exergy ratio, φ_{dry}, is estimated based on dry organic substances contained in the fuel as follows (Kotas, 1995):

$$\varphi_{dry} = 0.1882\ \frac{h}{c} + 0.061\ \frac{o}{c} + \ 0.0404\ \frac{n}{c} + 1.0437 \quad (4.13)$$

This formula is valid for oxygen to carbon mass ratio less than 0.667.

For the oxygen to carbon ratio higher than that and up to 2.67, the following formula is used to calculate the chemical exergy ratio:

$$\varphi_{dry} = \frac{\left(0.1882\frac{h}{c} - 0.2509\left(1 + 0.7256\frac{h}{c}\right) + 0.0404\frac{n}{c} + 1.0438\right)}{\left(1 - 0.3035\frac{o}{c}\right)} \quad (4.14)$$

The following formula is used for liquid fuels:

$$\varphi = 0.1882\ \frac{h}{c} + 0.0432\frac{o}{c} + 0.2169\ \frac{s}{c}\left(1 - 2.0628\frac{h}{c}\right) + 1.0401 \quad (4.15)$$

where *h*, *c*, *o* and *n* are the mass fraction of hydrogen, hydrogen, oxygen and nitrogen in the fuel, respectively.

The following simplification, which was proposed by Szargut and Styrylska (1964) can be also used to calculate the chemical exergy of a fuel:

$$\varphi = ex_{fuel}^{ch}/LHV \quad (4.16)$$

For a general gaseous fuel, C_aH_b, the following correlation can be used to calculate the chemical exergy ratio (Ahmadi et al., 2012):

$$\varphi = 0.0169\frac{b}{a} - \frac{0.0698}{a} + 1.033 \quad (4.17)$$

Therefore, the specific flow exergy for any component *i* of the inlet and outlet flow streams can be expressed as follows:

$$ex_i = (h_i - h_o) - T_o(s_i - s_o) + ex_i^{ch} \quad (4.18)$$

Here, the assumption of neglecting the potential and kinetic exergy terms is considered.

Exergy destruction:

In the exergy balance equation, the term $\dot{E}x_d$, which represents the exergy destruction rate in any component *i*, is proportional to entropy generation rate across that component, S_{gen}, as follows:

$$\dot{E}x_{d_i} = T_o.\dot{S}_{gen,i} \quad (4.19)$$

where $\dot{S}_{gen,i}$ denotes the entropy generation rate in each component.

From the above, the exergy balance equation can be reformulated as follows:

$$\frac{dEx_{cv}}{dt} = \sum\left(1 - \frac{T_0}{T}\right)\dot{Q} - \dot{W}_{cv} + P_o\frac{dV_{cv}}{dt} + \sum\dot{m}_{in}ex_{in} - \sum\dot{m}_{out}ex_{out} - T_o\dot{S}_{gen} \quad (4.20)$$

4.1.5 Energy and Exergy Efficiencies

The efficiency of a system can be defined as the measure of the effectiveness of that system performance. Energy efficiency for any thermodynamics process or system can be defined as the ratio of the useful output to the energy input to the system.

$$\eta = \frac{\sum useful\ output\ energy}{\sum input\ energy} = 1 - \frac{\sum energy\ loss}{\sum input\ energy} \quad (4.21)$$

Exergy efficiency is defined according to the second law of thermodynamics, and with respect to the exergy content of input and output streams. The concept of exergy efficiency provides deeper understanding of the performance of energy systems. It also differentiates the system irreversibilities from the effluent losses associated with the thermodynamic processes through the system. It gives a measure of the realistic potential for improving the system performance by decreasing the effluent losses:

$$\psi = \frac{\sum useful\ output\ exergy}{\sum input\ exergy} = 1 - \frac{\sum exergy\ loss}{\sum input\ exergy} \quad (4.22)$$

4.2 SUSTAINABILITY ANALYSES

Exergy analysis determines the quality of a thermodynamics process and gives an indicator and a potential tool for sustainability achievement. Enhancing the exergetic performance increases system efficiency and results in a reduction in its environmental impacts and the destructed exergy. Exergoeconomic and exergoenvironmental analyses provide a step further in sustainable development approach.

4.2.1 Exergoeconomic Analysis

Combining exergy and economic analyses of energy systems produces a tool with good potential for achieving sustainable and optimized performance of the system. Exergoeconomics give a description of integrating exergy based thermodynamic analysis and economic principles for providing information to would lead to better system design and operation in cost-effective manner (Ahmadi et al., 2011). This combination forms the basis of the relatively new field of thermoeconomics. The exergy model calculates the exergy content of each point in the system, and from the economic model, estimation of capital, operation and maintenance cost elements of the system can be done. The objectives of exergoeconomic analysis can be listed as stated by Bejan et al. (1996) as

follows; calculate the cost of system product streams, estimate the cost flow by understanding how cost of flow streams are formed, optimization of specific variable in a specific component and optimize the overall system.

The flow cost, $\dot{C}$ (\$/s), is the cost associated with a certain flow stream through the studied system. The cost balance equation is includes different terms based, cost associated with the exergy of inlet and outlet streams, capital cost of the system and O&M cost (Bejan et al., 1996):

$$\sum_i \dot{C}_{\mathrm{k}} + \dot{C}_{\mathrm{Q,k}} + \dot{Z}_{\mathrm{k}} = \sum_{\mathrm{e}} \dot{C}_{\mathrm{k}} + \dot{C}_{\mathrm{w,k}} \quad (4.23)$$

where i and e represent inlet and exit streams, respectively. $\sum_i \dot{C}_{\mathrm{k}}$ and $\sum_{\mathrm{e}} \dot{C}_{\mathrm{k}}$ are the total costs associated with exergy flows entering and exiting through the component k boundaries. $\dot{C}_{\mathrm{Q,k}}$ represents the total cost associated with thermal exergy flow in component k. $\dot{Z}_{\mathrm{k}}$ is the component capital cost and the costs associated with its O&M, and $\dot{C}_{\mathrm{w,k}}$ is the total costs associated with work in component k. The cost of exergy flow can be described as follows:

$$\dot{C}_{\mathrm{k}} = c_{\mathrm{k}} \dot{E}x_{\mathrm{k}} \quad (4.24)$$

Applying the exergy cost balance for all the system components results in a set of non-linear algebraic system of equations, which is solved for $\dot{C}_{\mathrm{k}}$ and c_{k}.

The ratio of exergy losses of the system to the capital costs of the system is introduced as the parameter R which provides information about the extent of the total exergy loss, i.e., exergy waste plus exergy destruction, of a system compared to the capital costs. This ratio can be expressed as:

$$R = \dot{L}/\dot{Z} \quad (4.25)$$

where $\dot{Z}$ is the capital cost and $\dot{L}$ is defined as follows:

$$\dot{L} = \dot{E}x_d + \dot{E}x_{loss} \quad (4.26)$$

where $\dot{E}x_{loss}$ represents the total exergy losses due to heat exergy transfer and flow exergy leaving the systems boundary.

Also, the exergoeconomic factor, f_k of the component k is defined as

$$f_k = \dot{Z}_k / \left(\dot{Z}_k + c_{F,k} \left(\dot{E}x_{d_k} + \dot{E}x_{loss} \right) \right) \quad (4.27)$$

where $c_{F,k}$ is the unit cost of exergy associated with fuel stream provided to the component.

4.2.2 Environmental impact analysis

Solid, liquid and gas residuals of any thermal processes through energy systems are mostly released to the environment, affecting the ecology of the environment. Actually, enhancing systems' performances and exergy analyses approaches have been raised by this issue. The amount of the greenhouse gas emission from a thermal process can be estimated through the thermodynamic. Comparative analysis, with similar conventional systems, may be applied to measure the enhancement and the environmental impact of the system. Environmental impacts of processes are directly related to the rate of fuel consumption. The ratio of the exergy destruction of a system to the inlet exergy by fuel characterized the efficiency of fuel consumption is given by

$$D_{\mathrm{p}} = \frac{\dot{E}x_{\mathrm{d}}}{\dot{E}x_{\mathrm{in}}} \quad (4.28)$$

Another parameter and indicator is the sustainability index, which illustrates the effectiveness of a process in terms of exergy input and the rate of exergy destruction in the system. Therefore, the higher the sustainability index, the lower the exergy destruction in the process. This means that the process has less environmental impacts. The sustainability index of a fuel resource can be defined as the inverse of the depletion factor.

$$SI = \frac{1}{D_{\mathrm{p}}} \quad (4.29)$$

4.2.3 Optimization Analysis

The main outcome of performing optimization analysis on energy systems is achieving maximum operating efficiency and minimizing the cost. The main outcome this would result in proper selection equipment and their configuration through the system processes. The first step in performing the optimization analyses is to identify the system boundaries and the effective operating parameters. For integrated energy systems, the process can be broken into optimization of the subsystems. After that, comes identifying the optimization

criteria. This may include energy, economic or environmental criteria. Selection of the decision variables is the following step. These are the variables based on which the optimization process is performed. These variables must be selected independent and represent the characteristics of the studies system. They also must be selected from the variables that affect the system performance and cost. Next step is the selection of an appropriate mathematical model of optimization.

Multigeneration system optimization requires multiple objectives with several constraints throughout the subsystems and overall system. In general, it is aimed to increasing overall system performance and decreasing its cost and environmental impact. It is generally not possible to optimize all objectives that have opposite directions. Multi objective optimization problems can be reduced to single objective functions by manipulating the constraints. For example, instead of increasing the efficiency, one can optimize the system by decreasing the depletion factor ($D_p = 1 - \psi$) and this option leads to a single objective, where cost and depletion factor are the components of the minimization of the objective function. The efficiency results then can be obtained from the optimized sustainability index of the system. Results of the optimization describe a Pareto frontier, which is better at higher amount of useful outputs from multigenerational system. Most single objective optimization methods, i.e., Lagrangian multipliers, genetic algorithms, and evolutionary methods (differential evolution, particle swarm, ant colony, etc.) can be used to optimize the system with properly defined objectives and constraints. The general formula of the exergy efficiency of the integrated systems to be optimized can be written as follows:

$$\psi = \frac{\dot{W} + \sum \dot{Q}_{cooling}\left(\frac{T_o}{T_c} - 1\right) + \sum \dot{Q}_{Heating}\left(1 - \frac{T_o}{T_c}\right) + \dot{Ex}_{H_2}}{\sum \dot{Ex}_{source}} \quad (4.30)$$

The total cost rate is calculated considering the levelized purchase equipment cost of the system components and their operating and maintenance cost, and the environmental impact cost considering the cost associated with the systems emissions, and the fuel cost as follows:

$$\dot{C}_{total} = \sum \dot{C}_{sys} + \dot{C}_f + \dot{C}_{env} \quad (4.31)$$

where $\dot{C}_{env} = 0.2C_{CO} + 0.024C_{CO_2} + 6.85C_{NO_x}$ (4.32)

In this study, genetic evolutionary algorithm is utilized for performing the optimization analysis. Evolutionary algorithm for optimization is inspired by mechanisms of biological evolution, such as reproduction, mutation, recombination and selection. There are different methods of evolutionary algorithm as artificial neural network, fuzzy logic, and genetic algorithm, which is utilized in this study. Optimal solution generated from genetic algorithm is based on the evolutionary techniques of inheritance, learning, natural selection and mutation. The optimization process is initiated by population of candidate solutions and then progresses through generations. During this process, each individual of the population is evaluated with respect to it fitness, which is governed by the defined objective function. Based on their fitness, multiple individuals are picked and modified using mutation technique, to produce new population. The newly generated population is employed in the following iteration of the optimization process, progressing towards an optimal solution (Goldberg, 1989; Schaffer, 1985).

4.3 SYSTEM 1: SOLAR PARABOLIC DISH – GAS TURBINE BASED SYSTEM

In this section the components and subsystems of the solar dish gas turbine system are thermally analyzed based on energy and exergy thermodynamics concepts. For the overall system performance, the total energy and exergy efficiencies are calculated based on the useful output commodities from the system. In this system, the useful outputs considered are the net power, cooling and hydrogen production from the generated hydrogen rich syngas.

The energy and exergy efficiencies of the overall system during solar availability mode are defined as

$$\eta = \frac{\dot{W}_{Turb} + \dot{Q}_{cooling} + \dot{m}_{H_2} LHV_{H_2}}{(\dot{Q}_u)_{solar} + (\dot{m} \cdot LHV)_{biomass}} \quad (4.33)$$

$$\psi = \frac{\dot{W}_{Turb} + \sum \dot{Q}_{cooling}\left(\frac{T_o}{T_c} - 1\right) + \dot{Ex}_{H_2}}{\dot{Ex}_{solar} + \dot{Ex}_{biomass}} \quad (4.34)$$

For the energy and exergy efficiencies during the period with unavailable solar radiation are written as

$$\eta = \frac{\dot{W}_{SOFC} + \dot{Q}_{cooling} + \dot{m}_{H_2} LHV_{H_2}}{\dot{Ex}_{biomass}} \quad (4.35)$$

$$\psi = \frac{\dot{W}_{SOFC} + \sum \dot{Q}_{cooling}\left(\frac{T_o}{T_c} - 1\right) + \dot{Ex}_{H_2}}{\dot{Ex}_{biomass}} \quad (4.36)$$

For the performance of the system during one day operating under both modes, the efficiencies can be formulated considering the hours of operation of each mode.

4.3.1 Solar Parabolic Dish

For the solar dish concentrator, the useful heat gain can be calculated using Hottel-Whillier equation (Armstrong, 1978) as follows:

$$\dot{Q}_u = A_{ap}.F_R.\left(S - A_r/A_{ap}.U_L.(T_{r,i} - T_o\right) \quad (4.37)$$

where F_R is the heat removal factor for the temperature gradients in the concentrator receiver and it can be calculated from the following formula:

$$F_R = \frac{\dot{m}_r.Cp_r}{A_r.U_L}.\left(1 - exp\left(-\frac{A_r.U_L.F_1}{\dot{m}_r.Cp_r}\right)\right) \quad (4.38)$$

In the previous two equations, A_r represents the receiver aperture area of the solar dish, A_{ap} is the concentrator aperture area, U_L is the total heat transfer coefficient, $T_{r,i}$ $\dot{m}_r, Cp_r$ are the gas inlet temperature mass flow rate and the specific heat at constant pressure values and F_1 is the concentrator efficiency factor which is taken as 0.9 in the presented analysis.

The solar concentration ratio C for the solar dish is defined as the ratio of the effective area of the aperture to the receiver area.

$$C = A_{ap}/A_r \quad (4.39)$$

and the absorbed flux S are to be calculated as follows

$$S = \eta_o \times I_b \quad (4.40)$$

Here, η_o is the optical efficiency which depends on the concentrator material properties. The thermal efficiency of the solar dish can be simply calculated as

$$\eta_c = \dot{Q}_u/\dot{Q}_s \quad (4.41)$$

where $\dot{Q}_s$ is solar heat transferred from the sun to the concentrator and is calculated as

$$\dot{Q}_s = I_b \times A_{ap} \quad (4.42)$$

The exergy of the solar radiation is calculated using Petela correlation which is given as function of the sun temperature T_s (Petela, 2005):

$$\dot{Ex}_s = I_b \times A_{ap}\left[1 - \frac{4 \cdot T_o}{3 \cdot T_s} + \frac{1}{3}\left(\frac{T_o}{T_s}\right)^4\right] \quad (4.43)$$

Then the absorbed exergy of the solar radiation is calculated as

$$\dot{Ex}_c = \eta_o \times \dot{Ex}_s \quad (4.44)$$

The exergy efficiency of the solar parabolic dish is calculated with respect to the solar losses as follows:

$$\psi_c = 1 - \frac{\sum \dot{Ex}_d}{\dot{Ex}_s} \quad (4.45)$$

Here, the total exergy destruction and exergy losses in the solar dish, represented by $\sum \dot{Ex}_d$ in the exergy efficiency, includes the exergy destruction associated with the heat transfer, exergy destruction due to irreversibilities cause by pressure drop, exergy loss due to optical properties and thermal leakage from the receiver .

4.3.2 Solid Oxide Fuel Cell

A direct internal reforming SOFC is considered. Schematic of the fuel cell is shown in Figure 4.1. The feeding gas stream to the anode is mixed with recirculated gas at the cell exit. This provides the needed water through the high water content gas stream leaving the cell. In this model, fuel cell electric current density is related to the molar flow rate of utilized hydrogen which helps in identifying the exit gas composition. Also, an insulated cell is considered to determine the amount of air leaving the cell carrying the released, unutilized heat. For the electrochemical model, the following reactions are considered where methane steam reforming and water-gas shift reactions, along with the electrochemical reaction occurs simultaneously at the cell (Colpan et al., 2007):

$CH_4 + H_2O \leftrightarrow CO + 3H_2$

$CO + H_2O \leftrightarrow CO_2 + H_2$

$H_2 + ½O_2 \rightarrow H_2O$

The equilibrium constants for the two governing reactions of the fuel cell can be calculated as function of the molar concentrations, reduced to partial pressure values, of

the reaction species. The value of equilibrium constants can be also calculated form the following correlation (Fryda et al., 2008):

$$\log K = A_0 + A_1 T + A_2 T^2 + A_3 T^3 + A_4 T^4 \quad (4.46)$$

where the values of the formula constants are shown in Table 4.1 for reforming and shifting reactions. In form of molar ratio, the equilibrium constants can be formed as follows as function of the molar concentration of the gas stream at the exit state of the cell (state 3).

$$K_{Reform} = \frac{y_{eq,H_2}^3 \cdot y_{eq,CO}}{y_{eq,CH_4} \cdot y_{eq,H_2O}} \left(\frac{P}{P_o}\right)^2 \quad (4.47)$$

$$K_{Shift} = \frac{y_{eq,H_2} \cdot y_{eq,CO_2}}{y_{eq,CO} \cdot y_{eq,H_2O}} \quad (4.48)$$

where y_i is the molar ratio of the species of equilibrium composition of the gas stream at the fuel cell exit.

To identify the composition of the gas stream at the fuel cell exit, the equilibrium compositions are to be calculated. Based on the fuel hydrogen utilization factor, hydrogen molar rate utilized can be expressed in relation to the reactions extents as follows:

$$c_H = \lambda \cdot (\dot{n}_1^{H_2O} + 3c_R + c_S) \quad (4.49)$$

where λ is operating condition parameter, introduced as function of the recirculation rate, r, and the utilization factor, U_f:

$$\lambda = U_f/(1 - r + rU_f) \quad (4.50)$$

Here, c_H, c_R and c_S are introduced as the extents of the three reactions occurring at the fuel cell. c_H represents the hydrogen conversion during the cell electrochemical reaction. c_R and c_S express methane and carbon monoxide conversions during reforming and shifting reactions.

The total molar flow rate of the gas steam at state 3, in Figure 4.1, can be expressed with respect to the inlet stream 2 as follows:

$$\dot{n}_3 = \dot{n}_2 + 2c_R \quad (4.51)$$

The molar rates of the gas stream composition for equilibrium state at the exit of the fuel cell can be calculated with respect to the inlet compositions as follows:

$$\dot{n}_3^{CH_4} = \dot{n}_2^{CH_4} - c_R \quad (4.52)$$

$$\dot{n}_3^{CO} = \dot{n}_2^{CO} + c_R - c_S \quad (4.53)$$

$$\dot{n}_3^{CO_2} = \dot{n}_2^{CO_2} + c_S \quad (4.54)$$

$$\dot{n}_3^{H_2} = \dot{n}_2^{H_2} + 3c_R + c_S - c_H \quad (4.55)$$

$$\dot{n}_3^{H_2O} = \dot{n}_2^{H_2O} - c_R - c_S + c_H \quad (4.56)$$

Table 4.1 Values of constants for the equilibrium constant equation (Fryda et al., 2008)

	Reforming	Shifting
A_0	-66.139488	13.209723
A_1	0.195027	-3.915×10^{-2}
A_2	-2.2523×10^{-4}	4.6374×10^{-5}
A_3	1.2406×10^{-7}	-2.547×10^{-8}
A_4	-2.6312×10^{-11}	5.47×10^{-12}

The molar rate equations coupled with equilibrium constant equations are used to identify the composition of gas stream leaving the cell. The molar rate of gas stream at state 2 is related to the known inlet stream, 1 by adding the recirculated rate.

$$\dot{n}_2^i = \dot{n}_1^i + r(y_{eq,i} \cdot \dot{n}_3^i) \quad (4.57)$$

Air is considered to carry the heat generated within the fuel cell. The molar flow rate of oxygen associated with the air stream (stream 5) can be calculated based on the conversion of hydrogen during the process as follows:

$$\dot{n}_5^{O_2} = \frac{1}{2}\left(\frac{c_H}{U_O}\right) \quad (4.58)$$

where U_O is the air utilization factor which is the oxidant in the cell reaction. The exit molar rate of air can be calculated considering an actual amount of $(c_H/2)$ of oxygen to be utilized in the reaction. The molar rates of accompanied nitrogen with the entering air can be calculated based on the normal oxygen to nitrogen ratio in atmospheric air.

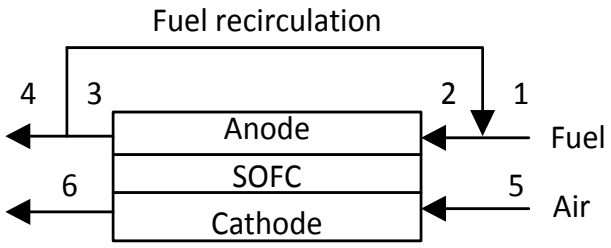

Figure 4.1 Schematic of DIR-SOFC

The electric current of the fuel cell can be expressed as function of the provided flow rate of hydrogen as follows:

$$I = 2\,F\,\lambda\,(\dot{n}_1^{H_2} + 3c_R + c_S) \quad (4.59)$$

which is to be simply reduced as function of the utilized hydrogen:

$$I = 2\,F\,c_H \quad (4.60)$$

where F is Faraday constant.

The cell voltage is calculated by identifying the different polarizations affecting the cell, and subtracting them from the Nernst open circuit voltage. The Nernst voltage is calculated as follows (Barbir, 2013):

$$E = \frac{\Delta G^o}{2F} - \frac{R.T}{2.F} \ln\left(\frac{P_{H_2O}}{P_{H_2}.P_{O_2}{}^{1/2}}\right) \quad (4.61)$$

where ΔG^o is the molar Gibbs free energy change, calculated with respect to the electrochemical reaction of the fuel cell. Values of partial pressure, P_i, in the previous equation are to be expressed in form of molar ratios of equilibrium streams.

The three polarizations affecting the fuel cell performance are ohmic, activation and concentration polarization. The ohmic losses are caused by the flow of electrons through the anode, cathode and interconnector and the ionic flow through the cell electrolyte. In this study, ohmic losses are estimated as a function of the cell components thickness, L, and specific electrical resistivity, ρ, which is temperature dependent, as follows:

$$V_{ohm} = i.\sum \rho_k L_k \quad (4.62)$$

where k represents the anode, cathode, electrolyte and interconnector parts of the fuel cell. Values of L_k for the different components are listed in Table 4.3. Components

resistivity is calculated as follows (Bang-Møller et al., 2013; Wongchanapai et al., 2012b):

$$\rho_k = C_1 \exp(C_2/T) \quad (4.63)$$

Here, C_1 and C_2 are given in Table 4.2, based on the data provided by Wongchanapai (2012b), for each of the fuel cell component.

The activation energy in fuel cell electrochemical reaction is the energy barrier which must be overcome by the reactant. Activation losses are accompanied with these barriers due to charge transfer through the three phase region of both electrodes.

Table 4.2 Specific resistivity for anode-supported SOFC model, Wongchanapai (2012b)

Component (material)	C_1	C_2
Anode (Ni/YSZ cermet)	2.98×10^{-5}	-1392
Cathode (LSM-YSZ)	8.114×10^{-5}	600
Electrolyte (YSZ)	2.94×10^{-5}	10,350
Interconnector (Doped $LaCrO_3$)	3.215×10^{-4}	0

The activation polarization is calculated as derived from reforming the Butler-Volmer equation as follows (Li, 2006):

$$V_{act} = \frac{R.T}{2.F}.\sinh^{-1}\left(\frac{i}{2.i_o^a}\right) + \frac{R.T}{2.F}.\sinh^{-1}\left(\frac{i}{2.i_o^c}\right) \quad (4.64)$$

where i_o^a and i_o^c are the anode and cathode exchange current density values, respectively, and are calculated from the semi-empirical correlations below (Campanari and Iora, 2004):

$$i_o^a = \gamma_a.\left(\frac{P_{H_2}}{P_o}\right)\left(\frac{P_{H_2O}}{P_o}\right)^m \exp\left(-\frac{E_{act}^a}{R.T}\right) \quad (4.65)$$

$$i_o^c = \gamma_c.\left(\frac{P_{O_2}}{P_o}\right)^n \exp\left(-\frac{E_{act}^c}{R.T}\right) \quad (4.66)$$

The pre-exponential factors γ_a and γ_c, the values of the activation energies E_{act}^a and E_{act}^c and the empirical constants m and n, are shown in Table 4.3. The concentration polarization is caused by the mass transport limitations of the reactants and is calculated as a function of the limiting current density at the anode and cathode:

$$V_{con,a} = -\frac{R.T}{2.F}\ln\left(1-\frac{i}{i_s^a}\right)+\frac{R.T}{2.F}\ln\left(1+\frac{P_{H_2}^{ex}.i}{P_{H_2O}^{ex}.i_s^a}\right) \quad (4.67)$$

$$V_{con,c} = -\frac{R.T}{4.F}\ln\left(1-\frac{i}{i_s^c}\right) \quad (4.68)$$

The following two equations are used to calculate the anode and cathode limiting current density values, which are given as function of the temperature and hydrogen and oxygen partial pressure at the fuel cell exit conditions:

$$i_s^a = \frac{2.F.P_{H_2}^{ex}.D_{eff}^a}{R.T.L_a} \quad (4.69)$$

$$i_s^c = \frac{4.F.P_{O_2}^{ex}.P.D_{eff}^c}{(P-P_{O_2}^{ex}).R.T.L_c} \quad (4.70)$$

where L_a and L_c are thicknesses, and D_{eff}^a and D_{eff}^c are effective gas diffusion factors, for the anode and cathode, respectively. The values considered for these parameters are given inTable 4.3. Based on the assumption of using excess air to release the generated heat at the cell, air utilization is to be determined through the energy balance equation of an insulated cell (Colpan et al., 2007). This equation can be simply written as:

$$\sum_{in} H_f + \sum_{in} H_{ar} = \dot{W}_{FC} + \sum_{out} H_f + \sum_{out} H_{ar} \quad (4.71)$$

Here, H_f and H_{ar} are the total enthalpy of fuel and air streams at inlet and exit of the fuel cell. Knowing the air utilization, power generated from the fuel cell is to be calculated from the following relation:

$$\dot{W}_{FC} = i.V.A.N_{stack}N_{element} \quad (4.72)$$

where i is cell current density, V is operating cell voltage, A is the active area, N_{stack} is number of stacks and $N_{element}$ is the number of elements in the cell.

The electric efficiency of the fuel cell here is calculated as:

$$\eta_{SOFC}^{en} = \frac{\dot{W}_{FC}}{\dot{n}_1\,LHV} \quad (4.73)$$

The exergy efficiency is calculated considering the exergy associated with the inlet fuel steam to the fuel cell:

$$\eta_{SOFC}^{ex} = \frac{\dot{W}_{FC}}{\dot{E}x_{f,in}} \quad (4.74)$$

The cost function of the SOFC is calculated based on the specific cost of the cell. The specific fuel cell cost is considered as 0.1442 \$/cm^2 (Autissier et al., 2007). The total purchase cost is calculated based on the total SOFC area after identifying the number of cells required.

Table 4.3 Solid Oxide Fuel Cell model input data

Anode-Supported SOFC Input Parameters	
Electrolyte thickness, L_e	0.04 mm (Chan et al., 2001)
Anode thickness, L_a	0.75 mm (Chan et al., 2001)
Cathode thickness, L_c	0.05 mm (Chan et al., 2001)
Operating current density	4000 A/m^2
Anode effective gas diffusion factor, D_{eff}^{a}	3.5×10^{-5} m^2/s (Costamagna and Honegger, 1998)
Cathode effective gas diffusion factor, D_{eff}^{c}	7.3×10^{-6} m^2/s (Costamagna and Honegger, 1998)
Anode pre-exponential factor, γ_a	5.7×10^{7} A/m^2 (Costamagna and Honegger, 1998)
Cathode pre-exponential factor, γ_c	7.0×10^{9} A/m^2 (Costamagna and Honegger, 1998)
Anode activation energy, E_{act}^{a}	140 kJ/mol (Wongchanapai et al., 2012b)
Cathode Activation energy, E_{act}^{c}	137 kJ/mol (Wongchanapai et al., 2012b)
Anode exchange current density constant, m	1
Cathode exchange current density constant, n	0.25
Fuel Utilization	83%
Recirculation ratio	20%
Operating temperature	750°C
Temperature difference across the cell	100°C
Operating pressure	1 bar

4.3.3 Helium Gas Turbine Cycle

The present model aims to investigate the system performance, through energetic and exergetic efficiencies, of an actual helium closed cycle recuperated gas turbine with intercooling, through energy and exergy analyses. The performance parameters are studied, and the effects of changing the operating parameters on the performance are also considered. The pressure losses on the cycle are taken into consideration in the energy and irreversibility analyses. Including the internal irreversibility calculations provides a more realistic analysis of the gas turbine. The performance of the gas turbine is defined in this work in a novel representation with respect to the exergy efficiency. The exergetic performance map is introduced as a more descriptive approach with respect to the actual potential of gas turbine performance improvement at certain operating condition. Exergetic loss map is also introduced as a new exergetic assessment map. It relates the exergy destruction ratio, with respect to the total exergy of fuel streams, to the specific work or the dimensionless work parameter.

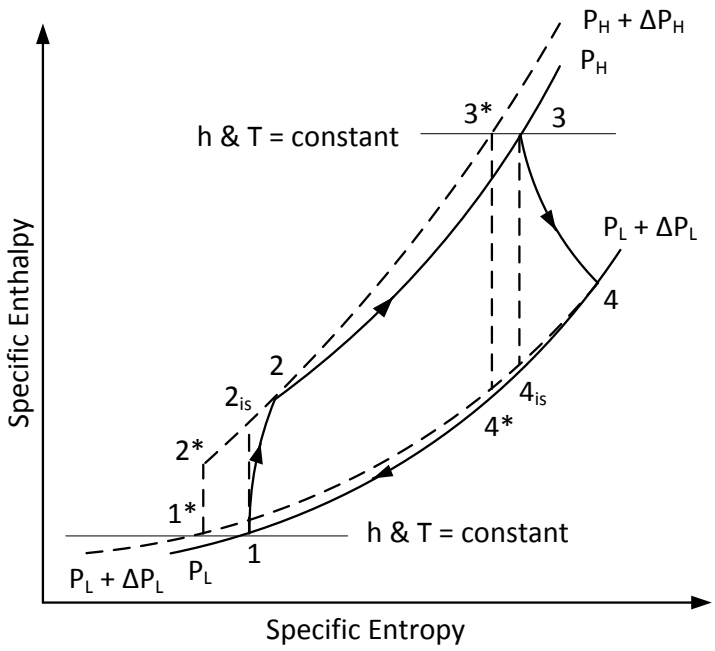

Figure 4.2 Enthalpy-entropy diagram of a realistic simple closed cycle gas turbine.

The enthalpy-entropy diagram for simple closed cycle gas turbine is shown in Figure 4.2. The diagram shows a realistic cycle that considers the pressure losses that

cause internal irreversibilities in the cycle heat exchangers. Turbine and compressor irreversibilities in form of the device adiabatic efficiency are considered in this diagram, as well. P_H and P_L on this diagram represent the highest and lowest actual operating pressure in the cycle, and the pressure ratio of the gas turbine is defined in this study based on these two values.

The recuperative closed cycle helium gas turbine considered in this study is shown in Figure 4.3. A two-stage compression with intercooling is considered for this system, while one turbine is used for power production and to drive the compressors. After being heated, helium expands through the turbine. The low pressure gas from the turbine enters a heat transfer recuperator to heat the cooler gas at the high pressure side of the cycle. The cooled helium leaving the recuperator is directed to another heat exchanger that works as a precooler before the compressor. The working fluid is further cooled in the precooler. Heat rejected from the cooler can be transferred to generator of an absorption cooling system for cogeneration. Two stage compressions with intercooler are used to raise the helium pressure to its highest value in the cycle. Then helium is heated by the turbine low pressure outlet gas through the recuperator before it goes to the main heat source.

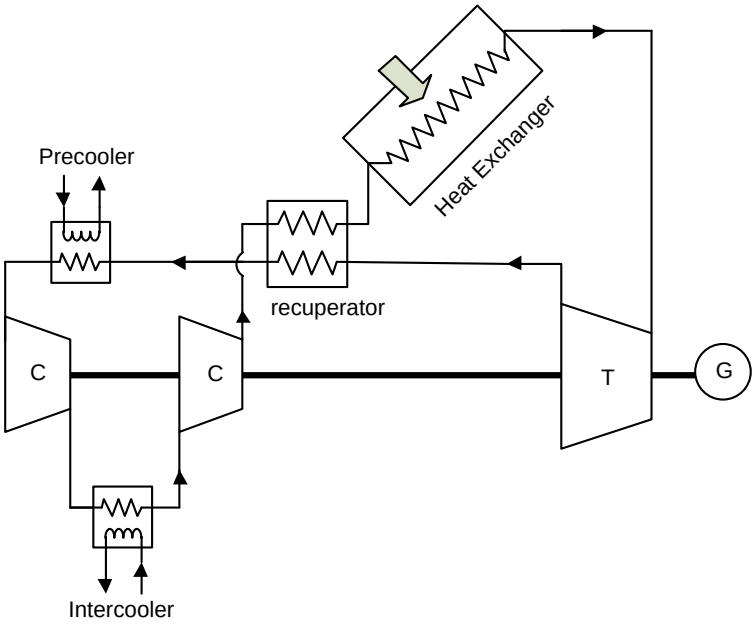

Figure 4.3 Schematic of recuperative closed cycle gas turbine with intercooler.

For the thermodynamic study, it is essential to make some assumptions for analysis and assessment. Here, we make the following assumptions for energy and exergy analyses of the system:

- Turbine and compressors are adiabatic.
- The plant operates at steady state conditions.
- Helium properties are assumed to be as for ideal gases.
- Heat source is considered as molten salt at constant temperature.
- The pressure ratio is defined in terms of the higher pressure, P_H, and lower pressure, P_L, of the cycle after considering the pressure losses.
- The ambient temperature and pressure are constant.
- No cogeneration and no use of the rejected heat of the cycle are considered in the exergy assessment calculations.
- The changes in kinetic and potential energies and exergies are negligible.

Energy Analysis

The helium gas turbine energy performance is investigated and modeled in the following subsections. The energy analysis of the components is performed and the components performance is described in form of the following parameters:

- Turbine and compressor polytropic efficiency.
- Plant pressure ratio.
- Plant temperature ratio.
- Heat exchangers effectiveness.
- Heat exchangers pressure loss coefficients.

The first law of thermodynamics is applied to each of system components. The following equation represents the concept of conservation of energy for an open system:

$$dE/dt = \sum \dot{Q} - \dot{W} + \sum_{in} \dot{m}\, h - \sum_{out} \dot{m}\, h \qquad (4.75)$$

where the changes in kinetic and potential energies across the system are considered negligible.

Exergy Analysis

The practical operation of any system is an irreversible operation, where work is destroyed based on the entropy generation rate that is associated with the operating

process. The amount of lost available work can be defined as the difference between the reversible work when no irreversibilities are considered, i.e., entropy generation is zero, and the system actual irreversible work.

$$\dot{W}_{loss} = \dot{W}_{rev} - \dot{W} \quad (4.76)$$

Table 4.4 The helium turbine plant operating parameters (Conn and Kuo, 1976)

Operating Parameters for base case	
Turbine polytropic efficiency	92%
Compressor polytropic efficiency	90%
Mechanical efficiency	99%
Recuperator effectiveness	88%
Precooler effectiveness	90%
Intercooler effectiveness	87%
Pressure loss in recuperator, hot side	2.1%
Pressure loss in recuperator, cold side	1.8%
Pressure loss in Precooler, hot side	1.2%
Pressure loss in Intercooler, hot side	1.3%
Turbine inlet temperature	850^{o}C
Compressor inlet temperature	40^{o}C
Turbine inlet pressure	70 bar
Plant temperature ratio	313K/1123K
Ambient temperature	25^{o}C
Hot source temperature	930^{o}C
Cooling water inlet temperature	25^{o}C

The lost available work is not an actual energy loss; it represents a lost opportunity to convert part of the energy utilized into a useful work. The lost available work was defined in a direct proportional relation with the entropy generation rate. This is better described by the exergy destruction term which expresses the system irreversibility as follows:

$$\dot{E}x_d = T_o.\dot{S}_{gen} \quad (4.77)$$

The temperature T_o is the defined as the dead state temperature. It is the temperature at which the system cannot undergo any state change through any interactions with the environment. The entropy generation for a general open system can be determined based on the second law of thermodynamics.

$$\dot{S}_{gen} = \frac{dS}{dt} - \sum \frac{\dot{Q}}{T} + \sum_{out} \dot{m}\, s - \sum_{in} \dot{m}\, s \quad (4.78)$$

where *T* is the temperature of the boundaries at which the heat transfer occurs**.**

$$\dot{W} = \sum \left(1 - \frac{T_o}{T}\right) \dot{Q} + \sum_{in} \dot{E}x + \sum_{out} \dot{E}x - \frac{d(E - T_o S)}{dt} - \dot{E}x_d \quad (4.79)$$

The term $\dot{E}x$ expresses the exergy flow rate or the exergy associated with the mass flow rate of the streams that enter or exit from the system. It is defined as:

$$\dot{E}x = \dot{m}\, ex = \dot{m}(h - T_o s) \quad (4.80)$$

The exergy destruction rate is applied on the prescribed gas turbine plant components as illustrated in the following section, considering the ideal gas behavior of the working fluid. The exergy destruction is expressed by taking external and internal irreversibilities into consideration. External irreversibilities are associated with the heat transfer between the working fluid and the hot and cold reservoirs at the source and dead state temperature values, respectively. Internal irreversibilities are the mainly accompanied with the finite pressure drop across the system devices. In the following sections, energy and exergy analyses of each for system components are presented.

Modeling of System Components

Compressor Modeling

The system in this study has two compression stages. The total pressure ratio is a design parameter as listed in Table 4.4. The compressor is considered adiabatic and its polytropic efficiency is also provided as in Table 4.4. Practically, helium compressor blade design is different than air compressor. It has to account for the flow separation and secondary flow occurrence to achieve a better performance (McDonald, 2012; No et al., 2007). Also, due to helium low molecular weight, a more reliable sealing mechanism needs to be integrated with the compressor and the other system components to avoid leakage (McDonald et al., 1994). Based on the defined pressure ratio and polytropic efficiency of

the compressor, and the plant temperature ratio, the power required to drive the compressor can be formulated as follows:

$$\dot{W}_C = \dot{m}\, c_p\, T_H\, \beta\, \left(\frac{r_c^k - 1}{\eta_{C,a}\, \eta_{mech}}\right) \quad (4.81)$$

where T_H is the highest temperature at the gas turbine plant, i.e., turbine inlet condition, β is the operational temperature ratio, and is defined as follows:

$$\beta = \frac{T_L}{T_H} \quad (4.82)$$

and k is function of the heat capacity ratio:

$$k = \frac{\gamma - 1}{\gamma} \quad (4.83)$$

The pressure ratio is defined as the ratio between the higher and lower pressure across the compressor, which is defined as follows, taking into consideration the pressure losses at the high and low pressure streams of the working fluid.

$$r_c = \frac{P_H}{P_L} \quad (4.84)$$

The compressor adiabatic and isentropic efficiencies are related as follows:

$$\eta_{C,a} = \frac{r_c^k - 1}{r_c^{k/\eta_{C,p}} - 1} \quad (4.85)$$

The temperature of the stream exits the compressor is to be estimated based on the inlet temperature of the working fluid:

$$T_{C,ex} = T_{C,in}\left(1 + \frac{r_c^k - 1}{\eta_{C,a}}\right) \quad (4.86)$$

Considering an adiabatic compression process, the exergy destruction rate associated with this process can be formulated as a function of the total pressure ratio of the gas turbine plant and the compressor adiabatic efficiency as follows:

$$\dot{E}x_{d,C} = \dot{m}\, T_o\, c_p\, \ln\left[\left(\frac{1}{r_c^k} - 1\right)\left(1 - \frac{1}{\eta_{C,a}}\right) + 1\right] \quad (4.87)$$

Practically, identical adiabatic efficiency values are chosen for the two operating compressors.

Intercooler Modeling

The high thermal conductivity and heat transfer coefficient of helium, compared with air, results in more compact designs of the utilized heat exchangers. The use of intercooler in

between compression stages is a standard feature of efficient gas compressors. The total compression required power is formulated as a function of the total pressure ratio and the compressors stage adiabatic efficiency as follows:

$$\dot{W}_C = \frac{\dot{m}\, c_p\, T_H\, \beta}{\eta_{mech}}\left(r_c^{k/N_C} - 1\right)\sum_{N_C}\left(\frac{1}{\eta_{C,a}}\right) \quad (4.88)$$

For two compression stages with intercooling and the same adiabatic efficiency of the two stages, the total compression work becomes

$$\dot{W}_C = 2.\dot{m}\, c_p\, T_H\, \beta\left(\frac{r_c^{k/2}-1}{\eta_{C,a}\, \eta_{mech}}\right) \quad (4.89)$$

which does not count for the pressure loss in the intercooler. For the definition of the total pressure ratio in this study as the final pressure after second compression stage over the lowest pressure at the inlet of the first compression stage, after considering the total pressure loss in the cycle, the second stage of compression would count for the drop in the pressure at the intercooler, which means a slightly higher pressure ratio would be required for the second compression stage to achieve the design total pressure ratio of the plant. This results in more required work to drive the high pressure compressor, even if the two compressors operate at the same adiabatic efficiency.

The heat transfer rate removed from the working fluid at the intercooling stage is formulated as follows with the assumption that the flow exits the intercooler at the inlet temperature of the preceding compressor:

$$\dot{Q}_{IC} = \dot{m}\, c_p\left(T_{C,ex} - T_H\, \beta\right) \quad (4.90)$$

where $T_{C,ex}$ is the temperature at the exit of the preceding compression stage, at the intercooler inlet.

In the intercooler, there are irreversibilities associated with the heat transfer within the temperature difference between the stream flow and the ambient, and irreversibility associated with the flow due to the pressure drop across the device. The exergy destruction in the intercooler can be described as follows, based on the output of the energy analysis:

$$\dot{E}x_{d,IC} = \left(\frac{\dot{Q}_{IC}}{T_{IC}/\,T_o}\right) - \dot{m}\, T_o\left[\left(s_{IC,in} - s_{IC,ex}\right)\Big|_{P_{IC}} - R\left(\frac{\Delta P}{P}\right)_{IC}\right] \quad (4.91)$$

Here, the destruction of exergy is expressed for an equivalent intercooler that works with no pressure loss, hence, slightly warmer, and then the entropy increase because of the pressure drop is added as it is expressed in the equation for an ideal gas assumption.

Gas Turbine Modeling

The efficiency of the helium turbine is highly affected by its design, which is a bit different from the conventional gas turbine design. It has shorter blade height and this results in an increase of the blade tip clearance leakage (McDonald, 2012; McDonald et al., 1994). On the other hand, compared with steam turbine, helium gas turbine is more economic due to the less material requirements as the blades of the former are ten times larger in length (Boyce, 2006; Frutschi, 2005). The power output of the gas turbine is formulated in the following form, as function of the plant pressure ratio:

$$\dot{W}_T = \dot{m}\ \eta_{T,a} c_p\ T_H \left[1 - \frac{1+k\cdot\sum\left(\frac{\Delta P}{P}\right)}{r_c^k}\right] \quad (4.92)$$

where the turbine adiabatic efficiency is calculated as a function of the polytropic efficiency of the turbine as follows:

$$\eta_{T,a} = \frac{1-(1/r_T)^{\frac{k}{\eta_{T,p}}}}{1-(1/r_T)^k} \quad (4.93)$$

The turbine pressure ratio is to be determined based on the defined pressure ratio of the compression stages, considering the pressure losses in the working fluid streams across the different system component, as follows:

$$r_T = \frac{P_{T,in}}{P_{T,ex}} = r_c \cdot \left[\frac{1-\left[\left(\frac{\Delta P}{P}\right)_{HE}+\left(\frac{\Delta P}{P}\right)_{R,c}\right]}{1+\left[\left(\frac{\Delta P}{P}\right)_{PC}+\left(\frac{\Delta P}{P}\right)_{R,h}\right]}\right] \quad (4.94)$$

The total pressure loss effect in the turbine work equation is the summation of the pressure loss coefficients in the hot and cold streams of the recuperator, the hot streams of the precooler and intercooler, and the cold stream of the main heat exchanger.

$$\sum\left(\frac{\Delta P}{P}\right) = \left(\frac{\Delta P}{P}\right)_R + \left(\frac{\Delta P}{P}\right)_{PC} + \left(\frac{\Delta P}{P}\right)_{IC} + \left(\frac{\Delta P}{P}\right)_{HE} \quad (4.95)$$

where the recuperator pressure loss is described as the summation of its hot and cold streams pressure losses.

$$\left(\frac{\Delta P}{P}\right)_R = \left(\frac{\Delta P}{P}\right)_{R,h} + \left(\frac{\Delta P}{P}\right)_{R,c} \quad (4.96)$$

The temperature value at the exit of the turbine is to be determined, as a function of the operating compressor pressure ratio, as follows:

$$T_{T,ex} = T_H\left(1 - \eta_{T,a}\left(1 - \frac{1}{r_T^k}\right)\right) \quad (4.97)$$

The irreversibility associated with the turbine, amounts to the following form, as a function of the gas turbine operating parameters:

$$\dot{E}x_{d,T} = \dot{m}\, T_o\, c_p\, \ln\left[1 - (r_T^k - 1)(\eta_{T,a} - 1)\right] \quad (4.98)$$

Here, the working fluid is treated as an ideal gas with constant specific heat.

Recuperator Modeling

From the defined recuperator effectiveness, the temperature at the exit of the cold stream, at the high pressure side, is determined:

$$T_{R,c,ex} = T_H\left[\beta(1-\varepsilon_R)\left(1 + \frac{(\sqrt{r_c})^k - 1}{\eta_{HC,a}}\right) + \varepsilon_R\left[1 - \frac{1 + k\cdot\sum\left(\frac{\Delta P}{P}\right)}{r_c^k/\,\eta_{T,a}}\right]\right] \quad (4.99)$$

This equation is derived based on recuperator effectiveness which can be defined as follows:

$$\varepsilon_R = \frac{T_{R,c,ex} - T_{R,c,in}}{T_{R,h,in} - T_{R,c,in}} \quad (4.100)$$

The hot stream exit temperature, on the low pressure side, is to be determined by applying the energy balance on the hot stream, at low pressure side, as follows:

$$T_{R,H,ex} = T_{R,H,in} - \dot{Q}_R/(\dot{m}\, c_p) \quad (4.101)$$

where $\dot{Q}_R$ is the heat transfer through the recuperator from the hot stream to cold stream. It is simply calculated from the energy balance of the cold stream:

$$\dot{Q}_R = \dot{m}\, c_p(T_{R,c,ex} - T_{R,c,in}) \quad (4.102)$$

By defining the exist streams of the recuperator, the analysis of the main heat exchanger and the precooler can be performed. Based on the two working fluid streams passing through the recuperator, the exergy associated with the recuperator can be formed as follows:

$$\dot{E}x_{d,R} = \dot{m}\, T_o\left[\left(s_{R,c,ex} - s_{R,c,in}\right)\big|_{P_H} + \left(s_{R,H,ex} - s_{R,H,in}\right)\big|_{P_L} + R\left(\frac{\Delta P}{P}\right)_R\right] \quad (4.103)$$

Same as for the other heat exchangers in this analysis, the entropy generation analysis is performed and is formed in a no pressure loss entropy differences, and then the internal irreversibility caused by the pressure losses in hot and cold streams is added. The total pressure coefficient in the recuperator is equal to both sides' pressure losses coefficients. In the recuperator case, pressure loss at both sides need to be considered as the irreversibility analysis is performed on both flow streams considering the heat transfer effect in form of sates difference between inlet and outlet streams.

Heat Exchanger Modeling

Based on the defined highest temperature of the gas turbine plant, the heat rate required to be supplied, to the working fluid, through the heat exchanger can be calculated as follows:

$$\dot{Q}_{HE} = \dot{m}\, c_p\, T_H \left(1 - \frac{T_{R,c,ex}}{T_H}\right) \quad (4.104)$$

The working fluid, after being heated by the hot, low pressure, stream at the recuperator, it passes through the main heat exchanger which provides the required amount of heat to reach the turbine inlet temperature with enough potential to gain the required power. The following equation expresses the destruction of exergy associated with this process:

$$\dot{E}x_{d,HE} = \dot{m}\, T_o \left[\left(\frac{-\int_{in}^{ex} Tds\big|_{P_H}}{T_{HE}}\right) + \left(s_{HE,ex} - s_{HE,in}\right)\big|_{P_H} + R\left(\frac{\Delta P}{P}\right)_{HE}\right] \quad (4.105)$$

The first term in the brackets represents the specific heat gained by the working fluid considering the heat transfer to happen at constant pressure, where:

$$\int_{in}^{ex} Tds\big|_{P_H} = q_{HE} \quad (4.106)$$

In the exergy destruction equation, the external irreversibility in the heat exchanger is expressed by the first two terms in the brackets. This part of irreversibility is associated with the heat transfer to the working fluid within the temperature difference between the source temperature T_{HE}, and the working fluid bulk temperature through the heat exchanger, considering no pressure loss to occur during the process. To add the effect of the pressure drop, the internal irreversibility is added in terms of pressure loss across the heat exchanger for ideal gas case as shown in the last term of the equation.

The temperature T_{HE} is the heating source temperature and is calculated, in analogous with the open gas turbine engine with combustion, based on the definition of the optimal effective flame temperature of the combustion products. It can be formulated as function of the heating molten salt temperature as follows:

$$T_{HE} = \frac{T_{s,in} - T_o}{ln(T_{s,in}/T_o)} \quad (4.107)$$

Further details regarding the calculation of the optimal flame temperature can be found in Bejan (2006).

Precooler Modeling

The heat released from the low pressure stream at the intercooler is determined as follows, based on the energy balance on this stream:

$$\dot{Q}_{PC} = \dot{m}\, c_p \left(T_{R,h,ex} - T_H\, \beta\right) \quad (4.108)$$

In the same way of calculating the exergy destruction in the intercooler, the exergy destruction in the precooler can be formed as follows:

$$\dot{E}x_{d,PC} = \left(\frac{\dot{Q}_{PC}}{T_{PC}/T_o}\right) - \dot{m}\, T_o \left[\left(s_{PC,ex} - s_{PC,in}\right)\Big|_{P_L} - R\left(\frac{\Delta P}{P}\right)_{PC}\right] \quad (4.109)$$

Here, the term $\left(s_{PC,ex} - s_{PC,in}\right)\Big|_{Pl}$ is the entropy difference considering the process through the intercooler occurs at constant pressure with no pressure losses. $R(\Delta P/P)_{PC}$ represents the entropy change as a result of the pressure loss at the working fluid side, considering ideal gas behavior.

Energetic Assessment

The thermal energy efficiency can be formulated, based on the shown analysis, in form of the gas turbine thermal design parameters for a closed recuperative gas turbine cycle with two compression stages as follows:

$$\eta_{th} = \frac{\left[\frac{r_c^k - 1 - k\cdot\sum(\Delta P/P)}{r_c^k/\eta_{T,a}}\right] - \left[\frac{\beta\left(r_c^k - 1\right)}{\eta_{C,a}\eta_{mech}}\right]}{1 - \left[\beta\left(1-\varepsilon_R\right)\left(1 + \frac{r_c^k - 1}{\eta_{C,a}}\right) + \varepsilon_R\left[1 - \frac{1 + k\cdot\sum(\Delta P/P)}{r_c^k/\eta_{T,a}}\right]\right]} \quad (4.110)$$

The optimal pressure ratio of the plant is determined at maximum thermal efficiency, by differentiating the previous formula with respect to pressure ratio, r_c, setting $d\eta_{th}/dr_c$ to zero for maximum efficiency. The pressure ratio for each compressor stage in this relation are assumed to be identical, however, with considering the pressure

loss in the intercooler, they will be slightly different as mentioned before, based on the given definition of the higher and lower pressure values of the gas turbine cycle.

Another parameter used to describe the system performance is the dimensionless work output of the gas turbine plant. The dimensionless work is used to express the results of the energetic performance of the system. It is to be calculated by relating the actual specific work output to the total potential of producing work expressed in terms of the temperature ratio and the turbine inlet temperature as follows:

$$W_{dimless} = \frac{w_{net}}{c_p T_H (1-\beta)} \quad (4.111)$$

Exergetic Assessment

The helium turbine plant performance can be described in different exergy parameters. The exergy efficiency of the overall plant performance can be expresses in terms of the useful exergy output of the plant over the exergy of the fuel supplied in form of exergy of the heat added to the system:

$$\psi = \frac{\dot{Ex}_{output}}{\dot{Ex}_f} \quad (4.112)$$

It can be also estimated based on the exergy destruction calculation as follows:

$$\psi = 1 - \frac{\sum \dot{Ex}_d}{\dot{Ex}_f} \quad (4.113)$$

Each of the exergy destruction rates in system components is described as percentage of the total exergy destruction:

$$y_D = \frac{\dot{Ex}_d}{\sum \dot{Ex}_d} \quad (4.114)$$

The exergy destruction can be expressed by the exergy destruction ratio as it is defined by relating the exergy destruction rate in each component to the total exergy rate of the fuel to the system.

$$Ex_R = \frac{\dot{Ex}_d}{\sum \dot{Ex}_F} \quad (4.115)$$

Another parameter is the sustainability index, which helps in giving an indication of the improvement potential for more efficient use of the available resources of the system as follows:

$$SI = \frac{1}{1-\psi} \quad (4.116)$$

The improvement potential for each of the system components can be measured in energy units based on the following relation (Gool, 1997):

$$IP = (1 - \psi)\left(\dot{E}x_{in} - \dot{E}x_{ex}\right) \quad (4.117)$$

4.3.4 Absorption Cooling System

Analysis of a single effect water-LiBr absorption cooling system is considered in this section. The cycle is shown in Figure 4.4. The analysis of the cycle is considered at steady state condition, mass, species and energy balance equations are applied on the system components based on the general form:

$$\sum \dot{m}_i = \sum \dot{m}_o \quad (4.118)$$

$$\sum (\dot{m}x)_i = \sum (\dot{m}x)_o \quad (4.119)$$

$$\dot{Q} - \dot{W} = \sum \dot{m}_o h_o - \sum \dot{m}_i h_i \quad (4.120)$$

The cycle COP is simply calculated considering the cooling effect as follow:

$$COP = \frac{Q_{evap}}{Q_{generator}} \quad (4.121)$$

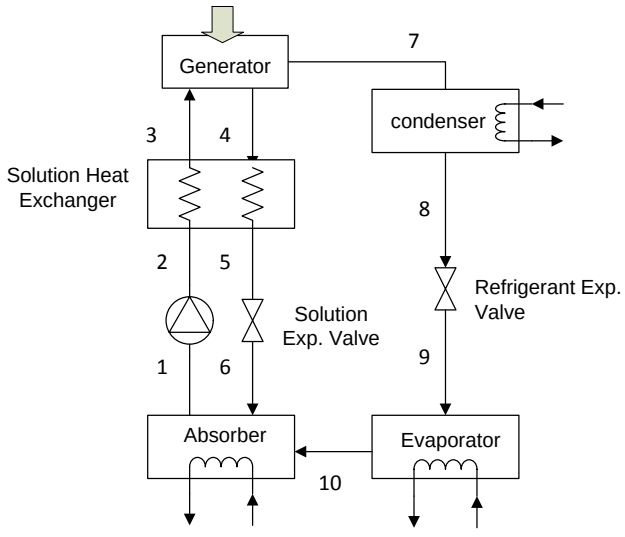

State 1: saturated liquid solution

State 2: subcooled liquid solution

State 3: subcooled liquid solution

State 4: saturated liquid solution

State 5: subcooled liquid solution

State 6: vapor-liquid solution

State 7: superheated steam

State 8: saturated liquid water

State 9: vapor-liquid water

State 10: saturated vapor

Figure 4.4 Single effect absorption cooling cycle with state definition

The performance measured based on the second law of thermodynamics is to be described with respect to the reversible coefficient of performance which is defined for a refrigeration machine with respect to the governing temperature values: heat source temperature, condenser environment cooling flow and evaporator environment temperature.

$$COP_{II} = \frac{COP}{COP_r} \quad (4.122)$$

All heat exchangers of the system are modeled using the LMTD method.

4.3.5 Biomass Thermal Properties

The thermal properties of biomass fuel are calculated based on the specific heating value which is presented by Jenkins (1989) as a function of temperature. It can be formulated in the modified form for dry biomass as follows:

$$c_{p,db} = 1.16 \times 10^{-3}\, T - 5.0854 \times 10^{-2} \quad (4.123)$$

where the temperature is in K. The moisture effect on the specific heat calculations can be expressed as:

$$c_{p,b} = c_{p,db}(1 - \omega) + \omega c_{p,w} \quad (4.124)$$

where ω is the moisture faction on wet basis and $c_{p,w}$ is the water specific heat. The enthalpy and entropy at different state points are calculated as:

$$h = h_o + \int_{T_o}^{T} c_p dT \quad (4.125)$$

$$s = s_o + \int_{T_o}^{T} c_p \frac{dT}{T} \quad (4.126)$$

The Gibbs free energy is calculated as function of operating temperature as shown in the following formula, which is introduced as modified from Basu (2010) expressed in kJ/kmol:

$$\Delta g_T^f = h_o^f + z_o T + z_1 T \ln T + z_2 T^2 + z_3 T^3 + z_4 T^4 + z_5 T^{-1} + z_6 \quad (4.127)$$

where h_o^f is enthalpy of formation at the reference temperature and pressure, and temperature is in K. Values of the coefficients in the previous formula are given in Table 4.5.

The enthalpy of formation of moist biomass is calculated as function of enthalpy of formation of the dry biomass and the moisture content as follows:

$$h_b^f = (h_{db}^f - 2.44\omega - 21.83H)(1 - \omega) \quad (4.128)$$

The enthalpy of formation of the dry biomass was calculated as follows (Basu, 2010):

$$h_{db}^f = 349.1C + 1178.2H - 103.4O + 100.5S - 15.1N \quad (4.129)$$

where C, H, O, S and N are weight fractions of ultimate biomass compositions.

The chemical exergy of the biomass fuel is calculated as function of the lower heating value where:

$$ex_b^{ch} = \beta . LHV_b \quad (4.130)$$

The factor β is calculated based on the composition of the biomass fuel using the following formula (Saidur et al., 2012):

$$\beta = \frac{1.044 + 0.016(H/C) - 0.3493(O/C)(1 + 0.0531H/C) + 0.0493(N/C)}{(1 - 0.4124O/C)} \quad (4.131)$$

Table 4.5 Coefficients of the empirical correlation for Gibbs free energy calculations, modified from Basu (2010)

	CO	CO_2	CH_4	H_2O
Z_0	-61.31	-120.7	223.4	-17.2
Z_1	-5.619	19.49	46.2	8.95
Z_2	1.19×10^{-2}	-3.133×10^{-2}	-1.13×10^{-2}	3.672×10^{-3}
Z_3	-3.1915×10^{-6}	1.224×10^{-5}	-6.595×10^{-6}	-2.6045×10^{-6}
Z_4	6.153×10^{-10}	-2.3153×10^{-9}	2.2157×10^{-9}	4.927×10^{-10}
Z_5	-244,550	-244,550	-244,550	0
Z_6	868	5,270	14,110	2,868

The lower heating value for the produced gas is calculated as function of the gas compositions heating values:

$$\overline{LHV}_{gas} = \sum_1^n (y_i \overline{LHV}_i)_{gas} \quad (4.132)$$

which gives the lower heating value in molar form.

The chemical exergy of the produced gas at any state can be calculated as follows:

$$\overline{ex}_{gas}^{ch} = \sum_1^n \left(y_i \overline{ex}_i^{ch} + RT_o y_i \ln y_i\right)_{gas} \quad (4.133)$$

which is function of the chemical exergy and molar fractions of all the species of the produced gas.

4.3.6 Biomass Gasification – SOFC

The proposed integrated system is schematically shown in Figure 4.5. The model considers steam as the gasification and drying medium for the provided biomass fuel. The dry biomass is assumed to go through the gasification process at 10% to 30% moisture content. The steam is supplied through the heat recovery steam generator, which utilizes the burner of fuel cell exhaust gas as heat source. The air required here is also provided to the fuel cell and, if needed, to the gasification process after being heater by the gasification produced gas. The biogas produced from the process is cooled to the inlet condition of the fuel cell. The heat is utilized to heat the supplied air. A certain percentage of the produced biogas is directed for hydrogen production unit, which is cooled down by supplying its heat to the air. The SOFC model is introduced as direct internal reforming solid oxide fuel cell DIR-SOFC. The amount of biogas directed to fuel the SOFC is based on the power desired from the fuel cell. The burner is assumed to operate under complete combustion condition where adiabatic flame temperature model is adopted for the process.

System Analysis

Thermodynamic analyses based on energy, exergy, chemical equilibrium, kinetics of gasification and SOFC analyses for the main sections of the system in Figure 4.5 are performed. The gasification hydrodynamics are also considered for determining the axial temperature distribution through the gasifier, energy and concentration equations through the gasifier are also introduced. The general form of energy and exergy balance equations, applied to the components of the proposed system, can be written based on first and second laws of thermodynamics.

$$\dot{Q}_{cv} - \dot{W}_{cv} = \sum \dot{m}_{in} h_{in} - \sum \dot{m}_{out} h_{out} \quad (4.134)$$

$$\dot{Ex}_{d_i} = \sum (1 - \frac{T_o}{T})\, \dot{Q}_{cv} - \dot{W}_{cv} + \sum \dot{m}_{in} ex_{in} - \sum \dot{m}_{out} ex_{out} \quad (4.135)$$

The exergy efficiency is generally defined as the exergy of the useful product with respect to the exergy of the system fuel:

$$\eta_{sys}^{ex} = \frac{\dot{Ex}_p}{\dot{Ex}_f} \quad (4.136)$$

For the integrated system, the term expressing exergy of useful outputs represents the produced hydrogen, the net power output, considering auxiliary power, and extra heat

of the exhaust, which passes through the heat recovery steam generator. The excess heat is considered to produce process steam at the same gasification steam condition.

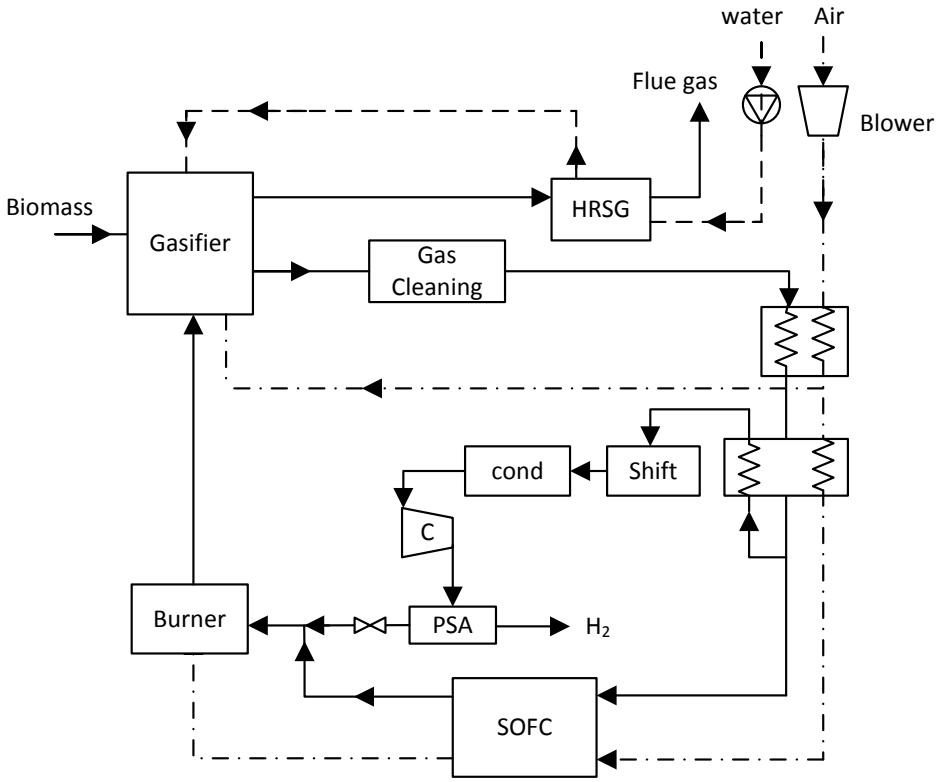

Figure 4.5 Schematic of the proposed integrated system

Greenhouse Gas Emissions

In this case study, the environmental assessment is performed by considering the amount of carbon dioxide produced per unit energy of the useful product. For steam gasification process for hydrogen production, the energy of the produced hydrogen is considered. The carbon dioxide emissions are also calculated for the integrated system considering the energy of the system useful output.

4.3.7 Energy and Exergy Analyses of Steam Biomass Gasification

The mass balance equations for the drying process using steam as drying medium for the biomass fuel before can be simplified as discussed in the literature (Abuadala et al., 2010; Hosseini et al., 2012):

$$\dot{m}_{db,in} = \dot{m}_{db,out} \quad (4.137)$$

$$\dot{m}_{m,in} + \dot{m}_{st,in} = \dot{m}_{m,out} + \dot{m}_{st,out} \quad (4.138)$$

$$\dot{m}_{b} = \dot{m}_{db} + \dot{m}_{m} \quad (4.139)$$

where $\dot{m}_{db}$, $\dot{m}_{m}$, $\dot{m}_{b}$ and $\dot{m}_{st}$ are dry biomass, moisture, steam and fed biomass mass flow rates. The subscripts in this model are considered as follows: *b, db, m, st, ar, p* for biomass, dry biomass, moisture, steam, air and products, respectively. The moisture mass flow rate is simply calculated as a function of the moisture content as follows:

$$\dot{m}_{m} = \dot{m}_{db}.\omega \quad (4.140)$$

In the current model, biomass is dried to 10% - 30% moisture content. Energy balance equation considering heat carried by the drying steam can be written as follows:

$$\dot{m}_{b,in}h_{b,in} + \dot{m}_{st,in}h_{st,in} = \dot{m}_{b,out}h_{b,out} + \dot{m}_{st,out}h_{st,out} \quad (4.141)$$

where the heat content of the biomass is considered as follows:

$$\dot{m}_{b}h_{b} = \dot{m}_{db}h_{db} + \dot{m}_{m}h_{m} \quad (4.142)$$

Based on the defined energy balance, exergy balance equation is formulated as:

$$\dot{E}x_{db,in} + \dot{E}x_{m,in} + \dot{E}x_{st,in} = \dot{E}x_{db,out} + \dot{E}x_{m,out} + \dot{E}x_{st,out} + \dot{E}x_{d,dryer} \quad (4.143)$$

where $\dot{E}x$ is the exergy rate associated with the corresponding flow which is calculated as follows:

$$\dot{E}x_{i} = \dot{m}_{i}ex_{i} \quad (4.144)$$

Here, it is considered that the volatile products of the current model are CO, CO_2, H_2, CH_4 and H_2O. The char is considered to be carbon. Two parameters are introduced as σ_{CO} and σ_{tar} to represent the splitting factors of the amount of oxidation to CO and the amount of carbon forming tar. The values considered for the two parameters are given in Table 4.6. In the gasification reaction, steam is controlled by steam to biomass ratio, excess air would be added if it is considered a provider of the heat required for gasification process and it is controlled by the air equivalence ratio. The gasifier reactions considered in the current model are listed in Table 4.7.

The combustion reaction, R1, is controlled by the factor α which is provided in Table 4.6. The reactions, R2, R3 and R4, are the gasification equilibrium reactions considered for carbon conversion into gaseous components (Prins et al., 2003). These are

the endothermic Boudouard reaction, which requires high operating temperature, the endothermic water-gas reaction and the exothermic hydrogasification reaction. Moreover, water-gas shift and methane formation reactions are coupled if the gasification temperature satisfies zero solid carbon unconverted, as specified in R5 and R6 in Table 4.7 (Karamarkovic and Karamarkovic, 2010).

Table 4.6 Gasification operating parameters

Gasifier input data	**[base case]**
Ultimate Analysis wt.% of Beech Chips	Schuster et al. (2001)
Carbon	48.26%
Hydrogen	5.82%
Oxygen	45.67%
Nitrogen	0.22%
Sulfur	0.03%
Lower heating value	17,794 kJ/kg
Temperature of steam	350°C*
Pressure of the gasifier	1 bar
Water content of fed biomass	55%*
Water content at the gasifier	20%*
Minimum fluidization velocity, V_{mf}	0.175 m/s (Milioli and Foster, 1995)
Gas diffusivity, D_g	$1.88x10^{-4}$ m^2/s (Basu, 2006)
Bed diameter	0.3 m*
Number of bed orifices, N_{or}	800*
Extended bed height, H_{eb}	0.6 m*
Bed Material	Silica sand
Diameter of sand particles, d_s	0.45 mm (Milioli and Foster, 1995)
Density of sand particles, ρ_s	2650 kg/m^3 (Milioli and Foster, 1995)
Splitting factor, σ_{CO}	0.3 (Petersen and Werther, 2005)
Splitting factor, σ_{tar}	0.005 (Petersen and Werther, 2005)
Combustion splitting coefficient, α	1.3 (Petersen and Werther, 2005)

Assumed data *

Table 4.7 Combustion and gasification reactions

	Reaction
R1	$\alpha C + O_2 \rightarrow 2(\alpha - 1)CO + (2 - \alpha)CO_2$
R2	$C + CO_2 \leftrightarrow 2CO$
R3	$C + H_2O \leftrightarrow CO + H_2$
R4	$C + 2H_2 \leftrightarrow CH_4$
R5	$CO + H_2O \leftrightarrow CO_2 + H_2$
R6	$CO + 3H_2 \leftrightarrow CH_4 + H_2O$

The energy balance equation for the gasifier can be written as follows:

$$\dot{n}_{b,in}\left(\bar{h}_b^f + \bar{h}_b - \bar{h}_b^o\right) + \dot{n}_{st,in}\left(\bar{h}_{st}^f + \bar{h}_{st} - \bar{h}_{st}^o\right) + \dot{n}_{ar,in}\left(\bar{h}_{ar}^f + \bar{h}_{ar} - \bar{h}_{ar}^o\right) = \sum_1^n \dot{n}_i\left(\bar{h}_i^f + \bar{h}_i - \bar{h}_i^o\right)_p \quad (4.145)$$

where the energy content of the supplied air is to be added as it is considered the heat provider stream (Hosseini et al., 2012) and It can be solely considered as the source of heat. It can be also introduced considering the amount of heat supplied as:

$$\dot{n}_{b,in}\left(\bar{h}_b^f + \bar{h}_b - \bar{h}_b^o\right) + \dot{n}_{st,in}\left(\bar{h}_{st}^f + \bar{h}_{st} - \bar{h}_{st}^o\right) + \dot{Q}_g = \sum_1^n \dot{n}_i\left(\bar{h}_i^f + \bar{h}_i - \bar{h}_i^o\right)_p \quad (4.146)$$

The exergy destruction can be calculated form the exergy balance:

$$\dot{E}x_{d,gasifier} = \dot{E}x_{b,in} + \dot{E}x_{st,in} + \dot{E}x_{ar,in} - \dot{E}x_p \quad (4.147)$$

where $\dot{E}x_p$ is the total exergy of the products stream.

4.3.8 Hydrodynamics thermal modeling of steam Fluidized Bed Gasifier

One dimensional model of a fluidized bed is introduced and formulated. The model is designed to analyze the temperature and gas concentration through the fluidized bed (FB) at different operation conditions. It also considers combustion (FBC) and gasification (FBG) of biomass fuels. In the presented work, fluidized bed gasification is considered. The fluidized bed gasifier is modeled in three different zones as stated by Basu (2006); dense bed, splashing zone and the freeboard zone. The species concentrations and the axial temperature distribution through the bed height are investigated by applying the mass and energy balance equations over the three different zones as described by Okasha (2007). The model considers the bubble and emulsion phases, which is known as the two phase theory of fluidization.

For the dense bed zone, where volatilization and drying occurs, bubbling fluidized type zone is considered. The axial variation of the species concentration through the bed height can be described by the following differential equations for the bubble and emulsion phases, respectively (Mostoufi et al., 2001; Nemtsov and Zabaniotou, 2008; Okasha, 2007; Radmanesh et al., 2006):

$$u_b d\bar{x}_{b,i} - \left[K_{be}\left(\bar{x}_{e,i} - \bar{x}_{b,i}\right) + \sum R_{b,i} + \frac{1}{A_{bed}.\delta}\left(\frac{dC_i}{dz}\right)\right] dz = 0 \quad (4.148)$$

$$u_e d\bar{x}_{e,i} - \left[K_{be}.\delta.\left(\bar{x}_{b,i} - \bar{x}_{e,i}\right) + \varepsilon_{mf}(1-\delta).\sum R_{e,i}\right]dz = 0 \quad (4.149)$$

where $d\bar{x}/dz$ expresses the rate of change in the concentration of the different species through the bed height, dC/dz is the local release rate of the species in kmol/m.s. R is the reaction rate, $\bar{x}$ is the species concentrations expressed in kmol/m^3. The other parameters and coefficients in the species mass balance equations are illustrated in the hydrodynamics equation as described in Table 4.8. The main parameters in this table are shown as a function of the bed diameter, D, the fluidization velocity, U_f, and the minimum fluidization velocity, U_{mf}.

The splashing zone is located over the dense bed and better mixing occurs as a result of the bubble bursting (Pemberton and Davidson, 1984). For the splashing zone the species balance equation can be written as follows where the reaction rates are considered as for the emulsion phase without considered the items related to the coarse char based on the assumption that this zone is coarse char free (Okasha, 2007).

$$u_{sp,g} d\bar{x}_{sp,i} = \left(\sum R_{sp,i}\right)dz \quad (4.150)$$

The following equation is used to determine the temperature profile (Okasha, 2007). This is applied to the splashing zone where the dense bed zone is considered to have a constant value at the bed temperature.

$$\frac{dT_{g,sp}}{dz} = \frac{\left[A_{sp}\left(\sum R_{sp,i}\, HR_i\right) - Q_s - Q_w\right]}{N_g.c_{p,g}} \quad (4.151)$$

where HR is the heat of reactions that occurs through the gasifier. Other terms in the previous equations are illustrated as follows: Q_s is the energy exchange with the ejected sand and Q_w expresses heat loss through the walls of combustion area, they can be calculated as follows:

$$Q_s = M_s\,.A_{sp}.c_{p,s}\left(\frac{dT_s}{dz}\right) \quad (4.152)$$

$$Q_w = L_{sp}\,.h_{ov}\left(T_{sp} - T_{am}\right) \quad (4.153)$$

where the peripheral of the splashing zone cross-section, L_{sp}, and the overall heat transfer coefficient, h_{ov}, are given in Table 4.9 Both Q_s and Q_w are calculated per unit length of the gasifier.

The sand temperature gradient in the calculation of the energy exchange with the ejected sand can be calculated as follows (Okasha, 2007):

$$\frac{dT_s}{dz} = 6 \,.\, h_{s,sp} . \frac{T_{g,sp} - T_s}{d_s \,.\, \rho_s . c_{p,s}} \quad (4.154)$$

where the sand specification and properties are shown in Table 4.9.

Table 4.8 Hydrodynamics equations considered for the bubbling fluidized bed model.

Name	Formula	Ref.
Bubble diameter	$d_B = d_l - (d_l - d_o)EXP\left(\frac{-0.3\ z}{D}\right)$	(Kunii and Levenspiel, 1991)
Limiting bubble diameter	$d_l = 0.24[(U_f - U_{mf}).D^2]^{0.4}$	(Kunii and Levenspiel, 1991)
Initial bubble diameter, m	$d_o = 0.794\left[\frac{(U_f - U_{mf}).D^2}{N}\right]^{0.4}$	(Kunii and Levenspiel, 1991)
Bubble velocity, m/s	$U_B = U_f - U_{mf} + 0.227\sqrt{d_B}$	(Davidson and Harrison, 1963)
Bed Fraction in Bubbles	$\delta_B = \frac{U_f - U_{mf}}{U_B} = 1 - \frac{U_{mf}}{U_e}$	(Davidson and Harrison, 1963)
Superficial gas velocity through emulsion, m/s	$U_e = (U_f + 2U_{mf})/3$	(Okasha, 2007)
Bubble-Cloud Transfer Coefficient, 1/s	$K_{B-C} = \left(\frac{4.5\ U_{mf}}{d_B}\right) + \left(\frac{10.35\sqrt{D}}{{d_B}^{1.25}}\right)$	(Radmanesh et al., 2006)
Cloud-Emulsion Transfer Coefficient, 1/s	$K_{C-E} = 3.226\sqrt{\frac{Dif.\varepsilon_{mf}}{{d_B}^{2.5}}}$	(Radmanesh et al., 2006)
Bubble- Emulsion Transfer Coefficient, 1/s	$K_{B-E} = \frac{K_{C-E}.K_{B-C}}{K_{C-E} + K_{B-C}}$	(Radmanesh et al., 2006)
Void Fraction at minimum fluidization	$\varepsilon_{mf} = 0.478/A^{0.018}$	(Kaushal et al., 2010)
Archimedes number	$A = \frac{g.\rho_g(\rho_p - \rho_g){d_B}^3}{{\mu_g}^2}$	(Gómez-Barea and Leckner, 2010)

The following exponentially decay function expresses the mass flux of ejected sand particles:

$$M_s = M_{s,o}\exp[-C_{ej}.(z - z_{eb})] \quad (4.155)$$

where M_s is in kg/m^{2}s and is function of the initial mass flux at the bed surface which is calculated as follows (Okasha, 2007; Pemberton and Davidson, 1984).

$$M_{s,o} = \beta\rho_s(U_f - U_{mf})(1 - \varepsilon_{mf}) \quad (4.156)$$

Table 4.9 Parameters and constant for the formulas of the basic case

Parameter	Value
Bed height above distributer, m	$z = 3$
Bed diameter, m	$D = 0.3$
Number of bed orifices	N_{or} = 800
Extended bed height, m	$z_{eb} = 0.6$
Specific heat of sand, kJ/kg.K	$c_{p,s} = 0.83$ (Basu, 2006)
Diameter of sand particles, mm	$d_s = 0.45$ (Milioli and Foster, 1995)
Density of sand particles, kg/m^3	$\rho_s = 2650$ (Milioli and Foster, 1995)
Average diameter of char particle, µm	$d_{ch} = 500$
Density of char, kg/m^3	$\rho_{ch} = 470$
Peripheral of splashing zone cross-section, m	$L_{sp} = 0.3$
Parameter in sand initial mass flux	$\beta = 0.1$ (Milioli and Foster, 1995)
Parameter in sand mass flux	$C_{ej} = 18$ (Okasha, 2007)
Diameter of fine char particles, µm	$d_{ch,fine} = 100$ (Chirone et al., 1999)
Minimum fluidization velocity, m/s	$U_{f,m} = 0.175$ (Milioli and Foster, 1995)
Air Equivalence Ratio coefficient	0.20-0.30
Steam to biomass coefficient	0.7
Gas diffusivity, m^2/s	$Dif_g = 1.88 \times 10^{-4}$ (Basu, 2006)
Splitting factor for Oxygen reacting to CO	$\varepsilon_{CO} = 0.3$ (Petersen and Werther, 2005)
Splitting factor for C reacting to Tar	$\varepsilon_{tar} = 5 \times 10^{-3}$ (Petersen and Werther, 2005)
Partial combustion splitting coefficient	$\alpha_1 = 1.3$ (Petersen and Werther, 2005)
Heterogeneous water-gas shift splitting coeff.	$\alpha_2 = 1.2$ (Petersen and Werther, 2005)

The upper limit of the splashing zone is identified by the setting the decay of flux of the ejected sand particles to 0.001 (Okasha, 2007). The mass and energy equations of the splashing zone are also applied to the freeboard zone.

The mass and energy balance equations are applied on the proposed gasification system over the three described zones considering the composition of the gasification product to be as follows: CO, CO_2, H_2, CH_4, H_2O, and O_2.

Devolatilization

During the devolatilization process, the particles of the biomass fuel tend to concentrate near the bed surface (Fiorentino et al., 1997). Volatiles can be assumed to be released in the bubble phase as described by Okasha (2007). The volatiles are considered as CH_y (Philippek et al., 1997) and can be calculated as tabulated in Table 4.10. The volatiles release distribution, calculated in kmol/ms, can be described as a function of bed height as given by Okasha (2007):

$$\frac{dC_i}{dz} = 4\,\bar{C}_i \frac{z^3}{{z_{eb}}^4} \qquad (4.157)$$

where z_{eb} is the extended bed height and $\bar{C}_i$ is the molar releasing rate of moisture, oxygen and volatile, which is expressed as follows:

$$\bar{C}_i = \frac{\dot{m}_f \cdot X_i}{MW_i} \qquad (4.158)$$

Here, the volatile combustion is considered to occur in two steps, where it reacts to form carbon monoxide and water vapor, then carbon monoxide oxidize to carbon dioxide in the second step (Dryer and Glassman, 1973; Howard et al., 1973; Philippek et al., 1997). Rate of hydrocarbon conversion and the reaction rate of carbon monoxide for these two steps are shown in Table 4.10.

The volatiles can be given according a stoichiometric reaction of a biomass fuel of the formula $C_{\alpha_C} H_{\alpha_H} O_{\alpha_O} S_{\alpha_S} N_{\alpha_N}$ as follows (Petersen and Werther, 2005):

$$\text{Biomass} \rightarrow A_1.CO + A_2.CO_2 + A_3.CH_4 + A_4.H_2 + A_5.H_2S + A_6.O_2 + A_7.N_2 + A_8.\text{tar} \qquad (4.159)$$

where the mole faction can be written as follows:

$A_1 = \varepsilon_{CO}.\alpha_O$

$A_2 = \alpha_O(1 - \varepsilon_{CO})/2$

$$A_3 = \alpha_c(1 - A_2 - \varepsilon_{CO} + \varepsilon_{tar})$$

$$A_4 = \frac{\alpha_H}{2} - \alpha_S - 2A_3$$

$$A_5 = \alpha_H$$

$$A_6 = \alpha_O(1 - A_2 - \varepsilon_{CO})$$

$$A_7 = \varepsilon_{tar}\alpha_S$$

Table 4.10 Devolatilization and char consumption equations

Name	Formula	Ref.
Devolatilization		
Molar releasing rate, kmol/s	$\bar{C}_{O_2} = \frac{\dot{m}_f \cdot X_O}{MW_{O_2}}$	
Released hydrocarbon mole fraction	$y = \frac{X_H MW_C}{(X_C - X_{FC})MW_H}$	(Philippek et al., 1997)
Rate of hydrocarbon primary reaction to CO (step 1), kmol/m^3.s	$R_{CH_y} = -k_{CH_y}(\bar{x}_{CH_y})^{0.7}(\bar{x}_{O_2})^{0.8}$ $where\ k_{CH_y} = 4.74 \times 10^{11} EXP\left(\frac{-2415}{T}\right)$	(Philippek et al., 1997)
Reaction rate of CO (step 2), kmol/m^3.s	$R_{CO} = -k_{CO}\,\bar{x}_{CO}\sqrt{\bar{x}_{O_2}\bar{x}_{H_2O}}$ $where\ k_{CO} = 1.3 \times 10^{11}\vartheta EXP\left(\frac{-15088}{T}\right)$	(Howard et al., 1973)
Char Combustion		
Combustion Rate of Char particles, kg/s	$R_{ch} = -72 m_{ch}.\ \bar{x}_{O_2} / \left[\rho_{ch}.d_{ch}.\left(\frac{1}{K_{ch}} + \frac{1}{K_m}\right)\right]$	(Leckner et al., 1992)
Char Kinetic coefficient, m/s	$K_{ch} = 1.045\, T_{ch} EXP\left(\frac{-70400}{R_\mu T_{ch}}\right)$	
Mass Transfer coefficient, m/s	$K_m = 0.03$	
Char Uniform Temperature, K	$T_{ch} = 0.84\, T_{bed} A^{0.05}$	(Leckner et al., 1992)
Carbon fines generation rate	$R_{ch,fine} = \alpha_{fine} R_{ch}$ $\alpha_{fine} = \left(\frac{1 - V_{ash} - \theta_{cr}}{\theta_{cr} - \theta_0}\right)$	(Salatino et al., 1998) (Scala and Chirone, 2006)

These equations are built considering some points. It is assumed that partial combustion producing CO or complete combustion to CO_2 may occur. This is controlled by the splitting factor ε_{CO}. The rest of carbon the volatiles is released in the form of methane and additional tar which is controlled by the splitting factor ε_{tar} which is experimentally measured. All sulfur and Nitrogen will be released as H_2S and N_2 considering no formation of Sulfur dioxide or Ammonia will be generated in the products.

Gasification and Char Consumption

After devolatilization, char gets consumed into different heterogeneous gasification reactions. The char consumption occurs in the gasifier is happening through the reaction with oxygen, water vapor or carbon dioxide. The shrinking particle model is used to describe the char oxidation in this model. This is because the ash layer get stripped off from the particles as a result of the mechanical stress when collide with the sand particles (Nemtsov and Zabaniotou, 2008). The oxidation of char particles is described by the gas-solid reaction introduced by Leckner et al. (1992) with introducing the mechanical factor α_1 which has a minimum value of one when a complete oxidation occurs, and a maximum value of two when the reaction results in a complete production of carbon monoxide. The char consumption while reacting with water vapor is known as the heterogeneous water-gas shift reaction which can be shown, with introducing the splitting factor α_2 given between 1 and 2, as in Table 4.11. At the same time, with the three char consumption reactions, oxidation of methane, carbon monoxide and hydrogen occurs. The water-gas shift reaction occurs when the available oxygen is consumed where carbon dioxide and hydrogen are produced through an equilibrium reaction of carbon monoxide and water vapor, depending on the reaction temperature. Methane steam reforming and dry reforming reactions are also considered. Table 4.11 shows the gasification reactions considered in the present model.

Table 4.10 lists the combustion rates of char and other char consumption parameters. It also shows the empirical formula used to calculate the uniform temperature of char. During the char burning process, it yields fines which are considered as a function of the char combustion rate as shown in Table 4.10. The parameter α_{fine} is dependent on fuel particle properties.

Table 4.11 Gasification reactions in the current model

Reaction	Reaction Rate
Heterogeneous	
$\alpha_1 C + O_2 \rightarrow 2(\alpha_1 - 1)CO + (2 - \alpha_1)CO_2$ (combustion)	(Luecke et al., 2004)
$C + \alpha_2 H_2O \rightarrow (2 - \alpha_2)CO + (\alpha_2 - 1)CO_2 + \alpha_2 H_2$	(Petersen and Werther, 2005)
$C + CO_2 \rightarrow 2CO$ (Boudouard reaction)	(Radmanesh et al., 2006)
Homogeneous	
$CO + 1/2\ O_2 \leftrightarrow CO_2$ (Carbon monoxide oxidation)	(Bryden and Ragland, 1996)
$H_2 + 1/2\ O_2 \leftrightarrow H_2O$ (Hydrogen oxidation)	(Radmanesh et al., 2006)
$CH_4 + 1/2\ O_2 \leftrightarrow CO + 2H_2$ (methane oxidation)	(Petersen and Werther, 2005)
$CO + H_2O \leftrightarrow CO_2 + H_2$ (water-gas shift reaction)	(Radmanesh et al., 2006)
$CH_4 + H_2O \leftrightarrow CO + 3H_2$ (methane steam reforming)	(Biba et al., 1978)
$CH_4 + CO_2 \leftrightarrow 2CO + 2H_2$ (CO_2 reforming)	(Petersen and Werther, 2005)

4.4 System 2: Solar Parabolic Trough–Organic Rankine Cycle Based System

In this section, the modeling of the solar trough, organic Rankine cycle and the electrolyzer are introduced. The overall energy and exergy efficiencies of the system are calculated based on the useful outputs of the systems as follows:

$$\eta = \frac{\dot{W} + \dot{Q}_{cooling} + \dot{m}_{H_2} LHV_{H_2} + (\dot{m}\cdot h)_{DHW} + (\dot{m}\cdot h)_{freshwater}}{(\dot{Q}_u)_{solar}} \quad (4.160)$$

$$\psi = \frac{\dot{W} + \sum \dot{Q}_{cooling}\left(\frac{T_o}{T_c} - 1\right) + \dot{Ex}_{H_2} + \dot{Ex}_{DHW} + \dot{Ex}_{freshwater}}{\dot{Ex}_{solar}} \quad (4.161)$$

4.4.1 Solar Parabolic Trough

The energy analysis of the parabolic trough is introduced in this section. The equations are based on the model presented by Al-Sulaiman et al. (2011). The useful heat power of the parabolic trough is calculated as funtion of the aperture area, A_{ape}, the receiver area, A_{rec} as follows:

$$\dot{Q}_u = A_{ape}.F_R.\left(S - A_{rec}/A_{ap}.U_L.(T_{r,i} - T_o\right) \quad (4.162)$$

where S is the solar absorber radiation calculated as $\eta_r \times I$ where η_r is the receiver efficiency, and F_R is the heat removal factor calculated as function of the flow through the receiver.

$$F_R = \frac{\dot{m}_r.Cp_r}{A_r.U_L}.\left(1 - exp\left(-\frac{A_r.U_L.F_1}{\dot{m}_r.Cp_r}\right)\right) \quad (4.163)$$

The total solar field area is calculated as function of the electrical power output, P, as given by Krishnamurthy et al. (2012):

$$A_{field} = P \times \frac{I}{\eta_{plant}} \times \frac{O+S}{O}/1000 \quad (4.164)$$

where O and S are the operation and storage hours of the day. The specific heat loss from the storages tanks is taken as:

$$\dot{q_{loss}} = 0.00017\, T_{ms}(°C) + 0.012\, kW/m^2 \quad (4.165)$$

4.4.2 Organic Rankine Cycle

The design of the evaporator and the condenser is discussed in this section. The regenerative heat exchanger overall heat transfer coefficient is taken relative to the ones for the evaporator and condenser. The evaporator, condenser and regenerative heat exchanger in the proposed system are shell and plate type heat exchangers (Madhawa Hettiarachchi et al., 2007). This type of heat exchangers matches well with the existing case because of its high heat transfer coefficient that results in more compactness, especially with the relatively low temperatures of the heat sources in the proposed regenerative geothermal organic Rankine cycle (Madhawa Hettiarachchi et al., 2007; Uehara et al., 1984). The specifications and material properties of the shell and plate heat exchangers used in this analysis are given in Table 4.12.

The logarithmic mean temperature difference (LMTD) method is used in the analysis of the heat exchangers and the calculation of the heat transfer area. The heat transfer rate is described as

$$\dot{Q} = U.A.LMTD \quad (4.166)$$

where *A* is the surface area of the heat exchanger and *U* is the overall heat transfer coefficient which is calculated as follows:

$$\frac{1}{\mathrm{U}} = \frac{1}{\alpha_{\mathrm{OF}}} + \frac{\mathrm{t}}{\mathrm{k_p}} + \frac{1}{\alpha_{\mathrm{w}}} \quad (4.167)$$

where α_{OF} is the convection heat transfer coefficient of the organic fluid, α_w represents the convection heat transfer coefficient for the hot source in the evaporator or the cooling water in the condenser. Also, *t* and *k* are the thickness and thermal conductivity of the heat exchanger plate material.

Table 4.12 Heat Exchanger Specifications

Element	
Heat transfer surface length, mm	1465
Width of the heat transfer plate, mm	605
Clearance at organic fluid side, mm	5
Clearance at water side, mm	5
Pitch of the flute, mm	1
Depth of the flute, mm	1
Plate material	Titanium
Plate thickness, mm	0.9
Number of plates	200

Source (Uehara et al., 1984; Uehara et al., 1985; Uehara et al., 1997).

Heat transfer coefficients for hot and cold water side and the organic fluid side are determined using empirical correlations from the literature (Nakaoka and Uehara, 1988a, b; Uehara et al., 1996; Uehara et al., 1997) based on the calculation of Nusselt Number as

$$\mathrm{Nu} = \alpha.\mathrm{D_{eq}}/\mathrm{k} \quad (4.168)$$

where D_{eq} denotes the approximate diameter which is approximated to equal twice the clearance of the heat exchanger plate (Uehara et al., 1984). For the water side heat transfer coefficient at the system heat exchangers, the following correlation is used to calculate Nusselt Number (Uehara et al., 1997):

$$Nu = 0.04\, Re^{0.8} Pr^{0.33} \quad (4.169)$$

where *Re* is Reynolds Number and *Pr* is Prandtl Number. The velocity of the water as for both geothermal source and cooling water is calculated as follows:

$$V = \frac{\dot{V}}{w.\delta x.N} \quad (4.170)$$

where $\dot{V}$ is the water volumetric flow rate, w and δx are the width of the plate and the clearance at the water side, respectively. *N* represents the number of the plates.

For the organic fluid heat transfer coefficient at the evaporator, the following correlations are used (Madhawa Hettiarachchi et al., 2007; Uehara et al., 1997)

$$Nu = \begin{cases} 1.18 \ \left(f_p X\right)^{0.919}.H^{-0.834}.(\rho_l/\rho_v)^{-0.448}, \ f_p X \leq 62 \\ 6.646\ (f_p X)^{0.919}.H^{-0.834}.(\rho_l/\rho_v)^{-0.448}, \ f_p X > 62 \end{cases} \quad (4.171)$$

where H represents the ratio between sensible heat and latent heat. f_p is the pressure factor and is presented as a function of the critical pressure and the atmospheric pressure as follows:

$$f_p = \left[\left(\frac{P}{P_{cr}}\right)^3 + 1\right]\left(\frac{P}{P_a}\right)^{0.7} \quad (4.172)$$

Here, X in the Nusselt correlation is a dimensionless parameter that is calculated as follows:

$$X = \mathrm{D}_{eq,ev}^{1.5}.q_E\sqrt{M.c_{p,l}.\rho_l^2/k_l.\sigma.h_{fg}.\rho_v} \quad (4.173)$$

where M is a constant value equals 6.129 m^2/N.s, D_{eq} is the equivalent diameter at the organic fluid side of the evaporator and is equal to double the clearance of the plate at the organic fluid side. For the convection heat transfer coefficient of the organic fluid at the condenser, the following correlation is used (Nakaoka and Uehara, 1988a; Uehara et al., 1985):

$$Nu = 2.018.(Bo.L)^{-0.1}.(Gr_l.Pr_l/H)^{1/4} \quad (4.174)$$

where Bo is Bond number, L is a dimensionless value that is function of the heat exchanger plate parameters and is calculated as follows:

$$L = \frac{p^2}{l.\delta h} \quad (4.175)$$

where p, l and δh are the pitch of the flutes on the heat exchanger plate, the heat transfer length and the depth of the flutes, respectively.

The Bond Number (Bo) and Grashof Number (Gr) are dimensionless numbers and are defined as

$$Bo = g.\rho_l.p^2/\sigma \quad (4.176)$$

$$Gr = \left(\frac{g.l^3}{\nu^2}\right)\left(\frac{\rho_l-\rho_v}{\rho_l}\right) \quad (4.177)$$

Exergoeconomic Analyses

The system economic analysis is performed taking into account the purchased components and equipment cost, operation and maintenance (O&M) cost and the cost of the energy input. The exergoeconomic (thermoeconomic) analysis is the study of the economic principles considering the exergy analysis of the system under study. The thermoeconomic analysis is performed by applying the cost balance equation on the system components where the steams crossing the components boundaries are expressed in the form of exergy cost rates of these streams. This equation can be formulated in a general form as follows:

$$\sum \dot{C}_{out} + \dot{C}_W = \sum \dot{C}_{in} + \dot{C}_Q + \dot{Z} \quad (4.178)$$

where $\dot{C}$ denotes the total cost rates of the exergy streams across a specific component in the system, and its values are expressed in \$/h. They are defined as follows:

$$\dot{C}_{out} = c_{out}\dot{E}x_{out} \quad (4.179)$$

$$\dot{C}_{in} = c_{in}\dot{E}x_{in} \quad (4.180)$$

$$\dot{C}_W = c_W\dot{W} \quad (4.181)$$

$$\dot{C}_Q = c_Q\dot{E}x_Q \quad (4.182)$$

Here, *c* denotes the average cost per exergy unit and is expressed in \$/GJ. The exergy rate values in these equations are determined based on the exergy analysis of the system.

The total cost rate associated with the products of the proposed system is expressed in the following equation as a function of the total fuel cost rate, $\dot{C}_{fuel}$ and the annual investment cost rate of the system components, $\dot{Z}_{total}$, as follows:

$$\dot{C}_{P,total} = \dot{C}_{fuel} + \dot{Z}_{total} \quad (4.183)$$

The annual investment cost rate of any component, $\dot{Z}$, is calculated for the proposed system. It is the summation of the annual capital investment cost rate and the annual O&M cost rate. The total capital investment (TCI) is considered in two parts; direct capital cost (DCC) and indirect capital cost (ICC). The direct capital cost for this study is the purchase equipment cost (PEC). The components and equipment are expressed as function of some design parameters. The indirect capital cost can be expressed as a function of the purchase cost of equipment or as a function of design parameters and operating conditions (Voros et al., 1998). In the following analysis,

the equipment purchasing cost is calculated as function of the components design parameters. The correlations used in this analysis are stated in the form of turbine work output, pumps power and heat exchangers surface area. These correlations are formed considering manufacturing information and data. The estimated cost from these correlations is in US Dollars (Heberle et al., 2012; Karellas and Schuster, 2008; Turton et al., 2012).

For the organic fluid expander, the following correlation is utilized to calculate the purchase cost:

$$\log_{10}(PEC_{exp}) = 2.6259 + 1.4398\log_{10}(\dot{W}_{exp}) - 0.1776[\log_{10}(\dot{W}_{exp})]^2 \quad (4.184)$$

where the expander work, $\dot{W}_{exp}$, is provided in kW.

The purchase costs for the heat exchangers, i.e., evaporator, condenser and regenerative heat exchanger, are calculated using the following correlation as a function of the heat transfer surface area:

$$\log_{10}(PEC_{HE}) = 4.6656 - 0.1557\log_{10}(A) + 0.1547[\log_{10}(A)]^2 \quad (4.185)$$

where A is surface area of the heat exchanger in m^2.

The purchase prices of the organic Rankine cycle pump are determined by applying the following formula which is a function of the pump power:

$$\log_{10}(PEC_{pump}) = 3.3892 + 0.0536\log_{10}(\dot{W}_{pump}) + 0.1538[\log_{10}(\dot{W}_{pump})]^2 \quad (4.186)$$

The total capital investment (TCI) is calculated for each component as 6.32 times the purchase equipment cost as given by Bejan et al. (1996).

The O&M cost of each specific equipment is taken as 20~25% of the purchase equipment cost, as given by Bejan et al. (1996). The fuel cost and O&M costs are exposed to cost escalation over the years of operation. Levelized values of these expenditures are obtained by using the constant-escalation levelization factor (CELF). This factor links the calculations of expenditures at the first year to an equivalent annuity (Bejan et al., 1996).

$$CELF = CRF \cdot \frac{k(1-k^n)}{1-k} \quad (4.187)$$

where k is function of the effective annual cost of money rate, i_{eff} and the nominal escalation rate, r_n, and *CRF* is the capital recovery factor. These factors are applied to the

fuel cost and O&M costs, and they are calculated based on the following equations (Bejan et al., 1996):

$$k = \frac{1+r_n}{1+i_{eff}} \quad (4.188)$$

$$CRF = i_{eff} \cdot \frac{(1+i_{eff})^n}{(1+i_{eff})^n - 1} \quad (4.189)$$

where n is the number of years, the values of i_{eff} and r_n are given in Table 4.13.

The annual investment cost rate of the components which is used in the thermoeconomic balance equation is calculated based on the operational time of the component expressed in hours.

Table 4.13 Assumed economic data for the economic and exergoeconomic modeling

Economic constant	
Effective annual cost of money, i_{eff}	12%
Nominal escalation rate, r_n	5%
Economic life, n	20 year
Annual operating hours, τ	7000 h

The cost rate of exergy destruction in each component is calculated with respect to the unit cost of the product of this component as follows:

$$\dot{C}_D = c_P \dot{E}x_d \quad (4.190)$$

where the unit cost of the component product is calculated though the unit costs of the exergy associated with the products from this component. The values of the unit cost of exergy streams are calculated from the thermoeconomic cost balance equation and the exergy destruction rates are provided from the thermodynamics analysis of the system. The exergoeconomic factor, f, and the relative cost difference, r, are determined for each of the system components as follows (Bejan et al., 1996):

$$r = (c_P - c_F)/c_F \quad (4.191)$$

$$f = \dot{Z}/\left(\dot{Z} + c_F \dot{E}x_d\right) \quad (4.192)$$

where c_P and c_F are the unit cost of the exergy associated with the component products and fuel, respectively, and they are calculated for each component of the system as follows:

$$c_P = \frac{\dot{C}_P}{\dot{E}x_P} \quad (4.193)$$

$$c_F = \frac{\dot{C}_F}{\dot{E}x_F} \quad (4.194)$$

where $\dot{C}_P$ and $\dot{C}_F$ refers to the cost rate of the product and fuel streams through a certain component, respectively, and $\dot{E}x_P$ and $\dot{E}x_F$ are the exergy rate of the product and fuel streams of that component, respectively.

Thermodynamics Optimization

The performance of the proposed organic Rankine cycle is optimized using a heat exchanger surface area based objective function (Madhawa Hettiarachchi et al., 2007; Shengjun et al., 2011; Uehara and Ikegami, 1990). The objective function used in this study is defined as the ratio of the total surface area of the heat exchangers to the useful output power as follows:

$$Obj = \frac{A_t}{\dot{W}} \quad (4.195)$$

where A_t is the total heat transfer surface area in m^2, and $\dot{W}$ is the net power in kW.

In the optimization process, the objective function is minimized considering the variable metric method with varying the pressure of the condenser and the temperature values at the expander inlet and condenser outlet as the decision variables. Superheating and subcooling are considered. The temperature of the pump inlet is arranged to be not less than 80~90°C.

4.4.3 PEM Electrolyzer

The modeling of the PEM electrolyzer is adopted from the model presented by Ni et al. (2008). The mass flow rate of the produced hydrogen from water electrolysis can be calculated from the mole balance as

$$\dot{N}_{H_2,out} = \frac{J}{2F} = \dot{N}_{H_2O,reacted} \quad (4.196)$$

where J is the current density and F is Faraday constant.

The Nernest equation is used to calculate the reversible potential of the electrolyzer. This equation is given as a function of the electrolyzer operating temperature as follows (Ahmadi et al. 2013):

$$V_0 = 1.229 - 8.5 \times 10^{-4}(T_{PEM} - 298) \quad (4.197)$$

The voltage of the PEM electrolyzer can be calculated as function of the reversible potential calculated by Nernst equation and the total potential losses occurring in the system.

$$V = V_0 + V_{act,a} + V_{act,c} + V_{ohm} \quad (4.198)$$

The activation overpotential is calculated for the anode and the cathode using the following equation (Ni et al., 2008):

$$V_{act} = \frac{RT}{F}\sinh^{-1}\left(\frac{J}{2J_o}\right) \quad (4.199)$$

where J_o is the exchange current, F is Faraday constant, R is the gas constant and T is the temperature. The ohmic losses can be defined as function of the overall ohmic resistance as follows (Ni et al., 2008):

$$V_{ohm} = J \cdot R_{ohm} \quad (4.200)$$

The exergy efficiency is calculated as function of the chemical exergy of hydrogen with respect to the electric power input and the heat energy added in heating the water to the electrolyzer operating temperature, and the heat added to the electrolyzer if needed.

$$\eta_{ex} = \frac{ex_{ch,H2}\dot{N}_{H2}}{\dot{W}+\dot{Ex}_Q+\dot{Ex}_{H2O}} \quad (4.201)$$

4.5 System 3: Solar Heliostat – Steam Turbine Based System

In the analysis of the proposed system, several assumptions are taken into consideration: the system operates at steady state with constant solar isolation, the changes in kinetic and potential energy and exergy are neglected, the pressure and heat losses in the pipelines are not considered.

4.5.1 Solar Heliostat and Receiver

The heliostat field model is adopted from the model presented by Xu et al. (2011). The heliostat field has a total aperture area of A_{field} that concentrates the sun rays on the central receiver. The rate of heat received by the receiver can be calculated simply as follows:

$$\dot{Q}_s = I \times A_{field} \quad (4.202)$$

where I is the solar radiation per unit area.

The exergy rate associated with this amount of heat is calculated with respect to the sun temperature as follows:

$$\dot{E}x_s = (1 - \frac{T_0}{T_{sun}})\dot{Q}_s \quad (4.203)$$

The rate of heat receiver by the receiver is calculated as:

$$\dot{Q}_{rec} = \eta_h \times \dot{Q}_s \quad (4.204)$$

$$\dot{Q}_{rec} = \dot{Q}_{rec,abs} + \dot{Q}_{rec,em} + \dot{Q}_{rec,ref} + \dot{Q}_{rec,conv} + \dot{Q}_{rec,cond} \quad (4.205)$$

where the absorbed heat rate and the associated exergy rate are calculated as follows:

$$\dot{Q}_{rec.abc} = \dot{m}_{ms} C_p (T_{ms,out} - T_{ms,in}) \quad (4.206)$$

$$\dot{E}x_{rec,abs} = (1 - \frac{T_0}{T_{ms,out}})\dot{Q}_{rec.abs} \quad (4.207)$$

where $\dot{m}_{ms}$, $T_{ms,out}$ and $T_{ms,in}$ are the mass flow rate and outlet and inlet temperature of the molten salt. C_p is the specific heat at constant pressure. Below are the main heat loss calculations. The exergy associated with the heat losses can be calculated as $(1 - \frac{T_0}{T_{rec,surf}})\dot{Q}_{rec.loss}$

The emissivity losses, $\dot{Q}_{rec,em}$, is given as

$$\dot{Q}_{rec.em} = \frac{\varepsilon_{avg} \times \sigma (T_{rec.surf}^4 - T_0^4) A_{field}}{C} \quad (4.208)$$

where ε_{avg} is the average emissivity of the receiver and can be calculated as

$$\varepsilon_{avg} = \frac{\varepsilon_w}{\varepsilon_w + (1 - \varepsilon_w) F_r} \quad (4.209)$$

and $T_{rec.surf}$ is the receiver surface temperature. C is the concentration ratio, defined as the ratio of heliostat field area to the aperture area.

$$C = A_{field}/A_{ape} \quad (4.210)$$

The reflection heat loss is calculated as follows:

$$\dot{Q}_{rec.ref} = \dot{Q}_{rec} \times \rho \times \frac{F_r}{A_{field}} \quad (4.211)$$

where ρ is the reflectivity of the receiver. F_r is the view factor and is calculated as the area ratio of aperture to receiver surface.

$$F_r = A_{ape}/\, A_{rec.surf} \quad (4.212)$$

The convection heat loss, $\dot{Q}_{rec,conv}$, is calculated as function of the forced and natural convection coefficients of air:

$$\dot{Q}_{rec.conv} = \frac{(h_{air.fc.insi} \times (T_{rec.surf} - T_0) + h_{air.nc.insi} \times (T_{rec.surf} - T_0)) A_{field}}{C \times F_r} \quad (4.213)$$

The conduction heat loss, which is the lowest heat loss to occur, is calculated as:

$$\dot{Q}_{rec.cond} = \frac{(T_{rec.surf} - T_0) A_{field}}{\left(\frac{\delta_{insu}}{\lambda_{insu}} + \frac{1}{h_{air,o}}\right) C \times F_r} \quad (4.214)$$

The receiver energy and exergy efficiencies can be calculated as

$$\eta_{en} = \frac{\dot{Q}_{rec,abs}}{\dot{Q}_{rec}} \quad (4.215)$$

$$\eta_{ex} = \frac{\dot{E}x_{rec,abs}}{\dot{E}x_{rec}} \quad (4.216)$$

The total energy and exergy efficiencies of the solar heliostat field are defined as

$$\eta_{en} = \frac{\dot{Q}_{rec.abs}}{\dot{E}x_s} \quad (4.217)$$

$$\eta_{ex} = \frac{\dot{E}x_{rec,abs}}{\dot{E}x_s} \quad (4.218)$$

Based on the data given by Kolb (2011), the cost of the heliostat can be calculated based on the specific cost of 200 \$/m^2.

4.5.2 Reverse Osmosis Desalination

The world is in a continuous demand of potable water. Main water demand is to cover domestic, agricultural, industrial demands. As a result of limited and geopolitical availability of fresh water on earth, desalination of brackish and seawater gained a great attraction to overcome the fresh water scarcity. There are various developed technologies of desalination. Reverse osmosis (RO) is one of the most promising seawater desalination

technologies and is appropriate for moderate production rate and for seawater desalination. The effects of operating parameters on the performance of the seawater reverse osmosis (SWRO) were investigated in different studies (Wilf and Klinko, 1994; Wilf and Klinko, 1999, 2001; Zhou et al., 2006). Increasing the temperature of saline water diminishes its viscosity and, hence, increases the permeability of the membrane. Increasing its operating pressure results in a similar effect. Different salinity of the water source also affects the desalination process as the product flow rate decreases with more salinity in the feeding water. The SWRO performance was studied thermodynamically based on the second law of thermodynamics (Aljundi, 2009; Cerci, 2002; Criscuoli and Drioli, 1999; Drioli et al., 2006). These studies show the high exergy destruction rates to occur at the RO module and the high pressure pump.

The economics of SWRO and the cost of the product water are of great importance and affect the choice of the design and operating parameters (Drioli et al., 2006; Malek et al., 1996; Marcovecchio et al., 2005; Wade, 1993). The economic studies of SWRO are limited in the literature. Wade (1993) performed an evaluation of the economics of distillation and RO desalination processes, and recommended RO plants as the most suitable alternative in high energy cost areas. Malek et al. (1996) studied the effect of different parameters on the unit cost of product water. Drioli et al. (2006) performed a cost analysis on an integrated membrane SWRO system and studies the system capacity and other parameters on the cost of product water. Marcovecchio et al. (2005) constructed a model which covered the study of the economics of a SWRO network.

The thermoeconomic analysis of RO desalination plants, by combining both exergy and economic analyses, is also limited in the literature. Romero-Ternero et al. (2005b) performed a thermoeconomic analysis of a SWRO facility at Santa Cruz, Spain, using the methodology described by Valero and Lozano (1993).

Exergy analysis is treated as a potential tool for system design, assessment and improvement. It provides an evaluation of the maximum work that can be extracted from a certain system relative to the surrounding environment. Relating the thermodynamics losses based on the second law and the capital costs is achieved by applying

exergoeconomic analysis. This gives a better understanding as exergy is actually reflecting the measure of the economic value of the processes.

The open literature indicates that energy and economic analyses of SWRO plant have extensively been studied and comparatively assessed. However, few studies considered exergy analysis and integrating the effect of the second law of thermodynamics in the economic and cost analysis of the plant.

In the present model, a comprehensive thermodynamic analysis of an SWRO plant is presented through energy and exergy to better understand the system operation and identify the destructions and losses in the system processes and components. Exergoeconomic analysis is also performed to investigate the effects of irreversibilities, occurring in the system components, on the product cost. The effects of the operating recovery ratio of the plant, the seawater source salinity, the seawater feeding temperature value and the dead state temperature on the energetic and exergetic performances and the costs of the product water are investigated parametrically.

System Description

The SWRO plant proposed for this study is designed to provide 7586 m^3 of fresh water per day with salinity less than 500 ppm. Seawater sources with different salinity values are used as water source to the RO plant. The flow diagram of the proposed system is shown in the schematic at Figure 4.6.

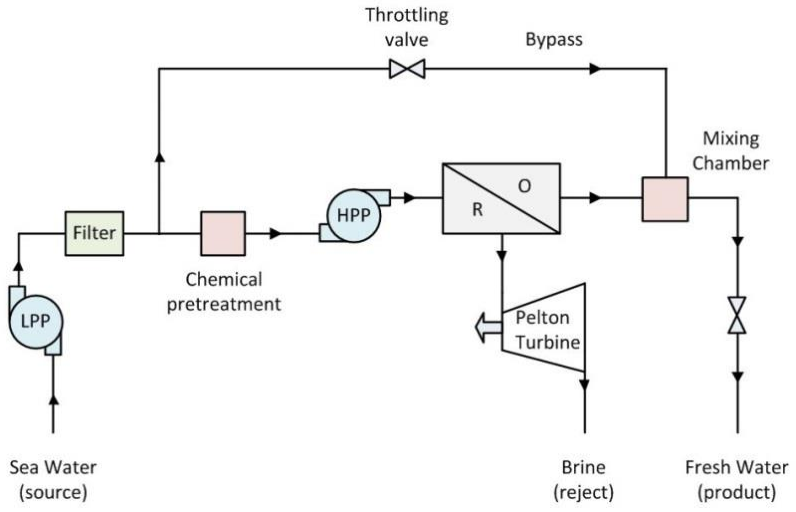

Figure 4.6 Schematic diagram of SWRO desalination plant with energy recovery turbine

Seawater is first pumped from atmospheric condition by the low pressure pump with a pressure ratio of 6.5. The mass flow rate of the withdrawn seawater is estimated based on the desired product flow rate. The saline water that exits the pump is then directed to a cartridge filter to get rid of any suspended particles. The process water is split where a small amount is extracted through the bypass path. The major part of the process water passes through a static mixer where certain chemicals are added to the saline water. The added chemicals are required to prepare the process water in the condition that fit the RO membrane modules without causing any damage to the elements. A pressure loss is encountered through the filter and chemicals mixer. The process water pressure is then raised to the RO operating pressure based on the osmotic pressure of the provided source as calculated in the system analysis section. The operating pressure in a practical RO plant most likely is more than double the osmotic pressure of the seawater source. In this study, the HPP raises the pressure to 60 bar and the brine is rejected from the RO modules at 51 bar. The permeate leaves the RO modules at 180 kPa and mixes with the bypass flow rate, after reducing its pressure to the RO back pressure, to achieve the required salinity of the final product water. The bypass flow rate is estimated based on the salinity of the source water and the required salinity of the product water.

One of the most common RO modules that are used in SWRO is the DuPont B10 hollow fiber RO modules (Crowder and Gooding, 1997; Hawlader et al., 1994; Malek et al., 1996; Marriott and Sørensen, 2003) which are proposed to be used in this study. This type is made from polyamide membranes, which proved a high salt retention compared with other designs (Hawlader et al., 1994; Marriott and Sørensen, 2003). The product recovery ratio and the salt rejection specification of this type are listed in Table 4.14. There are several devices that are designed for energy recovery from the brine of RO plants. Pelton turbines, which replaced Francis recovery turbines, are one of the most common used energy recovery devices that are commonly used with RO plants, because of their reliability and high efficiency. In the proposed system, an energy recovery Pelton turbine is, in this regard, integrated with the system for harnessing the energy of the brine flow.

The desalination process is a separation process during which, salt and water, composing the feed seawater, are separated. The product water (p) and brine (b) are the

two outgoing streams of the desalination process as shown in Figure 4.6. The product water has low concentration of dissolved salts.

Based on the defined characteristics of the product water and the salinity of the source water, the mass flow rates and molar and mass fractions of salt and water in the solution at each point of the system can be expressed as follows:

Seawater Source

The feeding mass flow rate of seawater can be defined based on the recovery ratio of the proposed RO plant as follows:

$$\dot{m}_t = \dot{m}_p / r_r \quad (4.219)$$

where the recovery ratio, r_r, represents the ratio of product water relative to the total feed water to the RO plant.

Table 4.14 SWRO plant operating and design parameters (El-Emam and Dincer, 2014b)

Parameters of the SWRO plant	
Product water flow rate	7586 m^3/day
Salinity of product water	450 ppm
Seawater salinity	35000 ppm (base case)
Seawater feeding temperature	25°C (base case)
High pressure pump efficiency, η_{HPP}	90%
Low pressure pump efficiency, η_{LPP}	87%
Pelton turbine efficiency, η_{PT}	79%
Plant load factor, f_l	90%
Membrane recovery ratio, r_r	0.55 (base case)
Membrane replacement factor, r_m	10%
Membrane salt rejection ratio	99%
Cost of chemical treatment, C_{ch}	0.018 \$/m^3
Cost of cartridge filters replacement	0.01 \$/m^3
Salt permeability coefficient, k_s	2.03×10^{-5} m^3/m^2.s.kPa
Water permeability coefficient, k_w	2.05×10^{-6} m^3/m^2.s.kPa
Dead state temperature	25°C (base case)

The molar fraction of the salt and water in the seawater source can be calculated based on the defined salinity of seawater as follows:

$$x_{s,t} = \frac{MW_w}{MW_w + MW_s.[(1/y_{s,t}) - 1]} \quad (4.220)$$

$$x_{w,p} = 1 - x_{s,p} \quad (4.221)$$

where $y_{s,t}$ is the salt mass fraction in the seawater source and equal to the salinity of the seawater in ppm $\times 10^{-6}$.

Product Water

The total mass flow rate of the final product water and its salinity are given design parameters. The salt flow rate in the product water is calculated as follows:

$$\dot{m}_{s,p} = y_{s,p}.\dot{m}_p \quad (4.222)$$

The salt molar fraction is to be determined from the following equation:

$$x_{s,p} = \frac{MW_w}{MW_w + MW_s.[(1/y_{s,p}) - 1]} \quad (4.223)$$

Also, for water mass flow rate and water mass and molar fractions in the product water, they can be calculated by simple mass balance of the product water:

$$\dot{m}_{w,p} = \dot{m}_p - \dot{m}_{s,p} \quad (4.224)$$

$$y_{w,p} = 1 - y_{s,p} \quad (4.225)$$

$$x_{w,p} = 1 - x_{s,p} \quad (4.226)$$

Bypass Water

The amount of bypass water, which mixes with the product water out of the RO to achieve the required salinity of final product, is to be calculated as follows:

$$\dot{m}_{bypass} = \dot{m}_p \left[\frac{y_{s,p} - y_{s,RO}}{y_{s,t} - y_{s,RO}}\right] \quad (4.227)$$

where $y_{s,RO}$ is the mass ratio of salt in the outlet permeate flow of the RO. In the proposed system, as given at Table 4.14, the RO membrane used in this plant produces permeate water with 1% of the source salinity.

Brine

The mass of the brine is calculated form the following mass balance:

$$\dot{m}_b = \dot{m}_t - \dot{m}_p \quad (4.228)$$

and its salinity expressed as mass and molar ratio of salt:

$$y_{s,b} = \frac{y_{s,t} - r_r . y_{s,RO}}{1 - r_r} \quad (4.229)$$

$$x_{s,b} = \frac{MW_w}{MW_w + MW_s . [(1/y_{s,b}) - 1]} \quad (4.230)$$

The water mass and molar ratios of the brine are calculated from the salt mass and molar ratios.

$$y_{w,b} = 1 - y_{s,b} \quad (4.231)$$

$$x_{w,b} = 1 - x_{s,b} \quad (4.232)$$

The molecular weights of the source, product water and brine are calculated using the following formula:

$$MW_i = x_{s,i} . MW_s + x_{w,i} . MW_w \quad (4.233)$$

where the salt molecular weight, MW_s, is taken as the value of the NaCl salt molecular weight which is given as 58.5 kg/kmol. The salinity at each state is expressed in ppm as follows:

$$Salinity = y_s \times 10^6 \quad (4.234)$$

Thermodynamics Analyses and Solution Properties

The first law of thermodynamics is applied to each device of the proposed RO plant at steady state condition.

$$\dot{Q} - \dot{W} + \sum \dot{m}_{in} h_{in} - \sum \dot{m}_{out} h_{out} = 0 \quad (4.235)$$

where $\dot{Q}$, $\dot{W}$ and h are heat transfer, work and specific enthalpy values of the streams crossing the device boundary.

Desalination is a pure separation process that requires work. Integrating the study of the second law in the desalination process gives the chance to evaluate the potential to minimize the work input. Exergy analysis is an effective thermodynamic technique that is based on integrating the second law of thermodynamics with the mass and energy balance equations for a better understanding of the proposed system performance. Exergy balance equation can be formulated as follows:

$$\dot{Ex}_{d_i} = \sum (1 - \frac{T_o}{T}) \dot{Q}_i - \dot{W}_i + \sum \dot{Ex}_{in} - \sum \dot{Ex}_{out} \quad (4.236)$$

where $\dot{Ex}_d$ is the exergy destruction rate that occurs at the device *i*. T_o is the dead state temperature which describes the situation at which the system cannot undergo any state change through any interactions with the environment. T is the temperature of the

boundaries at which the heat transfer occurs (Dincer and Rosen, 2007; Moran et al., 2011). $\sum \dot{E}x$ represents the exergy rate associate with the flow in or out from the device *i*.

In this study, the exergy efficiency for the overall desalination system is defined as the ratio between the minimum work required for the separation process to the actual work supplied to the system.

$$\eta_{ex} = \frac{\dot{W}_{min}}{\dot{W}_{act}} \quad (4.237)$$

It can be formulated in terms of exergy rates through the systems as follows for a SWRO:

$$\eta_{ex} = \frac{\dot{E}x_{out}}{\dot{E}x_{in}} = \frac{\dot{E}x_{outwater} - \dot{E}x_{seawater}}{\dot{W}_{net}} \quad (4.238)$$

where $\dot{E}x_{outwater}$ is the total exergy rate of the product water and the brine and $\dot{E}x_{seawater}$ is the total exergy rate of the seawater fed into the system.

Salinity of seawater and underground water sources are less than 5%, which categorizes seawater as a dilute solution and can be approximated in its behavior as an ideal solution. The molecules in solutions are surrounded by mixture of similar and dissimilar molecules. In ideal solutions, the self and cross interactions, that govern the solution behavior, are identical. In other words, the dissimilar molecules effect in the solution is negligible, and the molecules interact with each other in the same way as among themselves (Cerci, 2002; Matsoukas, 2013). There is no change in enthalpy or volume when the pure components form the solution, however, the entropy increases due to irreversibility associated with mixing process.

$$h = \sum y_i h_i = y_w h_w + y_s h_s \quad (4.239)$$

Here, h_w *and* h_s are the specific enthalpies of water and salt at each state expressed in kJ/kg.

$$s = \sum y_i s_i = y_w s_w + y_s s_s \quad (4.240)$$

where s_w and s_s are the specific entropy values of water and salt at each state in kJ/kgK and can be formulated in molar form as follows:

$$\bar{s} = \bar{s}_{Pure}(T, P) - \bar{R} \ln x \quad (4.241)$$

Here, $\bar{s}_{Pure}(T, P)$ is the specific molar entropy of each component of the solution at the pure substance condition at the state pressure and temperature. $\bar{R}$ is the universal gas

constant and x is the component molar fraction. Integrating this equation in the total specific entropy formula in the form or mass fractions, by dividing by the total molar mass at each specific state, gives:

$$s = y_w s_{w,pure}(T,P) + y_s s_{s,pure}(T,P) - R(x_w \ln x_w + x_s \ln x_s) \quad (4.242)$$

The specific enthalpy and entropy values of salt as a solution component are determined at each state, at the solution pressure and temperature, as function of the salt specific heat as:

$$h_s = h_{s,o} + \int_{T_o}^{T} c_{p,s} dT \quad (4.243)$$

$$s_s = s_{s,o} + \int_{T_o}^{T} c_{p,s} \frac{dT}{T} \quad (4.244)$$

where $h_{s,o}$ and $s_{s,o}$ are the salt specific enthalpy and entropy at reference condition. The values of $h_{s,o}$and $h_{s,o}$ at different reference temperature values are shown in Table 4.15 where the reference pressure is taken as 1 atm. The values listed in this table are based on assigning the values of enthalpy and entropy to zero at 0^oC (Cerci, 2002). The specific heat of salt, $c_{p,s}$, is defined as function of temperature in the modified formula of Bouzayani et al. (2007) as follows:

$$c_{p,s} = 0.786 + 0.00279(T - T_o) \quad (4.245)$$

Here, T and T_o are the state temperature and the reference temperature, respectively. The specific exergy at each state is defined as

$$ex = (h - h_o) - T_o(s - s_o) \quad (4.246)$$

where T_o is the dead state temperature as defined in Dincer and Rosen (2013).

Table 4.15 specific enthalpy and entropy values of salt at different reference temperatures

Reference Temperature, T_o	288.15 K	298.15 K	308.15 K
Specific Enthalpy, $h_{s,o}$ kJ/kg	12.3250	21.0455	29.288
Specific Entropy, $s_{s,o}$ kJ/kg.K	0.04473	0.07328	0.1009175

The operating pressure values across the system are set based on the osmotic pressure of the source seawater. The hydrostatic pressure, ΔP, applied across the desalination process has to be higher than the osmotic pressure difference, $\Delta \pi$ (Cipollina et al., 2009). The two pressure difference values are defined in El-Dessouky and Ettouny

(2002) as the difference between the average pressure of the feed seawater before the permeator and the brine rejected and the pressure of the product water:

$$\Delta P = 0.5\left(P_{feed} + P_{brine}\right) - P_{prod} \quad (4.247)$$

$$\Delta \pi = 0.5\left(\pi_{feed} + \pi_{brine}\right) - \pi_{prod} \quad (4.248)$$

The osmotic pressure in this study is calculated based on the solution concentration according to the following relation, which is used to determine the osmotic pressure values for the RO feed water, brine and product water:

$$\pi = \bar{R}T\sum G_i \quad (4.249)$$

where $\bar{R}$ is the universal gas constant, T is the operating temperature in K. The term G_i represent the concentration of the constitution i in the solution, in kmol/m^3.

Based on this relation, the osmotic pressure for each flow for each flow can be approximated in kPa as follows:

$$\pi_i = 75.84 \times 10^3 (y_{s,i}) \quad (4.250)$$

where i denotes the seawater, brine and product water streams.

The osmotic pressure can also be calculated directly from the states salinity expressed in ppm:

$$\pi = \frac{0.265 \times PPM \times T}{1000 - (PPM/1000)} \quad (4.251)$$

where T is in K and the osmotic pressure value is calculated in kPa.

Economic Analysis

In the thermodynamic analyses, the performances of the prescribed system components are studied. However, the economic analysis presented in this study focuses on the major components in the RO plants that constitute the bulk of the capital and operating cost of the plant (Malek et al., 1996; Wade, 1993). In this study, RO plant is divided in four main elements; seawater intake and pretreatment system (SWIP), high pressure pump, RO permeators section, Pelton turbine. The estimation of these major components cost and the annual operating and maintenance cost are to be done to calculate the product cost.

The total capital investment (TCI) is the summation of the direct and indirect cost. The direct cost items that are considered in this study include; the purchased equipment cost (PEC) which is to be estimated based on the operating parameters of each

component, the site development which is in the range of 10% of the total equipment cost, and the installation cost; considered as 20% of the total purchased equipment cost. The indirect cost includes; the engineering and supervision cost, buildings and construction cost and contingency cost. Wade (2001) considered each of the indirect cost items as 10%~15% of TCI for the RO plant, which matches with Bejan et al. (1996).

All items of the direct and indirect cost are represented in terms of the purchased equipment cost. In this study TCI is estimated as 6.32 times the purchased equipment cost as proposed by Bejan et al. (1996) for a new system construction.

In the following subsections, the purchased equipment cost PEC, energy of operation cost $\dot{c}_e$, and operation and maintenance O&M cost are discussed for the major components of the described system.

Seawater Intake and Pretreatment Section (SWIP):

The economic analysis of this section is simplified and formulated as a function of the volume flow rate of seawater source. The calculations of the cost of the SWIP and its operating cost include the intake pump. The capital cost of SWIP has been provided by Wade (1993) and was modified later to the provided correlation (Helal et al., 2008; Malek et al., 1996; Marcovecchio et al., 2005) which is used in this paper to estimate the PEC of SWIP.

$$PC_{SWIP} = 996 \,.\, \dot{V}_t^{\,4/5} \qquad (4.252)$$

where $\dot{V}_t$ is the total fed seawater volume flow rate in m^3/day.

The annual cost of the energy of the intake pump is estimated in this study using the following formula (Malek et al., 1996; Marcovecchio et al., 2005):

$$\dot{c}_{e,SWIP} = P_{SWIP} . \dot{V}_t . f_l . C_e / \eta_{SWIP} \qquad (4.253)$$

where $\dot{V}_t$in this equation is in to be provided in daily volume flow rate form, P_{SWIP} is the pressure after the intake pump in bar considering the feed to the pump is at atmospheric pressure, f_l is the plant load factor, C_e is the unit power cost in \$/kWh and η_{SWIP} is the intake pump efficiency.

The cost of chemical treatment in the pretreatment process is defined, on daily bases, as follows, based on the cost per m^3 of feed seawater (Helal et al., 2008; Marcovecchio et al., 2005):

$$\dot{c}_{op,ch} = \dot{V}_t . f_l . C_{ch} \quad (4.254)$$

where C_{ch} is the cost of chemical treatment per m^3 of the provided seawater, and is given in Table 4.14.

For the RO desalination sites, the cartridge filters replacement cost can be considered as 0.01 $ per m^3 of the produced water, which is also introduced in Romero-Ternero et al. (2005a). The other O&M cost for the intake, mechanical equipment and in SWIP are 4~5% of the TCI (Romero-Ternero et al., 2005b).

High Pressure Pump (HPP):

The PEC of the high pressure pump is estimated from the correlation given by Turton et al. (2012) as a function of the operating power required to drive the pump for achieving the required pressure difference.

$$\log_{10}(PC_{HPP}) = 3.3892 + 0.0536 \log_{10}(\dot{W}_{HPP}) + 0.1538[\log_{10}(\dot{W}_{HPP})]^2 \quad (4.255)$$

The power required to drive the pump is calculated from the thermodynamics energy analysis. The work in this correlation is in kW. The annual cost of the power provided to the HPP is to be calculated using the following formula (Marcovecchio et al., 2005):

$$\dot{c}_{e,HPP} = P_{HPP} . \dot{V}_{RO} . f_l . C_e / \eta_{HPP} \quad (4.256)$$

where $\dot{V}_{RO}$ is the daily volume flow rate of the seawater supplied to the RO membrane, after extracting the bypass ratio. The O&M cost for the pump, represented in mechanical equipment maintenance, is estimated as 4% of TCI as reported by Romero-Ternero et al. (2005a).

RO Permeator:

The cost of the RO membrane is reported in the literature as 60% of the total cost of the RO desalination plant (Fiorenza et al., 2003; Helal et al., 2008; Romero-Ternero et al., 2005a). In the current study, the capital cost of the RO permeator is calculated as the cost of one membrane times the number of used elements, which is simply presented as follows:

$$PC_{RO} = N . PC_m \quad (4.257)$$

where N is the number of membrane elements used in the system and PC_m is the cost per membrane.

Malek et al. (1996) introduced a formula for calculating the number of membrane elements of the same type used in this study. The formula is given as a function of the product flow rate from the permeator in the third year of operation which is to be determined based on the measure of the permeator degradation during the first three years of its operation. However, in this study, the number of membrane elements used is calculated as follows:

$$N = r_r \cdot \dot{V}_{RO}/\dot{V}_{el} \quad (4.258)$$

where $\dot{V}_{el}$ is the permeate flow rate per membrane element. The element permeate flow rate in this equation is taken as 1.5 m^3/h as a given characteristic of the membrane used. The element cost is expressed as a function of the area follows (Marcovecchio et al., 2005):

$$PC_m = 10 \cdot A \quad (4.259)$$

Here, the area, A, is to be calculated as follows, using a modified formula based on the method provided by El-Dessouky and Ettouny (2002):

$$A = \dot{m}_{el}.\, y_{s,RO}/k_s(\bar{y} - y_{s,RO}) \quad (4.260)$$

where, $\dot{m}_{el}$ is the mass flow rate of permeate through one element in kg/s and can be easily determined by changing the permeate volume flow rate in mass flow rate form as the density of the given seawater source is known. $y_{s,RO}$ is the salt mass fraction in the flow out from the RO membrane and it is provided in the plant characteristics as the membrane used in the study rejects 99% of the source salinity (Hawlader et al., 1994) as mentioned in the characteristics of the membrane in Table 4.14, k_s is the salt permeability coefficient. The value of $\bar{y}$ expresses the average salinity through the membrane element and is calculated using the modified formula of the equation provided by El-Dessouky and Ettouny (2002) as follows:

$$\bar{y} = \frac{(\dot{m}_t - \dot{m}_{bypass})y_{s,t} + \dot{m}_b.y_{s,b}}{\dot{m}_t - \dot{m}_{bypass} + \dot{m}_b} \quad (4.261)$$

Here, all the mass flow rates are determined from the mass balances in the analysis section which are formed based on the product water mass flow rate as a design parameter.

In this study, the cost of the RO membrane elements replacement is calculated based on the annual replacement factor of the membranes, r_m:

$$\dot{c}_{op,RO} = r_m cc_{RO} \quad (4.262)$$

and the value of r_m is provided in Table 4.14.

The RO membranes replacement cost, $\dot{c}_{op,RO}$, is estimated as 8% of the TCI (Romero-Ternero et al., 2005a). Other O&M costs are considered as 1% of the TCI.

Pelton Turbine:

The PEC of Pelton turbine is calculated based on the purchase cost as a function of the power produced from the turbine as introduced by (Turton et al., 2012):

$$\log_{10}(PC_{PT}) = 2.2476 + 1.4965 \log_{10}(\dot{W}_{PT}) - 0.1618[\log_{10}(\dot{W}_{PT})]^2 \quad (4.263)$$

The turbine mechanical O&M cost is about 4% of the TCI (Romero-Ternero et al., 2005a). Other RO plant O&M costs in the buildings and other equipment are estimated as 6% of the TCI of the RO plant (Romero-Ternero et al., 2005a, b). Marcovecchio et al. (2005) introduced a formula to calculate the total annual O&M cost of the RO plant based on the unit cost of O&M presented by (Wade, 2001) as 0.126 \$/m^3.

$$\dot{c}_{O\&M} = 0.126 \times f_l \times \dot{V}_p \quad (4.264)$$

where $\dot{V}_p$ is the annual volume flow rate of product water.

Exergoeconomic Analysis

The annual investment cost rate, $\dot{Z}$, of any components is the summation of the annual total capital investment rate, $\dot{Z}^{CI}$,and the annual O&M cost rate, $\dot{Z}^{OM}$. These two values are estimated by dividing the capital investment cost and the levelized value of O&M cost for each component, which are calculated in the economic analysis, by the annual operating hours of the plant, τ, which is given in Table 4.16 with the other parameters that are used in calculating the levelized cost values and exergoeconomic balance equations.

4.5.3 Steam Turbine

The thermodynamics energy and exergy balance equations are applied simply to the steam turbine. The capital cost of the steam turbine and the water pump are calculated as follows:

$$PEC_{ST} = 3880.5\left(\dot{W}_T\right)^{0.7}\left(1+\left(\frac{0.05}{1-\eta_T}\right)^3\right)\left(1+EXP\left(\frac{T_{in}-593}{10.42}\right)\right) \quad (4.265)$$

where the turbine inlet temperature is given in °C and turbine work in kW.

$$PEC_{Pump} = 705.48\left(\dot{W}_P\right)^{0.71} \quad (4.266)$$

Table 4.16 Economic data of the SWRO plant.

Economic parameters (assumed)	
Effective discount rate, i_{eff}	8%
Nominal escalation rate, r_n	5%
Economic life time, n	20 year
Annual operating hours, τ	8760 h

4.6 OTHER SYSTEMS

4.6.1 Coal Gasification-SOFC-Gas Turbine

This section is concerned with studying the thermodynamic performance of an integrated system based on coal gasification for the production of syngas using coal gasification, which is directed to a solid oxide fuel cell. The fuel cell outlet gas mixes with natural gas and then feeds the combustion chamber of a bottoming gas turbine system. A heat recovery steam generator is used to produce steam for a steam turbine with heat of the gas turbine exhaust. Exergy analysis is performed for different components of the system. Different values of the reference temperature, which directly affect the exergy performance, and their effects on the system performance are studied. A parametric study of the effects of the pressure ratio with varying fuel cell temperature is performed on selected components of the system. Figure 4.7 shows the main elements of an integrated gasification combined system.

The proposed system involves coal gasification and a SOFC unit integrated with gas and steam turbine cycles. Thermodynamic energetic and exergetic analyses are performed on the proposed integrated system. The effects of the different operating parameters on the system performance are investigated for two different coal types as a fuel supply to the gasifier.

Figure 4.8 shows a schematic of the combined cogeneration power plant. Atmospheric air (1) enters the air compressor. The compressor supplies compressed air to the gasifier, SOFC and the combustion chamber of the gas turbine cycle. Part of the delivered air is directed to the air separation unit where oxygen is separated and directed to the gasifier. The syngas produced from the gasification process is then cooled, purified and directed to supply the SOFC anode side. Preheated water from the heat recovery steam generator (HRSG) is used to cool the syngas. Superheated vapor from the cooler is then directed to the steam turbine for electricity production. Compressed air (7) is directed to the fuel cell cathode after being preheated through the recuperator using heat of the exiting gas from the fuel cell. Anode and cathode exit streams are mixed together and directed to the combustion chamber of the gas turbine bottoming cycle. It mixes with the supply fuel of the combustion chamber. The exhaust of the gas turbine is recovered in the HRSG for providing steam to the steam turbine. The additional heat recovered is used to produce saturated steam at low pressure.

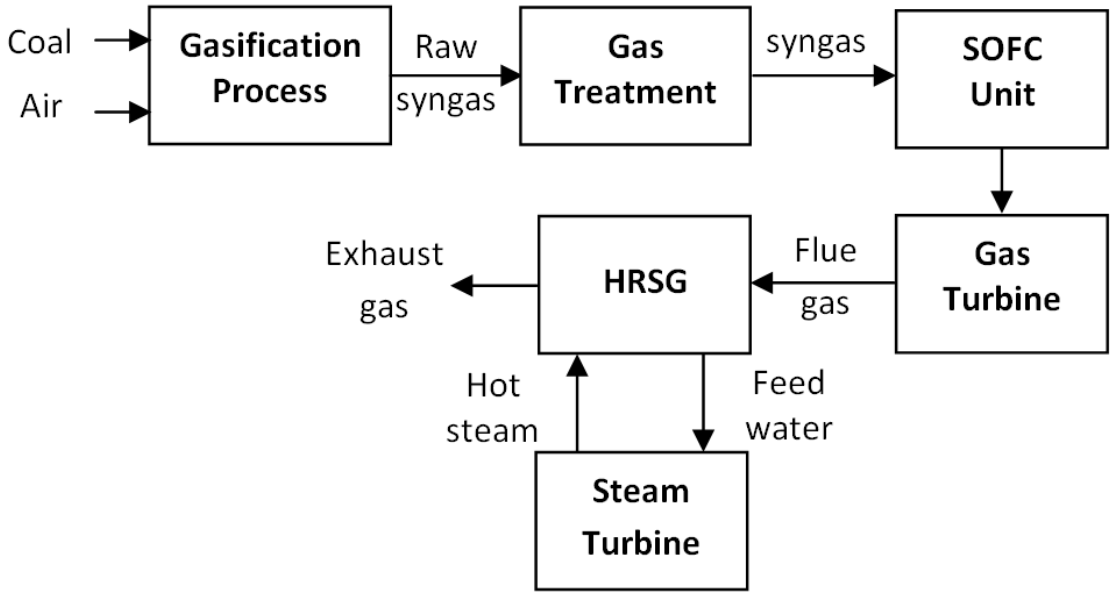

Figure 4.7 Typical plant components of an IGCC system

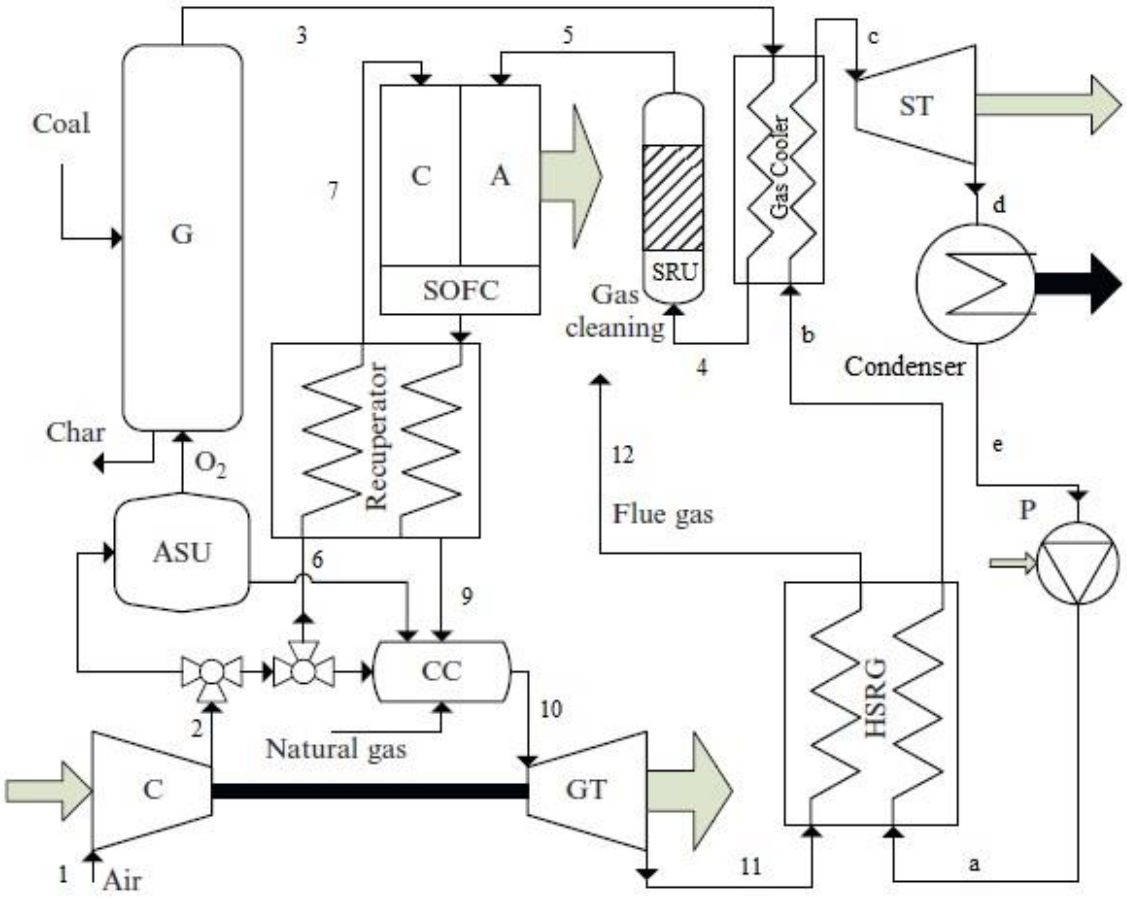

Figure 4.8 Schematic diagram for the preliminary case study system

The components in the system (Figure 4.8) are modeled by balance equations of mass, energy, entropy and exergy. The following assumptions were made. Atmospheric air is considered as an ideal gas with the composition of 21% oxygen and 79% nitrogen. All flow steams are assumed as ideal gases. No pressure losses are considered in the flow paths. Ambient temperature and pressure are constant. A steady state operation is assumed. Heat exchangers, compressors and the turbine are assumed adiabatic.

Coal Thermal Properties

The chemical exergy of the coal is calculated based on the following formula which is used for solid industrial fossil fuels (Kotas, 1995):

$$Ex_{ch,fuel} = \left(CV^0 + w.h_{fg}\right)\varphi_{dry} + 9{,}417s \qquad (4.267)$$

where CV^0 is the fuel calorific value, w and h_{fg} are fuel moisture content and water latent heat. s is sulfur mass fraction. The chemical exergy ratio φ_{dry} is estimated as follows:

$$\varphi_{dry} = 0.1882\ \frac{h}{c} + 0.061\ \frac{o}{c} + \ 0.0404\ \frac{n}{c} + 1.0437 \quad (4.268)$$

The mass fractions of carbon, hydrogen, oxygen and nitrogen are represented by *c*, *h*, *o* and *n* in the previous equation, respectively (Kotas, 1995). The typical syngas composition exiting the gasifier as percentage molar compositions is 10.6% CO_2, 51.6% CO, 0.1% CH_4, 35.1% H_2, and 2.6% N_2 and others. The reaction occurs in the gasifier using compressed oxygen, separated from air in the air separation unit, and it can be presented as follows:

$$\left(y_C C + y_{H_2} H_2 + y_{H_2} H_2 + y_{O_2} O_2 + y_{H_2O} H_2O + y_{N_2} N_2 + y_S S + ash\right) + X.O_2 \ \rightarrow Y.\left(y_{CO_2} CO_2 + y_{CO} CO + y_{CH_4} CH_4 + y_{H_2} H_2 + y_{N_2} N_2\right) + y_{H_2O} H_2O + Z.C + ash \quad (4.269)$$

where y_i is the molar fraction of the composition '*i*', and X, Y and Z are the mole fractions of oxygen, syngas and char, which can be calculated from the molar balance equations for individual elements in the chemical reaction. The syngas temperature can be determined from the energy balance of the gasifier.

Formulation of Energy and Exergy Efficiencies

The energy balance is formulated for the components of the system in Figure 4.8. The energy balance equation considering each component as a control volume in steady-state operation can be written as follows:

$$\dot{Q}_{cv} - \dot{W}_{cv} = \sum_{in} \dot{n}_i h_i - \sum_{out} \dot{n}_i h_i \quad (4.270)$$

where $\dot{n}_i$ and h_i represent the molar flow rate and specific molar enthalpy of the flow stream into and out from each component in the system.

The exergy balance is formulated for the system components operating at a steady state condition as follows:

$$0 = \sum(1 - \frac{T_o}{T})\ \dot{Q}_{cv} - \dot{W}_{cv} + \sum_{in} \dot{n}_i ex_i - \sum_{out} \dot{n}_i ex_i - \dot{E}x_{d_i} \quad (4.271)$$

where ex_i is the specific molar flow exergy for each component of the inlet and outlet flow streams. It can be defined by neglecting the kinetic and potential energy changes, as follows:

$$ex_i = (h_i - h_o) - T_o(s_i - s_o) + ex_{ch} \quad (4.272)$$

where $ex_{ch,i}$ is the specific molar chemical exergy of the flow streams. The specific chemical exergy of different species in a gas mixture can be written as follows:

$$ex_{ch} = \sum y_i . ex_{ch,i} + RT_o \sum y_i . ln\, y_i \quad (4.273)$$

where y_i is the molar fraction of the component '*i*' in the gas mixture. The molar specific chemical exergies for the gas species in the analysis are shown in Table 4.17. The enthalpy and entropy values for each component of the gas are calculated using polynomial equations as a function of the temperature.

The energy efficiency can be expressed as a ratio of the generated power to the lower heating value of the fuel.

$$\eta_{th} = \frac{\dot{W}}{\dot{n}_f . LHV} \quad (4.274)$$

The energy efficiency of the integrated system based on the heating value of the fuel can be determined as follows:

$$\dot{W}_{net} = \dot{W}_{SOFC} + \dot{W}_{GT,net} + \dot{W}_{ST} - \dot{W}_{pump} \quad (4.275)$$

The exergy efficiency for each component is defined based on the total exergy output to the total exergy input as follows:

$$\psi = \frac{\dot{E}x_{out}}{\dot{E}x_{in}} \quad (4.276)$$

The total exergy efficiency of system is defined based on fuel exergy as follows:

$$\psi = 1 - \frac{\sum \dot{E}x_{d,i}}{\sum \dot{E}x_{fuel} + \dot{E}x_{air,in}} \quad (4.277)$$

Table 4.17 Specific chemical exergy values for different components

Chemical Exergy (kJ/kmol)			
CH_4	836,510	H_2O	9,340
C_2H_6	1,504,360	H_2	20,340
C_3H_8	2,163,190	O_2	253,680
CO_2	27,900	N_2	720
CO	275,000		

Source: Kotas (1995)

Coal Gasification

Two different types of coal have been used in the gasifier. The gasification process occurs at elevated temperatures, and the pressure was limited to 15 bar. The composition of the coal, heating value and water content are shown in Table 4.18.

Solid Oxide Fuel Cell Unit

The solid oxide fuel cell unit uses the syngas produced from the gasification process. The supply fuel is mixed with circulated gas that exists from the anode side. The steam reforming process of methane and the water gas shift reaction occurs in the anode side where the electrochemical reaction also occurs. The compressed air is directed to the cathode side as it works as an oxidant. The electrons, which are produced at the anode side, are directed to the cathode side and reacted with the oxygen molecules. The oxide ions produced from this reaction at the cathode side diffuse to the anode through the electrolyte layer. The electric current is produced by the flow of electrons. The SOFC is assumed to be internally reforming, and the reforming and shift reactions maintain equilibrium conditions.

Table 4.18 Ultimate analysis of the coal types in the study

Coal ultimate analysis wt.%	Case 1	Case 2
C	58.8	63.75
H	3.80	4.50
O	12.2	6.88
N	1.30	1.25
S	0.30	2.51
Moisture content	19.6	11.12
LHV (kJ/kg)	21,920	25,886
HHV (kJ/kg)	23,200	27,135

In the analysis of the solid oxide fuel cell, it is assumed to be insulated and the following assumptions are used. The solid oxide fuel cell works at a steady state condition. The pressure drop across the fuel cell is neglected. The gas mixture is leaving the fuel cell at a chemical equilibrium condition.

Gas Turbine Cycle

The mixed gas exiting from the fuel cell is directed to the combustion chamber after it flows through the recuperator. The gas is then mixed with natural gas. The exhaust gas is expanded then in the gas turbine, it produces mechanical work. The natural gas has the following composition: 93.9% CH_4, 3.2% C_2H_6, 1.1% C_3H_8, 1% CO_2 and 0.8% N_2. Compressed air is added for the combustion process. The separated nitrogen from the air separation unit is also mixed in the combustion chamber for limiting the temperature at the gas turbine inlet to 1250^oC, and to help reduce the formation of nitrous oxides.

4.6.2 Molten Carbonate Fuel Cell-Gas Turbine System

In this system, energy and exergy analysis for a biogas fueled MCFC combined with gas turbine are applied to modified version of the combined electricity and hydrogen production system studied by Verda and Nicolin (2010). The objective of this paper is to study the system efficiency and the performance of different compartments of the hybrid system and the irreversibilities in these devices from the exergetic point of view. A parametric study is performed to investigate the effect of operating parameters on the system performance.

System Description

The system studied is shown in the schematic diagram, Figure 4.9. A Purified landfill biogas fueled MCFC is operated. The biogas fuel composition is considered as: 50% CH_4, 35% CO_2, 13.5% N_2, 1.5% O_2 and 1% H_2. Desulfurization and dehalogenation steps are done before the biogas enter the system as the fuel contains halogens and siloxanes as 18 and 0.2 mg/m^3, respectively, also it contains hydrogen sulfide, sulfuric acid, sulfur dioxide, mercaptans, hydrochloric acid, hydrogen fluoride and ammonia as 103, 2, 4, 3, 1, 2 and 15 ppm, respectively, and these components are considered harmful for the fuel cell and the reformer.

The system is composed of micro gas turbine, integrated with molten carbonate fuel cell unit and pressure swing absorption system. Compressed air is extracted after the compressor to feed the fuel cell cathode. The rest of the compressed air is directed to the combustion chamber after being preheated in the recuperator using the exhaust gases out from the turbine. Biogas is mixed with the Injected exhaust gases of the fuel cell cathode

in the combustion chamber. Combustion products expand in the gas turbine producing mechanical work to run the compressor and produce electric power. After partial recovery of its enthalpy, exhaust gases is then directed to the heat recovery steam generator (HRSG) producing steam required for reforming the methane for the fuel cell. The Produced steam is mixed with biogas fuel and the mixture is preheated in the regenerative heat exchanger using the heat of the flow out from the reformer. Methane is converted into hydrogen at the reformer, this happens through an endothermic reaction. The heat required for the reforming reaction is provided by the catalytic burner. Flow out from the reformer is cooled to fuel cell inlet temperature, through the regenerative heat exchanger. This flow is then divided into two parts. One part is directed to the fuel cell anode side. The other part is directed to for hydrogen generation system. The exit anode flow of the fuel cell is then mixed with the exit flow from hydrogen generation system and a part of the exit flow of the fuel cell cathode site. This mixture enters the catalytic burner and the exhaust from the CB, a hot mixture rich of CO_2, is directed to the cathode side of the fuel cell after being mixed with the compressed air at the compressor exit. The part of the flow extracted upstream the fuel cell anode side is directed to the shift reactor, after being cooled, for increasing the hydrogen concentration in the flow, then the flow enters the condenser where condensed water is extracted and mixed with demineralized water and is used as a feed water to the HRSG after being preheated in the heat exchanger (cooler 2). The reduced humidity flow out from the condenser is compressed and enters the pressure swing adsorption system (PSA) for hydrogen separation. The flow out from the PSA is then heated through (cooler1) flows before it is directed to mix with the anode exit flow.

Thermodynamic Analysis

The analysis of the components in the system shown in Figure 4.9 is presented using the balance equations of mass, energy, entropy and exergy. The following assumptions were considered during making a steady state analysis of the system using EES software (Engineering Equation Solver):

- Atmospheric air is used and is considered as ideal gas with the composition of 21% oxygen and 79% Nitrogen.
- All flow steams are considered as ideal gases and ideal gas relations and properties were employed.

- The ambient temperature and pressure are constant.
- The operation of all devices is at steady state condition.
- The heat required for the reforming process is supplied from the catalytic burner and there are no heat losses from the reformer and the catalytic burner to the surroundings.
- All kinetic and potential exergies changes are neglected.
- The Heat exchangers, compressors and turbine are adiabatic.
- The air compressor pressure ratio is 4.
- All units are expressed in the SI system.

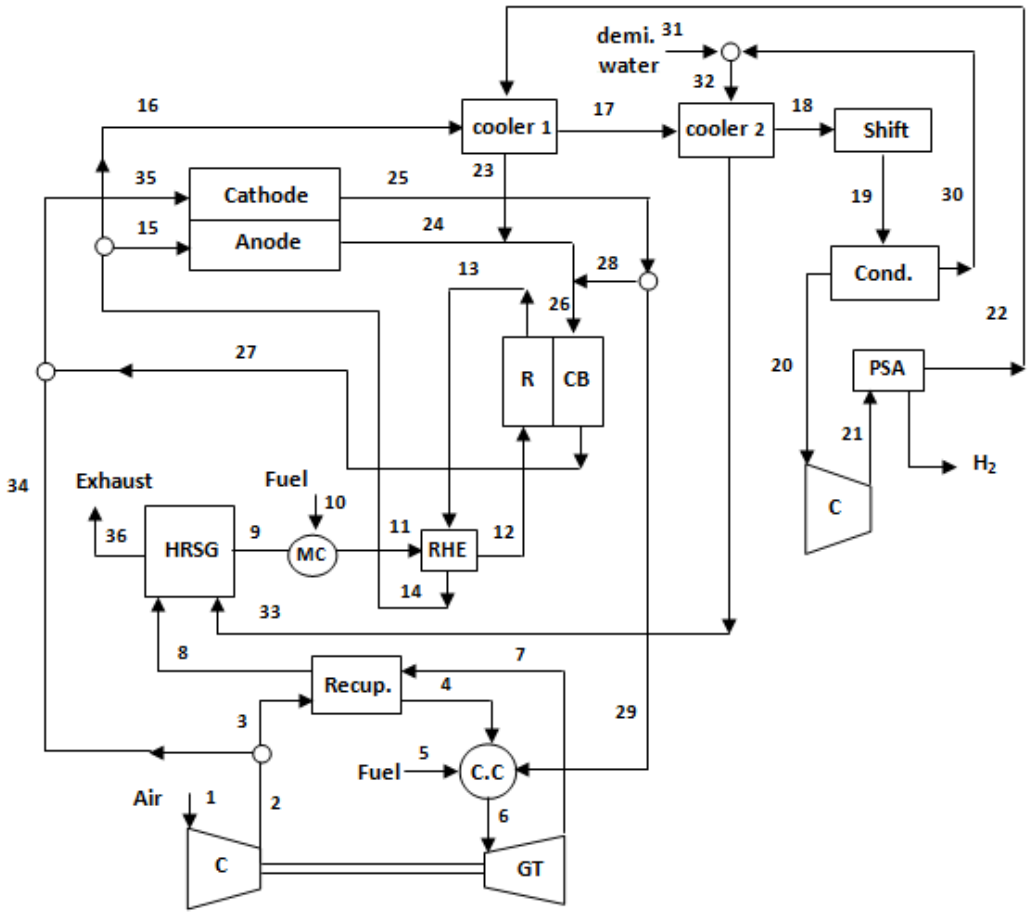

Figure 4.9 Schematic of the System (C: compressor, GT: gas turbine, Recup: recuperator, HE: heat exchanger, HRSG: heat recovery steam generator, R: reformer, CB: catalytic burner).

Half-cell of MCFC reactions

The operating principle of molten carbonate fuel cell depends on the indirect reaction between hydrogen and oxygen from air to produce electricity and water and heat as byproduct. Figure 4.10 illustrates the operation and reactions occur in the MCFC. Hydrogen reacts with the carbonate ions travelling thought the electrolyte. This reactions produce water and carbon dioxide, and generated electrons at the anode side. The generated electrons travel to the fuel cell cathode side, through external circuit, resulting in electric current flow. In the presence of carbon monoxide, water gas shift reaction can occur in the anode side too. In presence of electrons, oxygen reacts with carbon dioxide, at the cathode side. This reaction generates carbonate ions that migrates through the electrolyte to the anode.

Hydrogen used in fuel cell anode side is generated from the methane which is the main energy carrier in the biogas fuel. Methane reacting with water in the reformer produces the hydrogen required.

Anode : $2H_2 + 2CO_3^{2-} \rightarrow 2H_2O + 2CO_2 + 4e^-$

$CO + H_2O \rightarrow CO_2 + H_2$ (water-gas shift reaction)

Cathode: $O_2 + 2CO_2 + 4e^- \rightarrow 2CO_3^{2-}$

Steam Reforming of Methane: $CH_4 + H_2O \rightarrow CO + 3H_2$

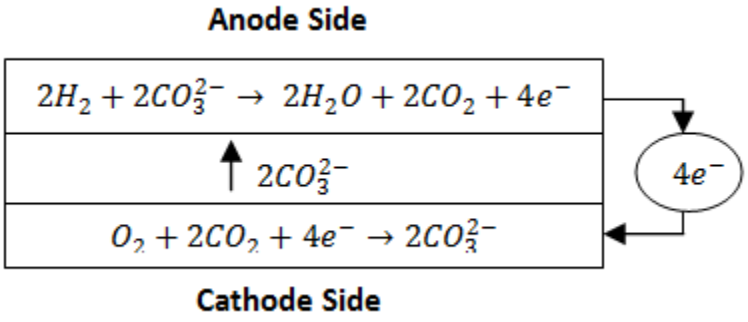

Figure 4.10 MCFC operating principle and reactions

Compressor

The incoming atmospheric air is compressed through the adiabatic compressor, and the power required for the compressor is supplied by the turbine. The mass, energy, entropy and exergy balance equations describing the performance of the compressor can be written as follows:

$$\dot{n}_1 = \dot{n}_2 \quad (4.278)$$

$$\dot{n}_1 \bar{h}_1 + \dot{W}_C = \dot{n}_2 \bar{h}_2 \quad (4.279)$$

$$\dot{n}_1 \bar{s}_1 + \dot{S}_{gen} = \dot{n}_2 \bar{s}_2 \quad (4.280)$$

$$\dot{n}_1 \overline{ex}_1 + \dot{W}_C = \dot{n}_2 \overline{ex}_2 + Ex_{d,C} \quad (4.281)$$

where $\dot{W}_C$ is the electric power required to drive the compressor and *n* is the molar flow rate. $\bar{h}_i \; and \; \overline{ex}_i$ represent the molar enthalpy and molar exergy in (kJ/kmol) for compositions of the flows through the system, and Ex_d is the total exergy destruction through the studied component in (kW).

Combustion chamber

The biogas (flow 5) is mixed with the injected cathode exhaust (flow 29) and the compressed preheated air (flow 4) in the combustion chamber, and the energy balance equation can be presented as:

$$\dot{n}_4 \bar{h}_4 + \sum_{i=1}^{N} \dot{n}_{i,5} \, \bar{h}_{i,5} + \sum_{i=1}^{N} \dot{n}_{i,29} \, \bar{h}_{i,29} = \sum_{i=1}^{N} \dot{n}_{i,6} \bar{h}_{i,6} \quad (4.282)$$

where '*n*' is the molar flow rate and 'i ' represent the species entering and leaving the system. The following equation is used for entropy generation calculation:

$$\dot{n}_4 \bar{s}_4 + \sum_{i=1}^{N} \dot{n}_{i,5} \, \bar{s}_{i,5} + \sum_{i=1}^{N} \dot{n}_{i,29} \, \bar{s}_{i,29} + \dot{S}_{gen} = \sum_{i=1}^{N} \dot{n}_{i,6} \bar{s}_{i,6} \quad (4.283)$$

The exergy balance equation can be written as follows:

$$\dot{n}_4 \overline{ex}_4 + \sum_{i=1}^{N} \dot{n}_{i,5} \, \overline{ex}_{i,5} = \sum_{i=1}^{N} \dot{n}_{i,6} \overline{ex}_{i,6} + Ex_{d,CC} \quad (4.284)$$

Gas Turbine

The combustion products (flow 6) expand thought the gas turbine producing the mechanical work that drive the compressor and also produce electric work following the balance equations as

$$\sum_{i=1}^{N} \dot{n}_{i,6} = \sum_{i=1}^{N} \dot{n}_{i,7} \quad (4.285)$$

$$\sum_{i=1}^{N} \dot{n}_{i,6}\, \bar{h}_{i,6} = \sum_{i=1}^{N} \dot{n}_{i,7}\, \bar{h}_{i,7} + \dot{W}_T \quad (4.286)$$

where $\dot{W}_T$ is the turbine output power.

The entropy generation rate can be calculated from the entropy balance equation as follows:

$$\sum_{i=1}^{N} \dot{n}_{i,6}\, \bar{s}_{i,6} + \dot{S}_{gen} = \sum_{i=1}^{N} \dot{n}_{i,7}\, \bar{s}_{i,7} \quad (4.287)$$

Table 4.19 Chemical exergy values of species composing the flow mixtures through the system (Kotas, 1995)

Component	Standard Chemical Exergy [kJ/kmol]	Component	Standard Chemical Exergy [kJ/kmol]
CH_4	836,510	O_2	3970
CO_2	27,900	N_2	720
CO	275,430	H_2O (g)	11,710
H_2	253,680	H_2O (l)	3120

The exergy destruction rate in the gas turbine can be calculated from the following exergy balance equation:

$$\sum_{i=1}^{N} \dot{n}_{i,6}\, \overline{ex}_{i,6} = \sum_{i=1}^{N} \dot{n}_{i,7}\, \overline{ex}_{i,7} + \dot{W}_T + Ex_{d,Turb} \quad (4.288)$$

Recuperator

The turbine exhaust gases are used to preheat the compressed air entering the combustion chamber. No reaction takes place in the recuperator, so the compositions of flows entering and leaving are unchanged. Mass balance equations can be expressed as

$$\dot{n}_3 = \dot{n}_4 \quad (4.289)$$

$$\sum_{i=1}^{N} \dot{n}_{i,7} = \sum_{i=1}^{N} \dot{n}_{i,8} \quad (4.290)$$

For the energy balance equation, it is written as

$$\dot{n}_3 \bar{h}_3 + \sum_{i=1}^{N} \dot{n}_{i,7}\, \bar{h}_{i,7} = \dot{n}_4 \bar{h}_4 + \sum_{i=1}^{N} \dot{n}_{i,8} \bar{h}_{i,8} \quad (4.291)$$

The entropy and exergy balance equations can be also written as follows:

$$\dot{n}_3 \bar{s}_3 + \sum_{i=1}^{N} \dot{n}_{i,7}\, \bar{s}_{i,7} + \dot{S}_{gen} = \dot{n}_4 \bar{s}_4 + \sum_{i=1}^{N} \dot{n}_{i,8} \bar{s}_{i,8} \quad (4.292)$$

$$\dot{n}_3 \overline{ex}_3 + \sum_{i=1}^{N} \dot{n}_{i,7}\, \overline{ex}_{i,7} = \dot{n}_4 \overline{ex}_4 + \sum_{i=1}^{N} \dot{n}_{i,8} \overline{ex}_{i,8} + Ex_{d,Recup} \quad (4.293)$$

Heat recovery steam generator

The exhaust gases heat energy (flow 8) is recovered in the HRSG producing steam for the reforming process, the mass and energy balance equations can be expressed as follows:

$$\dot{n}_{33} = \dot{n}_9 \quad (4.294)$$

$$\sum_{i=1}^{N} \dot{n}_{i,8} = \sum_{i=1}^{N} \dot{n}_{i,36} \quad (4.295)$$

$$\dot{n}_{33}\bar{h}_{33} + \sum_{i=1}^{N} \dot{n}_{i,8}\,\bar{h}_{i,8} = \dot{n}_9\bar{h}_9 + \sum_{i=1}^{N} \dot{n}_{i,36}\,\bar{h}_{i,36} \quad (4.296)$$

The entropy and exergy balance equations for the HRSG can be written as:

$$\dot{n}_{33}\bar{s}_{33} + \sum_{i=1}^{N} \dot{n}_{i,8}\,\bar{s}_{i,8} + \dot{S}_{gen} = \dot{n}_9\bar{s}_9 + \sum_{i=1}^{N} \dot{n}_{i,36}\,\bar{s}_{i,36} \quad (4.297)$$

$$\dot{n}_{33}\overline{ex}_{33} + \sum_{i=1}^{N} \dot{n}_{i,8}\,\overline{ex}_{i,8} += \dot{n}_9\overline{ex}_9 + \sum_{i=1}^{N} \dot{n}_{i,36}\,\overline{ex}_{i,36} + Ex_{d,HRSG} \quad (4.298)$$

Mixing chamber

The biogas fuel (flow 10) is mixed with the steam out from the HRSG (flow 9) in the mixing chamber producing the mixture to be reformed. The mass and energy balance equations through the mixing chamber can be expressed as:

$$\dot{n}_9 + \sum_{i=1}^{N} \dot{n}_{i,10} = \sum_{i=1}^{N} \dot{n}_{i,11} \quad (4.299)$$

$$\dot{n}_9\bar{h}_9 + \sum_{i=1}^{N} \dot{n}_{i,10}\,\bar{h}_{i,10} = \sum_{i=1}^{N} \dot{n}_{i,11}\,\bar{h}_{i,11} \quad (4.300)$$

The entropy and exergy balance equations considering the molar specific entropies and exergies of the flow compositions can be written as

$$\dot{n}_9\bar{s}_9 + \sum_{i=1}^{N} \dot{n}_{i,10}\,\bar{s}_{i,10} + \dot{S}_{gen} = \sum_{i=1}^{N} \dot{n}_{i,11}\,\bar{s}_{i,11} \quad (4.301)$$

$$\dot{n}_9\overline{ex}_9 + \sum_{i=1}^{N} \dot{n}_{i,3}\,\overline{ex}_{i,10} = \sum_{i=1}^{N} \dot{n}_{i,11}\,\overline{ex}_{i,11} + Ex_{d,MC} \quad (4.302)$$

Regenerative heat exchanger

The mixture stream (flow 11) is heated through the regenerative heat exchanger with flow (13) discharged from the reactor. It is used to control the temperature of the flow (13) which is directed to the inlet of the fuel cell anode.

$$\sum_{i=1}^{N} \dot{n}_{i,11} = \sum_{i=1}^{N} \dot{n}_{i,12} \quad (4.303)$$

$$\sum_{i=1}^{N} \dot{n}_{i,13} = \sum_{i=1}^{N} \dot{n}_{i,14} \quad (4.304)$$

The energy balance for the RHE reads:

$$\sum_{i=1}^{N} \dot{n}_{i,11}\,\bar{h}_{i,11} + \sum_{i=1}^{N} \dot{n}_{i,13}\,\bar{h}_{i,13} = \sum_{i=1}^{N} \dot{n}_{i,12}\,\bar{h}_{i,12} + \sum_{i=1}^{N} \dot{n}_{i,14}\,\bar{h}_{i,14} \quad (4.305)$$

For the entropy balance equation:

$$\sum_{i=1}^{N} \dot{n}_{i,11}\, \bar{s}_{i,11} + \sum_{i=1}^{N} \dot{n}_{i,13}\, \bar{s}_{i,13} + \dot{S}_{gen} = \sum_{i=1}^{N} \dot{n}_{i,12}\, \bar{s}_{i,12} + \sum_{i=1}^{N} \dot{n}_{i,14}\, \bar{s}_{i,14} \quad (4.306)$$

The exergy balance equation can be expressed as:

$$\sum_{i=1}^{N} \dot{n}_{i,11}\, \overline{ex}_{i,11} + \sum_{i=1}^{N} \dot{n}_{i,13}\, \overline{ex}_{i,13} = \sum_{i=1}^{N} \dot{n}_{i,12}\, \overline{ex}_{i,12} + \sum_{i=1}^{N} \dot{n}_{i,14}\, \overline{ex}_{i,14} + Ex_{d,RHE} \quad (4.307)$$

Reformer

The fuel and steam mixture (flow 12) passes through the reformation reaction to produce the MCFC fuel. The mass and energy balance equations for the reformer process read:

$$\sum_{i=1}^{N} \dot{n}_{i,12} = \sum_{i=1}^{N} \dot{n}_{i,13} \quad (4.308)$$

$$\sum_{i=1}^{N} \dot{n}_{i,12}\, \bar{h}_{i,12} + \dot{Q}_R = \sum_{i=1}^{N} \dot{n}_{i,13}\, \bar{h}_{i,13} \quad (4.309)$$

where $\dot{Q}_R$ is the heat required for the endothermic reformation reaction. It is supplied from the catalytic burner. The entropy generation can be calculated from the entropy balance equation:

$$\sum_{i=1}^{N} \dot{n}_{i,12}\, \bar{s}_{i,12} + \dot{Q}_R/T_o + \dot{S}_{gen} = \sum_{i=1}^{N} \dot{n}_{i,13}\, \bar{s}_{i,13} \quad (4.310)$$

The exergy balance reads:

$$\sum_{i=1}^{N} \dot{n}_{i,12}\, \overline{ex}_{i,12} + \dot{Q}_R \left(1 - \frac{T_0}{T_R}\right) = \sum_{i=1}^{N} \dot{n}_{i,13}\, \overline{ex}_{i,13} + Ex_{d,Reform} \quad (4.311)$$

where T_R is the average temperature of the reactor, which represents the temperature on the boundary where heat transfer occurs.

Catalytic Burner

Flow (24) out from the fuel cell anode side is mixed stream (23) and a portion of the cathode exit stream, and the mixture is burned producing carbon dioxide which is required for the cathode side reaction. Mass and energy balance equations can be written as follows:

$$\sum_{i=1}^{N} \dot{n}_{i,26} = \sum_{i=1}^{N} \dot{n}_{i,27} \quad (4.312)$$

$$\sum_{i=1}^{N} \dot{n}_{i,26}\, \bar{h}_{i,26} = \sum_{i=1}^{N} \dot{n}_{i,27}\, \bar{h}_{i,27} + \dot{Q}_{CB} \quad (4.313)$$

where $\dot{Q}_{CB}$ is the heat out from the catalytic burner and supplied to the reformer.

The entropy and exergy balance equations can be also presented as

$$\sum_{i=1}^{N} \dot{n}_{i,26}\, \bar{s}_{i,26} + \dot{S}_{gen} = \sum_{i=1}^{N} \dot{n}_{i,27}\, \bar{s}_{i,27} + \dot{Q}_{CB}/T_o \quad (4.314)$$

and

$$\sum_{i=1}^{N} \dot{n}_{i,26}\, \overline{ex}_{i,26} = \sum_{i=1}^{N} \dot{n}_{i,27}\, \overline{ex}_{i,27} + \dot{Q}_{CB}\left(1 - \frac{T_0}{T_{CB}}\right) + Ex_{d,CB} \quad (4.315)$$

where T_{CB} is the catalytic burner temperature, considering an average temperature of the catalytic burner.

MCFC

The energy, entropy and exergy balance equations for the MCFC are presented considering the stack with its both sides as one unit.

$$\sum_{i=1}^{N} \dot{n}_{i,15}\, \bar{h}_{i,15} + \sum_{i=1}^{N} \dot{n}_{i,35}\, \bar{h}_{i,35} = \dot{W}_{FC} + \sum_{i=1}^{N} \dot{n}_{i,24}\, \bar{h}_{i,24} + \sum_{i=1}^{N} \dot{n}_{i,25}\, \bar{h}_{i,25} \quad (4.316)$$

where $\dot{W}_{FC}$ is the electric energy produced from the fuel cell unit.

$$\sum_{i=1}^{N} \dot{n}_{i,15}\, \bar{s}_{i,15} + \sum_{i=1}^{N} \dot{n}_{i,35}\, \bar{s}_{i,35} + \dot{S}_{gen} = \sum_{i=1}^{N} \dot{n}_{i,24}\, \bar{s}_{i,24} + \sum_{i=1}^{N} \dot{n}_{i,25}\, \bar{s}_{i,25} \quad (4.317)$$

$$\sum_{i=1}^{N} \dot{n}_{i,15}\, \overline{ex}_{i,15} + \sum_{i=1}^{N} \dot{n}_{i,35}\, \overline{ex}_{i,35} = \dot{W}_{FC} + \sum_{i=1}^{N} \dot{n}_{i,24}\, \overline{ex}_{i,24} + \sum_{i=1}^{N} \dot{n}_{i,25}\, \overline{ex}_{i,25} + Ex_{d,FC} \quad (4.318)$$

The molar exergy terms for the flow states through the system can be calculated from the following equation considering exergy terms for all the compositions in flow mixtures. It represents the sum of the physical, thermal and chemical exergetic terms.

$$\overline{ex}_i = \bar{h}_i - \bar{h}_{i,0} - T_0\left(\bar{s}_i - \bar{s}_{i,0}\right) + RT_0 \ln X_i + \overline{ex}_i^{ch} \quad (4.319)$$

where $\overline{ex}_i^{ch}$ is the chemical exergy (kJ/kmol) of mixture composition. The chemical exergy values used are considered to be constant as shown in Table 4.19 (Kotas, 1995), and X_i is the mole fraction of species *i*. For the operating cell voltage:

$$V_{Cell} = E_{eq} - j(R_{ohm} + \eta_{an} + \eta_{ca}) \quad (4.320)$$

where E_{eq} is the equilibrium cell potential which can be determined using Nernst Equation as follows (Dicks, 2004):

$$E_{eq} = \frac{-\Delta\bar{g}_f}{z.F} + \frac{R.T}{z.F} \ln\left(\frac{P_{H_2}.P_{O_2}^{0.5}.P_{CO_{2,c}}}{P_{H_2O}.P_{CO_{2,a}}}\right) \quad (4.321)$$

where *z* is the number of electrons transferred through the fuel cell, per reacting mole of fuel, $-\Delta\bar{g}_f$ is the molar change in Gibbs free energy of formation, *F* is Faraday constant, P_i represents partial pressure of the different species at the inlet section of the fuel cell.

The ohmic losses, R_{ohm}, represents the resistance of electrolyte against the carbonate ions flow assuming that the bipolar plates are prefect conductors ohmic losses can be estimated from the experimental expression provided by Koh et al. (2000):

$$R_{ohm} = 0.5 \times 10^{-4} \times EXP\left[3016\left(\frac{1}{T_{FC}} - \frac{1}{923}\right)\right] \quad (4.322)$$

The anode and cathode overpotential are determined using the following empirical relations which are valid for operating temperature range of 600-700^{o}C (Koh et al., 2000):

$$\eta_{an} = 2.27 \times 10^{-9} \times EXP\left(\frac{6435}{T_{FC}}\right) P_{H_2}^{-0.42}.P_{CO_2}^{-0.17}.P_{H_2O}^{-1.0} \quad (4.323)$$

$$\eta_{ca} = 7.505 \times 10^{-10} \times EXP\left(\frac{9298}{T_{FC}}\right) P_{O_2}^{-0.43}.P_{CO_2}^{-0.09} \quad (4.324)$$

The MCFC operates with reactants utilization factor of 0.75. Reactants utilization is defined as the ratio of the difference between inlet and outlet anodic molar flows of hydrogen and carbon monoxide to the anode inlet hydrogen and carbon monoxide molar flow rates. The nominator represents the net fuel consumption in the MCFC.

$$U = \frac{\left(\dot{n}_{H_{2_{15}}} - \dot{n}_{H_{2_{24}}}\right)_{in,an} - \left(\dot{n}_{H_{2_{15}}} - \dot{n}_{H_{2_{24}}}\right)_{out,an}}{\left(\dot{n}_{H_{2_{15}}} - \dot{n}_{H_{2_{24}}}\right)_{in,an}} \quad (4.325)$$

The utilization of hydrogen, carbon monoxide and carbon dioxide can be calculated from the definition of utilization factor as follows:

$$U_{H_2} = \left(\dot{n}_{H_{2_{15}}} - \dot{n}_{H_{2_{24}}}\right)/\dot{n}_{H_{2_{15}}} \quad (4.326)$$

$$U_{CO} = \left(\dot{n}_{CO_{15}} - \dot{n}_{CO_{24}}\right)/\dot{n}_{CO_{15}} \quad (4.327)$$

$$U_{CO_2} = \left(\dot{n}_{CO_{2_{35}}} - \dot{n}_{CO_{2_{25}}}\right)/\dot{n}_{CO_{2_{35}}} \quad (4.328$$

Coolers

A conventional heat exchanger is used to utilize the heat accompanied with flow (16) extracted from the reformer to heat flow (22) before it is injected to the catalytic burner. The energy and exergy balance equations can be written as follows:

$$\sum_{i=1}^{N} \dot{n}_{i,16} = \sum_{i=1}^{N} \dot{n}_{i,17} \quad (4.329)$$

$$\sum_{i=1}^{N} \dot{n}_{i,22} = \sum_{i=1}^{N} \dot{n}_{i,23} \quad (4.330)$$

$$\sum_{i=1}^{N} \dot{n}_{i,16}\,\bar{h}_{i,16} + \sum_{i=1}^{N} \dot{n}_{i,22}\,\bar{h}_{i,22} = \sum_{i=1}^{N} \dot{n}_{i,17}\,\bar{h}_{i,17} + \sum_{i=1}^{N} \dot{n}_{i,23}\,\bar{h}_{i,23} \quad (4.331)$$

$$\sum_{i=1}^{N} \dot{n}_{i,16}\,\overline{ex}_{i,16} + \sum_{i=1}^{N} \dot{n}_{i,22}\,\overline{ex}_{i,22} = \sum_{i=1}^{N} \dot{n}_{i,17}\,\overline{ex}_{i,17} + \sum_{i=1}^{N} \dot{n}_{i,23}\,\overline{ex}_{i,23} + Ex_{d,cooler1} \quad (4.332)$$

The flow out from cooler 1 is used to preheat the HRSG feed water (flow 33), and as cooler1, energy and exergy equations are composed as for conventional heat exchanger.

$$\sum_{i=1}^{N} \dot{n}_{i,17} = \sum_{i=1}^{N} \dot{n}_{i,18} \quad (4.333)$$

$$\dot{n}_{32} = \dot{n}_{33} \quad (4.334)$$

$$\dot{n}_{32}\bar{h}_{32} + \sum_{i=1}^{N} \dot{n}_{i,17}\,\bar{h}_{i,17} = \dot{n}_{33}\bar{h}_{33} + \sum_{i=1}^{N} \dot{n}_{i,18}\,\bar{h}_{i,18} \quad (4.335)$$

$$\dot{n}_{32}\overline{ex}_{32} + \sum_{i=1}^{N} \dot{n}_{i,17}\,\overline{ex}_{i,17} = \dot{n}_{33}\overline{ex}_{33} + \sum_{i=1}^{N} \dot{n}_{i,18}\,\overline{ex}_{i,18} + Ex_{d,cooler2} \quad (4.336)$$

Energy Efficiency

The system energy efficiency is calculated as follows:

$$\eta = \frac{\dot{W}_{FC} + \dot{W}_T - \dot{W}_C}{LHV_f(\dot{n}_{f,CC} + \dot{n}_{f,FC})} \quad (4.337)$$

where $\dot{n}_{f,CC}$ and $\dot{n}_{f,FC}$ represents the biogas flow rates entering the combustion chamber and the fuel used for the fuel cell, LHV_f is the lower heating value of the biogas fuel used in the described system.

Exergy Efficiency

The exergy efficiency is calculated using the following formula:

$$\psi = \frac{\dot{W}_{FC} + \dot{W}_T - \dot{W}_C}{\sum \dot{n}_i \overline{ex}_i} \quad (4.338)$$

where 'i' denotes the inlet fuel, water and air.

Chapter 5

RESULTS AND DISCUSSION

In this chapter, the results of the analyses performed on the proposed systems are presented. The performed thermodynamic energy and exergy modeling as well as economic and environmental assessments of the systems, illustrated in the previous chapter, are applied to each of the systems and their subsystems. The systems are assessed by the energy and exergy efficiencies. The effects of different operating parameters on the system performance are investigated. The results of the main subsystems models are also introduced. The main subsystems are investigated thermodynamically, thermoeconomically and optimized for the best operating parameters. Subsystems models validations are performed and presented in the results, as well.

5.1 SYSTEM 1: SOLAR PARABOLIC DISH – GAS TURBINE BASED SYSTEM

In this section, the results of the analyses performed on the proposed solar dish integrated system are introduced. The system is introduced as presented earlier in Figure 3.1. In system modeling, several assumptions were made. All system and subsystems processes are considered to operate as steady state. Through the analyses of the gas turbine, gasification and SOFC, helium and air are considered as ideal gases. Pressure losses in the main heat exchangers are considered as listed in Table 5.1. Also changes in kinetic and potential energy and exergy are neglected. The main input parameters for the base case of the system operation are listed in Table 5.1. In the exergy analyses, the reference pressure and temperature values are considered as 101.3 kPa and 25°C, respectively, unless indicated differently for testing the effect of changing this condition on the system and subsystems performance.

Throughout this section, the results are presented, first by the overall performance measured by energy and exergy efficiency of the system performing in its different modes, and the exergy destruction in the main system components calculated at the base condition.

Table 5.1 Input parameters of the solar dish based integrated system

Parameter	Value
Solar Dish Concentrator	
Solar radiation	850 W/m2
Concentrator diameter	15 m
Receiver diameter	1.2 m
Sun temperature	6000 K
Optical efficiency	0.85
Collector efficiency factor	0.9
Overall heat transfer coefficient	150 W/m2K
Gasifier	
Gasification temperature	750°C
Steam to biomass ratio	0.7
SOFC	
Operating temperature	700-750°C
Operating current density	4000 A/m2
Gas Turbine	
Compression ratio	2.8
Temperature at compressor inlet	300 K
Compressor inlet pressure	30 bar
Turbine polytropic efficiency	92%
Compressor polytropic efficiency	90%
Mechanical efficiency	99%
Recuperator effectiveness	88%
Precooler effectiveness	90%
Intercooler effectiveness	87%
Pressure loss in recuperator, hot side	2.1%
Pressure loss in recuperator, cold side	1.8%
Pressure loss in Precooler, hot side	1.2%
Pressure loss in Intercooler, hot side	1.3%
Absorption Chiller System	
Evaporator temperature	2°C
Weak solution concentration	0.568

The effects of different operating parameters of the system on the overall performance are introduced, subsequently. These system energy and exergy efficiencies, as well as the cost rate and greenhouse gas emissions rate are tested. Subsequently, the results of the system optimization are listed.

After introducing the results of the integrated system analyses, the results and validations of the main subsystems and components are discussed. The performance of the solar dish, LiBr absorption chiller system, regenerative helium gas turbine and the SOFC are assessed based on the described models. The gasification-SOFC subsystem is also investigated separately and the system analyses results are listed and discussed. For a better understanding of the gasification process, the results of the hydrodynamics model of the gasifier, considering the presented fluidized bed mode, are discussed. The modes of operation are shown in the illustrative curve in Figure 5.1, showing the two modes of operation over one day.

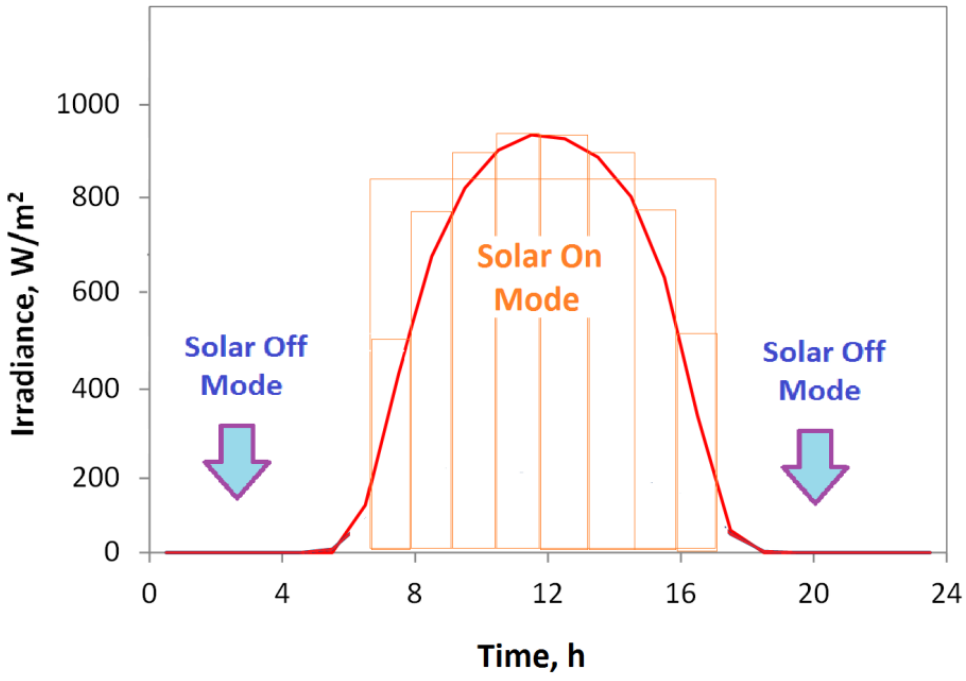

Figure 5.1 Illustration of operation mode with respect to the variation in solar radiation density

The overall system performance of the integrated solar dish can be seen as shown in Figure 5.2. The figure shows the efficiencies and greenhouse gas emissions for three different cases of the system operation. The analysis of the Solar Off case represents the model performing on the gasification-SOFC system when the solar radiation is not available. The energy and exergy efficiencies consider the power produced through the SOFC and the heat provided to the absorption chiller system and the production of rich hydrogen syngas for hydrogen production. The Solar On mode results represent the analyses during the availability of solar radiation. The heat is provided to the system through the solar dish for power production through the helium gas turbine. In this mode, the steam biomass gasification is mainly dedicated for hydrogen production and providing backup heat for preheating the gas turbine working fluid.

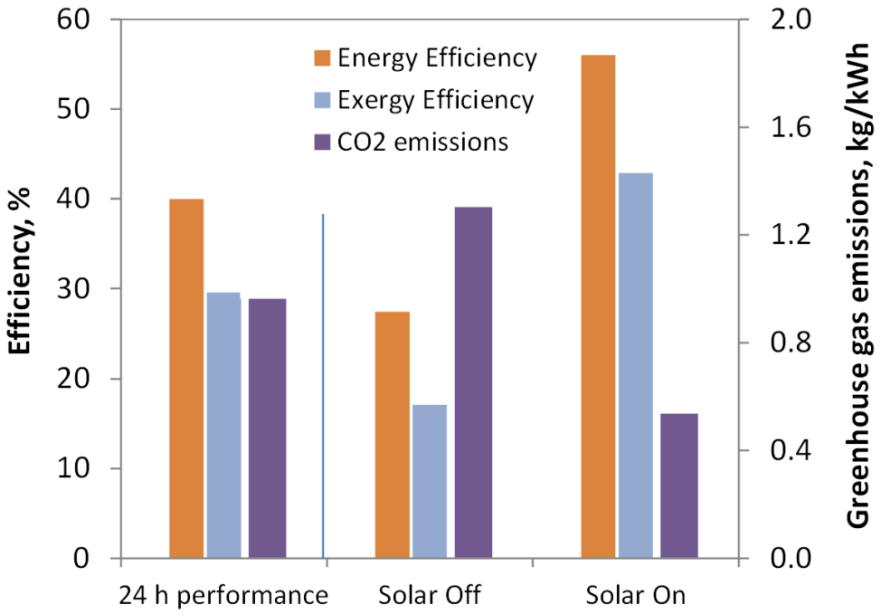

Figure 5.2 Integrated system efficiency and greenhouse gas emissions

The 24-hour performance considers calculating the energy and exergy efficiencies as well as the emissions considering the total useful output of the system and the total energy input based on their hours of operation during the day. It is assumed that the solar source is available for average of 10 hours during the day. The energy and exergy

efficiencies are 27.47% and 17.12% for the Solar Off mode, while it operates at 56.04% and 42.88% for the Solar On mode, for energy and exergy efficiencies, respectively. This is because in the Solar Off mode, almost 90% of the produced syngas is introduced to the fuel cell unit to satisfy the power production required of the system. The emissions of carbon dioxide with respect to the amount of useful energy produced are found to be 1.3 and 0.53 kg/kWh. The overall performance based on the sources hours availability shows energy efficiency of 39.99% and exergy efficiency of 27.47%.

The exergy destruction rates occurring in the main subsystems during operation are illustrated in Figure 5.3. The main exergy destruction occurs in the gasification subsystem where chemical and electrochemical reactions are considered in the gasifier and the fuel cell unit, including high temperature exhaust gases. Even with the utilization of the heat content of exhaust gases for production of steam for gasification, still the gasification shares with the most exergy destruction in the system.

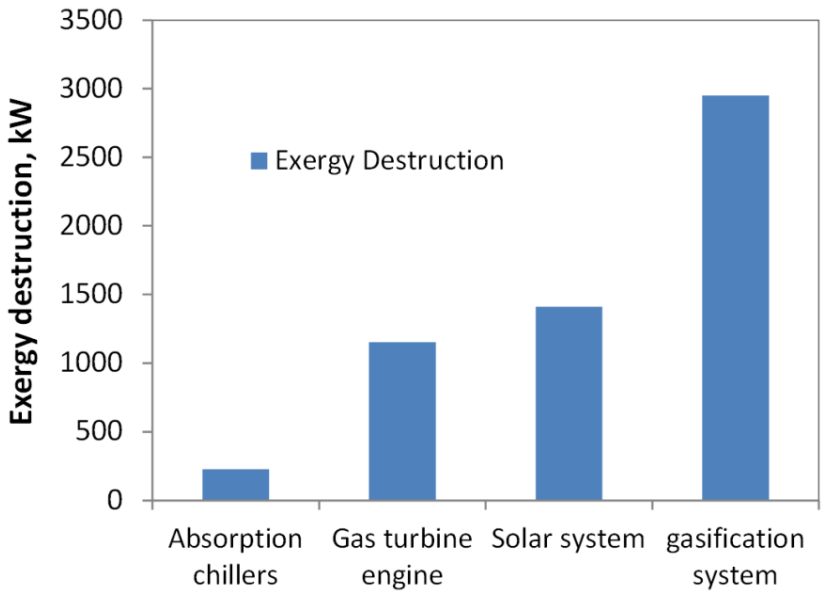

Figure 5.3 Exergy destruction in the main system components

The solar dish receiver temperature has a large effect on the system performance as it drives the main prime mover of the integrated system through controlling the gas turbine performance. The effect of the receiver temperature on the solar dish exergy

efficiency is shown in Figure 5.4. The exergy efficiency increases rapidly with the receiver temperature and it reaches a maximum of 27.33% at about 506K when operating at the base condition. The exergy efficiency starts decreasing gradually after that with the increase in the receiver temperature as shown. The effect of the receiver temperature on the helium gas turbine performance is shown in the same figure. The exergy efficiency increases with the heat source temperature. It can be seen that the operating temperature is constrained with receiver temperature of about 510K. This is based on the compressor inlet temperature and compression ratio of the gas turbine engine.

The effect of the receiver temperature on the overall system performance is shown in Figure 5.5. These results are considering the day performance. The receiver temperature range is chosen reasonably to accommodate the system required outputs. The overall energetic and exergetic efficiencies decreases slightly with the increase in the receiver temperature. This is mainly caused by the increase of energy and exergy supplied to the system during the solar radiation availability. The energy efficiency changes from 41.56% to 39.14% while the exergy efficiency changes from 29.81% to 29.4%.

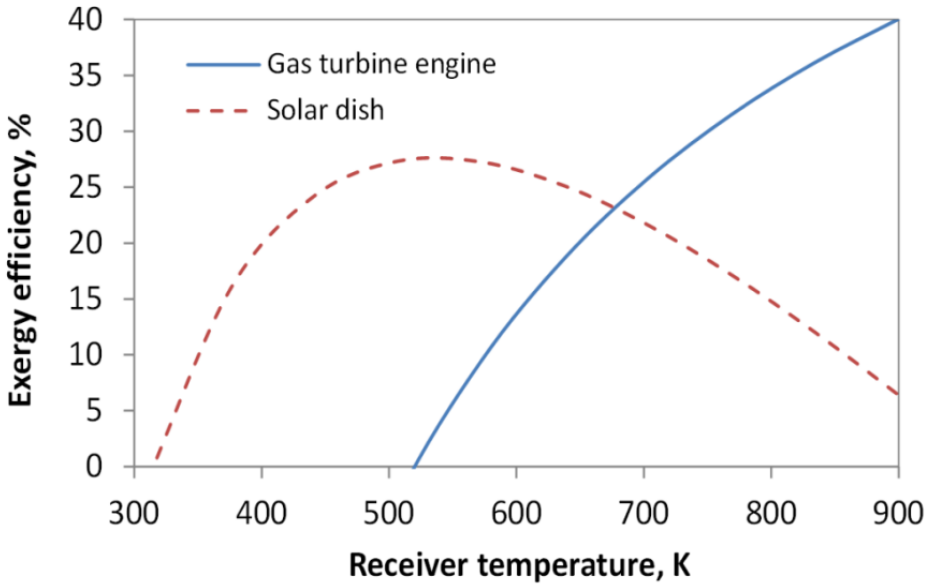

Figure 5.4 Effect of the solar receiver temperature on the dish and gas turbine exergy efficiency

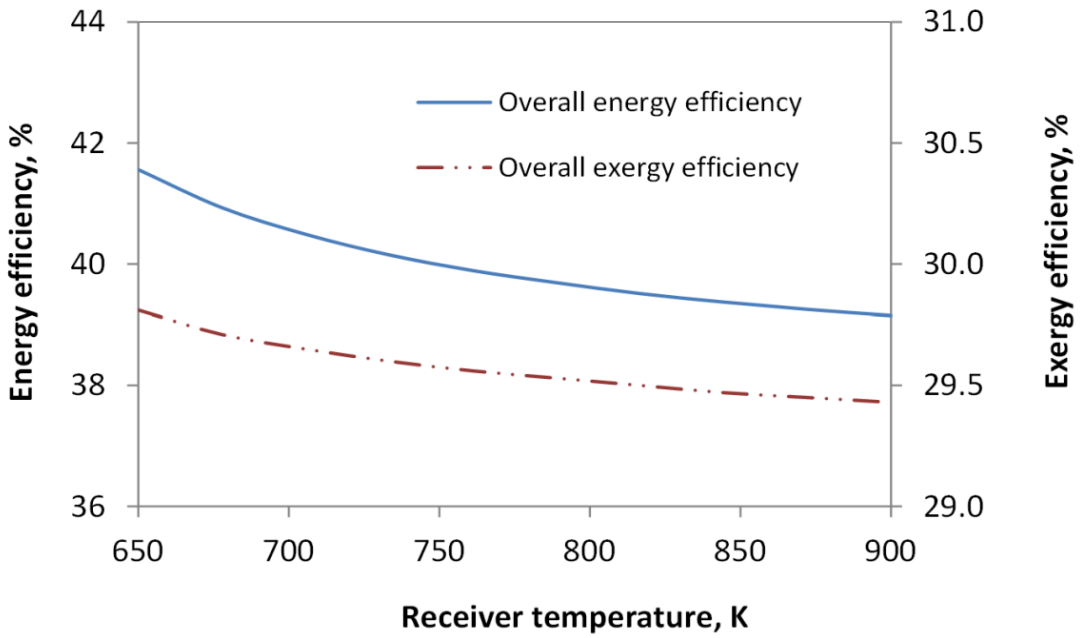

Figure 5.5 Effect of the solar receiver temperature on system efficiency for 24-hour performance

The effects of the receiver temperature, during Solar On mode, on the cost rate and the greenhouse gas emissions of the system operation are shown in Figure 5.6. The results show a reduction in the carbon dioxide emissions from the system per unit of produced energy. The increase of the solar receiver temperature would limit the need of the preheating of helium, by the gasifier products, before entering the receiver. The total cost rate is experiencing a reduction over the receiver temperature range. This is accompanied with a reduction of the environmental cost rate too, as part of the total cost rate, and reduction of fuel cost considering lower need of biomass. Considering the same design power output, the solar dish cost and the cost of the gas turbine cycle heat exchangers would be lower with higher receiver temperature. The energy and exergy efficiencies of the system during solar radiation availability are shown in Figure 5.7 at different receiver temperature values. The exergy efficiency decreases while energy efficiency increases. The reduction in the exergy efficiency is caused by the increase of solar exergy destruction at higher receiver temperature values.

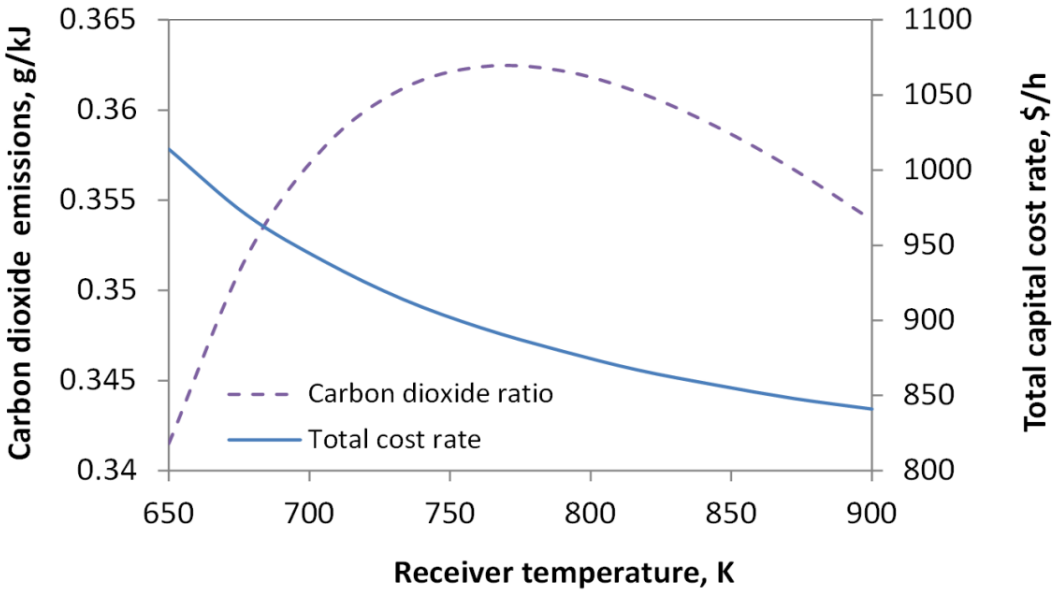

Figure 5.6 Total cost rate and emissions at different receiver temperature values for 24-hours performance

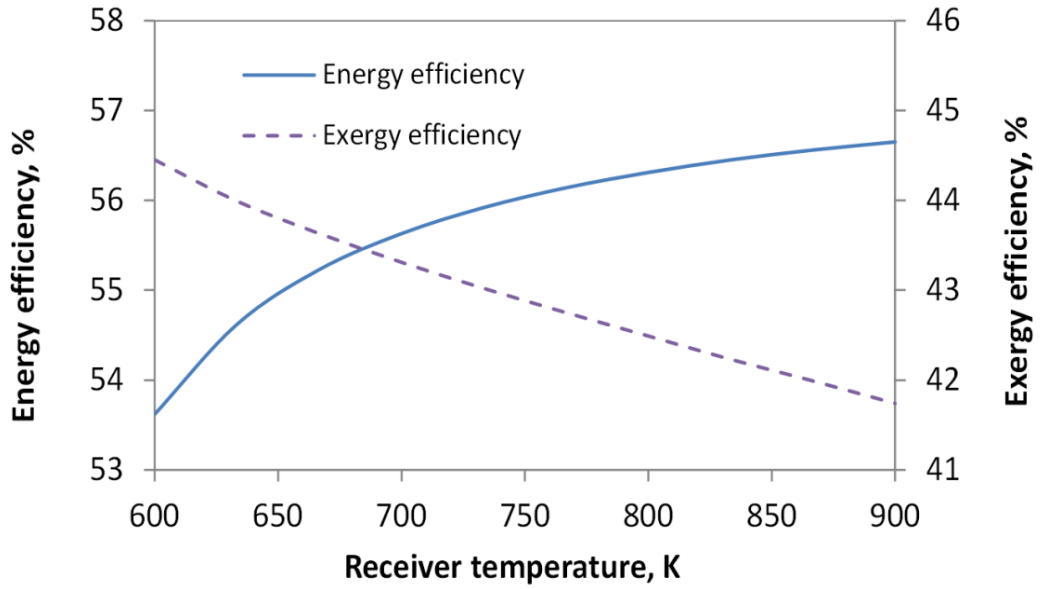

Figure 5.7 Efficiency of the integrated system during solar availability at different receiver temperature values during solar radiation availability (Solar On mode)

The gas turbine compression ratio is an important parameter for the performance of the gas turbine. The analyses are performed based on keeping all other operating parameters constant. The system performance is tests based on the defined 24 hours

performance efficiencies and the results are shown in Figure 5.8. The results show an increase in both energy and exergy efficiencies of the overall system performance. However, the effect on the energy efficiency is higher where the values changed from 39.4% to 42.91% when the exergy efficiency increased with 0.33%. For the solar radiation mode, the results in Figure 5.9 shows that the energy efficiency increases until reaches a maximum of 56.04% at a compression ratio of 2.842 before is starts decreasing. This is directly related to the optimum compression ratio from the gas turbine analyses. The exergy efficiency has a different trend with the compression ratio. It appears that the exergy efficiency decreases with the compression ratio.

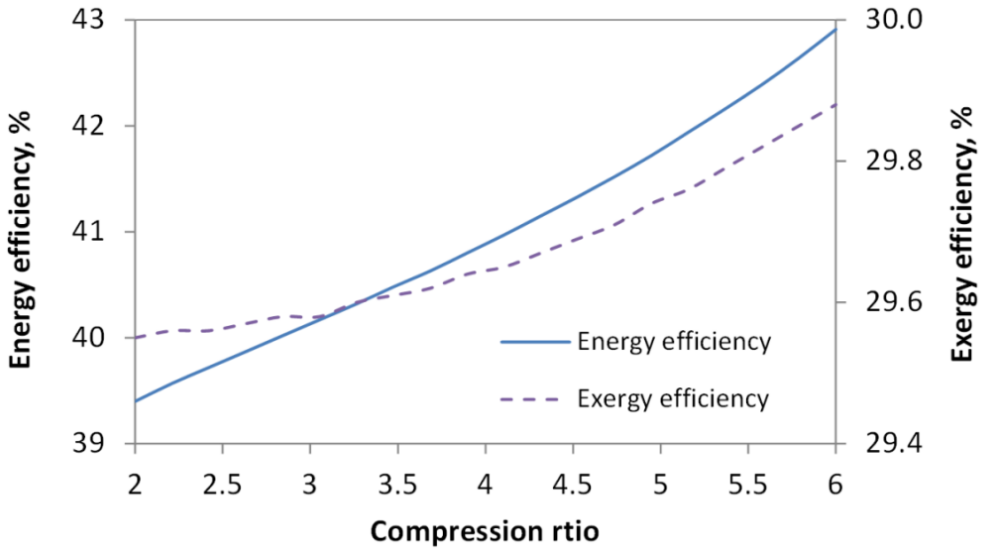

Figure 5.8 Effect of the gas turbine compression ratio on the on the system performance for 24-hours performance

Figure 5.10 shows the cost rate and emissions rate for the overall system 24-hour performance, at different compression ratios. The cost rate is found to be increasing in significantly from 856 to 1120$/h for the tested pressure ratio values. For the same net power output of the system, increasing the compression ratio would require a larger gas turbine to provide the power required for the compression. Also larger heat exchanger, especially the intercooler, would be resulting in the cost rate increase. Carbon dioxide emissions decrease by 48.6 g/kWh of useful output. The exergetic performance of the

absorption chiller cycle is also shown where it gradually decreases from the compression ratio. This is mainly cause of the available energy provided at the intercooler.

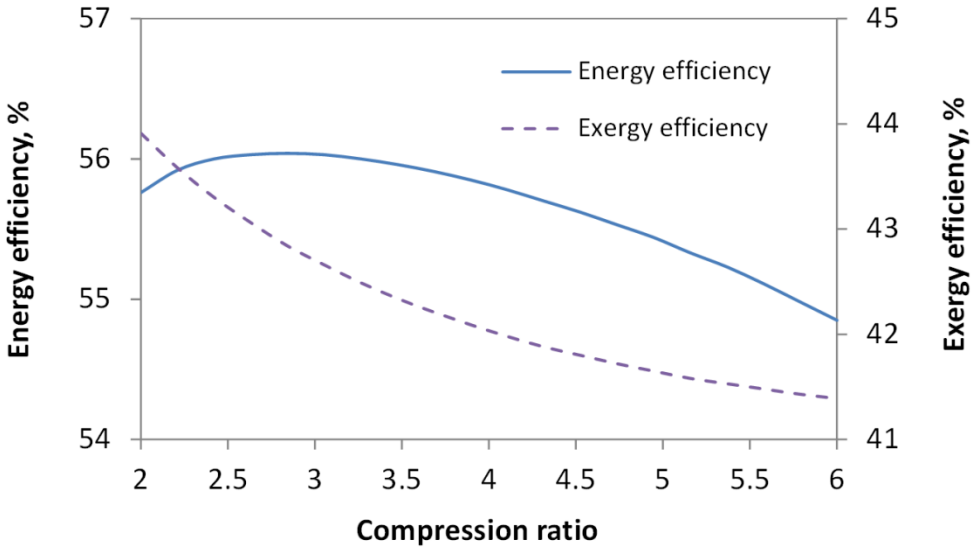

Figure 5.9 Effect of the gas turbine compression ratio on the on the system performance during solar radiation availability (Solar On mode)

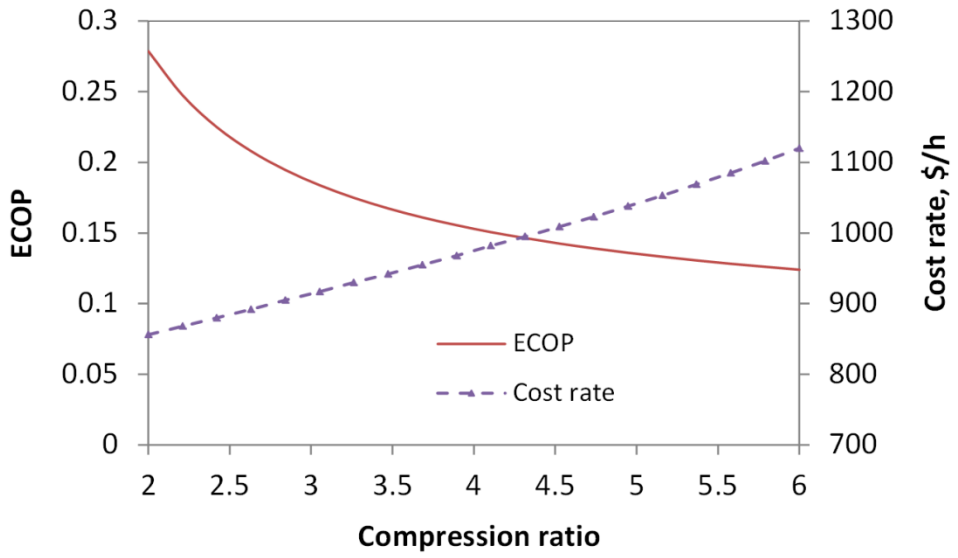

Figure 5.10 Effect of compression ratio of the gas turbine engine on the cost rate and the exergetic COPs for 24-hour performance

The gasification temperature is an important parameter that affects the performance of the proposed system. Changing the gasification temperature affects the composition of the produced syngas and the accompanied exergy rate. It also affects the number of fuel cell stacks required to cover the required output power. The temperature of gasification is varied in reasonable operating range and parametric studies are performed to investigate the effect of gasification temperature on the system performance.

The overall day performance considering both operation with solar availability and gasification driven system, it is found that increasing the gasification efficiency causes a linear reduction in the energy efficiency from 41.61% to 35.49% and the exergy efficiency from 30% to 28.43%. Figure 5.12 shows the effect of gasification temperature on the performance of the system during Solar Off mode. During this mode, the steam gasification process is mainly providing syngas to the SOFC for covering the required power. The energy efficiency is reduced from almost 29% to 23.32% when the exergy efficiency is reduced from 17.28% to 16.7%. During solar availability, the effect of the gasification temperature on the energy and exergy efficiencies is discussed in Figure 5.13. Increasing the gasification temperature causes a reduction in the hydrogen yield, which is a main parameter in the efficiency calculation during solar availability period.

The optimization is performed based on the evolutionary genetic algorithm. The main objective of the optimization analysis of the proposed system is to maximize the overall exergy efficiency with minimizing the cost rate. The decision variables selected in the performed study are shown in Table 5.2. They are selected as follows; gas turbine compression ratio, varying between 1.5 and 4, turbine inlet temperature, which is set to vary from 700 to 950K, gasification temperature, set to vary between 700 to 850°C, turbine polytropic efficiency from 80 to 92%, compressors polytropic efficiency from 70% to 95%, regenerative and precooler overall heat transfer coefficient, set from 1.5 to 4 kW/m^{2}K., the regenerator effectiveness set 88 to 93% and the evaporator temperature set from 2 to 7°C. The objective functions considered for the optimization analysis of this system are written as follows:

$$\eta_{ex} = \frac{\dot{W} + \dot{Ex}_{Cooling} + \dot{Ex}_{H_2}}{S.\dot{Ex}_{solar} + O.\dot{Ex}_{biomass}} \quad (5.1)$$

where S and O are the number of hours of operation of each energy source, as ratio of the total number of daily operating hours.

$$\dot{C}_{total} = \sum \dot{C}_{sys} + \dot{C}_f + \dot{C}_{env} \quad (5.2)$$

Table 5.2 Decision variables for the optimization analysis

Parameter	**Value**
Gas turbine compression ratio	1.5 – 4
Turbine inlet temperature, K	700 – 950
Turbine polytropic efficiency, %	80 – 92
Compressor polytropic efficiency, %	70 – 95
Regenerator effectiveness, %	88 – 93
Heat exchangers heat transfer coeff., kW/m^{2}K	1.5 – 4
Gasification temperature, ^{o}C	700 – 850
Evaporator temperature, ^{o}C	2 – 7

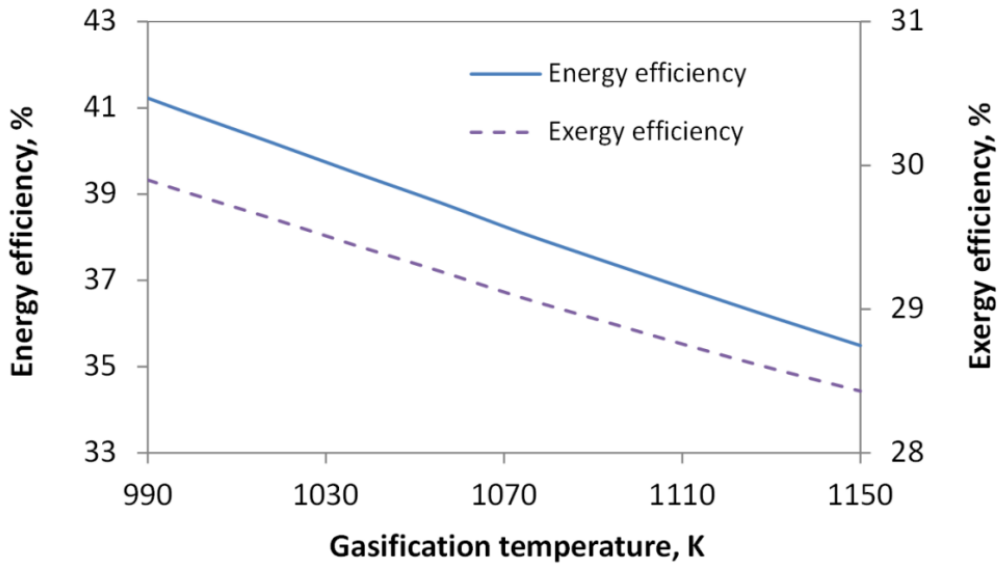

Figure 5.11 Effect of gasification temperature on the overall system performance for 24-hours performance

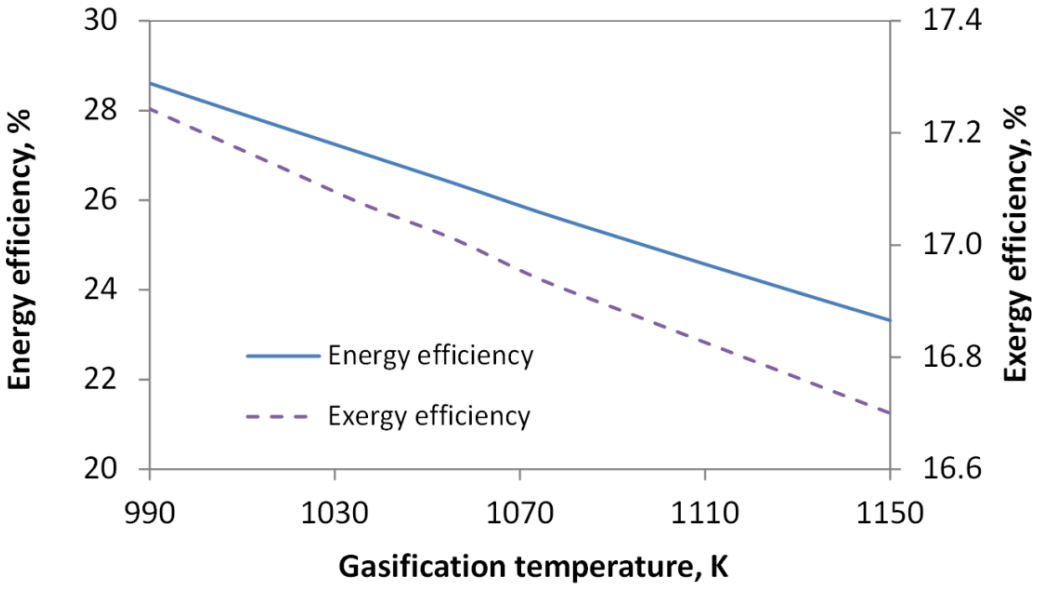

Figure 5.12 Effect of gasification temperature on the system performance (Solar Off mode)

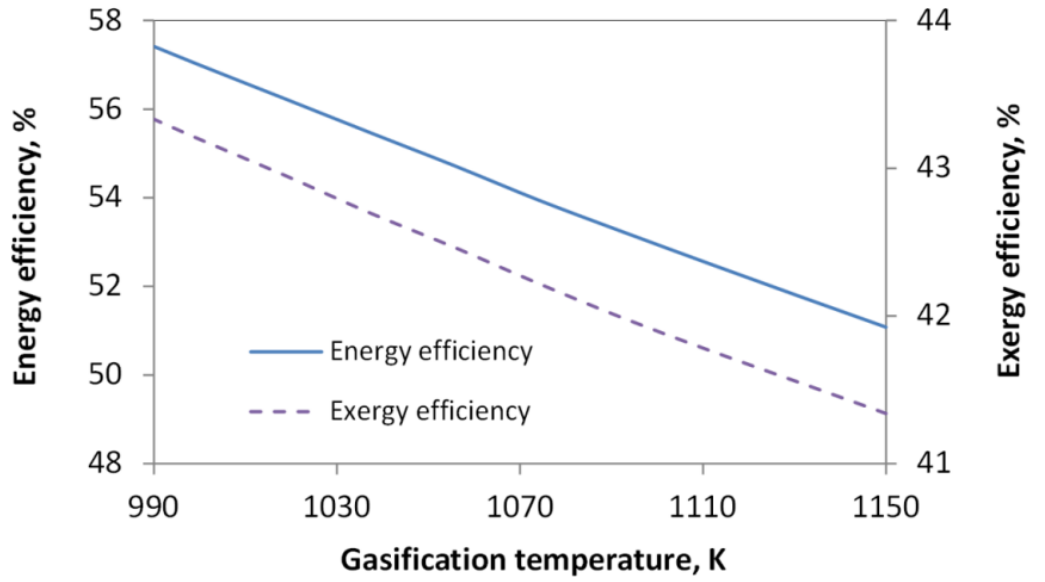

Figure 5.13 Efficiency of the integrated system during solar availability (Solar On mode) at different gasification temperatures

The genetic algorithm is performed for 250 generations, using population of 100 and mutation of 0.084. Figure 5.14 shows the Pareto frontier solution of the optimization results. The curve shows the best rank of combinations of high exergy efficiency with low

total cost rate for the system design and operation. All points on the shown curve are considered as optimum solution. The high ends of the curve represent two points that will not be of interest to be considered for the system design. Point A is selected, as shown on the Pareto optimum curve and the system analyses results representing the main system output are listed in Table 5.3. This point is assumed to be selected as the desirable final solution. Figure 5.15 and Figure 5.16 show the scattered distribution of the design parameters that were considered as the decision variables during the optimization process.

Table 5.3 System output at the optimized point A

Parameter	Value
Overall exergy efficiency	29.57%
Total cost rate	884.5 $/h
Environmental cost rate	57.64 $/h
Overall energy efficiency	39.99%
Solar On energy efficiency	56.04%
Solar Off energy efficiency	27.47%
Solar On exergy efficiency	42.88%
Solar Off exergy efficiency	17.12%
Solar concentration ratio	225
Number of solar dish concentrators	11
COP	0.7788
ECOP	0.197
Evaporator cooling load	430 kW
Biomass mass flow rate	0.4496 kg/s
Hydrogen yield	78.7 g/kg of dry biomass
SOFC cell voltage	0.695 V
Number of SOFC stacks	378

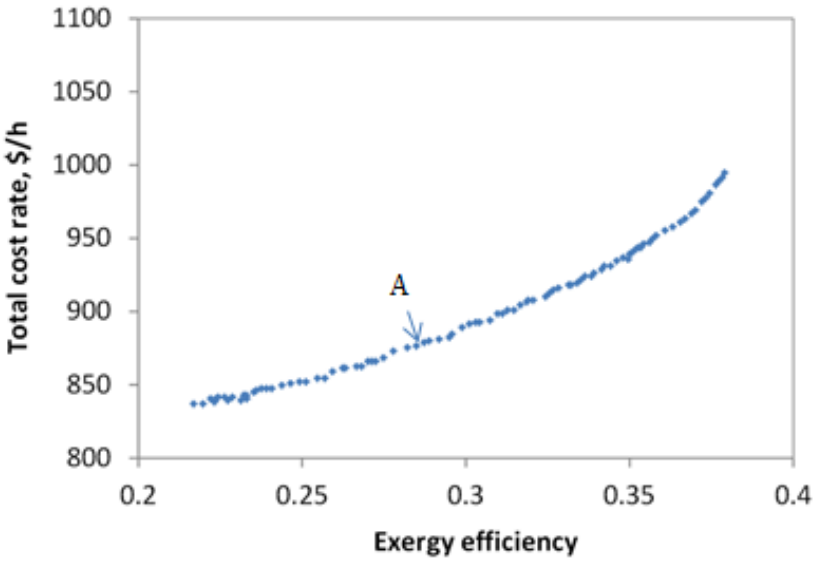

Figure 5.14 Pareto frontier for the best trade off values

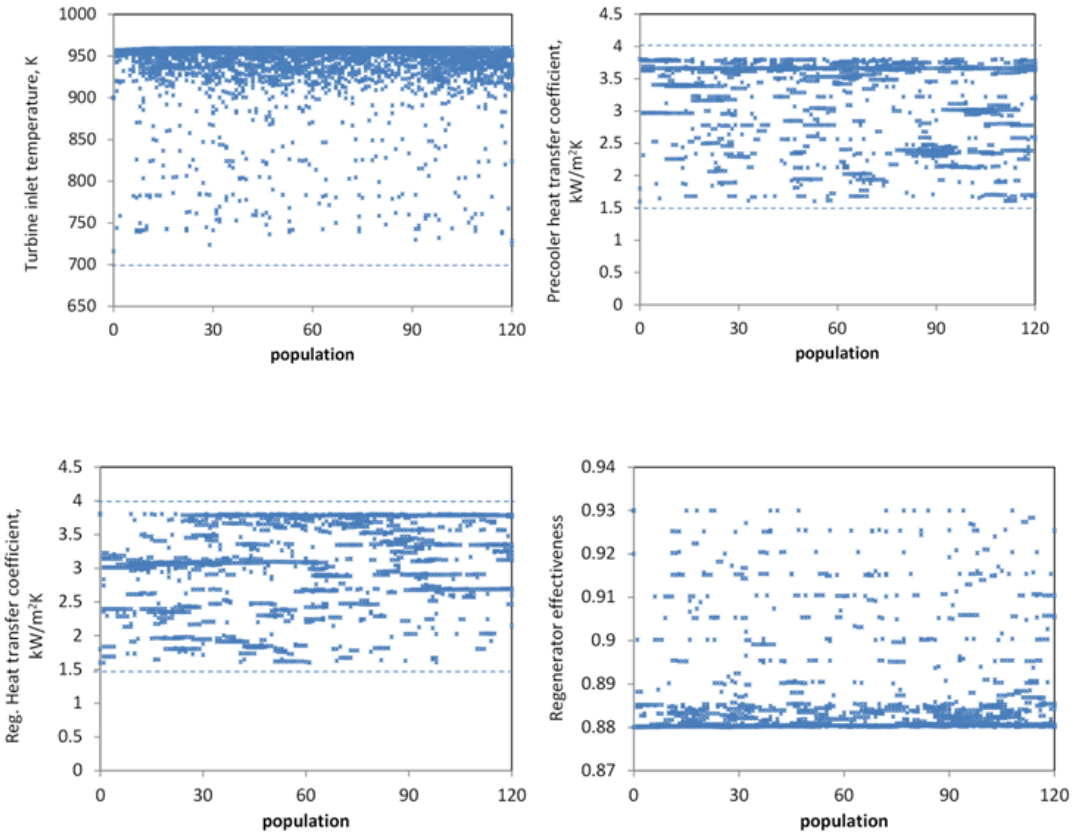

Figure 5.15 Scattered distribution of the optimization decision variables

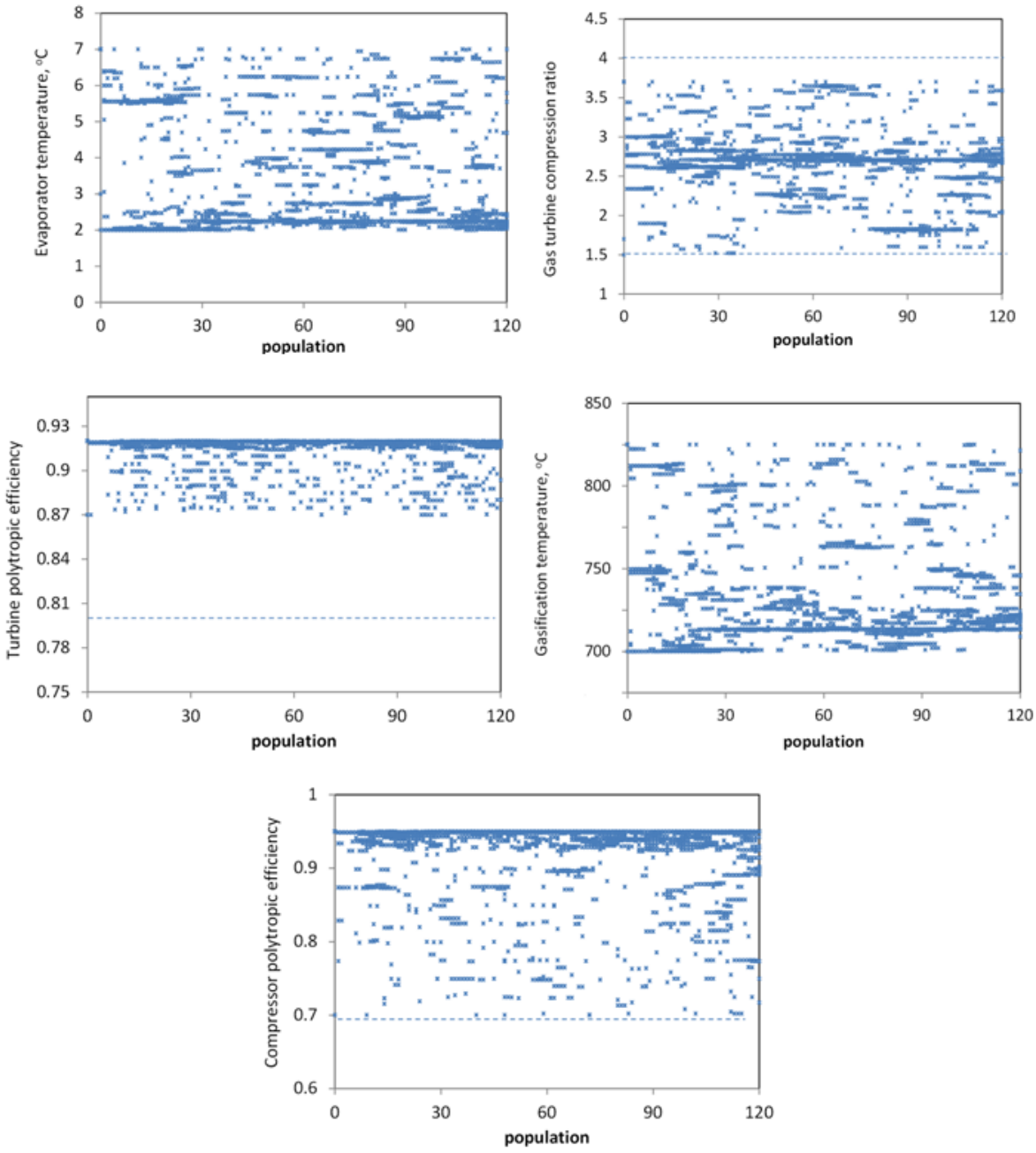

Figure 5.16 Scattered distribution of the optimization decision variables

Solar Dish Analysis

The exergetic performance of the solar dish analysis is measured mainly by the exergy efficiency. In Figure 5.17, the exergy efficiency is found to increase with the solar parabolic dish concentration ratio when all other parameters are kept constant. The results

reflect an increase in the efficiency with increasing the dish radius. The figure also shows the effect of increasing the receiver temperature on the exergy efficiency of the solar dish. The exergy efficiency is calculated based on the exergy losses and exergy destructions occurring in the solar dish.

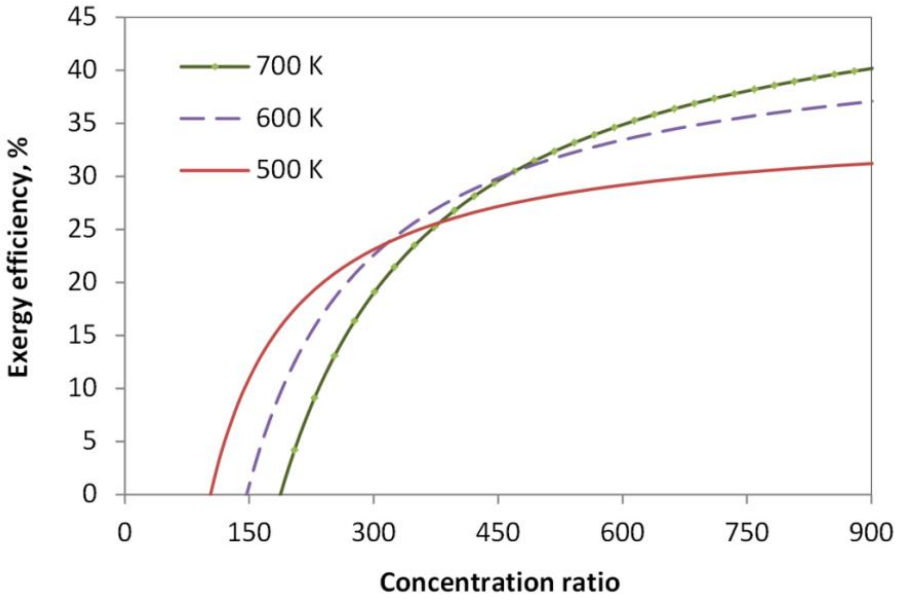

Figure 5.17 Effect of concentratio ratio of the solar dish on the exergy efficiency of the dish

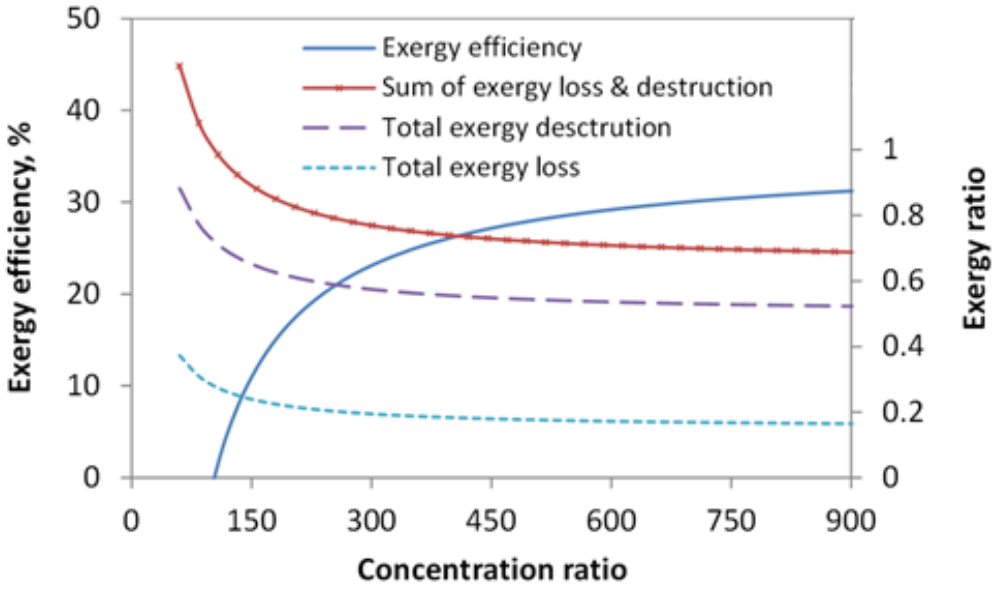

Figure 5.18 Exergetic performance of the solar dish with concentration ratio

Figure 5.18 shows the variation of the exergy losses and destructions as ratio of the exergy of the input solar radiation. The results presented at receiver temperature of 500K and it also shows the exergy efficiency at the corresponding temperature.

The effect of the receiver temperature on the solar dish exergetic performance is presented in Figure 5.19. The performance is measured with respect to the exergy efficiency as well as the exergy losses presented as ratio of the solar exergy input. All other values of the solar dish parameters are kept constant. It can be seen that the exergy efficiency increases with the receiver temperature until it reaches an optimum value and then starts decreasing.

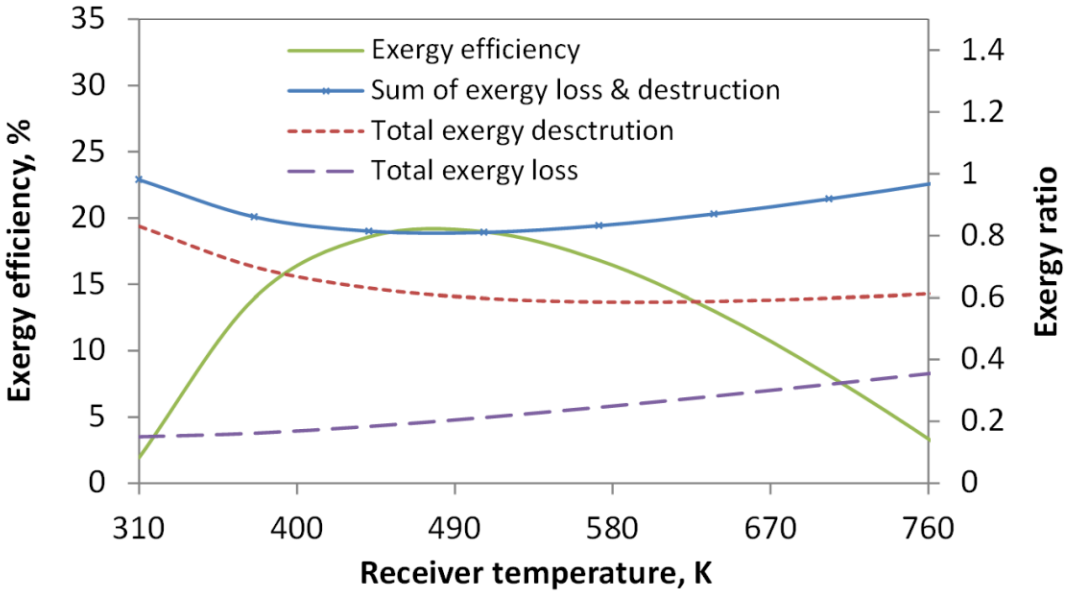

Figure 5.19 Exergetic performance of the solar dish at different recevier temperatures

In Figure 5.20, both exergy losses and exergy destructions of the solar dish are presented. The results show that increasing the receiver temperature causes a reduction in the absorption destruction and slight reduction in the exergy loss due to pressure loss. The optical exergy loss is not a function of receiver temperature. The exergy destruction with conduction and leakage increases slightly, but still at values lower than the other elements of exergy destruction.

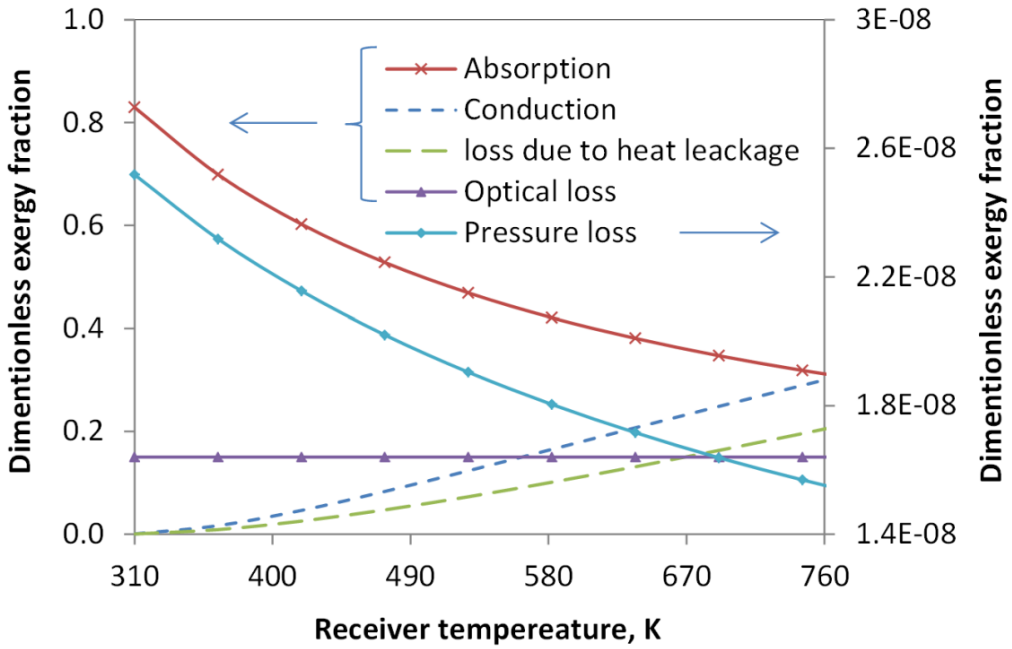

Figure 5.20 Solar dish exergy losses and exergy destruction items at different receiver temperatures

Absorption Chiller System

The model of the absorption chiller system is compared with data from the literature, from Gong et al. (2004), as shown in Figure 5.22. This figure shows the different components energy values as well as the COP of the system. The system is performing at regenerator temperature of 80°C, evaporator temperature of 2°C. The validation is made for 10 kW of evaporative cooling. The values of the heat to the absorber are calculated as 12.76 kW and 13.68 kW, for the desorber as 13.2 kW and 14.14 kW, for the condenser as 11.36 kW and 10.46 kW, for the current model and the reference model, respectively. The system COP is calculated as 0.757 when the reference model presented 0.707. The system is also validated through the exergy destruction rates through the system components as well as the exergetic COP, as shown in Figure 5.22.

The absorption chiller performance is measured through COP and exergetic COP at different operating parameters. The results in Figure 5.23 show change of the absorption chiller performance at different heat source temperature values. It can be seen that a maximum of exergetic COP is achieved at about 0.214 at source temperature of

90°C then the performance drops, when the energetic COP shows a rapid increase up to 93.3°C and then slightly increase over the span of tested temperature values.

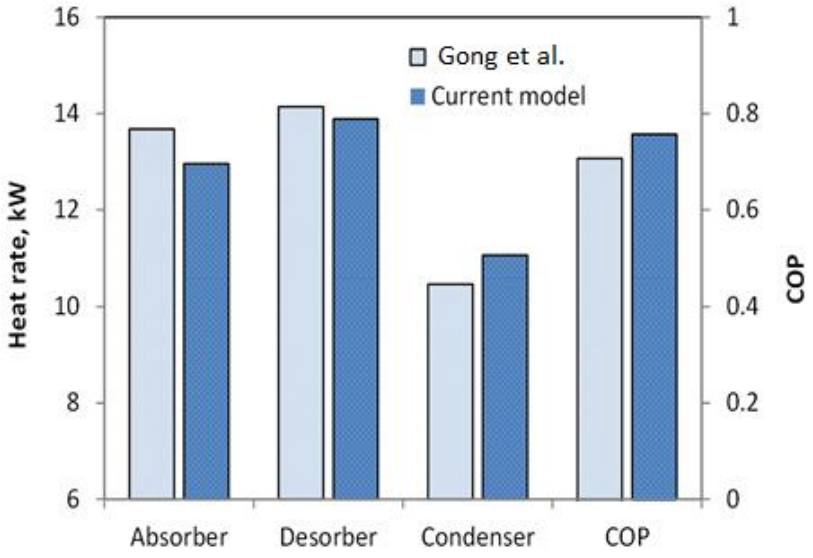

Figure 5.21 Comparison of the energy model with data provided in Gong et al.(2014)

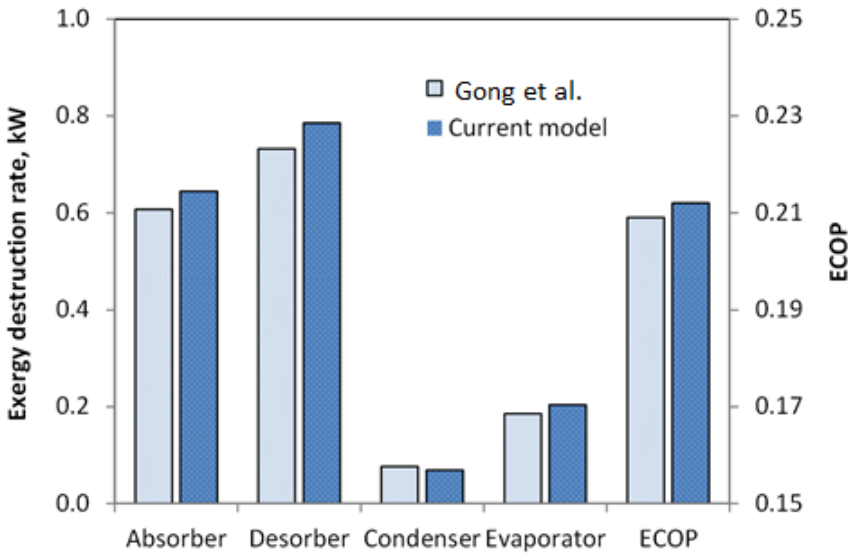

Figure 5.22 Comparison of exergy model results with Gong et al.(2014)

The effects of varying the heat sink temperature on the absorption chiller performance are shown in Figure 5.24. Increasing the sink temperature causes a reduction

in the system performance as shown in both energetic and exergetic COP values. The evaporator inlet temperature is varied to test its effect on the system performance. The results are shown in Figure 5.25.

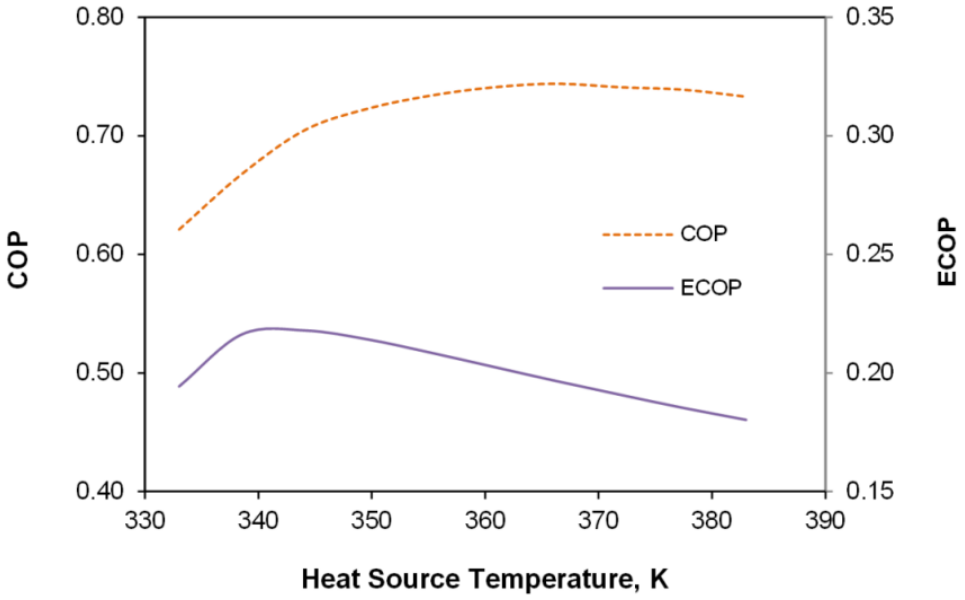

Figure 5.23 Effect of heat source temperature on the system performance

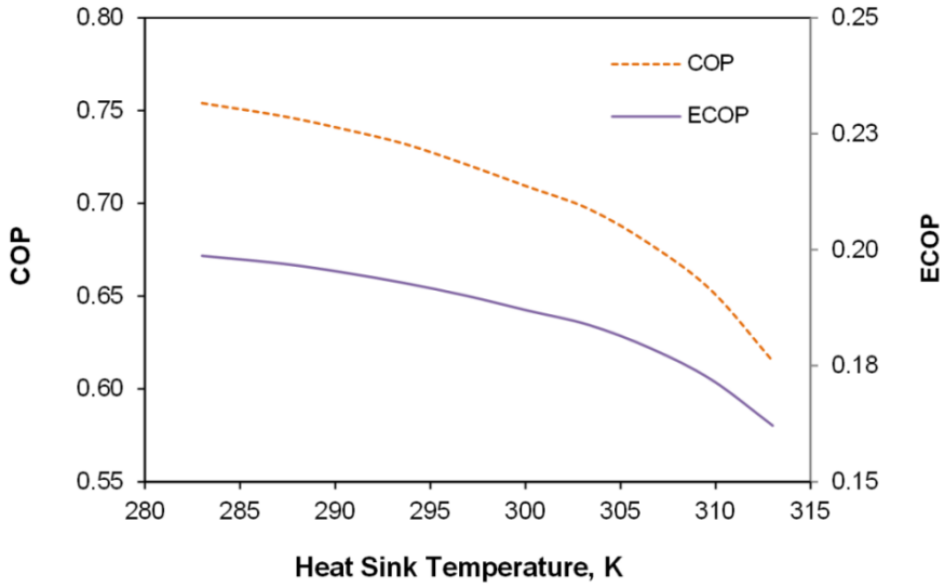

Figure 5.24 Effect of varying the sink temperature on the system performance

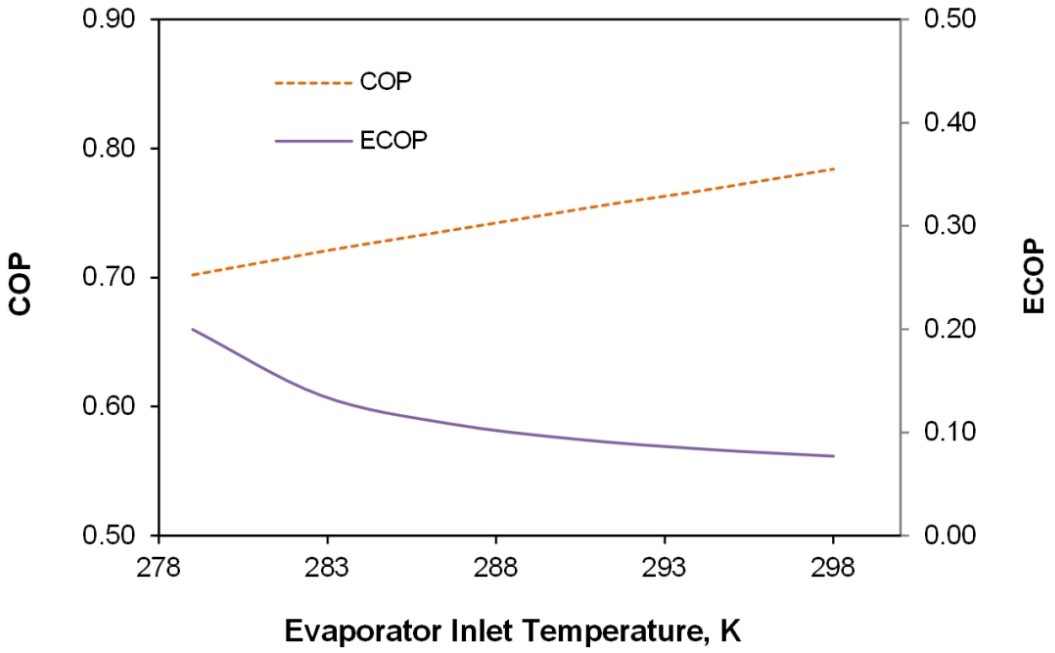

Figure 5.25 Performance variation with evaporator inlet temperature

Solid Oxide Fuel Cell model

The model of the direct internal reforming cell considered in the current study is compared with the results of the model introduced by Colpan et al. (2007) and the validated with the experimental results reported by Tao et al. (2005) as shown in Figure 5.26. The results presented here are representing the performance evaluation based on current density versus voltage and power and based on cell efficiency at different SOFC operating parameters. Effects of recirculation ratio and fuel utilization factor are tested and the results have the same trend of the ones reported in the literature. Recirculation of fuel is important in this kind of fuel cell as it helps initiating the steam reforming and waster-gas shift reaction as reported by Colpan et al. (2007). Figure 5.27 and Figure 5.28 demonstrate the effect of recirculation ratio on the cell output parameters. Figure 5.27 shows cell voltage and cell produced power with current density at different recirculation ratio values. At low current density values, the increase in recirculation ratio does not affect the cell performance significantly, as it can be also seen from the results in Figure 5.28 with regards to the cell efficiency as well. However, this is accompanied with a reduction in the fuel needed and in the air utilization ratio; hence, higher air flow rate

would be needed. Cell voltage, power and efficiency drop with the increase of recirculation ratio at higher current density values.

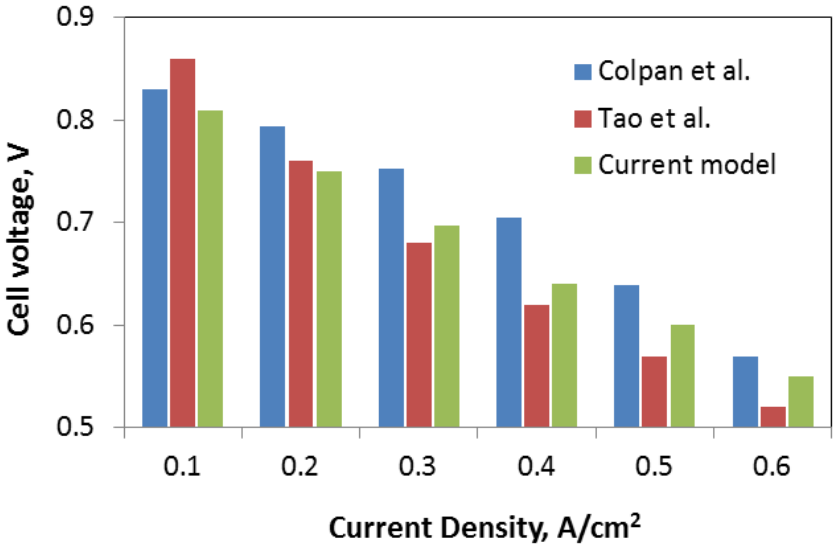

Figure 5.26 Validation of the DIR-SOFC model with Colpan et al. (2007) and Tao et al. (2005)

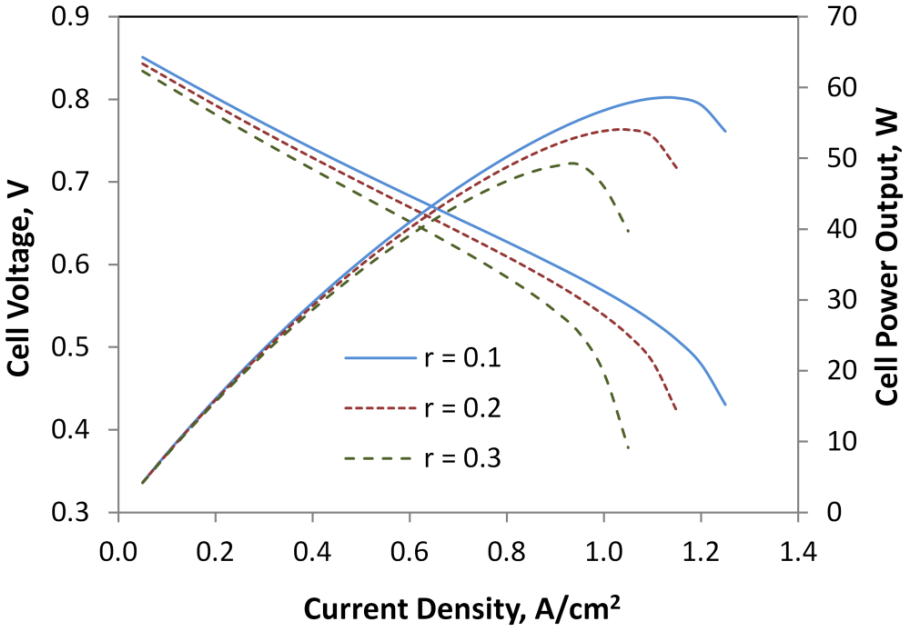

Figure 5.27 SOFC performance at different recirculation ratios

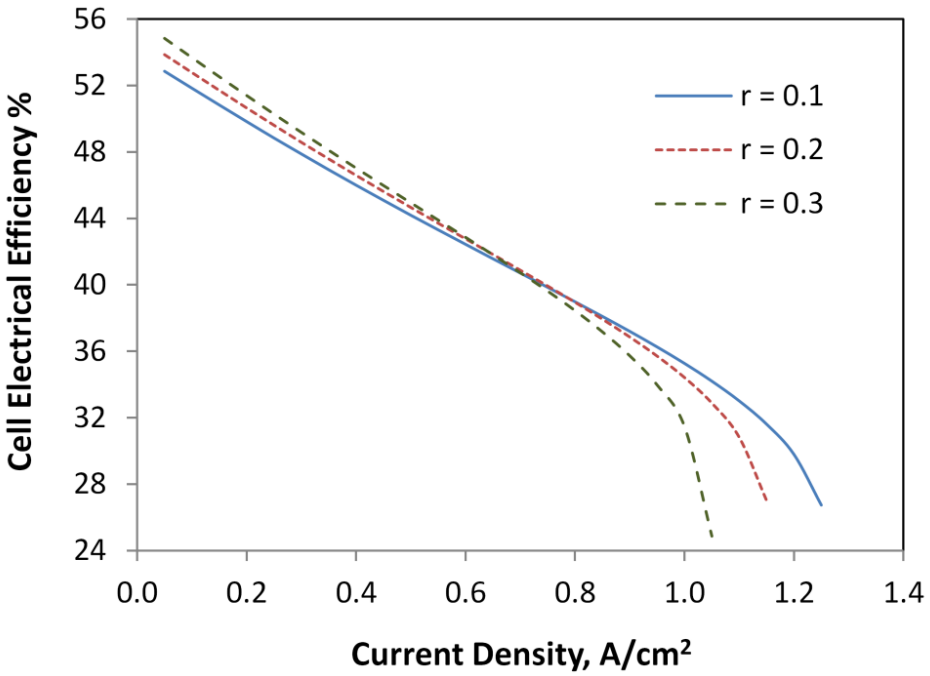

Figure 5.28 SOFC efficiency at different recirculation ratios

The results in Figures 5.29 and 5.30 show the effect of fuel utilization on the performance of the modeled cell. Figure 5.29 shows the cell output voltage and power versus current density at different fuel utilization ratios. It can be seen that increasing the fuel utilization ratio results in a reduction in the cell output parameters. In Figure 5.30, significant effect on cell efficiency is noticed with varying fuel utilization factor, compared with effect of recirculation ratio. Lower fuel utilization factor provides a wider range of operating current density. At low current density values, higher efficiency is achieved at higher fuel utilization factor values.

Biomass Gasification-SOFC

In this section, both biomass gasification and direct internal reforming SOFC subsystem are assessed through thermodynamic efficiencies, energetically and exergetically. In the gasification process, steam is considered as a drying and gasification medium. The effects of changing the operating parameters on system performance are investigated through parametric studies.

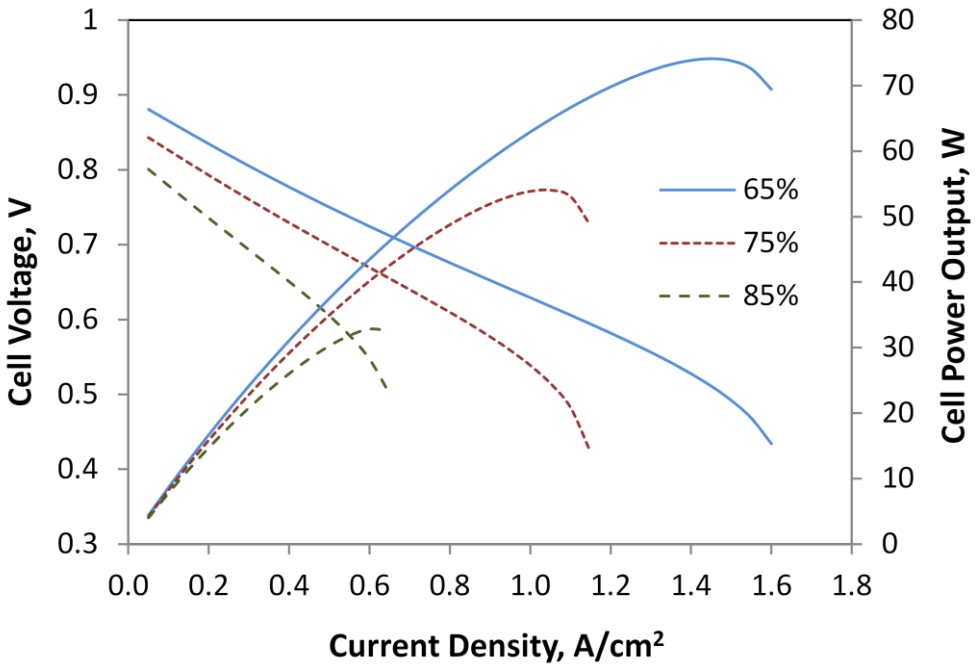

Figure 5.29 SOFC performance at different fuel utilization ratios

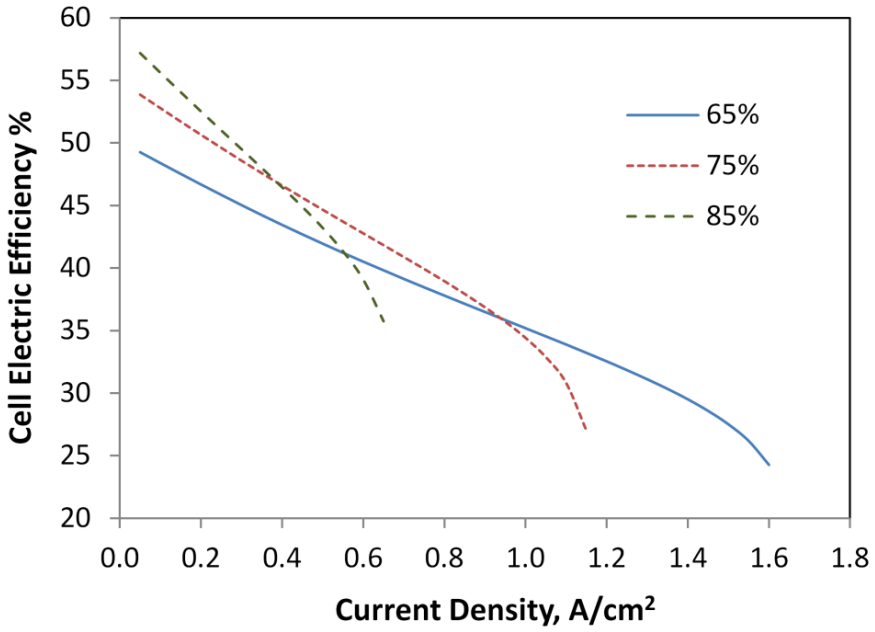

Figure 5.30 SOFC efficiency at different fuel utilization ratios

The results of the presented thermodynamic analyses of the subsystem of steam gasification and SOFC are presented and discussed in this section. The effects of different

operating parameters on the gasifier and the fuel cell performances are investigated. The results with respect to the integrated system are concluded in studying the system efficiency as shown in Table 5.4. The performance of gasification process is investigated through applying parametric studies on the proposed model. The effect of steam biomass ratio on the performance considering gasification for hydrogen production and the gasification process are studied. The performance is described in terms of energy and exergy efficiencies.

Table 5.4 Efficiency assessment of the system and system sub-processes

SB	$\eta_{H_2}^{en}$	$\eta_{H_2}^{ex}$	η_{Gasif}^{en}	η_{Gasif}^{ex}	η_{SOFC}^{en}	η_{SOFC}^{ex}	η_{Sys}^{en}	η_{Sys}^{ex}
0.7	47.10%	38.54%	75.97%	58.36%	46.90%	36.73%	54.74%	45.21%
1.2	50.09%	37.16%	72.72%	52.20%	47.15%	37.45%	55.31%	45.92%
2.0	51.50%	35.02%	67.93%	45.11%	47.85%	39.12%	55.92%	47.42%

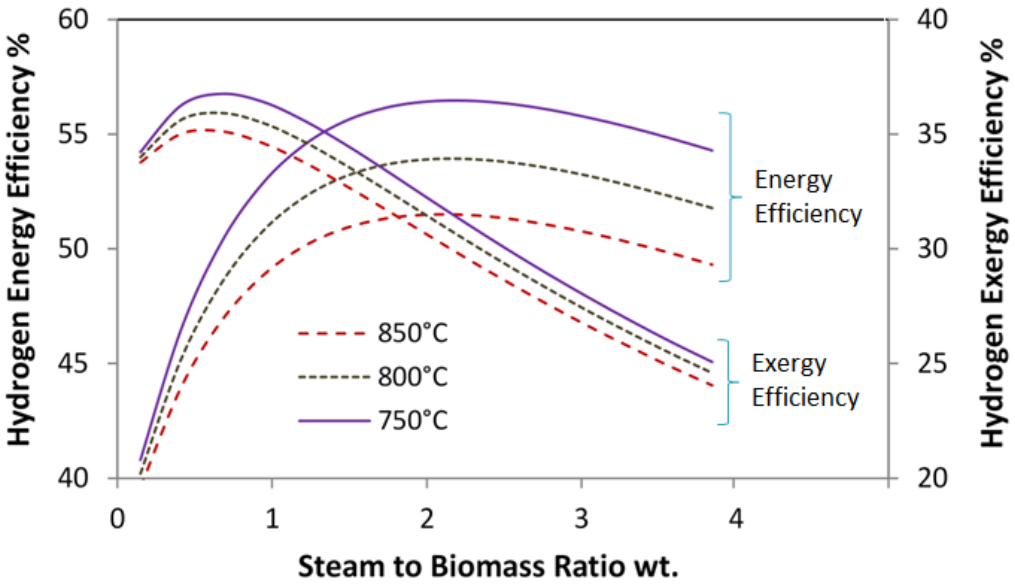

Figure 5.31 Effect of SB ratio on hydrogen efficiency at different gasification temperatures

Figures 5.31 and 5.32 show the hydrogen efficiency and the gasification process efficiency with performing the gasification at different temperature values of the biomass gasification process. The results in Figure 5.31 show that efficiency decreases with the increase in the gasification temperature. At each operating temperature of the gasifier, energy efficiency increases with the steam to biomass ratio till it reach a maximum at the

steam biomass ratio of 2.2 with maximum efficiency of 56.46, 53.50 and 51.48% at 750, 800 and 850°C, respectively. The exergy efficiency of hydrogen shows similar trend of performance. However, the maximum values of exergy efficiency occur at lower values of steam to biomass ratios at 0.670, 0.677 and 0.69 SB ratios for 750, 800 and 850°C, respectively. Maximum exergy efficiency values, for each corresponding case, can be recorded as 36.76, 35.92 and 35.12%, respectively. The performance of the hydrogen measured in exergy efficiency deteriorates at SB values higher than 1.7, 1.4 and 1.2 for 750, 800 and 850°C cases, respectively, which is not the case for energy efficiency. The results in Figure 5.32 show the effect of SB ratio on the efficiency of the gasification process at different gasification temperature. The increase of gasification temperature causes a reduction in the both gasification energy and exergy efficiency.

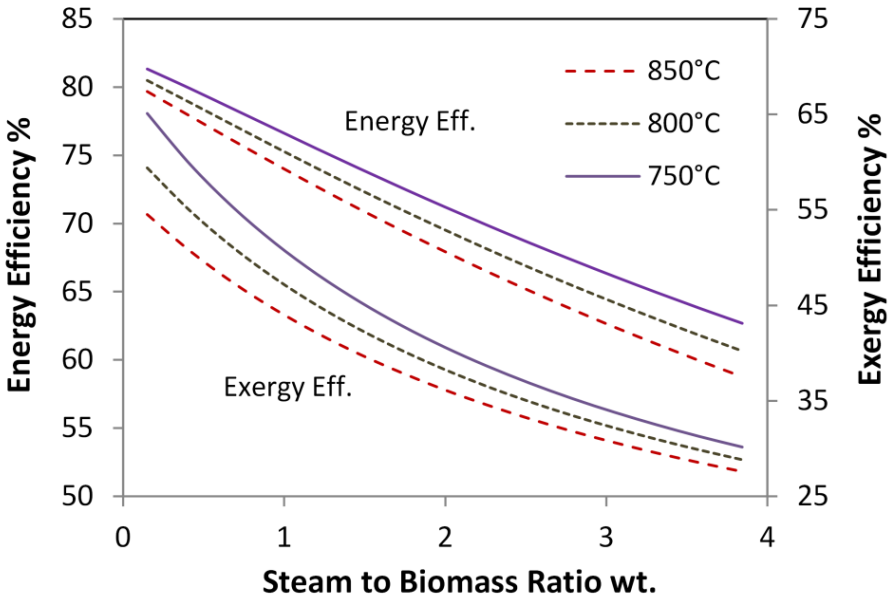

Figure 5.32 Effect of SB ratio on gasification efficiency at different gasification temperatures

The effects of changing moisture content of the biomass fed to the gasifier after being dried are studied at different SB ratios as shown in Figures 5.33 and 5.34. Hydrogen energy and exergy efficiency values, as shown in Figure 5.33, increases with the increase of the moisture contact of the biomass during the gasification process. The effect of increasing the SB ratio on the energy efficiency deteriorates after certain value. However, it highly affects the exergy efficiency negatively. The maximum exergy

efficiency values of 30.82, 35.12 and 40.2% are achieved at 0.70, 0.677 and 0.42 of SB values for moisture contents of 10, 20 and 30%, respectively. The effect on the gasification energy and exergy efficiency is similar to the effect of decreasing the gasification temperature as shown in Figure 5.34.

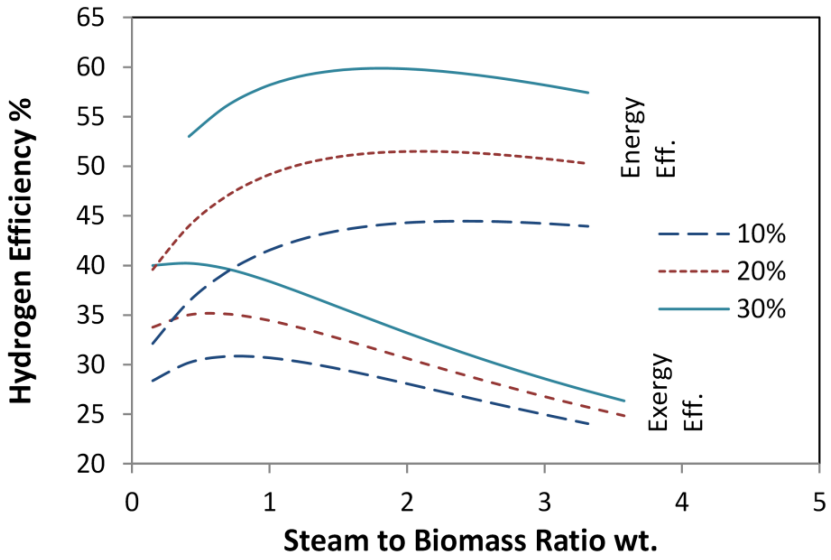

Figure 5.33 Effect of SB ratio on hydrogen efficiency at different moisture contents

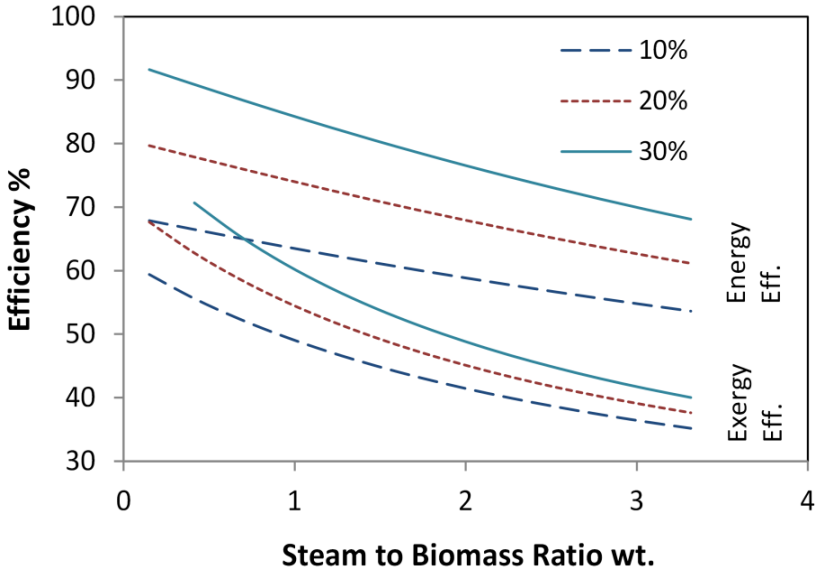

Figure 5.34 Effect of SB ratio on gasification efficiency at different moisture contents

The results shown in Figure 5.35 show the molar percentage of the gas species produced from the gasification process, operating at base case conditions with varying the SB ratio. The values are represented in dry condition. From reported results, an increase of SB ratio results in a shift in product gas equilibrium towards the production of hydrogen. However, this results in a lower heating value of the produced gas.

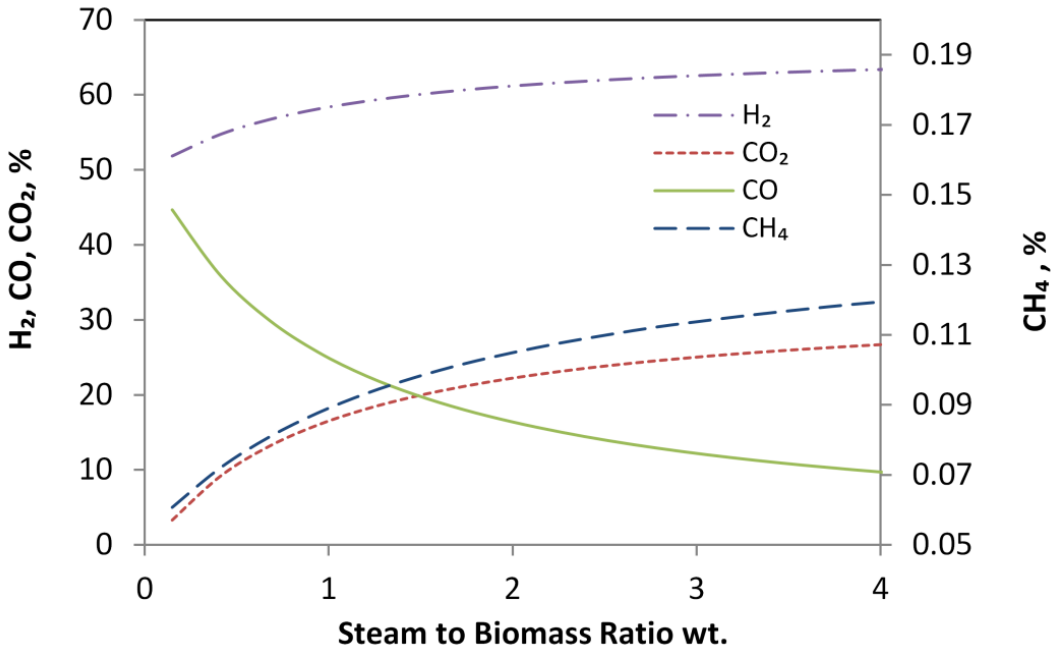

Figure 5.35 Effect of SB ratio on product gas species concentrations dry basis

Figure 5.36 shows the effect of changing the gasification temperature over the integrated system energy and exergy efficiency. The energy efficiency increases from 55.49 to 58.01% with changing the gasification temperature from 700 to 800^{o}C. Exergy efficiency also increases from 45.64 to 46.89% over the same temperature range. This is considering the less amount of extra heat utilized in producing process steam where most of the heat of the combustion gases are used towards the gasifier. The produced process steam is calculated as 356, 230.4 and 165.5 kg/h of steam at 350^{o}C and 3 bar, at 700, 750 and 800^{o}C of gasification temperature, respectively.

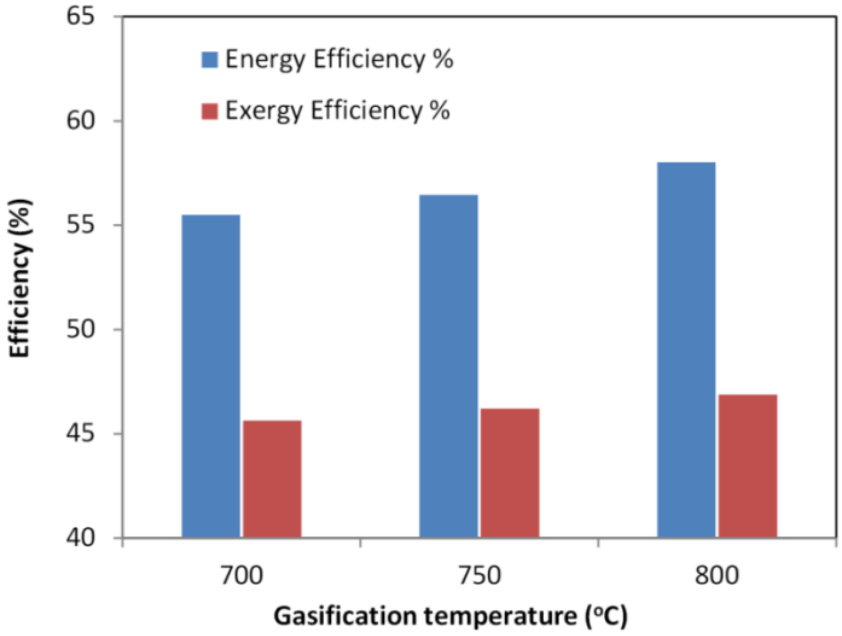

Figure 5.36 System performance assessment for the integrated system at different gasification temperatures

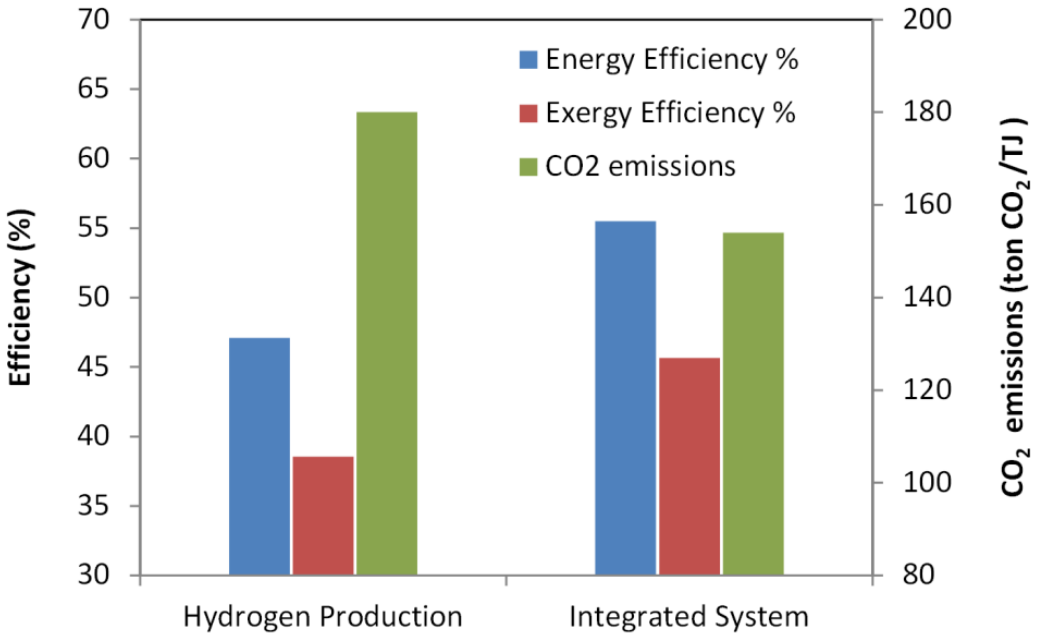

Figure 5.37 Efficiency and greenhouse gas emissions for hydrogen production and integrated system options for biomass gasification and SOFC subsystem

The two cases of considering steam gasification for hydrogen production and the integrated system are compared on the bases on energy and exergy efficiency values as shown in Figure 5.37. A greenhouse gas emission is also shown based on carbon dioxide emissions per unit of produced useful energy. The base cases are considered for the results presented accordingly. The carbon dioxide emission for steam gasification process is calculated as 180 ton of carbon dioxide per TJ of produced hydrogen energy. The results show also the energy and exergy efficiency values as 47.1 and 38.53%. For the integrated system, the exergy and energy efficiency increased compared with steam gasification without integrating the fuel cell. This is because of the produced power and the extra heat utilized to produce the process steam. However, The integrated system shows an increase of 8.39% and 7.1% in the energy and exergy efficiencies, also lower carbon dioxide emissions is achieved.

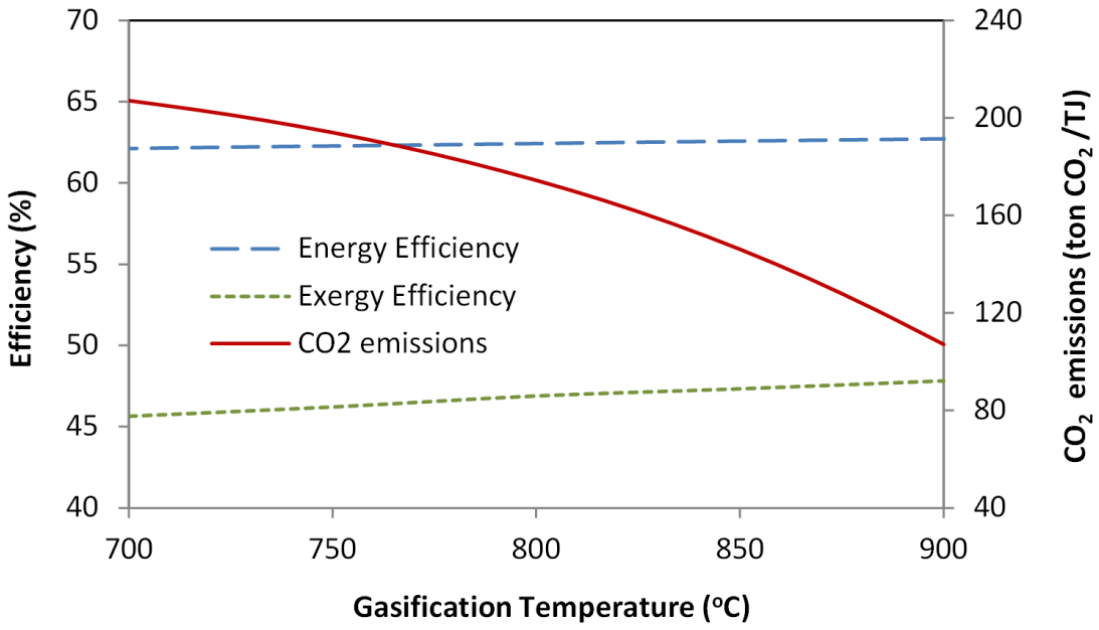

Figure 5.38 Integrated system performance at different gasification temperature values

The results in Figure 5.38 show the effect of varying the gasification temperature on the overall performance of the integrated system. The increase of gasification temperature causes an enhancement in the system energy and exergy efficiencies, which is accompanied with reduction in the carbon dioxide emissions per unit of energy produced. Figure 5.39 shows a comparison of the carbon dioxide emissions of the

integrated system proposed in the current study with results reported in the literature. The following studies are considered for the comparison: Carpentieri et al. (2005) studied integrated biomass gasification system with carbon dioxide removal and the emissions are calculated as 49.4 ton CO_2 per TJ of produced energy for his system. Mann and Spath (1997) reported a higher value of emissions, 254 ton CO_2 per TJ, for the conventional integrated biomass gasification combined cycle, Koroneos et al. (2008) investigated biomass gasification plant for hydrogen production and reported 140 ton CO_2 per unit energy produced. The results of Hosseini et al. (2013) shows emission of 205 ton CO_2/TJ of produced energy for integrated biomass gasification, SOFC and gas turbine system.

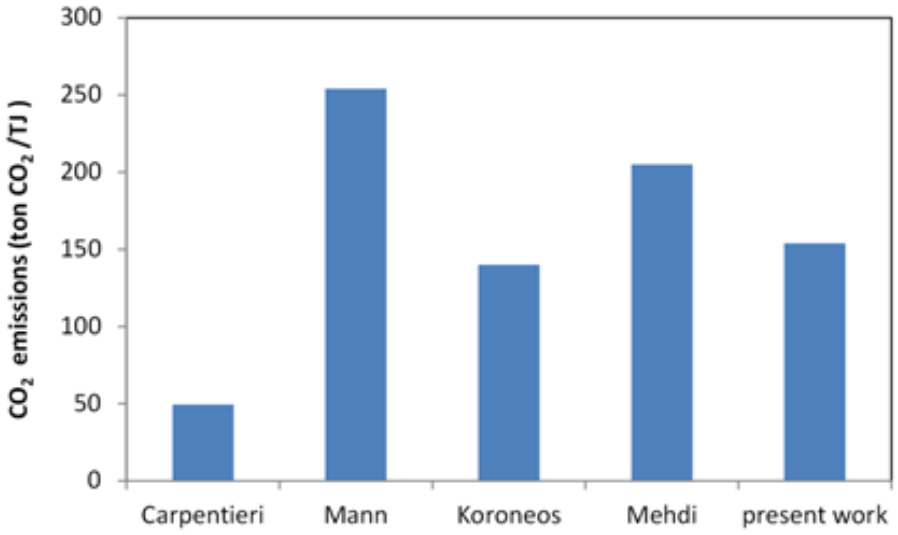

Figure 5.39 Comparison of CO_2 emissions of the present gasification SOFC with the results reported in the literature (Carpentieri et al., 2005; Mann and Spath, 1997; Koroneos et al., 2008; Hosseini et al., 2012)

In the following, the results of axial temperature and gas concentrations distribution through the gasifier are presented considering bubbling fluidized bed gasifier. The results also shows parametric studies to study the influence of different operating parameters like operating bed temperature, fluidization velocity, steam to biomass ratio, air equivalence ratio and bed material, on the gasification process. The model is validated in two different aspects as shown in Figure 5.40 and Table 5.5. The results of the temperature profile considering the combustion of rice straw pellets at 0.5 m/s of

fluidization velocity, a bed height of 3 m above distribution, and static bed height of 30 cm, is validated with data measurements and shows good agreement as shown in Figure 5.40. The bed temperature is 850^{o}C and excess air of 0.3 is considered in this case. Also gasification gas species concentrations are validated with the results reported in the literature. The results listed in Table 5.5 gives the validation of the fluidized bed gasification model with respect to the gas species concentrations at different gasification temperature as values. The results show good agreement with both cases of comparison.

Table 5.5 Fluidized bed model validation with Kaushal et al. (2010)

Composition of dry gas		Gasification Temperature				Error (RMS)
		700^{o}C	750^{o}C	800^{o}C	850^{o}C	
H_2 %	Model	41.7	43.9	45.9	48.2	1.6%
	Ref.	38.7	44.2	46.6	47.2	
CO %	Model	27.2	29.5	30.4	31.9	2.6%
	Ref.	25.1	26.4	27.9	29.4	
CO_2 %	Model	19.6	16.3	14.7	12.2	2.2%
	Ref.	16.2	14.1	12.8	12.1	
CH_4 %	Model	6.9	6.2	5.8	5.0	1.0%
	Ref.	8.4	6.2	4.9	3.9	

The effects of gasifier operating parameters on the axial temperature distribution of the fluidized bed gasifier are investigated. The results presented in Figures 5.41 to 5.43 show the axial temperature profile at values of operating parameters of the fluidized bed. The bed height in these figures is shown from the point after the bed zone where isothermal operation is considered for this zone. The bed temperature is taken as the base case condition of 800^{o}C for Figures 5.41 to 5.42. In Figure 5.43, the temperature is varied when all other operating parameters are kept at base case condition. The results shows that the temperature profile start with an increasing trend through 15% of the gasifier height where the freeboard zone exist. Temperature then starts to decease as a result of the endothermic reactions occurring through the bed height and the heat interaction with the surrounding environment. The overheat that occurs in all the represented curves demonstrates the effect of oxidation reaction and the position of this zone appears to be affected by the operating conditions Figure 5.41 demonstrates the effect of varying

fluidization velocity on the axial temperature profile through the gasifier height. Three values of fluidization velocity are considered as shown in the figure. At higher fluidization velocity, better mixing occurs which is expected to result in more uniform temperature through the splashing and freeboard zones. Overheat of 22.29, 42.5 and 68^{o}C occurs with increasing the velocity of fluidization through the indicated values. This results in higher output temperature as well for the gases leaving the fluidized bed.

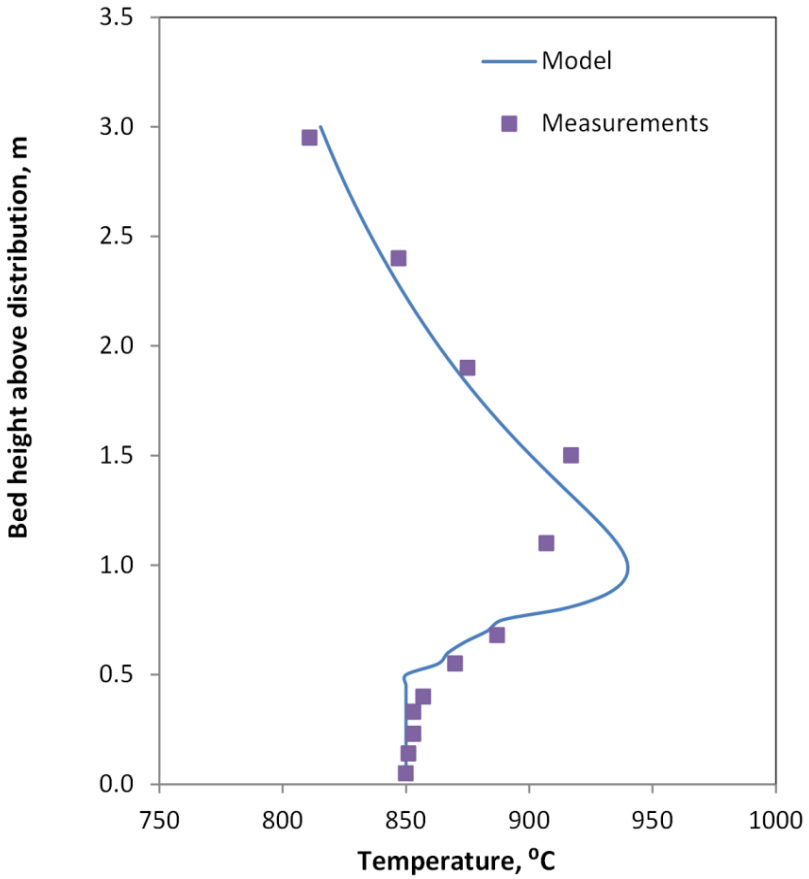

Figure 5.40 Validation of axial temperature profile with experimental measurements of Okasha et al. (2005)

Figure 5.42 demonstrates the influence of air equivalence ratio on the gases temperature profile through the fluidized bed gasifier. Fluidization velocity is kept constant at 1 m/s and temperature of the bed at 800^{o}C. Increasing air equivalence ratio cause the maximum temperature, representing the peak of oxidation period, to shift towards higher temperature value. This is caused by the excess oxygen flowing through

the gasifier. However, it can be seen that fluidization velocity has greater effect on the overheating temperature values, compared with the effect of equivalence ratio.

The results shown in Figure 5.43 represent the effect of changing bed temperature on the profile of axial temperature though the fluidized bed gasifier. Temperature values are varied with 50^{o}C above and under 800^{o}C which is the bed temperature at the base case. Other operating conditions are kept constant at 0.25 for equivalence ratio and 1 m/s for fluidization velocity. It appears that at lower temperature, the temperature levels are relatively high, through the freeboard zone, where some oxidation still occurs to some extent in this zone compared with higher bed temperature where oxidation happens right after the splashing zone and then the temperature tends to decrease with the effect of the endothermic reactions after that.

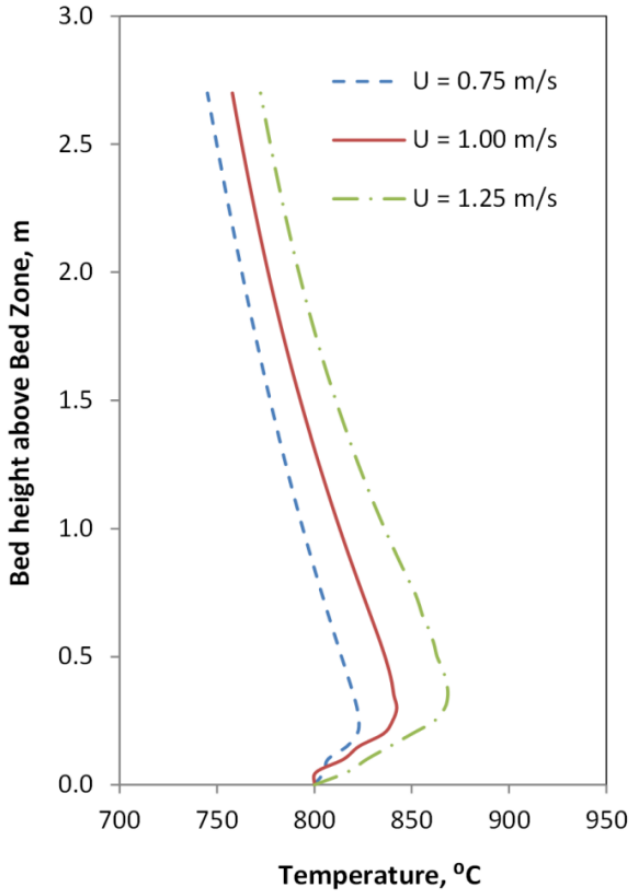

Figure 5.41 Temperature profile at different fluidization velocity values

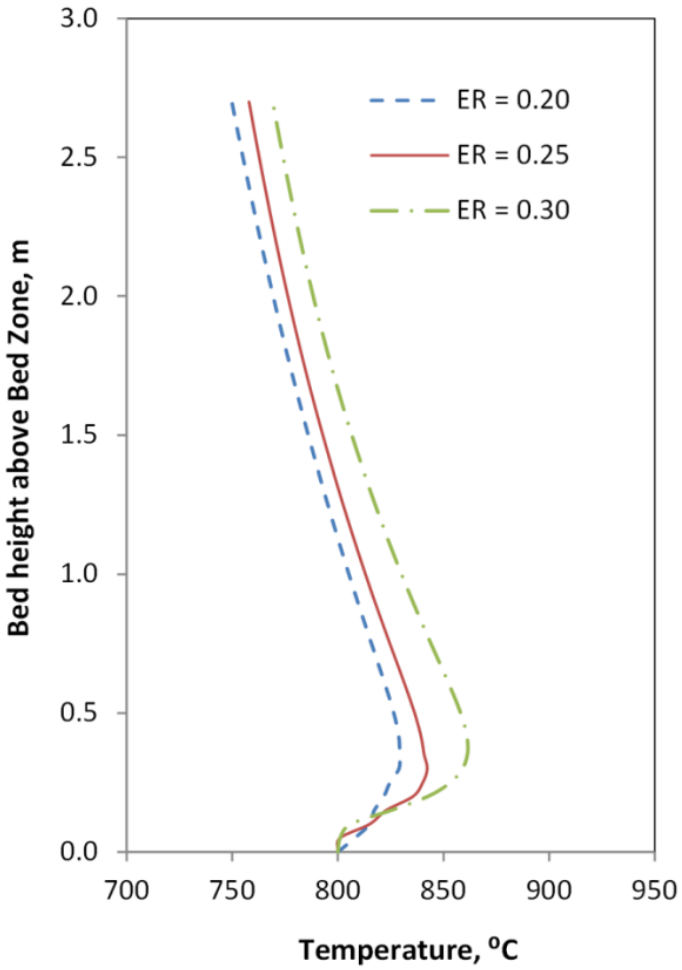

Figure 5.42 Temperature profile at different air equivalence ratios

Figure 5.44 shows the gas species concentrations, represented in molar concentration percentage, through the fluidized bed height. With the consumption of oxygen, it is noticed, as shown in the temperature profile figures, that an increase of temperature occurs with solid fuel oxidation reaction near the distributor zone. This is reflected on the composition of the gas at this zone where carbon dioxide has a peak of concentration and oxygen is consumed near the distributor. The produced gas compositions, for the base case, for the presented model are listed as follows, 18.9, 11.7, 13.53 and 4.6% of carbon dioxide, carbon monoxide, hydrogen and methane, respectively.

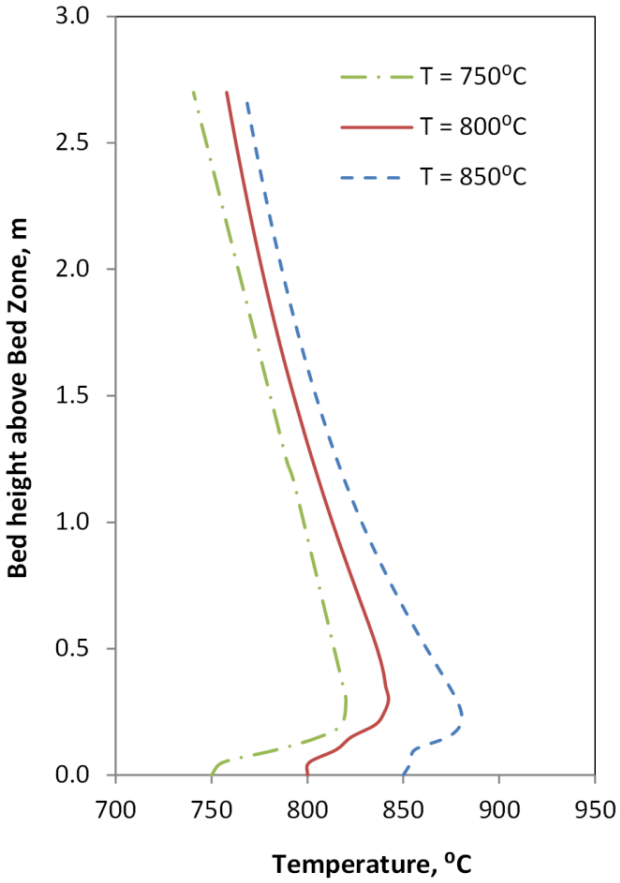

Figure 5.43 Temperature profile at different bed temperature values

Helium Gas Turbine

For verifying the modeling code of the helium gas turbine, the results for a case study are compared in the following section with data of a helium gas turbine operating with power reactor as presented in Conn and Kuo (1976). The turbine inlet conditions are 871^{o}C and 69 bar. The compressor inlet temperature and pressure are 43.3^{o}C at 26.2 bar. This gas turbine is of 500 MW power and operates at 46% of thermal efficiency. The adiabatic efficiency of the turbine and the high and low pressure compressors are 91, 89 and 89%, respectively. The effectiveness of the recuperator, intercooler and precooler are 88, 88 and 92%, respectively. Considering the same losses in the heat exchangers streams, Table 5.6 shows the comparison of the results of thermodynamic properties and parameters of the current model compared with the data provided in the literature. This model is presented and the results are published by El-Emam and Dincer (2014a).

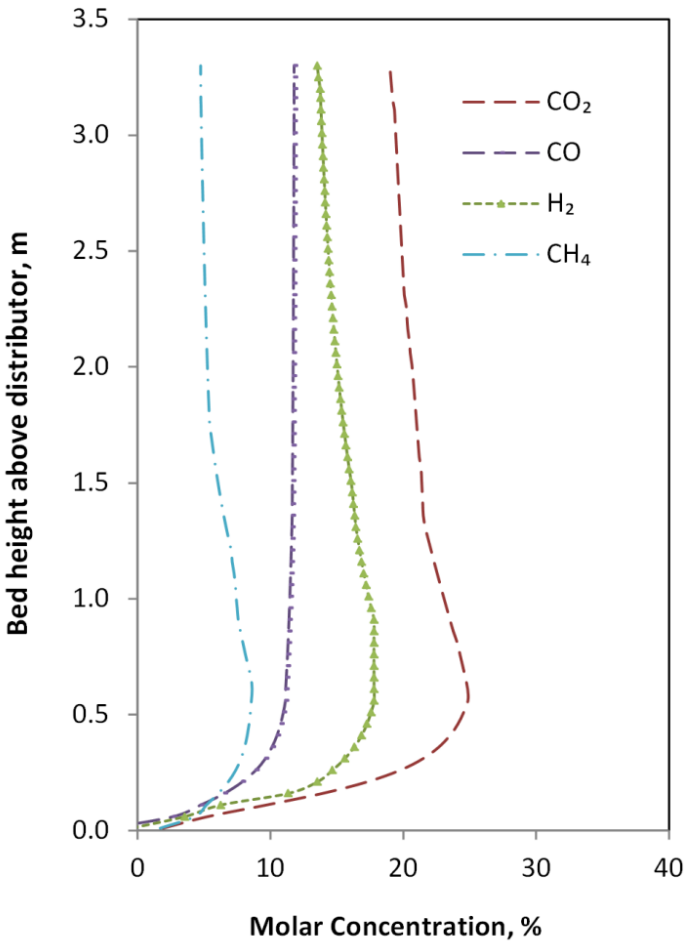

Figure 5.44 Gases concentration profile through the fluidized bed height

Table 5.6 Thermodynamic simulation model verification

Parameter	Current Model	Literature data	Difference
Specific Heat in Regenerator	1802 kJ/kg	1883 kJ/kg	4.30 %
Specific Heat in Intercooler	427.2 kJ/kg	428.6 kJ/kg	0.32 %
Specific Heat in Precooler	683.1 kJ/kg	685.9 kJ/kg	0.41 %
Overall Thermal Efficiency	45.68 %	46 %	0.70 %
Temperature after Compression	127.5^{o}C	125.5^{o}C	1.59 %
Temperature after Expansion	521.9^{o}C	537.7^{o}C	2.93 %

The energy and exergy analyses are performed on the prescribed system in the base case operating conditions as shown in Table 4.4.

Table 5.8 shows the results of the energy and exergy analyses for the overall system performance. The results show that for the same compressor inlet temperature, increasing the turbine inlet temperature results in a higher energy and exergy efficiency as a result of the higher operating optimal pressure ratio of the gas turbine plant. In the same Table, the increase of the specific work output, which reflects the enthalpy potential of producing useful work, is shown. This causes a decrease in the helium flow rate demand, for the same power output. This highly affects the economic viability of the heat exchangers and turbomachinery as the mass flow rate is to be increased by 40% for a decrease in the temperature ratio from 2.8 to 2.4 at the same compressor inlet temperature.

Figures 5.45 and 5.46 show the results of the parametric study of the pressure ratio effect on different performance parameters. The results in these figures are calculated at the base condition.

Table 5.7 Results of the energy and exergy analysis of the system components

	y_D [%]	η_{ex} [%]	y_D [%]	η_{ex} [%]	y_D [%]	η_{ex} [%]
	313K/923K		313K/1023K		313K/1123K	
Gas Turbine	7.56	96.8	7.91	97.1	8.23	97.3
LP Compressor	6.26	90.4	6.44	90.6	6.71	90.6
HP Compressor	6.39	90.5	6.63	90.5	6.87	90.6
Intercooler	10.4	97.6	11.4	97.2	12.4	96.8
Precooler	19.5	95.1	21.7	94.1	24.1	93.0
Recuperator	13.6	87.9	14.4	88.7	15.2	89.3

Table 5.8 Gas turbine performance assessment based on the thermal analyses

Turbine Inlet temperature		650°C	750°C	850°C
System performance	Optimal pressure ratio	2.407	2.648	2.74
	Temperature ratio	0.34	0.306	0.278
	Thermal efficiency	37.64%	41.91%	45.48%
	Exergy Efficiency	50.07%	55.75%	60.51%
	Specific net work	545.7 kJ/kg	732 kJ/kg	933 kJ/kg
	Sustainability index	2.0	2.3	2.5

Figure 5.45 shows the change of the energy and exergy efficiencies with the pressure ratio. The energy efficiency shows a maximum of 45.48% at a pressure ratio of 2.74. However, the exergy efficiency reaches a maximum of 60.6% at pressure ratio of 2.78. It is important to note that exergy efficiency is higher than the corresponding energy efficiency due to the fact that the exergy of the heat added is considered as the exergy input in calculating the exergy efficiency. The dimensionless work is also shown in the same figure; it is as an indication of the produced power with respect to the theoretical maximum potential. It gives a peak at the pressure ratio of 6.2. At this value, the energy and exergy efficiency drops to 39.1 and 52%, respectively.

Figure 5.46 shows the change of exergy destruction in the system components, as percentage of the total exergy destruction, with increasing the pressure ratio. For a pressure ratio more than 3.4, the changes in the percentages for the turbine, compressors, main heat exchanger and the precooler are very small compared with the other heat exchangers of the system.

Figures 5.47 to 5.50 show the results of the energy and exergy analyses at different temperature ratios with respect to the turbine inlet temperature. All other operating parameters are kept constant at the base case condition shown in Table 4.4. Figure 5.47 shows the effect of changing the pressure ratio on the dimensionless work and the total exergy destruction rate of the plant. Increasing the temperature ratio at constant turbine inlet temperature causes a reduction in the work output as the enthalpy difference drops. The maximum work occurs at higher pressure ratio for higher turbine inlet temperature. The total exergy destruction rate has a fully reversed trend.

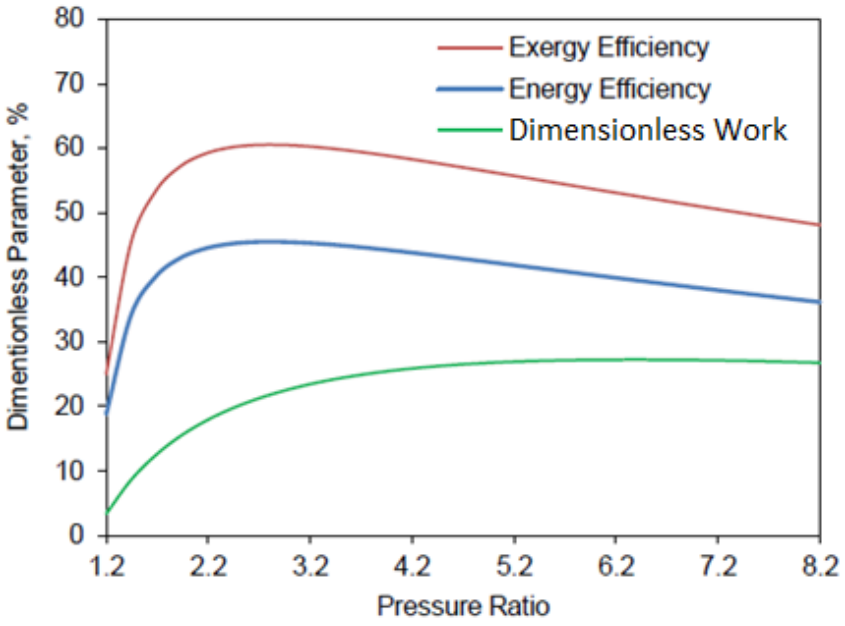

Figure 5.45 Effect of pressure ratio on the gas turbine performance

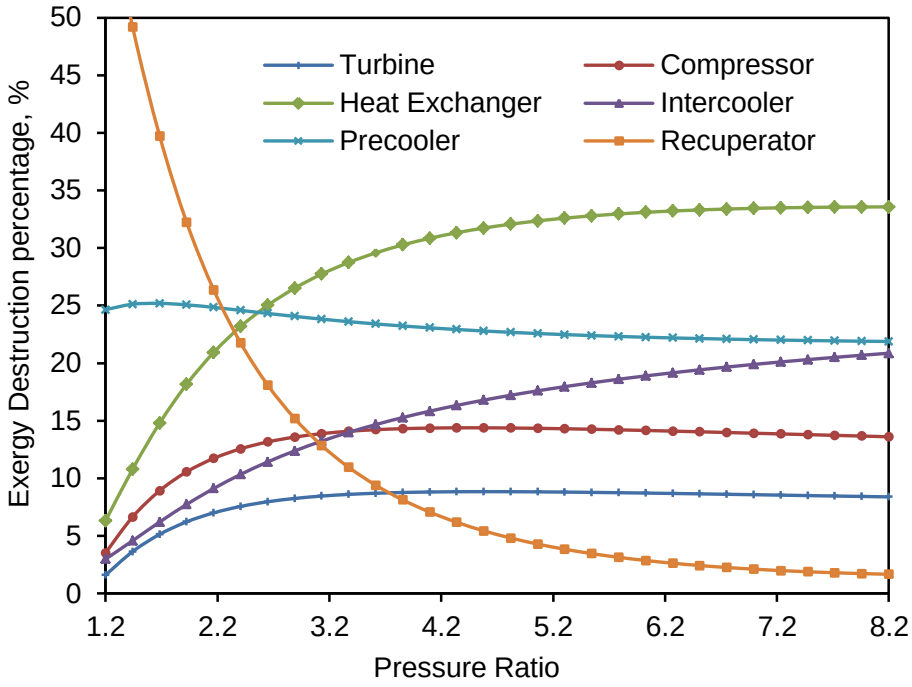

Figure 5.46 Effect of pressure ratio on the exergy destruction rates as percentage of the total exergy destruction

In Figure 5.48, as a result of the increase in work output, the exergy efficiency is higher for higher turbine temperature. But with the increase of pressure ratio, even with the increase in work output, the exergy efficiency drops after the peak as a result of the increase in the exergy rate of streams provided to the system with respect to the product exergy rates.

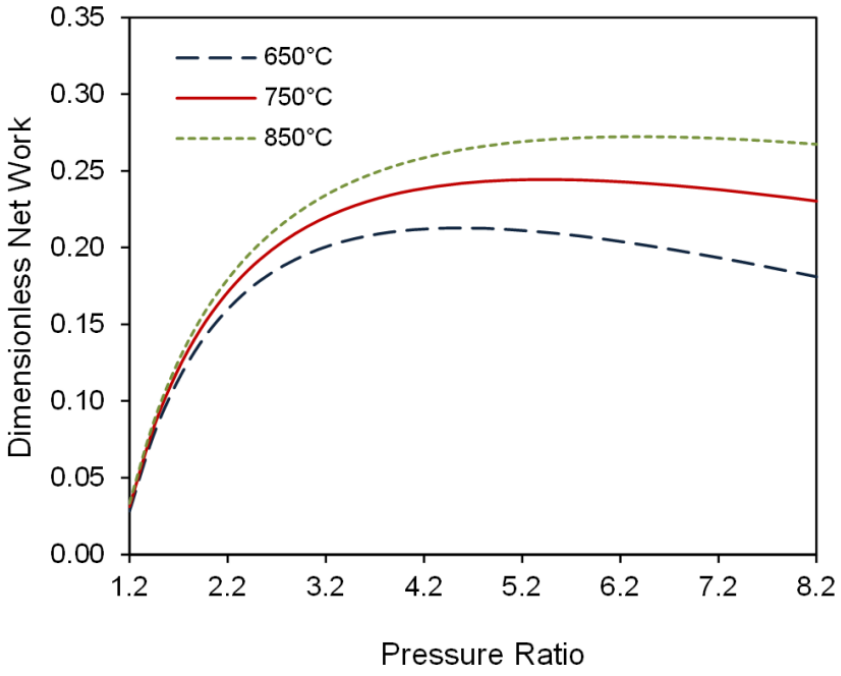

Figure 5.47 Pressure ratio effect on the gas turbine performance at different turbine inlet temperatures

Figure 5.49 shows the exergetic performance of the studied helium turbine as exergetic performance map. The exergetic performance map shows the effect of pressure ratio and temperature ratio on the performance of the gas turbine and its output. It measures the performance in terms of the exergy efficiency and the dimensionless work. Figure 5.50 also shows the exergetic loss map which shows the exergy destruction ratio, with respect to the exergy of the streams provided to the system components, and the specific network output. The gas turbine operation is described on the map at constant lines of temperature at different operating pressure ratio.

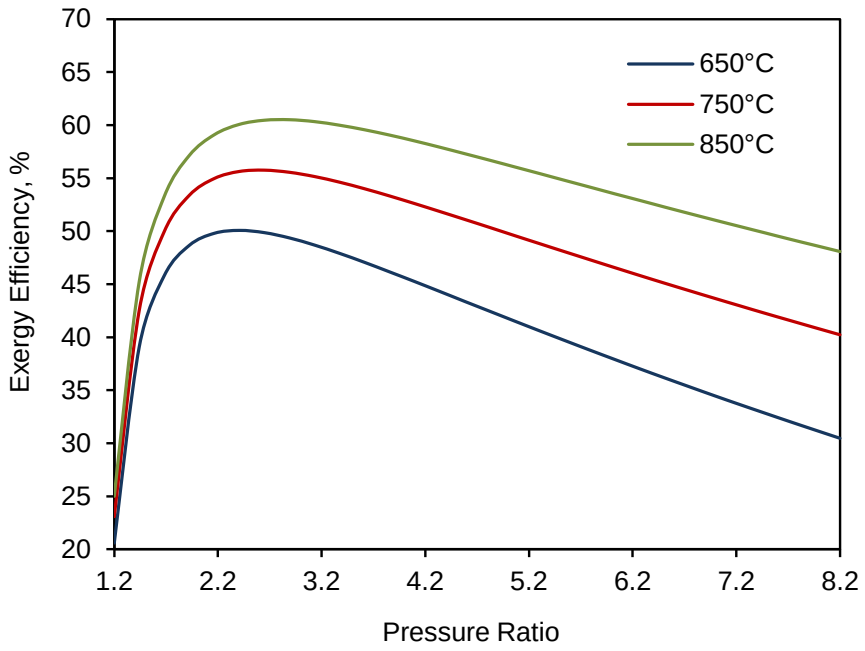

Figure 5.48 Gas turbine exergy efficiency vs pressure ratio at different turbine inlet temperatures

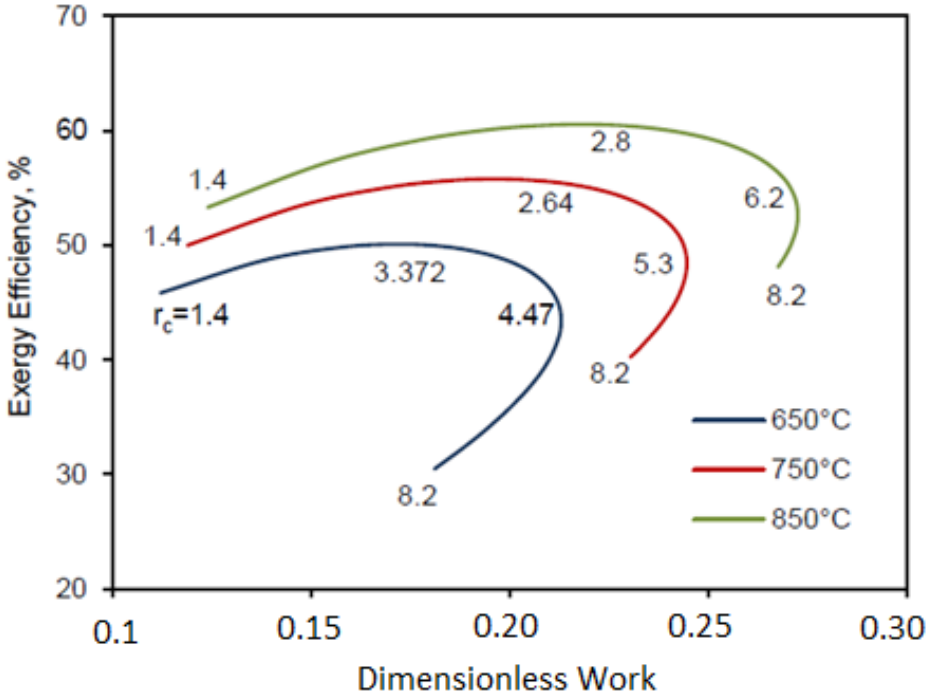

Figure 5.49 Exergetic performance map at different turbine inlet temperatures

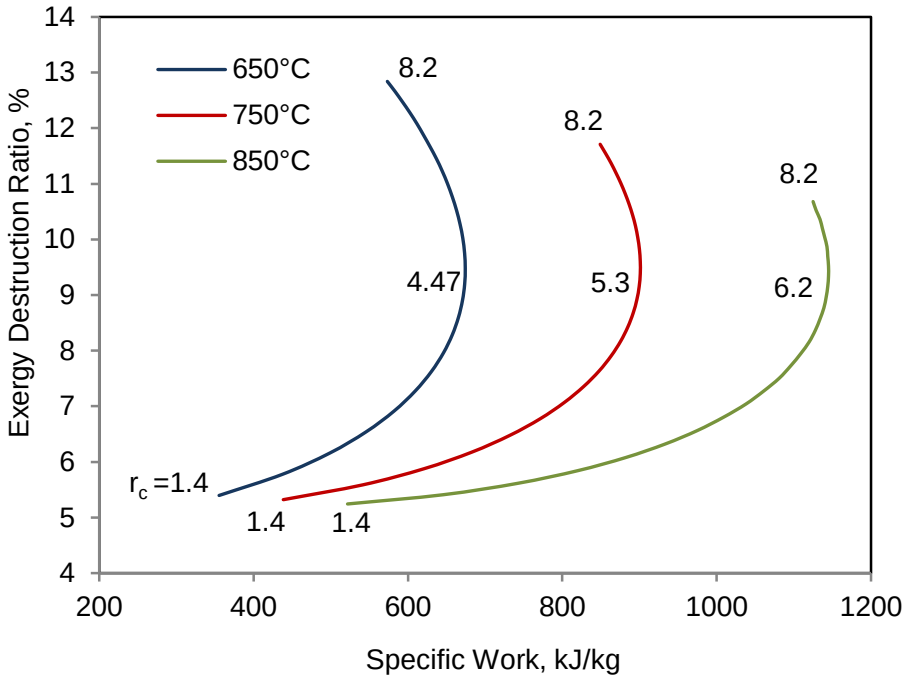

Figure 5.50 Exergetic loss map at different turbine inlet temperatures

5.2 System 2: Solar Parabolic Trough – Organic Rankine Cycle Based System

In this system, a parabolic trough concentrator, equipped with two tank molten salt storage system, is utilized to provide heat to an organic Rankine cycle, and the system is designed to produce 200-500 kW of net electric power. A PEM electrolyzer is integrated with the system to produce hydrogen and the heat required for it performance is provided by the solar heat transfer fluid after leaving the main ORC heat exchanger. The ORC turbine is providing the required electric power to the electrolyzer as well as to RO system that is integrated to provide fresh water at design rate of 40 kg/s. The heat content of organic fluid leaving the turbine is utilized to provide domestic hot water at 50°C, and then to an absorption chiller system with evaporator heat of 500-800 kW. The main operating and design parameters and inputs of the system are provided in Table 5.9. The parabolic trough model is performed based on the model introduced by (Al-Sulaiman et al., 2011). The heat transfer fluid mass flow rate is calculated based on the heat to be provided to the ORC and the electrolyzer.

Table 5.9 Operating and design parameters of the proposed integrated system

Parameter	Value
Solar Parabolic Trough (Al-Sulaiman et al., 2011)	
Heat transfer fluid (HTF)	Therminol-66
Width of the collector	5.76 m
Length of the collector	12.27 m
Solar radiation during high sun radiation	850 W/m^2
Solar radiation during low sun radiation	500 W/m^2
Storage medium	HitecXL
HTF cost	3$/kg (Krishnamurthy et al., 2012)
Concentrators cost rate	320 $/m^2
Storage specific cost	22 $/kWh$_{th}$
Organic Rankine Cycle	
Working fluid	n-octane
Turbine inlet pressure	22 bar
Turbine isentropic efficiency	85%
Evaporator effectiveness	88%
Turbine exit pressure	35 kPa
Pump inlet temperature	85°C
Pinch temperature of heat exchangers	6°C
PEM Electrolyzer (Ni et al., 2008)	
Operating temperature	80°C
Operating current density	5000 A/m^2
Anode activation energy, $E_{act,a}$	76 kJ/mol
Cathode activation energy, $E_{act,c}$	18 kJ/mol
Water content at anode-membrane, λ_a	14
Water content at cathode-membrane, λ_c	10
Anode exchange current density, $J_{ref,a}$	1×10^5A/m^2
Cathode exchange current density, $J_{ref,c}$	10 A/m^2
Specific cost	1000 $/kW (Genç et al., 2012; Li et al., 2009)
Absorption Chiller System	
Solution circulation ratio	11.05
Heat exchanger effectiveness	0.78
Purchase equipment cost, $	$1144.3(\dot{Q}_{Evap}[kW])$
Reverse Osmosis	
Salinity of product water	450 ppm
Seawater salinity	35000 ppm
Capital cost, $	$0.98(m\ [kg])^3$

Figure 5.51 shows the relationship between the solar trough parameters with respect to the ORC turbine inlet temperature. All other parameters are kept at the base

case condition. Increasing the turbine inlet pressure reflects on a direct increase in the total solar concentrator area required which mean higher cost rate. The value of the HTF to organic fluid mass ratio is constrained by the inlet temperature of the ORC pump. The values shown on the lines are representing the corresponding ORC turbine pressure value of the operating point.

Figure 5.52 shows the performance chart of the overall system showing the exergy efficiency and the cost rate estimated at different operating turbine pressure and temperature values. The figure shows the maximum efficiency to occur at the peak values of total cost rate for each temperature value studied. The highest cost rate occurs at the turbine pressure values of 15 bar, 17.3 bar and 17.4 bar for the turbine inlet temperature value of 543, 553 and 563K, respectively.

The results in Figure 5.53 show the effect of the ORC turbine inlet pressure on overall energy and exergy efficiency of the system performing at turbine inlet temperature. The cycle lower pressure and other operating parameters are kept constant at the base case condition. The pressure values for each case are constrained by the corresponding saturation temperature. Higher overall energy efficiency is achieved by increasing the turbine inlet pressure. However, the exergy efficiency starts to increase and then slightly decreases after reaching a maximum value. Also increasing the superheating temperature of the working fluid of the organic cycle causes an increase of the exergy efficiency and a reduction in the energy efficiency. The enhancement in the energy efficiency with the increase in the turbine inlet temperature is less than 0.5% for each pressure value.

In Figure 5.54, the effect of varying the turbine inlet pressure on the solar concentrator total area is studies. The figure also discusses the change in the required HTF mass flow rate as a ratio of the ORC fluid mass flow rate. Increasing the turbine pressure directly causes a reduction in the amount of heat required to be fed to the ORC, considering constant inlet temperature. The total trough area is proportional to the turbine work with increases with higher turbine pressure. The effect of increasing the superheating temperature of the organic fluid shows an increase of the HTF flow rate and the total concentrator area.

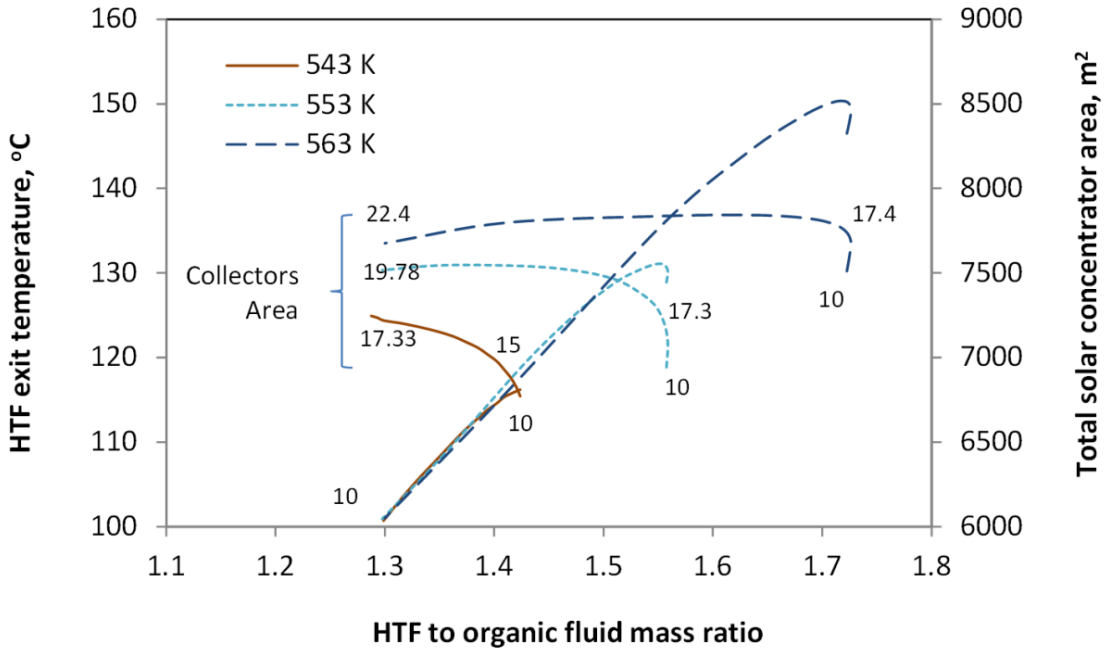

Figure 5.51 Solar parabolic trough performance parameters

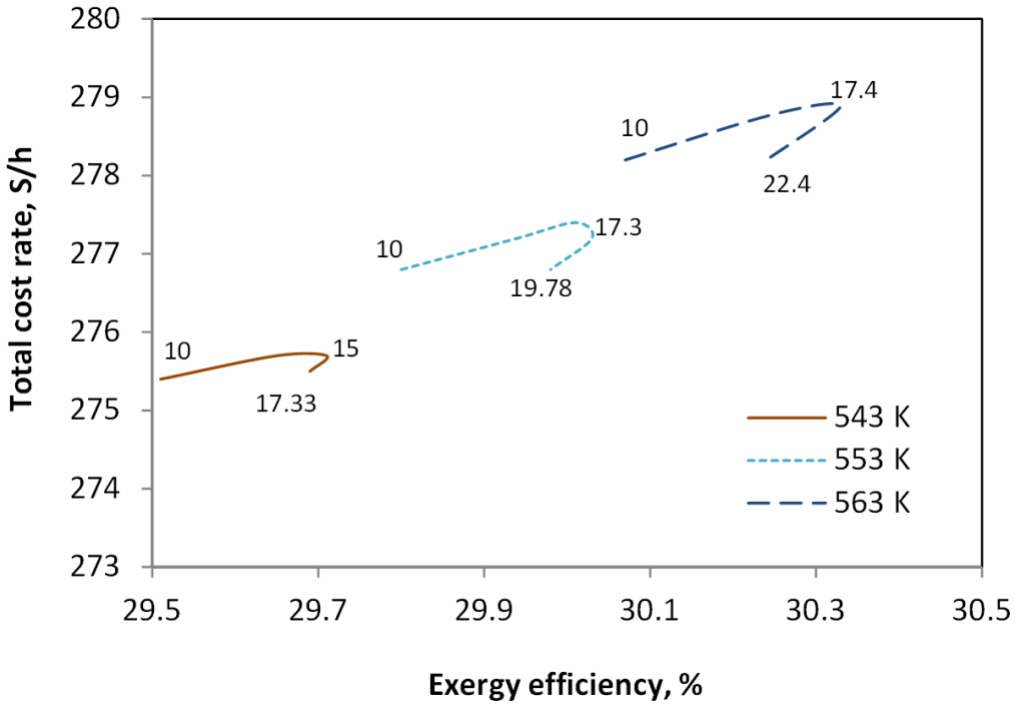

Figure 5.52 The system exergy efficiency vs. total cost rate

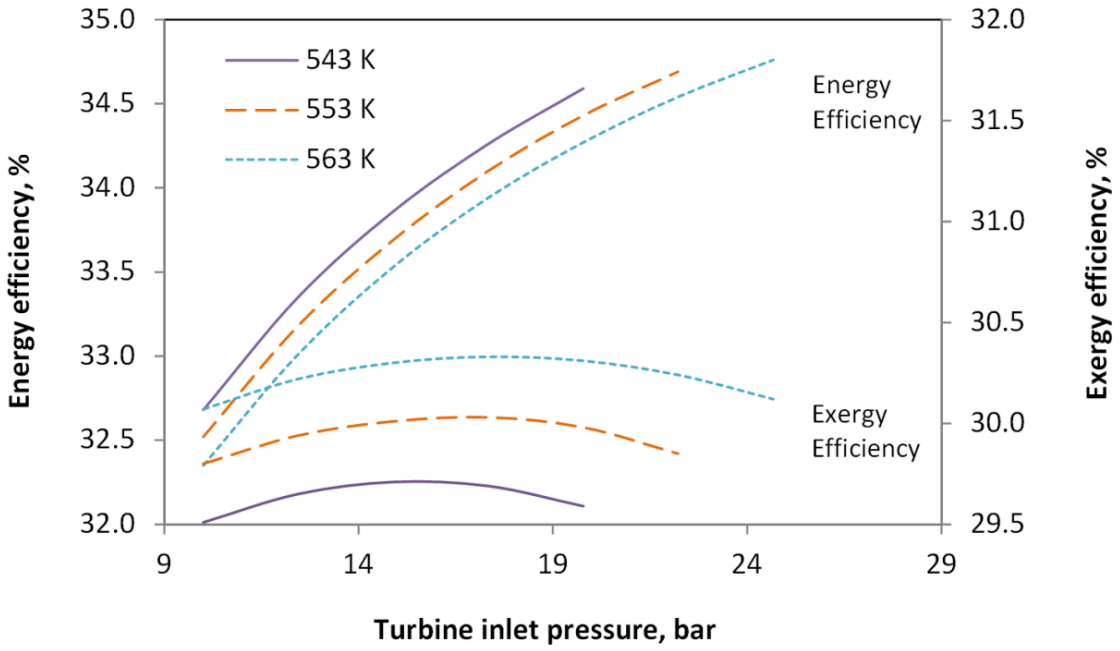

Figure 5.53 Effect of ORC turbine inlet pressure on the system performance at different turbine inlet temperature values

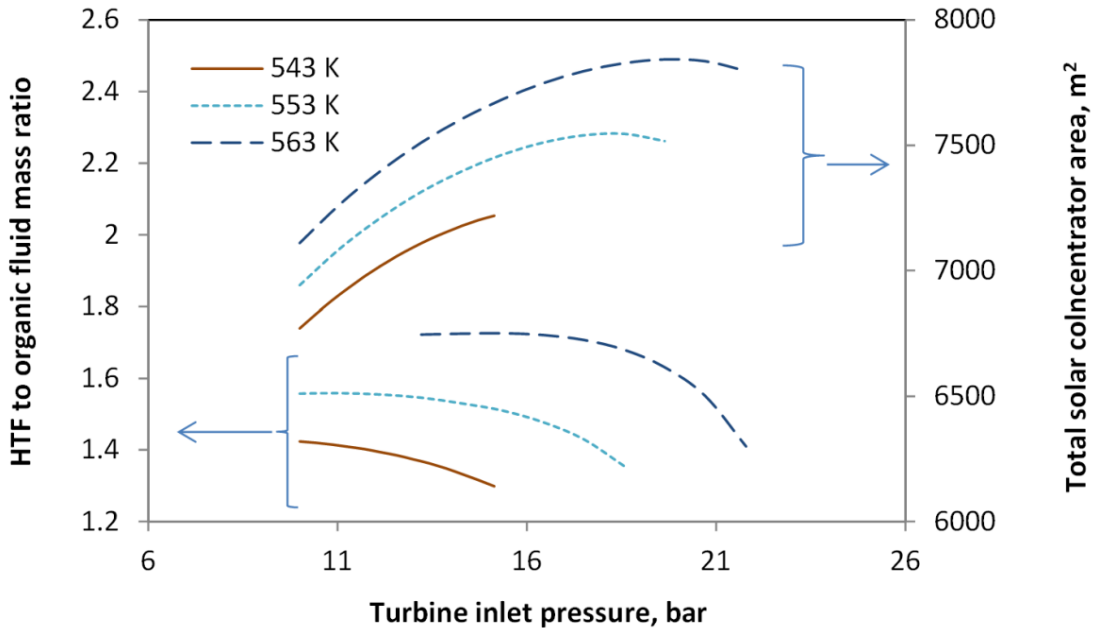

Figure 5.54 Effect of ORC turbine inlet pressure on the required solar concentrator and the HTF to organic fluid mass ratio at different turbine inlet temperature values

Figure 5.55 shows the effect of the inlet pressure of the turbine on the total cost rate and the absorption cooling system. Lower cost rate is increasing with the pressure values as the purchase cost of the equipment would increase, the cost rate starts to decrease when less concentrator area is required and associated with the drop in the net power of the system after certain pressure values. The higher the superheating temperature the higher the pressure value at which the cost rate starts to decrease. This is related to the results in Figure 5.56 showing the net power output from the system. The figure shows that the higher the turbine inlet temperature, the more mass flow rate of generated domestic hot water.

Figure 5.57 shows the effect of the pinch temperature of the ORC main heat exchanger on the required HTF flow rate with respect to the super heating temperature. The limits of the pinch temperature are constrained based on temperature differences between the two fluids. This directly affects the heat exchanger area.

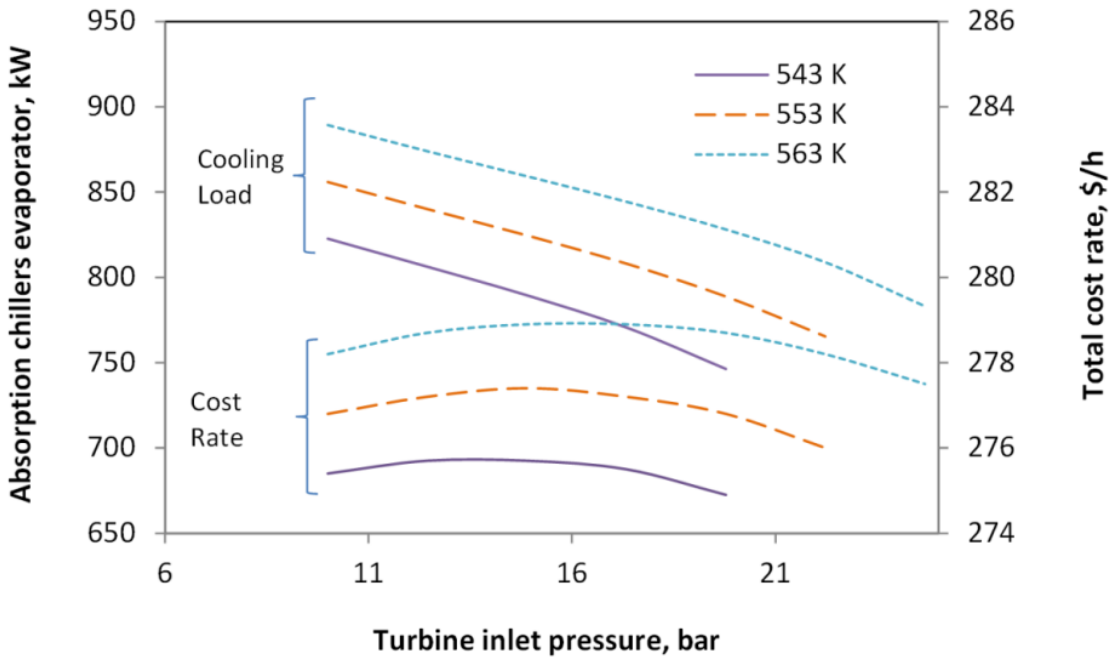

Figure 5.55 Effect on ORC turbine inlet pressure on the cost rate and the absorption cooling system at different turbine inlet temperature values

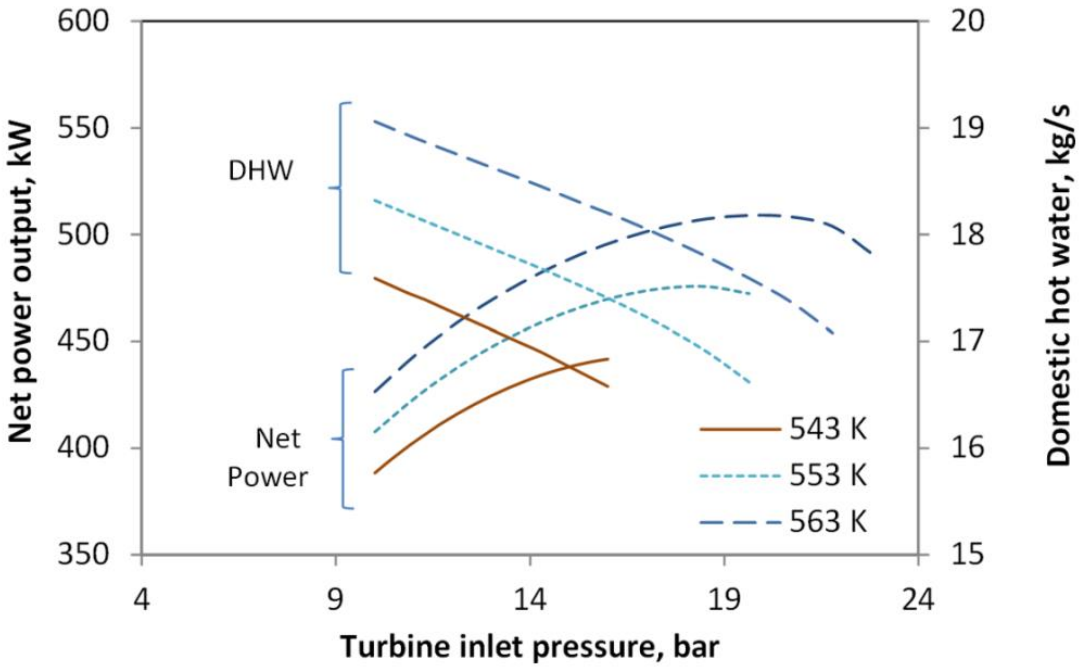

Figure 5.56 Effect of ORC turbine inlet pressure on the net power output and domestic hot water production at different turbine inlet temperature values

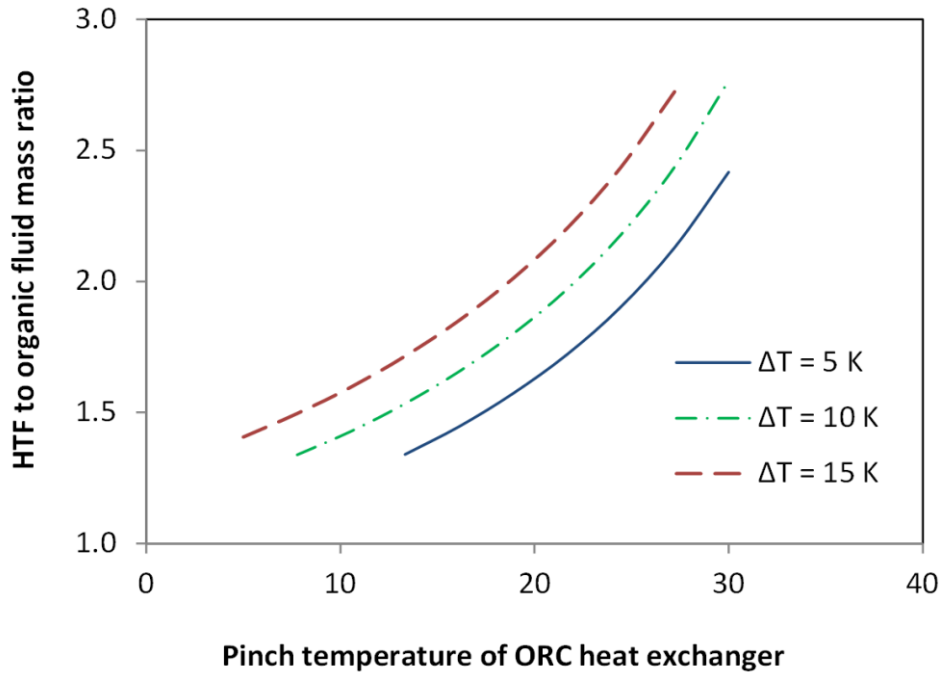

Figure 5.57 Effect of the ORC heat exchanger pinch temperature on the mass ratio of HTF to the organic fluid at different superheating temperatures

The optimization study performed on this system is performed using the genetic algorithm with generation number of 150, population of 67 and mutation rate of 0.03. The objective functions are defined as the exergy efficiency to be maximized with minimizing the capital cost. The two functions can be defined as follows:

$$\eta_{ex} = \frac{\dot{W}+\dot{E}x_{Cooling}+\dot{E}x_{H_2}+\dot{E}x_{DHW}+\dot{E}x_{freshwater}}{\dot{E}x_{solar}} \quad (5.3)$$

$$\dot{C}_{total} = \sum \dot{C}_{sys} \quad (5.4)$$

The decision variables set for this analysis are; turbine isentropic efficiency, 80%-90% turbine inlet temperature, set 450-660 K, evaporator temperature, 2°C-7°C, evaporator pinch temperature, 5°C-30°C, effectiveness of the solar heat exchanger, 80%-90%, pump inlet temperature set higher than 85°C. These variables are also listed in Table 5.10 The Pareto frontier is shown in Figure 5.58 showing the relation between the two objectives considered in this analysis. It shows almost a linear relation between the two objectives. The curve represents all best points resulted from the analysis. The two extreme points of the curve represent the highest gained efficiency of 39% with the highest cost rate of 309.56 $/h when the other end represents the lowest exergy efficiency point with 21.7% associated with cost rate of 241.7 $/h.

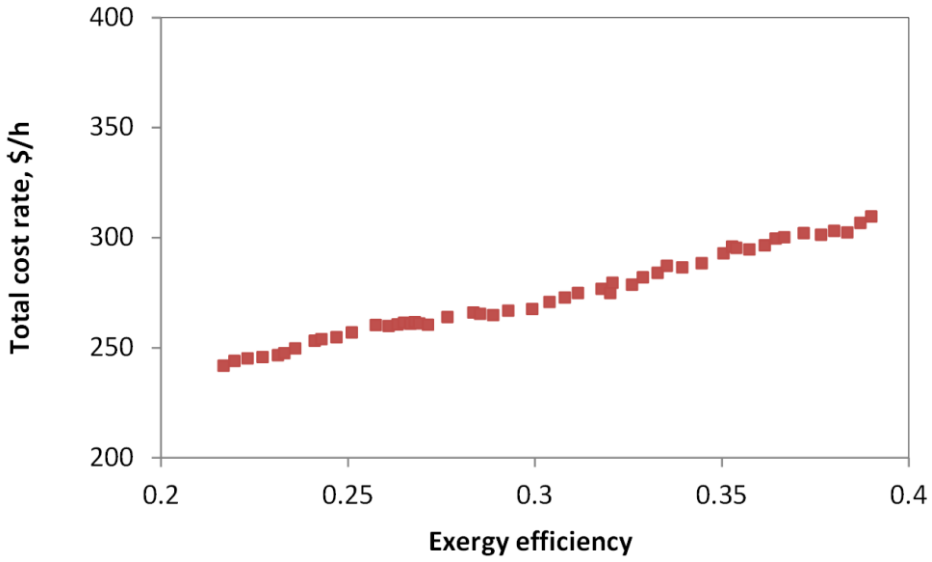

Figure 5.58 Pareto frontier curve for best value of the optimization results

Table 5.10 Decision variables for the optimization process

Parameter	Value
Turbine isentropic efficiency, %	80 - 90
Turbine inlet temperature, K	450 - 660
Heat exchanger effectiveness, %	80 – 90
Heat exchanger pinch temperature, ^{o}C	5 - 30
Pump inlet temperature, ^{o}C	< 85
Evaporator temperature, ^{o}C	2 - 7

For the model of the electrolyzer considered in the present study, Figure 5.59 shows the validation of the modeled PEM electrolyzer with the data presented by Ni et al. (2008). The model shows good agreement with respect to the operating voltage. Figure 5.60 represents the change of exergy efficiency of the PEM electrolyzer with the current density. The efficiency is calculated based on the chemical exergy of the produced hydrogen with respect to the total electric power and the exergy associated with heat added to bring the water to the electrolyzer operating temperature.

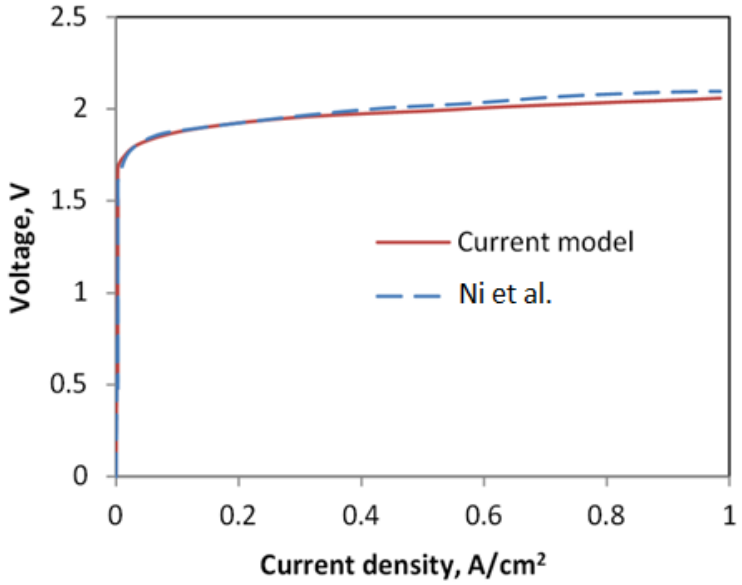

Figure 5.59 Validation of the PEM electrolyzer model with Ni et al. (2008)

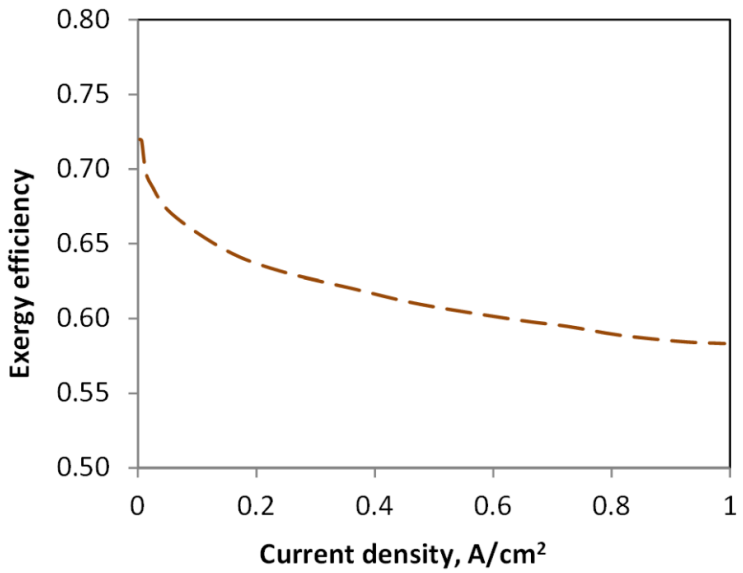

Figure 5.60 Electrolyzer exergy efficiency at different operating current densities

5.3 System 3: Solar Heliostat – Steam Turbine Based System

Based on the described model, the heliostat and receiver performances are assessed as well as the overall system performance. The main parameters considered for the heliostat and the receiver are shown in Table 5.11. The system produces net power of 4 MW, with the integration of PEM electrolyzer that is proposed to produce 1.25 kg of hydrogen per hour, and a reverse osmosis unit for sea water desalination, producing 90 kg/s of fresh water, absorption chiller system and providing domestic hot water.

The performance of the solar heliostat system strongly depends on the incident solar isolation. To investigate that effect, the amount of solar radiation received is considered as a variable parameter ranging from 200 to 1000 W/m^2, to evaluate its effect on the solar system, and the overall system performance. Figure 5.61 shows the variation of the performance of the receiver, measured by the energy and exergy efficiencies. The increase of the solar radiation received increases the efficiency of the receiver. Over the tested solar flux, energy efficiency increased from 75% to 89% and the exergy efficiency increased from 39% to 51%. The main losses occurring in the receiver are function of the receiver surface temperature which slightly changes over the tested range of solar flux. This can be seen in Figure 5.64 where the temperature varies with in 50°C over the tested solar flux range. This means, with higher solar flux, the heat losses from the receiver

increases slightly, resulting in higher efficiency. The total energy and exergy efficiencies of the total solar system performance and the overall integrated system are shown in Figure 5.62, for the heliostat performance, and Figure 5.63, for the overall system performance. It can be seen that the efficiencies increase in a trend that is related to the receiver efficiency. From the three figures, the efficiency increases in a noticeable way through the low solar flux range, after 400 W/m^2, the enhancement in the efficiencies is less.

Table 5.11 Main properties of the solar field

Parameter	**Value**
Heliostat width and height	10 m
Mirror reflectance	0.9
Minimum heliostat distance to tower ratio	0.75
Maximum heliostat distance to tower ratio	7.5
Mirror washing water	0.7 L/m^2
Annual washes	60
Receiver type	external
Receiver diameter	8 m
Coating emittance	0.88
Receiver tube diameter	40 mm
Receiver tube thinness	1.25 mm
Minimum receiver height to diameter ratio	0.8
Maximum receiver height to diameter ratio	1.6
Maximum tower height	250 m

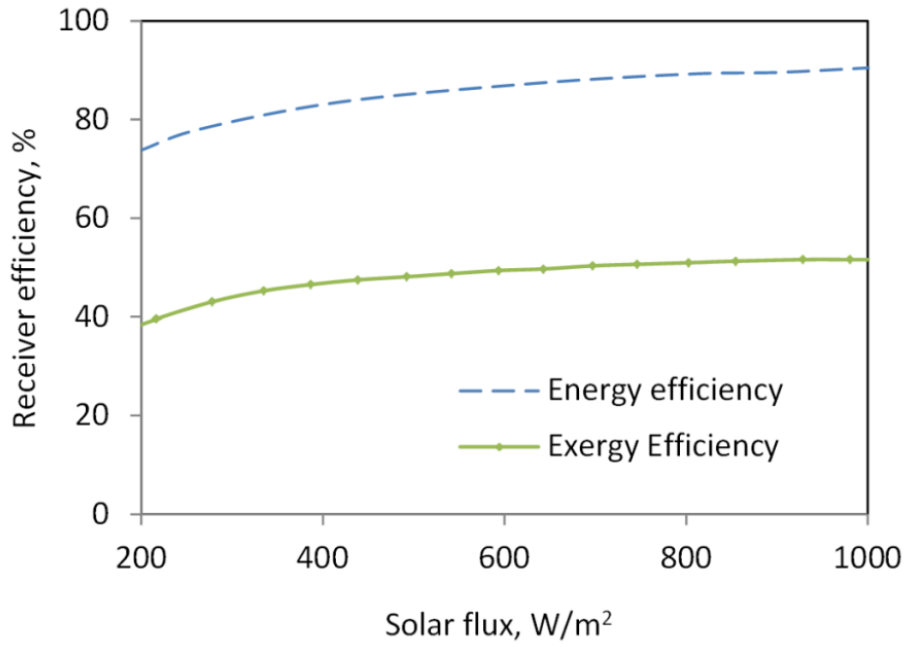

Figure 5.61 Effect of solar flux on the efficiency of the receiver

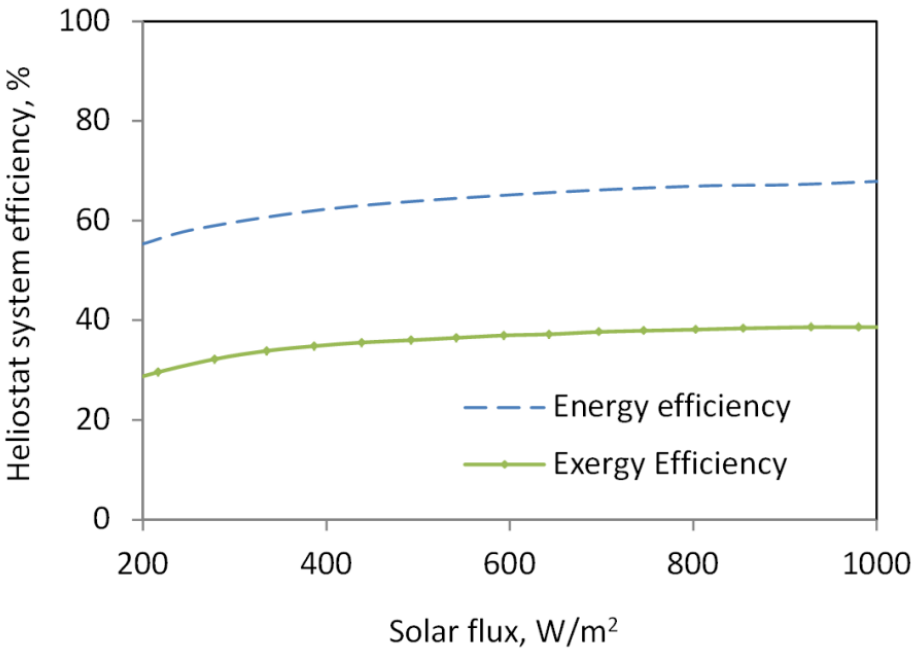

Figure 5.62 Effect of solar flux on the efficiency of the solar system

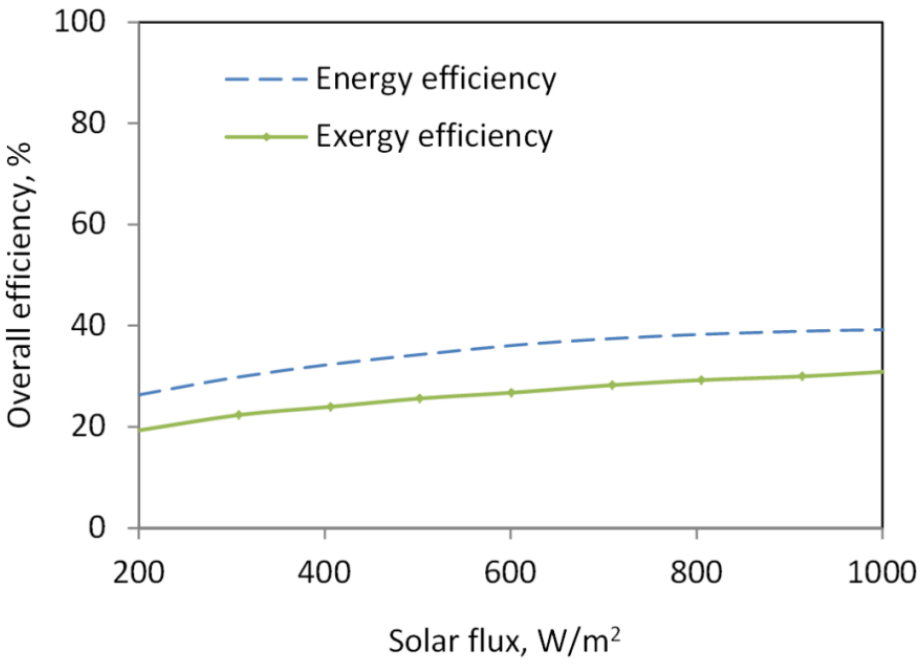

Figure 5.63 Effect of the solar flux on the overall system efficiency

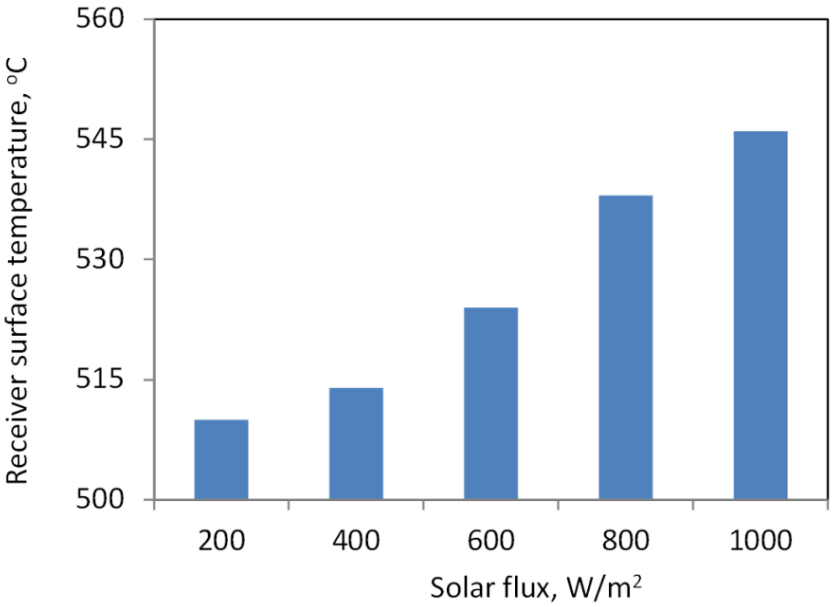

Figure 5.64 Variation of receiver surface temperature with solar flux

The heliostat field and solar tower are optimized for this system using System Advisor Model (SAM) software that is produced by the National Renewable Energy Laboratory. The system is optimized with respect to the weather data of Aswan city in

Egypt. All weather conditions and the parameters required for the analysis are provided in Table 5.12 and Figures 5.65 to 5.67. The results of the heliostat optimized distribution are shown in Figure 5.68, where the shown arrow refers to the direction of the Equator, with respect to the selected location. Numbers of heliostats at each radial zone specified in the figure are listed in Table 5.13. The results in Table 5.14 show the optimized specifications of the solar field main parameters.

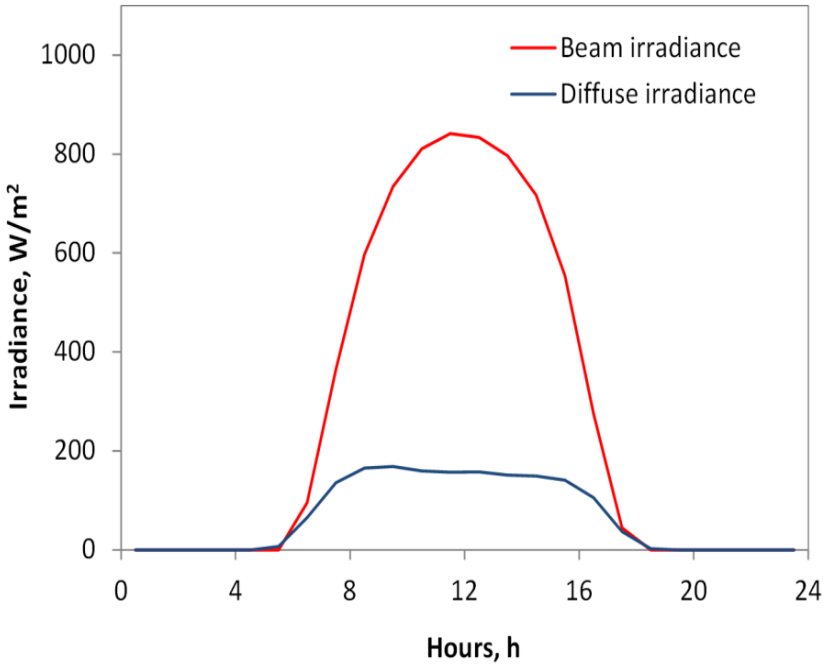

Figure 5.65 Daily solar irradiance distribution for the selected location

Table 5.12 Location specifications and parameters

Parameter	**Value**
Location	Aswan, Egypt
Latitude	23.97°
Longitude	32.78°
Elevation	194 m
Annual direct normal irradiance	2433.5 kWh/m^2
Annual dry bulb temperature	26.2°C
Average wind speed	5.1 m/s

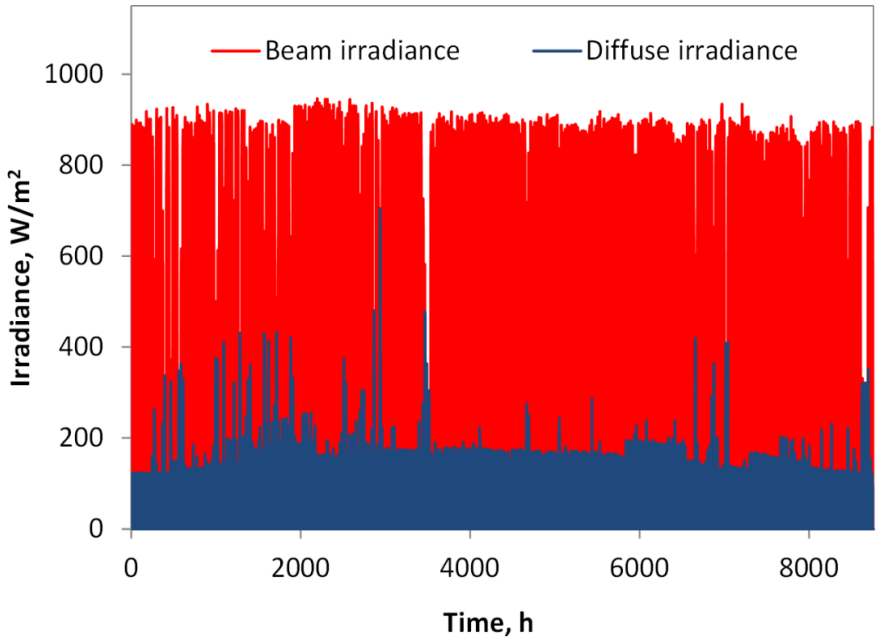

Figure 5.66 Annual distribution of the solar irradiance at the selected location

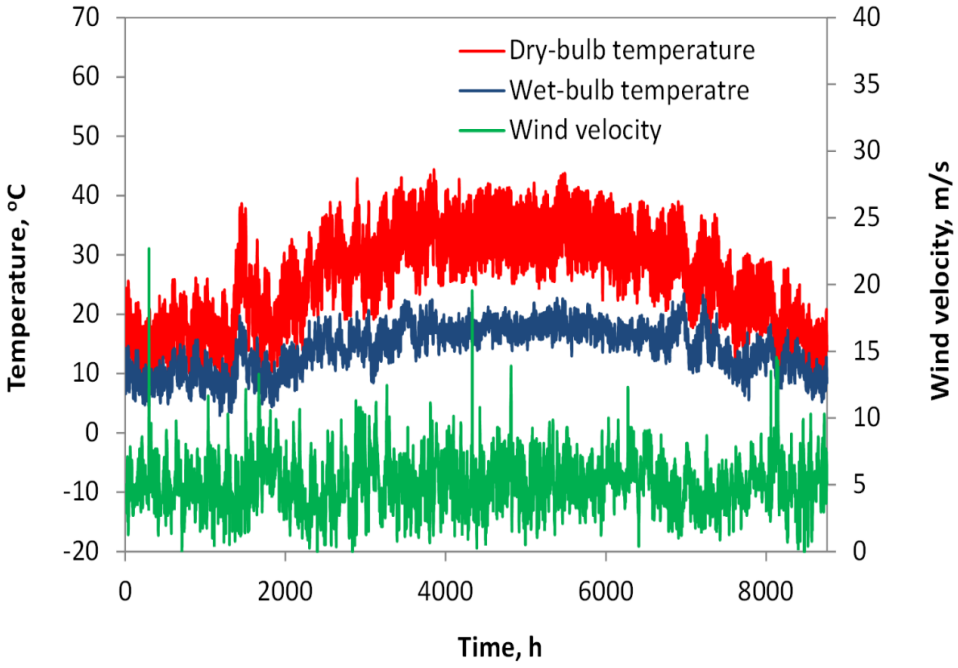

Figure 5.67 Annual distribution of dry and wet bulb temperatures and the wind velocity for the selected location

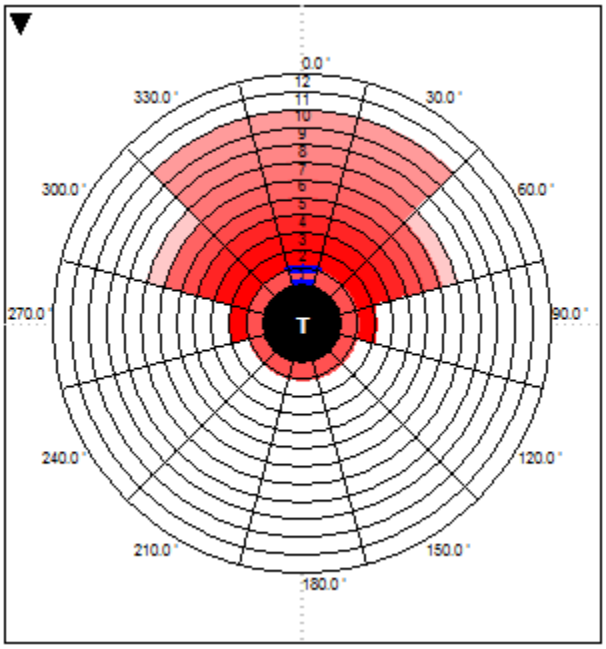

Figure 5.68 The radial distribution of heliostat with respect to the solar tower

Table 5.13 Number of heliostats per radial zone

	0	**30**	**60**	**90**	**120**	**150**	**180**	**210**	**240**	**270**	**300**	**330**
Rad. 1	2	2	2	2	2	2	2	2	2	2	2	2
Rad. 2	7	7	7	7	0	0	0	0	0	7	7	7
Rad. 3	9	9	9	0	0	0	0	0	0	0	9	9
Rad. 4	10	10	10	0	0	0	0	0	0	0	10	10
Rad. 5	10	10	10	0	0	0	0	0	0	0	10	10
Rad. 6	10	10	10	0	0	0	0	0	0	0	10	10
Rad. 7	10	10	4	0	0	0	0	0	0	0	4	10
Rad. 8	10	10	0	0	0	0	0	0	0	0	0	10
Rad. 9	10	10	0	0	0	0	0	0	0	0	0	10
Rad. 10	10	10	0	0	0	0	0	0	0	0	0	10

Table 5.14 Results of heliostat field optimization

Parameter	**Value**
Number of heliostat	396
Total reflective area	38,412 m^2
Maximum distance from the tower	403.7 m
Radial step size for layout	35.6 m
Receiver height	6.4 m
Tower height	63.3 m

The following results represent the performance of the RO system. The analysis is performed for the base case with the operating parameters shown in Table 4.14. At recovery ratio of 0.55, the cost rate of the product water is estimates as 2.451 $/m^3 and the exergy efficiency is calculated as 5.82%. Varying the feed seawater temperature, while keeping all other parameters constants, has a very limited effect on the cost rate of product water. At 15^{o}C it gives 2.45 $/m^3 while at 35^{o}C the product cost rate is 2.441 $/m^3. For the base case considered, the exergy destruction mainly occurs in the RO module and the high pressure pump as 67.8% and 17.16% of the total exergy destruction, respectively.

Effects of Seawater Salinity:

Seawater with different salinities is used to investigate the effect of the source salinity on the product cost. Increasing the water salinity caused a predicted increase in the product cost rate per unit volume of product water. At salinity of 25000, 35000 and 45000 ppm, the product cost are estimated as 2.228, 2.233 and 2.25 $/m^3, respectively. However, the product cost presented per unit of the energy utilized in the system decreased with the increase of the salinity of the source seawater. The product costs are calculated to be 62.8, 54.2 and 48.09 $/MJ when the used seawater with the salinities of 25000, 35000 and 45000 ppm, respectively.

Effects of Recovery Ratio:

Figures 5.69 to 5.72 primarily show the results of the parametric analyses of varying the recovery ratio from 35% to 75% and its effect on different performance and economic parameters, all other operating parameters are kept at the base case condition as defined in Table 4.14.

In Figure 5.69, the change in the power required to drive the system pumps, and the power produced by the Pelton turbine are shown at different recovery ratio values. There is a large reduction of 53% in the required power for the HPP with increase in recovery ratio, at constant feed water rate. However, the net power curve shows a relatively low reduction in the input power with increasing the recovery ratio. Also the product cost rate changes are presented in the same figure and it shows that at recovery ratio of 75%, the product cost decreases to 1.8 $/m^3, respectively.

Figure 5.70 shows the effect of recovery ratio of the RO plant on the exergoeconomic factor of the four major components on the plant. A slight increase occurs in the HPP and the SWIP where their values changes from 93.14% and 99.13% to 93.22% and 99.25%, respectively, with varying the recovery ratio from 35% to 75%. However, the exergoeconomic factor of the Pelton turbine and the RO modules are significantly affected. The RO module factor increased from 65.1% to 68.5%, and for Pelton turbine, it decreased from 99% to 51.27% due to the lower mass flow rate of the brine.

The low value of the exergoeconomic factor for any component is an indicator of the potential to increase the cost savings. This can be achieved by improving the component performance, hence reducing the exergy destruction in this component. This may come on the expense of the capital investment cost of the component.

Figure 5.71 shows the result of the parametric study of varying the recovery ratio and its effect on the mass flow rate of the feeding seawater, at constant product mass flow rate. The variation in the calculation of the membrane area is also shown. The figure shows the change in product cost represented by unit of energy used as well, at a water salinity of 35000 ppm. At a recovery ratio of 55% for the base case, the membrane area is calculated as 154.9 m^2.

Effects of Dead-Sate Temperature:

Figures 5.72 to 5.76 show the results of the parametric analysis performed with varying the dead state temperature and investigating their effects on the system parameters. Figure 5.72 shows the cost of exergy destruction of the major system components per unit volume of the product water. The highest cost associated with the exergy destruction occurs in the RO modules. This is because this component experiences high exergy destruction rate which is clearly shown in Figure 5.73 that presents the exergy destruction ratios at different dead state temperature values.

Figure 5.72 also shows that the unit exergy destruction cost of the RO module increases with the increase of the dead state temperature. This is related to the results presented in Figure 5.73, which shows that the exergy destruction ratio of the RO module increases with the increase in dead state temperature. However, other exergy destruction costs decease with increasing the dead state temperature.

The results presented in Figure 5.73 show the exergy destruction ratios for the system components taking the energy recovery Pelton turbine into consideration. Figure 5.74 shows the exergy destruction ratios in the system components with the elimination of the energy recovery device and replacing it with an expansion valve.

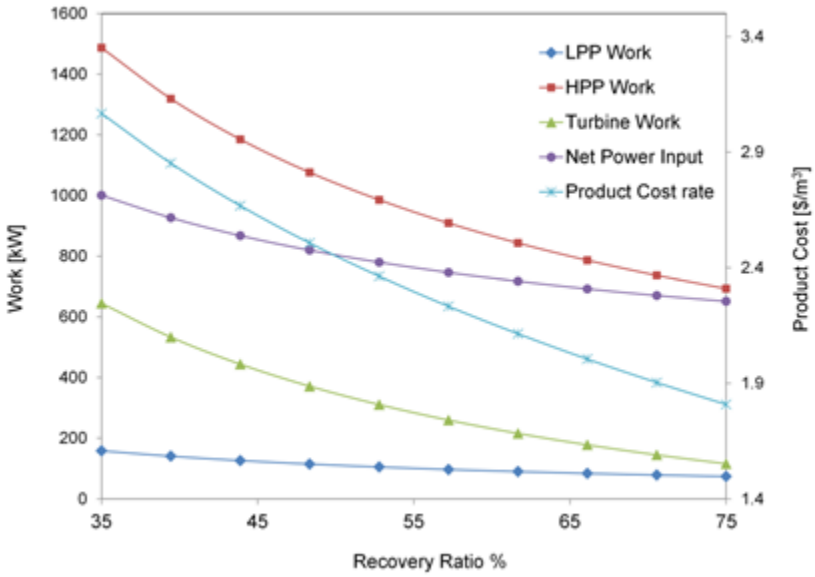

Figure 5.69 Effect of the recovery ratio on the work and product cost per unit volume of product water

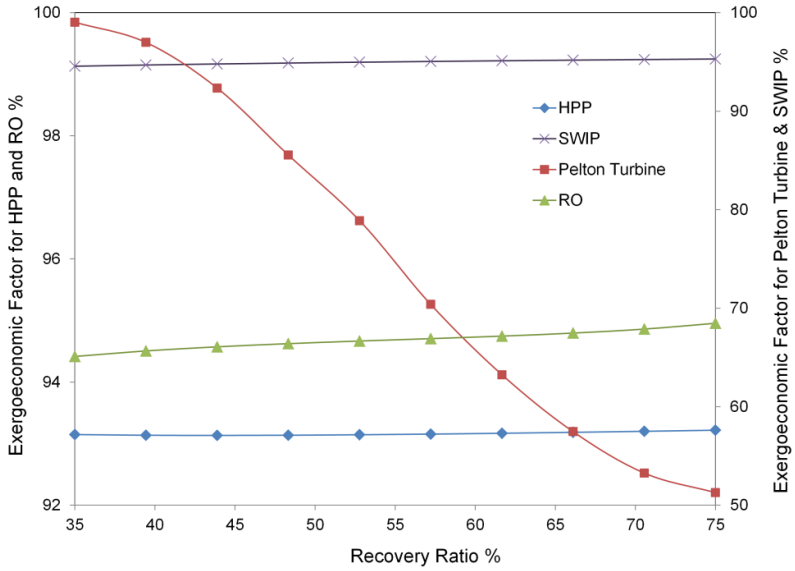

Figure 5.70 Effect of the recovery ratio on the exergoeconomic factor of the major system components

The results in Figure 5.74 exhibit large exergy destruction in the expansion valve as the brine is rejected from the RO module at very high pressure, and the pressure energy potential is not utilized. Adding an energy recovery device decreases the exergy destruction and hence, increases the exergy efficiency of the system as shown in Figure 5.75, but this comes on the expenses of the cost increase with purchasing the energy recovery system and the added cost of its annual operating and maintenance cost. For the base case, a reduction in the total exergy destruction by using the Pelton turbine becomes 35.5%, compared with the case where an expansion valve is used instead of energy recovery.

Figure 5.76 shows the effect of the dead state temperature on the exergoeconomic factor for the major system components. Increasing the dead state temperature causes a reduction in the exergoeconomic factor of all the devices but the reduction was significant in the HPP and the energy recovery Pelton turbine. Figure 5.77 shows the exergy efficiency of the overall system at different dead state temperature values with three different feed water temperature values. Generally, increasing the seawater source temperature causes an increase in the exergy efficiency. However, the exergy efficiency deceases with increasing the dead state temperature.

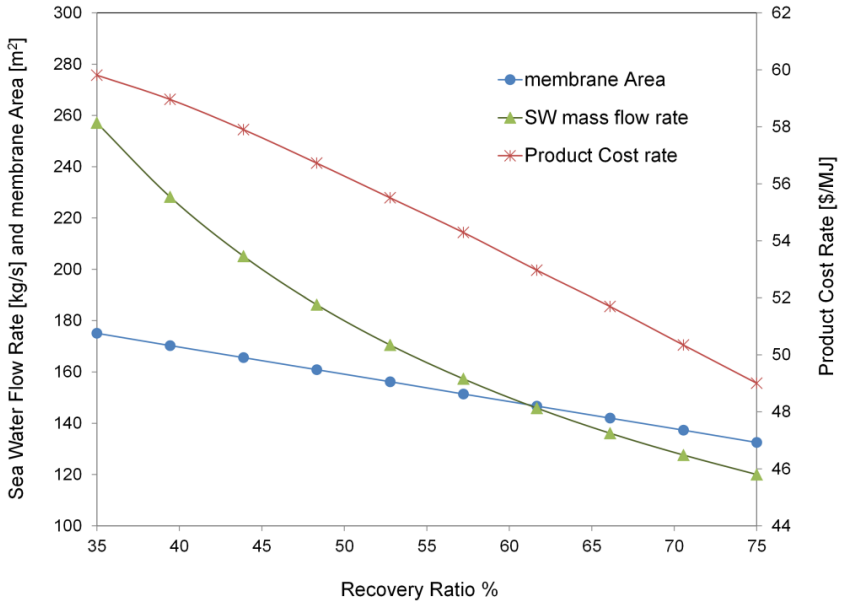

Figure 5.71 Effect of the recovery ratio on the seawater fed mass flow rate, the membrane area and product cost rate per unit energy input

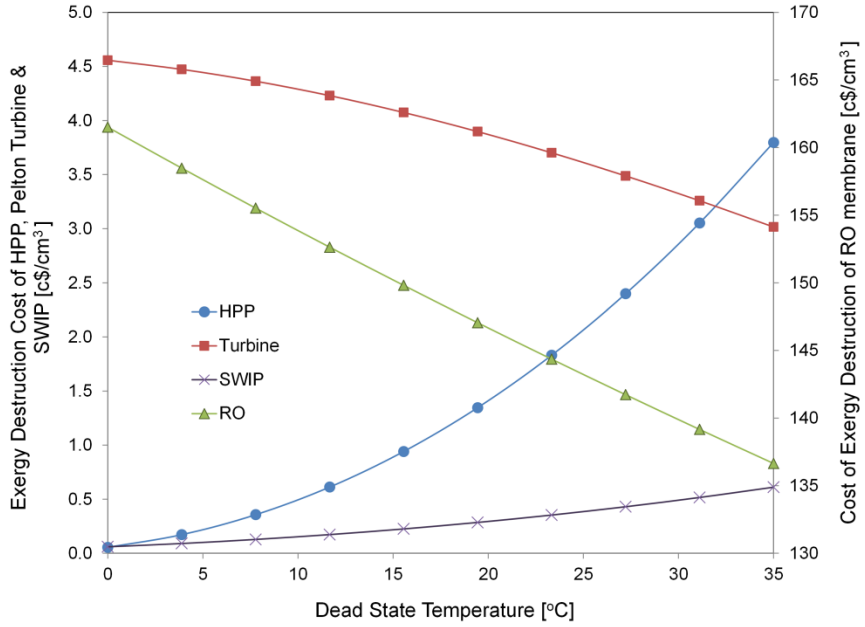

Figure 5.72 Effect of dead state temperature on the cost associated with exergy destruction in the major system components

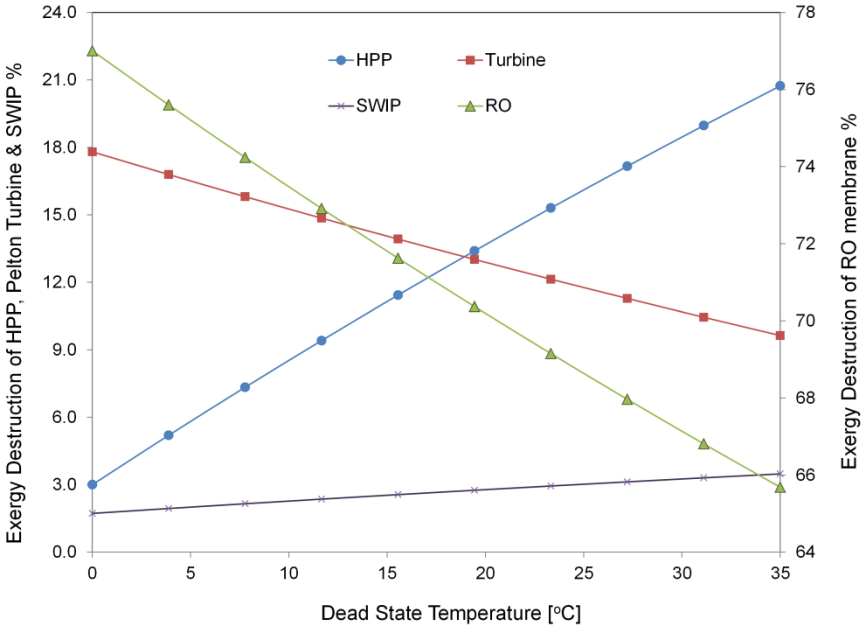

Figure 5.73 Effect of dead state temperature on the exergy destruction in the major system components as a percentage of the total exergy destruction in the system

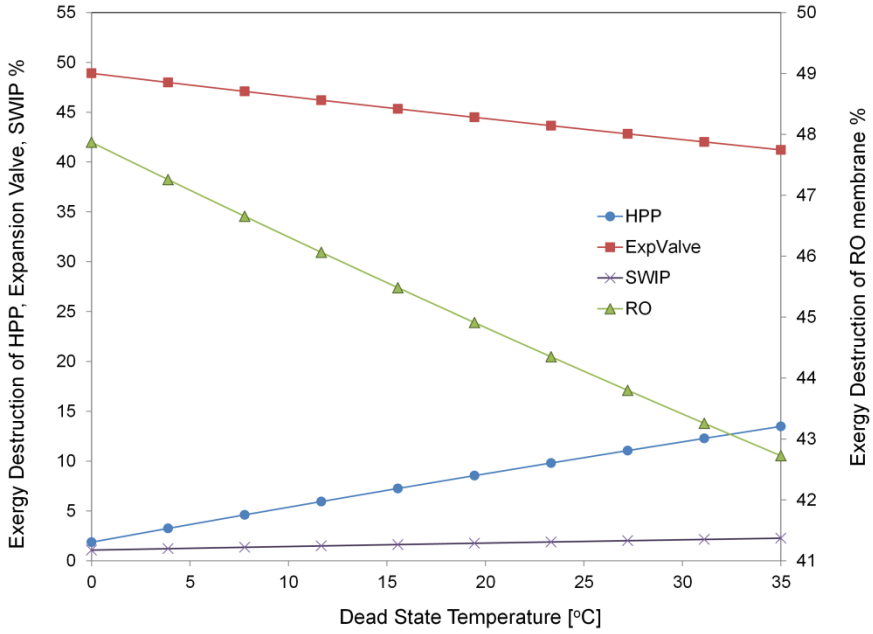

Figure 5.74 Effect of dead state temperature on the exergy destruction ratios as a percentage of the total exergy destruction without using energy recovery Pelton turbine

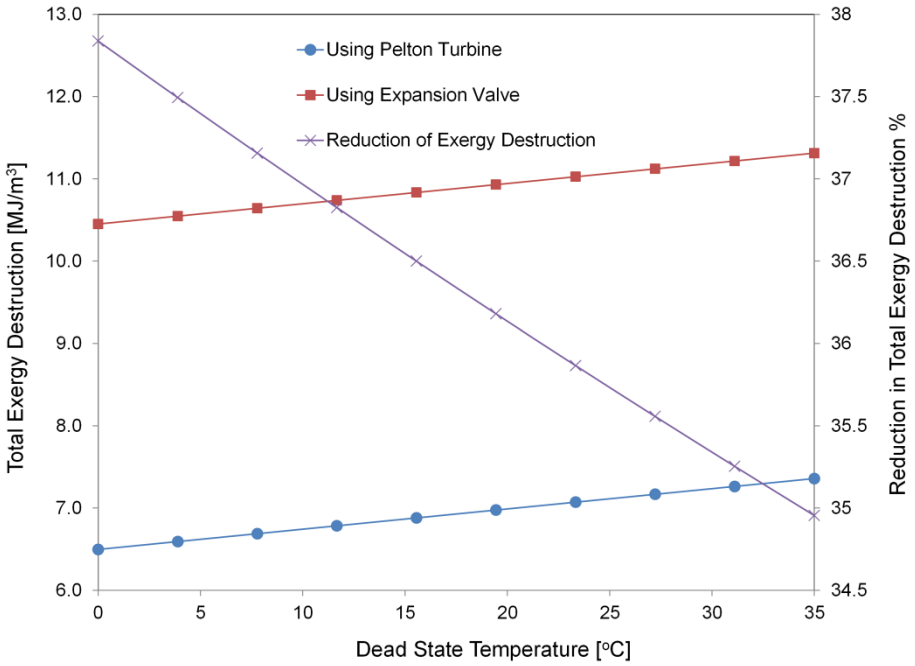

Figure 5.75 Effect of using energy recovery Pelton turbine on the total exergy destruction at different dead state temperature values

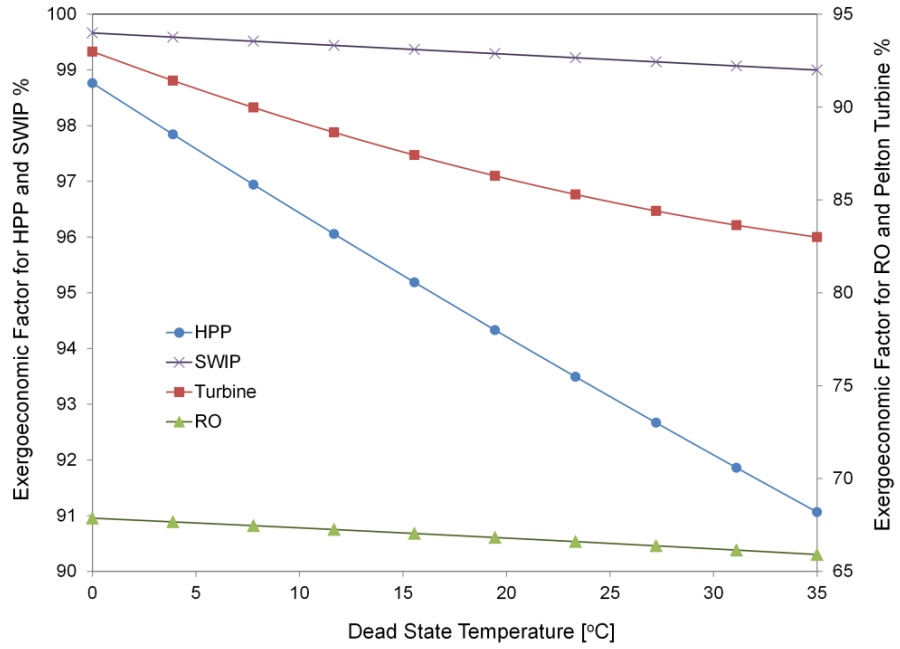

Figure 5.76 Effect of dead state temperature on the exergoeconomic factor of the major system components

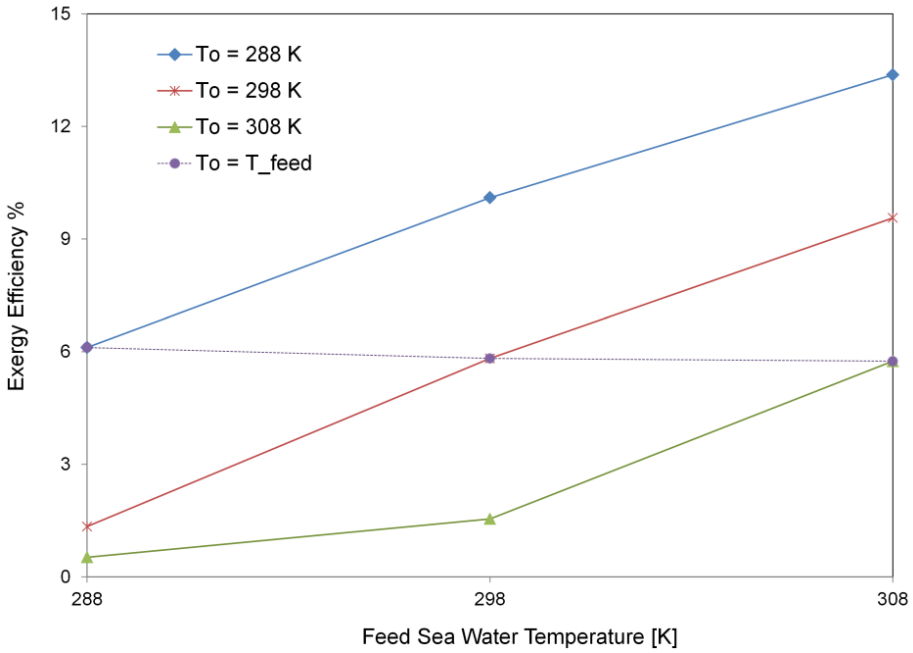

Figure 5.77 Exergy efficiency of the SWRO plant vs seawater feeding temperature values at different values of dead state temperatures

5.4 OTHER SYSTEMS

5.4.1 Coal Gasification-SOFC-Gas Turbine

Based on the thermodynamic model of the system, an EES (Engineering Equation Solver) code is written to study the performance of the system components. The results of this system are discussed in El-Emam et al. (2012). Table 5.15 shows the performance data in the system analyses. A parametric study is performed to investigate the effects of changing the pressure ratio through the system on the exergetic performance of different system components. Comparisons between two different types of supply fuels to the gasifier are performed. The exergy destruction and exergy efficiency of different components are studied. Based on an energy analysis of the system for the case 1 type of fuel, the power produced by the steam turbine is 5.41 MW. The fuel cell produces 12.8 MW of electric work at 55.8% energy efficiency. The gas turbine network output is 19.3 MW. Under the same operating conditions, the overall energy and exergy efficiencies of the system were calculated as 38.1% and 27%, respectively. As a comparison with the overall performance of the integrated system, using the case 2 type of fuel results in overall energy and exergy efficiencies of 36.7%, and 23.2%, respectively. The analyses and results in Figures 5.79 to 5.83 are performed at a compressor pressure ratio of 15. Table 5.15 shows the data of the system performance and Table 5.16 shows the gas composition for case 1 at different states corresponding to Figure 4.8.

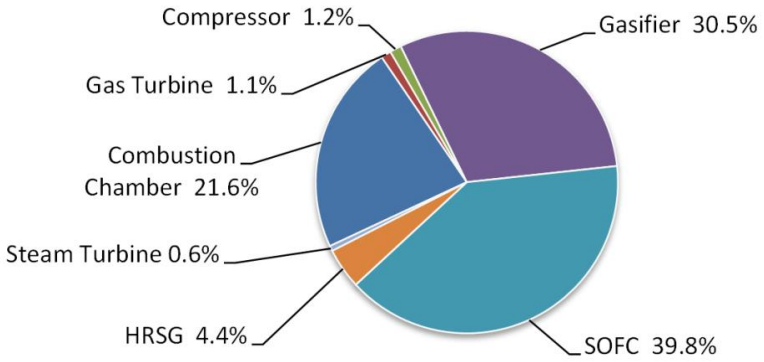

Figure 5.78 Exergy destruction in the system components for case 1

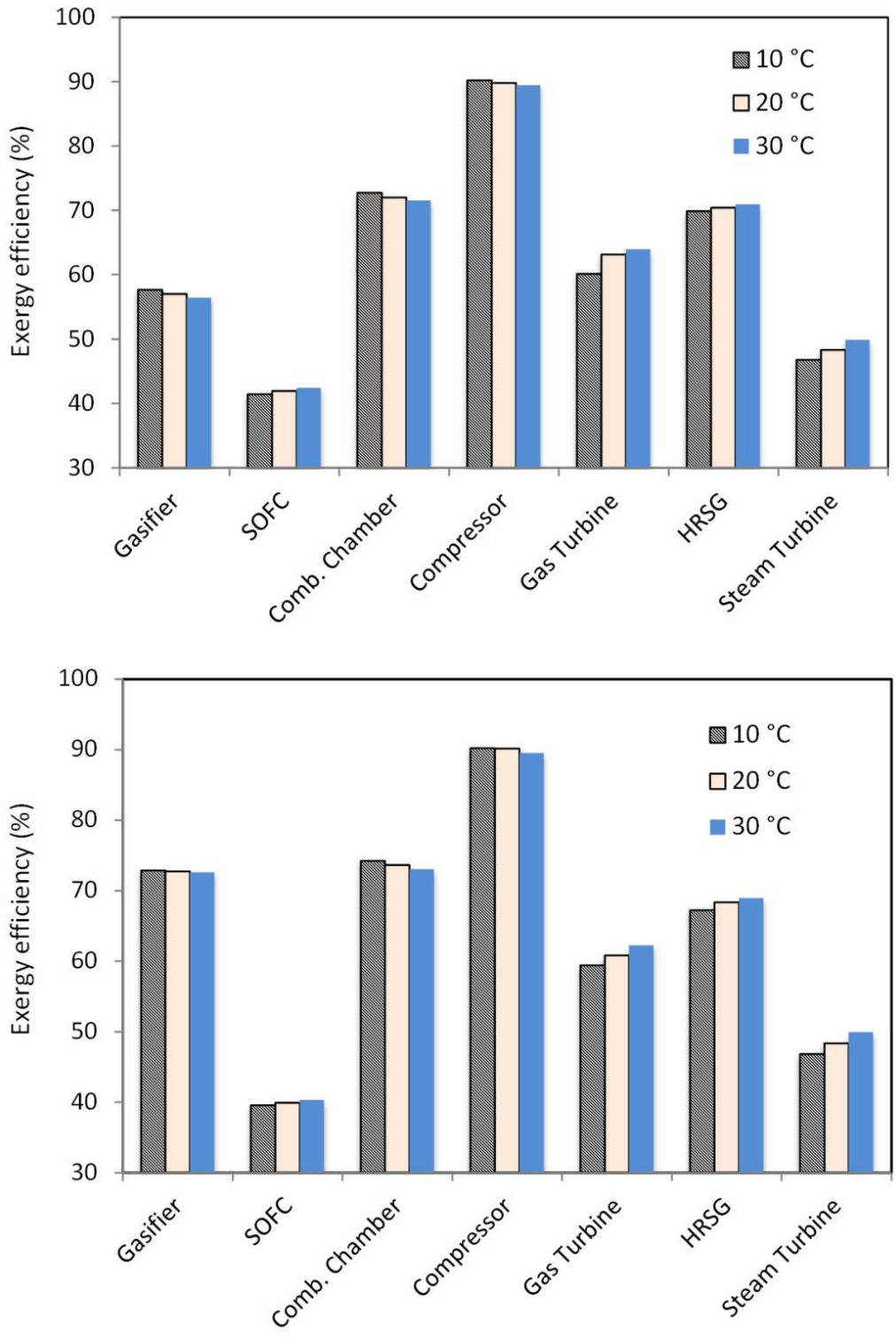

Figure 5.79 Exergy efficiency in the system components for cases (a) 1 and (b) 2

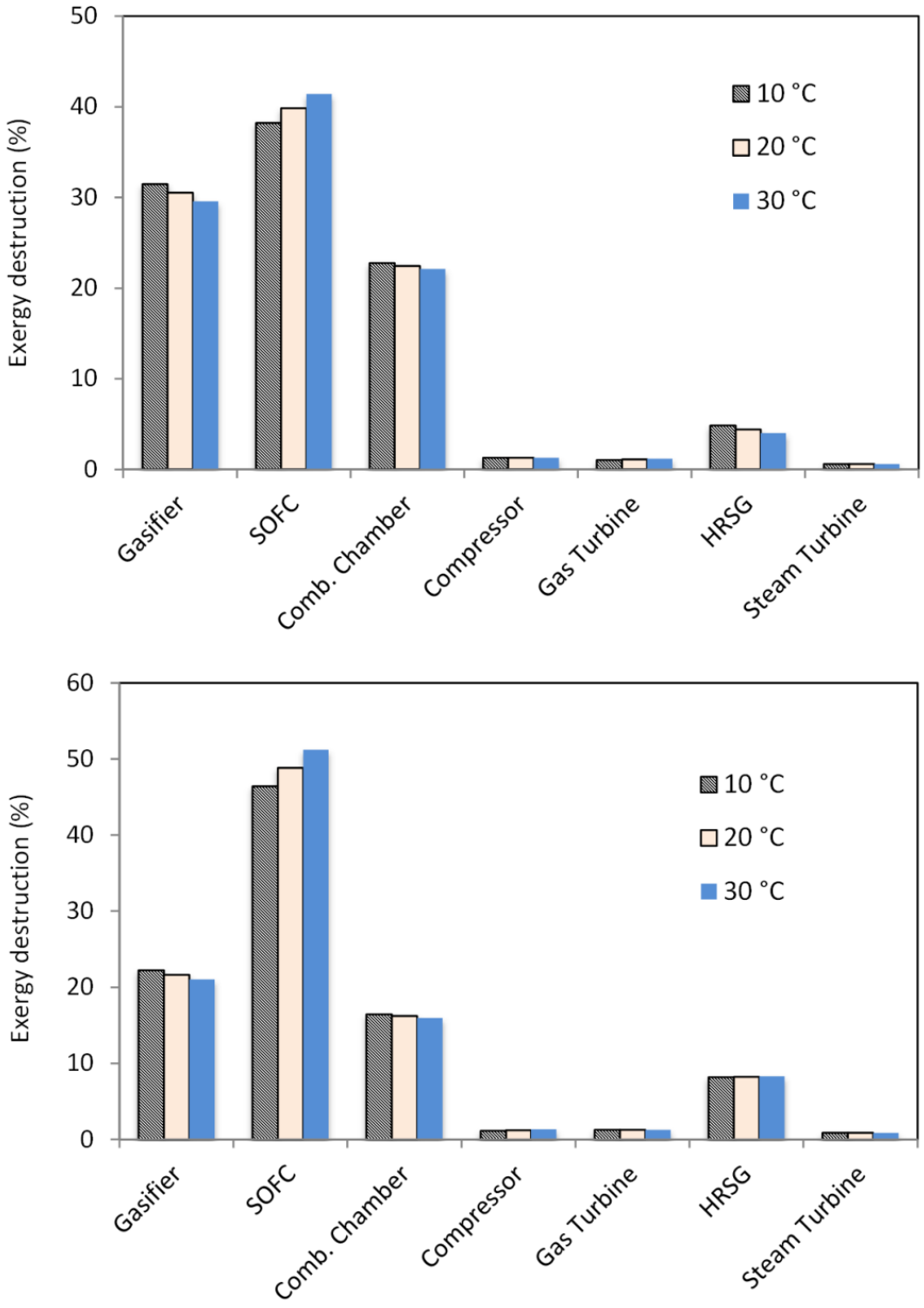

Figure 5.80 Exergy destruction in components as percentage of total exergy destruction for cases (a) 1 and (b) 2

The exergy destruction in the system component for case 1 is shown as a percentage of the total exergy destruction in the whole system in Figure 5.78. The most significant exergy destruction occurs in the fuel cell. Significant exergy destruction can also be noticed in the gasifier, combustion chamber and the HRSG as well. Figure 5.79 shows the effect of changing the reference temperature on the exergetic performance of different components of the system for the two different types of coal. The performance is characterized by the exergy efficiency of the devices. Three different values of reference temperature have been studied: 10, 20 and 30^{o}C, respectively.

In Figure 5.80, the devices performances are presented based on the exergy destruction as a percentage of the total exergy destruction within the integrated system, at different reference temperature values, for two different cases. In Figure 5.80, it appears that the exergy destruction is affected by the change of reference temperature. Exergy destruction increases with temperature for the gasifier, combustion chamber and HRSG, however it decreases for the fuel cell, as it is shown for the two cases. The results shown in Figure 5.81 compare between the exergy destruction as a percentage of the exergy of the fuels fed for different devices in cases 1 and 2, at the reference temperature of 20^{o}C.

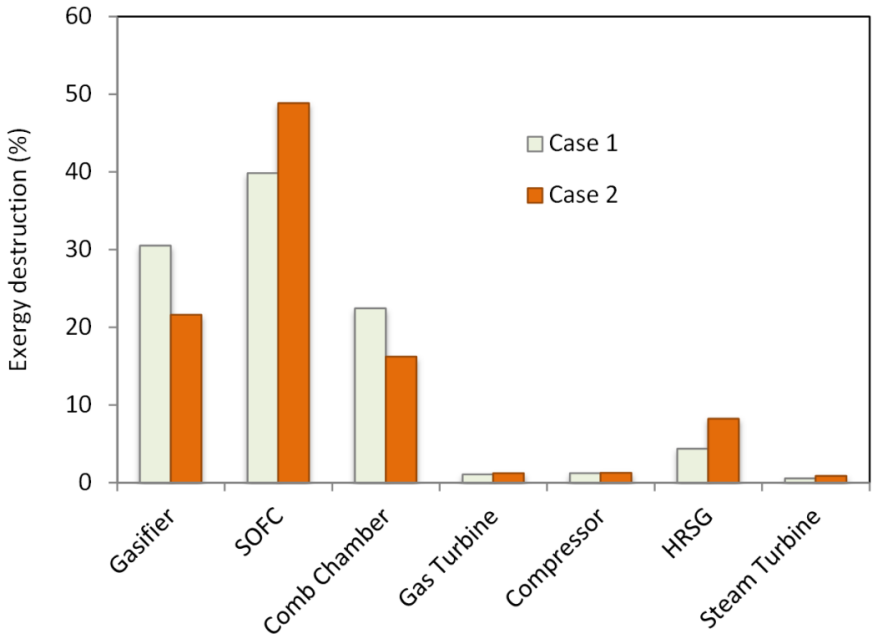

Figure 5.81 Exergy destruction as a percentage of the total fuel exergy input for cases 1 and 2 at T_o = 20^{o}C

Figure 5.82 shows a comparison between the exergy efficiency of different devices performing in case 1 and 2. Figures 5.83 to 5.85 show the effects of changing the pressure ratio of the gas turbine compressor on the exergetic performance of the gasifier, fuel cell and combustion chamber, where the dominant exergy destruction occurred. The exergetic performance is presented by the exergy efficiency and the exergy destruction as a percentage of the exergy of fuel input. Two different fuel cell operating temperatures are investigated for the fuel cell and the combustion chamber. The fuel cell operating temperature has no effect on the gasifier. Figure 5.83 shows that increasing the pressure ratio enhances the exergy efficiency of the gasifier. The output syngas will be at a higher pressure and temperature, causing a higher exergy output of the system. For the solid oxide fuel cell, Figure 5.84, increasing the pressure ratio decreases the exergy destruction. This is might be as a result of the increase of the fuel cell work with the increase of the pressure ratio, so the exergy destruction decreases and exergy efficiency increases. On the other hand, increasing the fuel cell operating temperature decreases the exergy efficiency of the fuel cell and the exergy destruction increases.

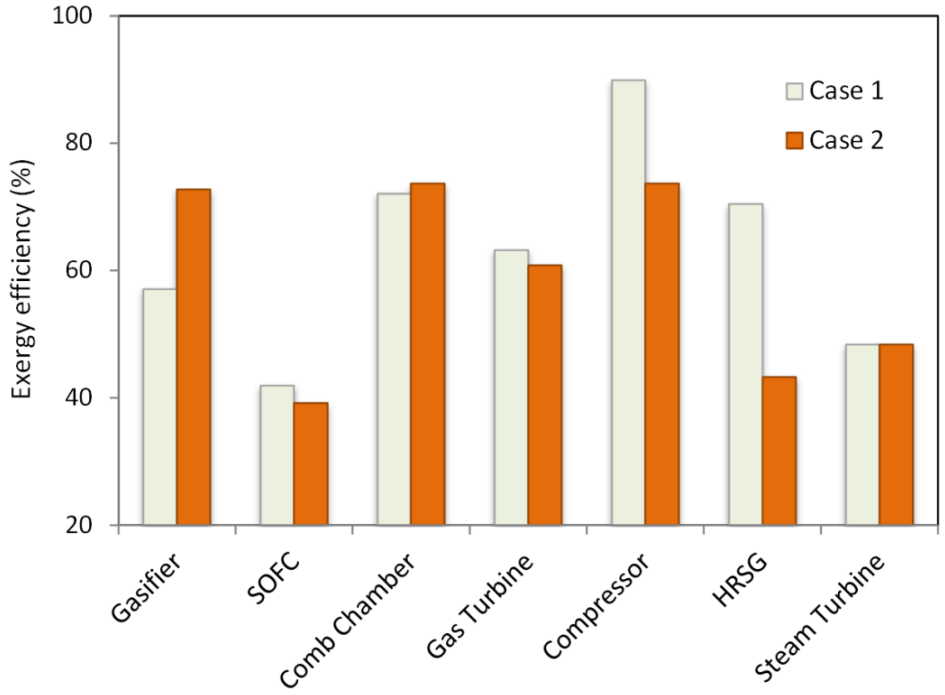

Figure 5.82 Exergy efficiency of the system components for cases 1 and 2 at $T_o = 20^oC$

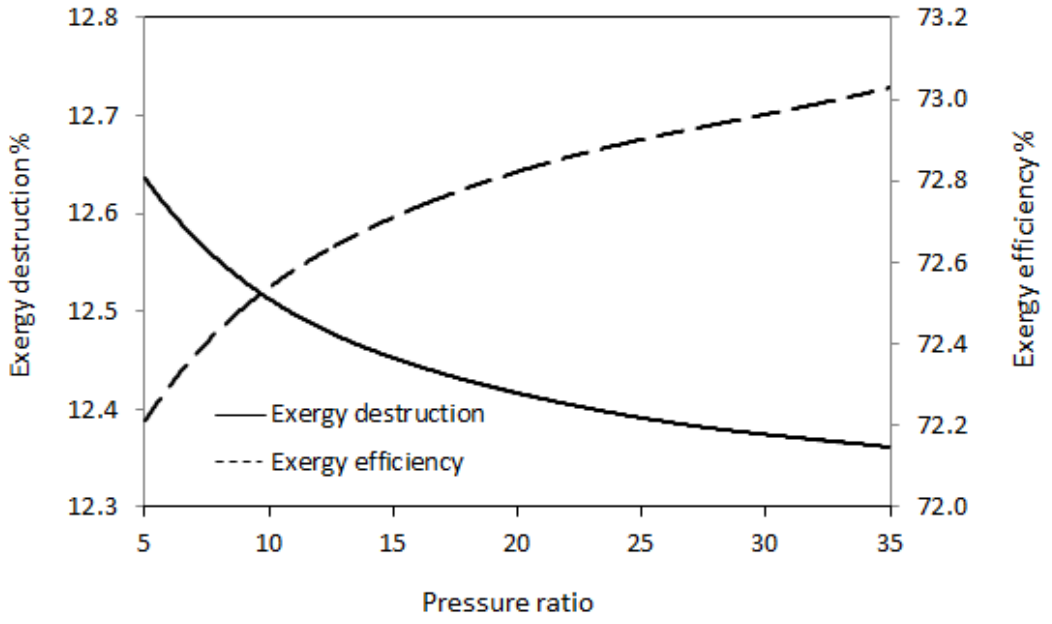

Figure 5.83 Pressure ratio effect on the performance of the gasifier

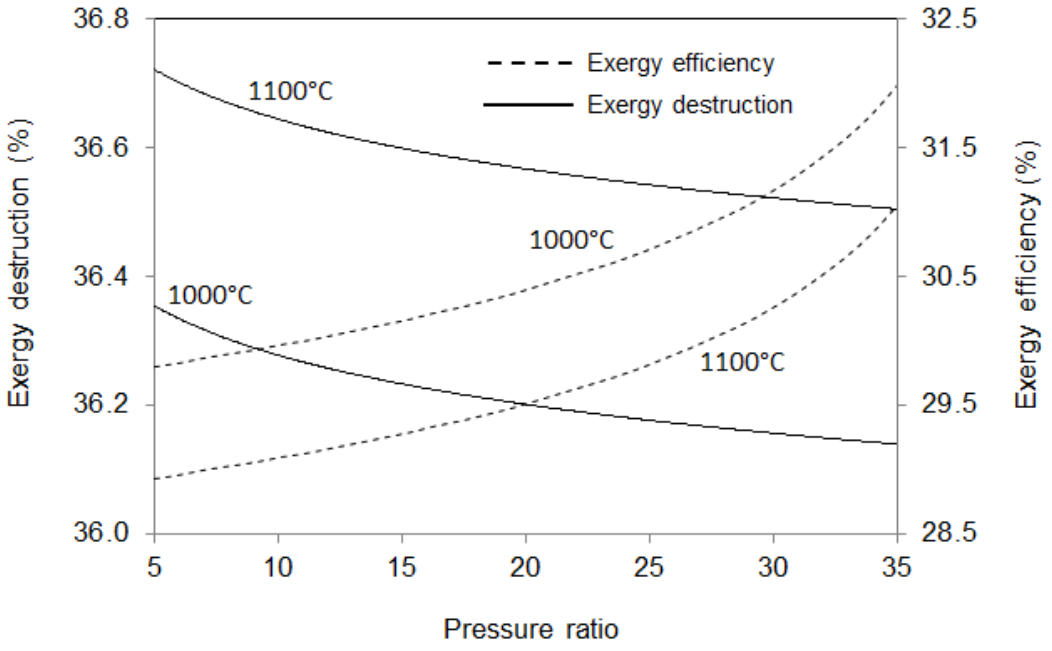

Figure 5.84 Pressure ratio effect on the fuel cell performance at different fuel cell operating temperatures

Figure 5.85 shows the effect of pressure ratio variation on the combustion chamber. Increasing the pressure ratio causes a decrease in the combustible gases in the exhaust of fuel cell, which is directed to the combustion chamber. This implies a reduction in the extent of combustion, and decrease in exergy destruction of the combustion chamber. However, after a pressure ratio value of 25, performance enhancements is lower, due to mixing with natural gas. Increase in fuel cell temperature increases its exit flow delivered to the combustion chamber, causing higher exergy destruction in the combustion chamber.

Table 5.15 Performance data for the system operation in the base case

Performance parameters (assumed)	
Compressor pressure ratio	15
Gas turbine inlet temperature, K	1450
SOFC operating temperature, K	1273
Steam turbine inlet temperature, K	823
Steam turbine inlet pressure, bar	80
Coal feeding rate, tons/hr	6.69
Gas turbine isentropic efficiency, %	85
Compressor isentropic efficiency, %	85
Pump isentropic efficiency, %	96
Atmospheric air; O_2, N_2 (% vol.)	21, 79

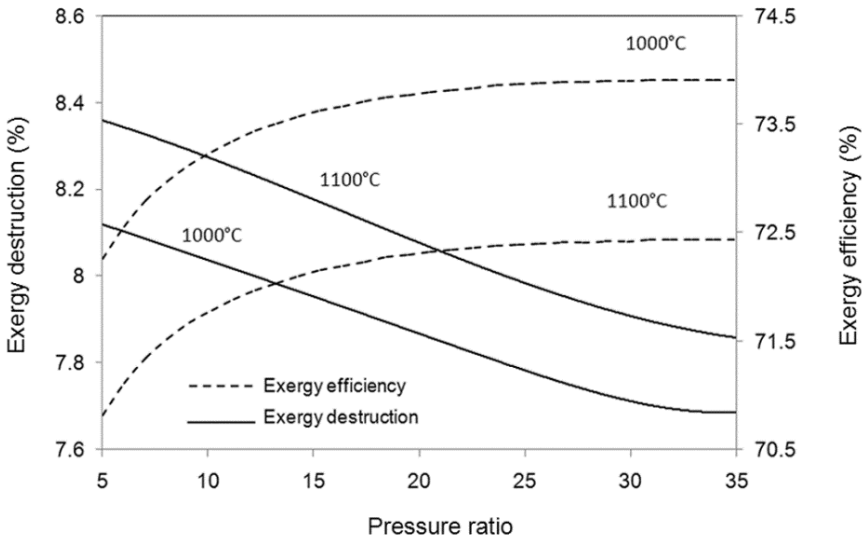

Figure 5.85 Pressure ratio effect on the combustion chamber performance at different fuel cell operating temperatures

Table 5.16 Gas state point data and composition through the system for case 1

State	Temperature [K]	flow rate [tons/h]	Molar composition, %						
			CH_4	CO_2	CO	H_2	H_2O	O_2	N_2
1	293	84.67	0	0	0	0	0	21	79
2	733	84.67	0	0	0	0	0	21	79
3	1885	7.38	0.1	10.6	51.6	35.1	0	0	2.6
4	850	7.38	0.1	10.6	51.6	35.1	0	0	2.6
5	850	7.38	0.1	10.6	51.6	35.1	0	0	2.6
6	733	36.14	0	0	0	0	0	21	79
7	850	36.14	0	0	0	0	0	21	79
8	1273	43.52	0	14.87	0.25	3.13	5.44	8.88	67.43
9	1100	43.52	0	14.87	0.25	3.13	5.44	8.88	67.43
10	1450	117.07	0	9.844	0	0	11.57	1.202	77.38
11	746.6	117.07	0	9.844	0	0	11.57	1.202	77.38
12	435	117.07	0	9.844	0	0	11.57	1.202	77.38

5.4.2 Molten Carbonate Fuel Cell-Gas Turbine System

The analysis presented is applied to the system under consideration, with different values of operating parameters. It is found that the values of energy and exergy efficiency are as 42.89% and 37.75% for the overall system and 37.45% and 33.54% for the fuel cell device efficiency when operated at 650^{o}C, considering the environment temperature as 20^{o}C. The power generated from the fuel cell is 375.9 kW and the turbine work produced is 314.3 kW, and the net output power from the turbine is estimated as 190.4 kW. This model and its results are published elsewhere (El-Emam and Dincer, 2011).

The results shown in Figures 5.86 to 5.88 represent the fuel cell and overall system performance at fuel cell operating temperature of 650^{o}C, environment temperature of 20^{o}C and pressure of 4.5 bar.

Figure 5.86 represents the cell voltage output and the fuel cell and overall energy efficiency vs. current density at fuel cell operating temperature of 650^{o}C. It can be seen that the increase of current density, decreases cell voltage, as it is expected. The energy efficiency for the fuel cell starts with an increasing trend till it reaches a maximum value at the current density of 364 mA/cm^2, and then it decreases with increasing the current density. The same trend occurs for the curve representing the energy efficiency of the hybrid system.

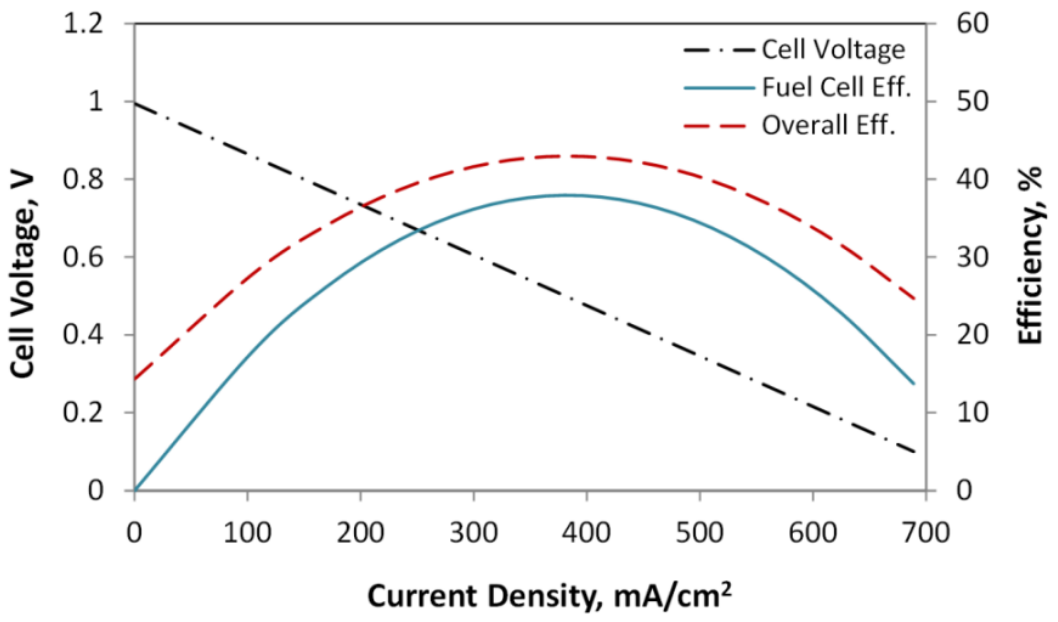

Figure 5.86 Cell Voltage and energy efficiencies of the fuel cell and the overall system vs. current density at 650^{o}C

In Figure 5.87, the variation of exergy destruction and energy and exergy efficiencies of the fuel cell device are shown with varying current density at fuel cell operating temperature of 650^{o}C. It is clear that the energy and exergy efficiency have the same trend, increasing with the increase of current density and reach a peak of 37.45% and 33.54%, respectively, at current density value of 364 mA/cm^{2}, then start to decrease with increasing the current density.

The energy efficiency values are higher than exergy efficiency curve because of the difference between the fuel energy and exergy contents. The exergy destruction curve shown in Figure 5.87 shows that the exergy destruction values decrease with the increase of current density tell it reach the minimum value of 41 kW. The produced power of the fuel cell variation with current density is shown in Figure 5.88 at fuel cell operating temperature of 650^{o}C; also the energy and exergy efficiencies of the overall system are presented.

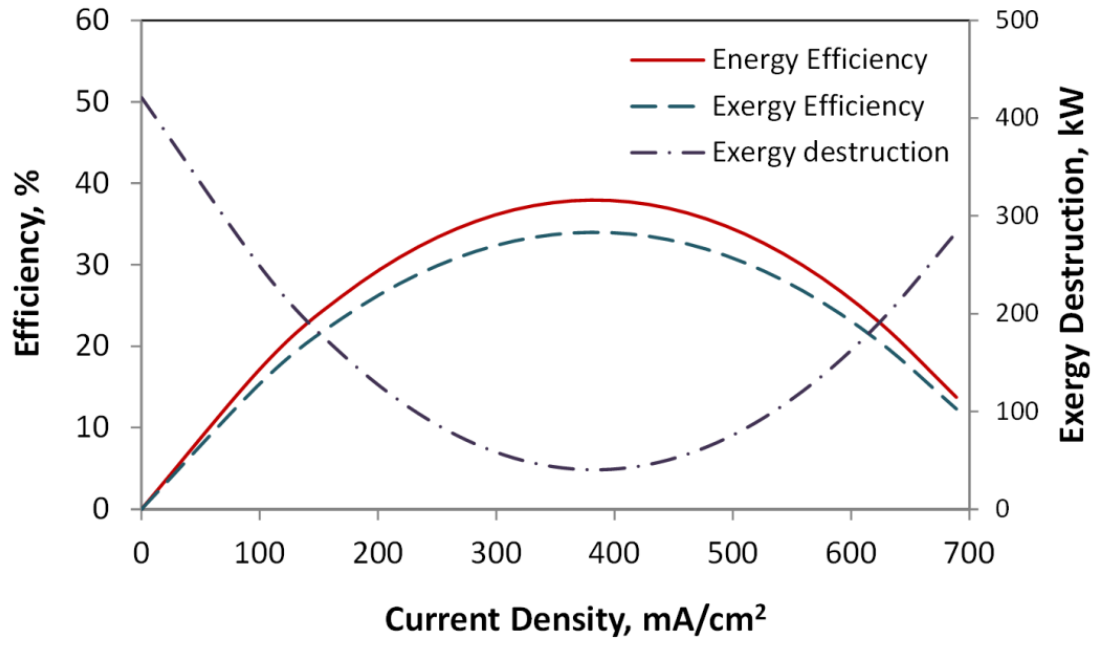

Figure 5.87 Energy and exergy efficiencies and exergy destruction of the fuel cell vs. current density at 650°C

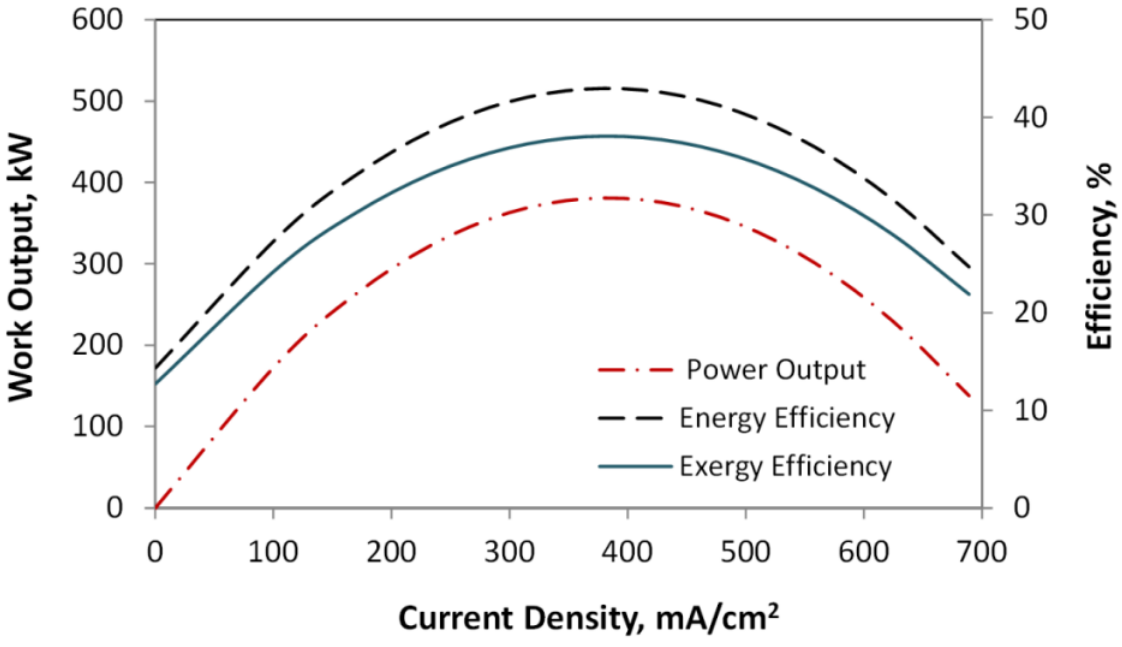

Figure 5.88 The MCFC output power and overall hybrid energy and exergy efficiencies vs. current density at 650°C

Figure 5.89 shows the exergy destruction of different devices of the hybrid system as a percentage of the total exergy destruction in these devices. It is important to work in minimizing the exergy destruction, which is caused by the systems irreversibilities, to increase the exergy efficiency of these devices operation.

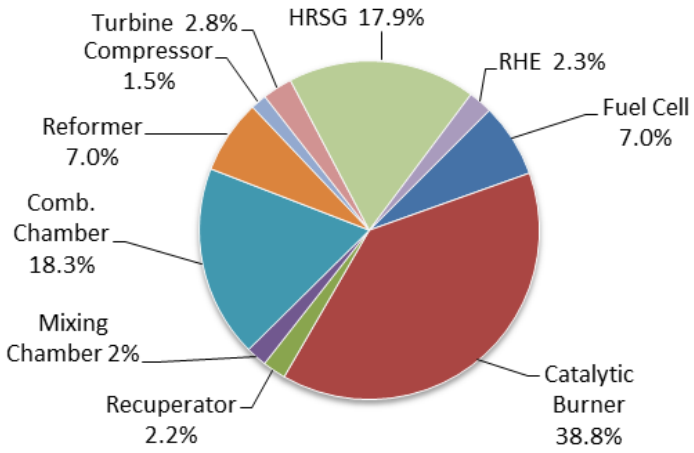

Figure 5.89 Exergy destruction in different devices in the hybrid system

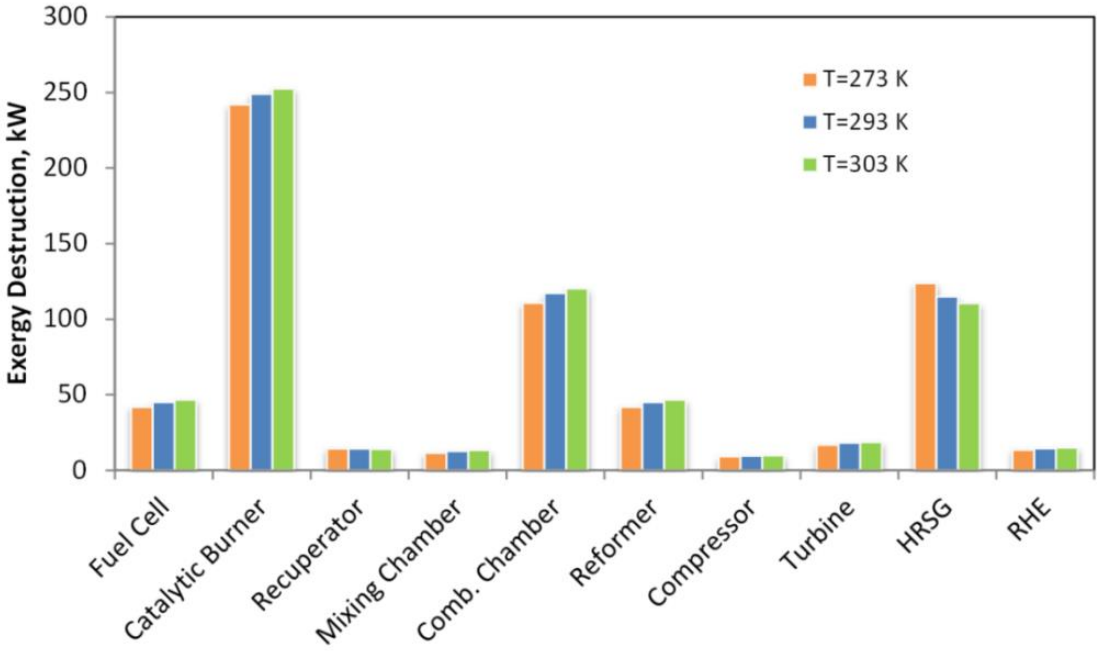

Figure 5.90 Effect of changing the reference temperature on exergy destruction of different devices in the system

The exergy destruction is mainly affected by the surrounding conditions. Figure 5.90 shows the effect of changing the value of the environment temperature on the exergy destruction occurred in the different devices in the system. The exergy can be calculated as the entropy generation times the surrounding temperature, so decreasing the entropy generation will lead to decrease of the exergy destruction. Figure 5.91 shows also the effect of changing the environment temperature on the exergy efficiency of different devices of the hybrid system.

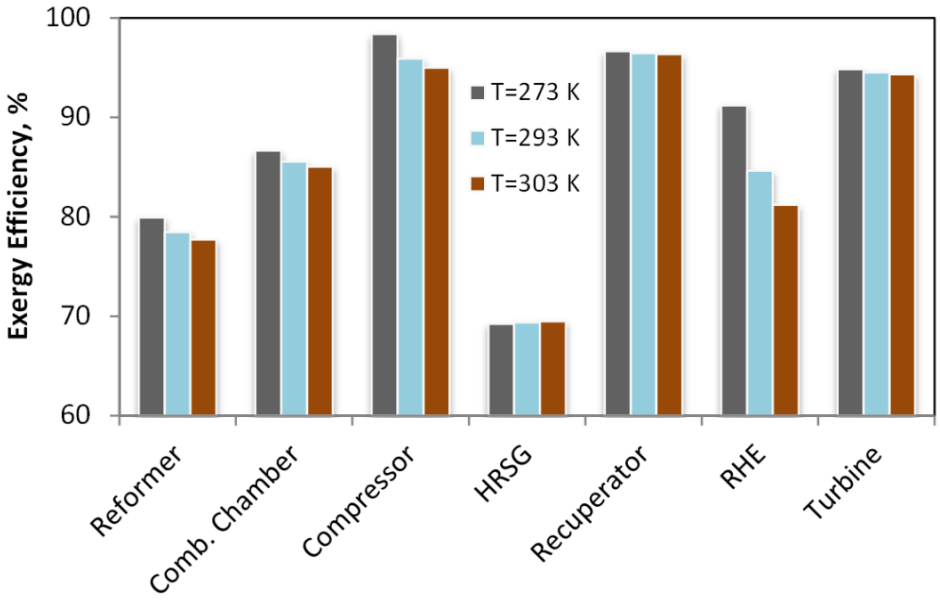

Figure 5.91 Effect of changing the reference temperature on exergy efficiency of different devices in the system

Chapter 6

CONCLUSIONS AND RECOMMENDATIONS

6.1 CONCLUSIONS

Multigeneration energy systems use the waste heat of their main prime mover to sustain a simultaneous production of heat, cooling, fresh water, hot water and hydrogen production, besides electric power production. These applications are of great importance and receive a great deal of attention because of the high and efficient performance and the environmentally benign operation of these systems.

In system 1, multigeneration integrated energy system, driven by solar dish concentrators and biomass gasification–SOFC, is studied. The system is designed to provide electric power, cooling, and hydrogen production. The power output of the system is provided from regenerative helium gas turbine during day time, and from SOFC unit at night time. The fuel cell stack number is calculated to provide the same net power.

- For the overall system, operating for one day on both solar dish, when solar radiation is available, and biomass gasification, when the solar power is not available, the highest exergy destruction occurs in the gasification system. This is due to the irreversibilities associated with exergy destruction due to the chemical reactions occurring in the gasifier, SOFC and the burner, also due the high operating temperature of these components.
- The system operates at 39.99% energy efficiency and 27.47% exergy efficiency when operates at the optimum point selected based on the optimization results.
- The receiver temperature controls the performance of the helium gas turbine as the hot source temperature. The overall system efficiency decreases with the higher receiver temperature, with lower effect on the exergy efficiency compared with energy efficiency. The cost rate is highly affected by the receiver temperature.
- The turbine compression ratio affects both energy and exergy efficiencies of the system performance. For the day assessment, the energy and exergy efficiency

increases, however, considering the solar driven period, the exergy efficiency of the overall system reaches a peak of 56.04% before it starts to decrease.

- The gasification temperature affects the gasification driven system performance; hence, the overall day performance is affected. Increasing the gasification temperature causes a reduction in the system energy and exergy efficiencies.
- From the optimization study results, the system should be designed with high turbine and compressor isentropic efficiencies. The lower the heat exchangers effectiveness, the less efficient the system is, yet the higher the cost.
- Environmental assessment is performed through the estimation of carbon dioxide emissions and how it is affected by the other operating parameters, and through including the environmental cost in as a cost parameter.
- Exergetic performance and losses map are presented to describe the gas turbine performance at different operating points.
- Steam to biomass ratio has a great effect on gasification performance and the produced gas species concentrations.
- Optimum steam to biomass ratio for maximum hydrogen exergy efficiency for the base case is 0.677.
- The effect of gasification temperature on the hydrogen efficiency is significant where higher energy and exergy efficiency values are achieved at lower gasification temperature values.

In system 2, organic Rankine cycle driven by solar parabolic trough is designed to provide electric power. The system is integrated with desalination unit, absorption chiller system and electrolyzer for covering the demands of fresh water and cooling and producing hydrogen. The system is also providing domestic hot water. The integrated system is analyzed, assessed and optimized. Several parametric studies are performed to understand and assess the system performance. Different ORC operating parameters are tested and their effect on the performance is evaluated.

- Increasing the turbine inlet pressure causes an increase in both energy and exergy efficiency, however, the exergy efficiency starts to decrease after reaching a peak

point. The pressure value, at which the maximum exergy is calculated, increases with higher turbine inlet temperature.

- The solar trough performance is assessed with respect to the operating parameters of the organic Rankine cycle.
- The total trough area and the heat transfer fluid are presented with respect to the operating pressure and temperature values of the ORC turbine.
- The total cost rate is expressed against the overall exergy efficiency of the system for better understanding of the system performance at different operating parameters.
- The optimization results give a set of optimized points that satisfy the operation at maximum efficiency with minimum cost rate, with respect to the set of decision variables considered for the analysis.

In system 3, solar heliostat based integrated system is analyzed. The integrated system is designed for producing electric power, cooling, fresh water, hydrogen and domestic hot water. The performance of the system is measured by energy and exergy efficiencies. The effect of the solar radiation intensity on the receiver energy and exergy efficiencies is studies. The overall system efficiencies are affected by the receiver efficiency. The heliostat solar field is optimized based on the system operating parameters. Number of heliostats is calculated as 396 and the tower height as 63.3 m. As a summary of the results of RO system, the proposed SWRO desalination plant, integrated with the system, is considered for a comprehensive thermodynamic and thermoeconomic study. The main concluding remarks are as follows:

- The exergy efficiency of the overall system is 5.82%, and the product cost is 2.451 $\$/m^3$ for seawater source with salinity of 35000 ppm operating at $25^{\circ}C$.
- For the base case considered, the largest exergy destructions appear to be 67.8% for the RO module and 17.16% for the high-pressure pump.
- Using a Pelton turbine, as an energy recovery option, the exergy destruction is reduced by 35.5%, compared with the case using an expansion valve.
- Increasing the recovery ratio decreases the unit cost.

In conclusion of the coal gasification integrated system, coal gasification technology integrated with a solid oxide fuel cell is a promising alternative for energy

sustainability. As a conclusion of the analyses of the coal gasification integrated system, thermodynamic analyses based on energy and exergy are performed to investigate the performance of the integrated system and determine the extent of the system components to be enhanced for higher efficiency. Two different types of coal have been used in the gasification process. The total energy and exergy efficiencies of the system were calculated as 38.1% and 27%, respectively, for case 1, and 36.7% and 23.2%, respectively, for case 2. The effect of variations in pressure ratio of the gas turbine compressor on different devices has also been studied. For the gasifier, SOFC, and the combustion chamber, increasing the pressure ratio enhances the performance of these devices. It decreases the exergy destruction across the device. Increasing the fuel cell operating temperature causes more exergy destruction in the combustion chamber and the fuel cell. Three different reference temperature values are applied to study its effect on the exergetic performance of different devices.

In conclusion of the molten carbonate fuel cell integrated system, energy and exergy performance of the system has been investigated. Moreover, a parametric study was performed to examine the effect of different operating parameters on the efficiencies and irreversibilities of different compartments of the system. The maximum MCFC output power was estimated to be 314.3 kW when operates at 650^{o}C. The overall efficiencies were calculated as 42.89% and 37.75%, for energy and exergy efficiencies, respectively. The catalytic burner, HRSG and the combustion chamber show high values of exergy destruction which give a potential of improvement. Exergy destruction of different devices in the studied system is affected by changing the ambient temperature. Also, within the operating temperature range of the MCFC the energy and exergy efficiencies of the MCFC and the overall system increases with increasing the temperature.

6.2 RECOMMENDATIONS

The results and analyses presented in this thesis can be helpful in the design of new advanced integrated energy systems for multigeneration purposes. From the performed analyses, the following studies should be considered for future work:

- Designing and building the integrated energy systems presented in this study, by studying the potential of converting existing plants to multigeneration systems.
- Conducting experimental investigations on these integrated energy systems to achieve better understanding of the integrated systems operation.
- Studying various exergy, exergoeconomic and environmental impact parameters of these integrated systems to be able to identify the potential avoidable exergy destruction portions and their effect on the economics of the integrated systems and the associated environmental impact.
- Further optimization analyses on these systems by considering other operating conditions and parameters which includes applying different techniques of optimization, decision variables and objective functions.

References

Abuadala, A., Dincer, I., 2012. A review on biomass-based hydrogen production and potential applications. International Journal of Energy Research 36, 415-455.

Abuadala, A., Dincer, I., Naterer, G.F., 2010. Exergy analysis of hydrogen production from biomass gasification. International Journal of Hydrogen Energy 35, 4981-4990.

Agbossou, K., Chahine, R., Hamelin, J., Laurencelle, F., Anouar, A., St-Arnaud, J.-M., Bose, T.K., 2001. Renewable energy systems based on hydrogen for remote applications. Journal of Power Sources 96, 168-172.

Ahmadi, P., Almasi, A., Dincer, I., 2012. Multi-objective optimization of a combined heat and power (CHP) system for heating purpose in a paper mill using evolutionary algorithm. International Journal of Energy Research 36, 46-63.

Ahmadi, P., Dincer, I., Rosen, M.A., 2011. Exergy, exergoeconomic and environmental analyses and evolutionary algorithm based multi-objective optimization of combined cycle power plants. Energy 36, 5886-5898.

Ahmadi, P., Dincer, I., Rosen, M. A., 2013. Energy and exergy analyses of hydrogen production via solar-boosted ocean thermal energy conversion and PEM electrolysis. International Journal of Hydrogen Energy, 38, 1795-1805.

Akkaya, A.V., Sahin, B., Huseyin Erdem, H., 2008. An analysis of SOFC/GT CHP system based on exergetic performance criteria. International Journal of Hydrogen Energy 33, 2566-2577.

Al-Sulaiman, F., Dincer, I., Hamdullahpur, F., 2010. Exergy analysis of an integrated solid oxide fuel cell and organic Rankine cycle for cooling, heating and power production. Journal of Power Sources 195, 2346-2354.

Al-Sulaiman, F.A., Dincer, I., Hamdullahpur, F., 2011. Exergy modeling of a new solar driven trigeneration system. Solar Energy 85, 2228-2243.

Algieri, A., Morrone, P., 2012. Comparative energetic analysis of high-temperature subcritical and transcritical Organic Rankine Cycle (ORC). A biomass application in the Sibari district. Applied Thermal Engineering 36, 236-244.

Aljundi, I.H., 2009. Second-law analysis of a reverse osmosis plant in Jordan. Desalination 238, 207-215.

Armstrong, P. R., 1978, Extension of the Hottel-Whillier equation to multi-stage collector systems. The American Solar Energy Society Conference, Denver, USA.

Athanasiou, C., Coutelieris, F., Vakouftsi, E., Skoulou, V., Antonakou, E., Marnellos, G., Zabaniotou, A., 2007. From biomass to electricity through integrated gasification/SOFC system-optimization and energy balance. International Journal of Hydrogen Energy 32, 337-342.

Autissier, N., Palazzi, F., Marechal, F., Van Herle, J., Favrat, D., Thermo-economic optimization of a solid oxide fuel cell, gas turbine hybrid system, Journal of Fuel Cell Science and Technology, 4(2), 2007, 123-129.

Badr, O., Probert, S.D., O'Callaghan, P.W., 1985. Selecting a working fluid for a Rankine-cycle engine. Applied Energy 21, 1-42.

Bang-Møller, C., Rokni, M., Elmegaard, B., 2011. Exergy analysis and optimization of a biomass gasification, solid oxide fuel cell and micro gas turbine hybrid system. Energy 36, 4740-4752.

Bang-Møller, C., Rokni, M., Elmegaard, B., Ahrenfeldt, J., Henriksen, U.B., 2013. Decentralized combined heat and power production by two-stage biomass gasification and solid oxide fuel cells. Energy 58, 527-537.

Barbir, F., 2013. PEM fuel cells. 2th ed. Waltham, Massachusetts. Elsevier.

Barlev, D., Vidu, R., Stroeve, P., 2011. Innovation in concentrated solar power. Solar Energy Materials and Solar Cells 95, 2703-2725.

Basu, P., 2006. Combustion and gasification in fluidized bed. CRC.

Basu, P., 2010. Biomass Gasification and Pyrolysis: Practical Design and Theory. Elsevier.

Bejan, A., 2006. Advanced Engineering Thermodynamics. Wiley.

Bejan, A., Tsatsaronis, G., Moran, M., 1996. Thermal Design and Optimization. John Wiely, NewYork.

Biba, V., Macak, J., Klose, E., Malecha, J., 1978. Mathematical modeling for the gasification of coal under pressure. Ind Eng Chem Process Des Dev. Industrial & Engineering Chemistry Process Design and Development 17, 92-98.

Bouzayani, N., Galanis, N., Orfi, J., 2007. Comparative study of power and water cogeneration systems. Desalination 205, 243-253.

Boyce, M.P., 2006. Gas Turbine Engineering Handbook, 3rd ed. Gulf Professional Publishing.

Bryden, K.M., Ragland, K., 1996. Numerical modeling of deep fixed bed combustor. Energy Fuel 10, 269-275.

Buck, R., Friedmann, S., 2007. Solar-Assisted Small Solar Tower Trigeneration Systems. Journal of Solar Energy Engineering 129, 349-354.

Calva, E.T., Núñez, M.P., Toral, M.A.R.g., 2005. Thermal integration of trigeneration systems. Applied Thermal Engineering 25, 973-984.

Campanari, S., Iora, P., 2004. Definition and sensitivity analysis of a finite volume SOFC model for a tubular cell geometry. Journal of Power Sources 132, 113-126.

Cao, J.-C., Liu, F.-Q., Qin, Z.-H., Cao, S.-H., Zhang, S.-F., 2004. Energy and exergy analysis, and thermoeconomic performance of a BCHP system. Journal of Dong Hua University (English Edition) 21, 36-42.

Carpentieri, M., Corti, A., Lombardi, L., 2005. Life cycle assessment (LCA) of an integrated biomass gasification combined cycle (IBGCC) with CO2 removal. Energy Conversion and Management 46, 1790-1808.

Cengel, Y.A., Boles, M.A., 2011. Thermodynamics an Engineering Approach, 7th ed. McGraw-Hill, New York.

Cerci, Y., 2002. Exergy analysis of a reverse osmosis desalination plant in California. Desalination 142, 257-266.

Chan, S.H., Khor, K.A., Xia, Z.T., 2001. A complete polarization model of a solid oxide fuel cell and its sensitivity to the change of cell component thickness. Journal of Power Sources 93 (2001), 130-140.

Chicco, G., Mancarella, P., 2005. Planning aspects and performance indicators for small-scale trigeneration plants, International Conference on Future Power Systems, pp. 6.

Chicco, G., Mancarella, P., 2006a. From cogeneration to trigeneration: profitable alternatives in a competitive market. Energy Conversion, IEEE Transactions on 21, 265-272.

Chicco, G., Mancarella, P., 2006b. Planning evaluation and economic assessment of the electricity production from small-scale trigeneration plants. WSEAS Transactions on Power Systems 1, 393-400.

Chicco, G., Mancarella, P., 2007. Trigeneration primary energy saving evaluation for energy planning and policy development. Energy Policy 35, 6132-6144.

Chirone, R., Marzocchella, A., Salatino, P., Scala, F., 1999. Fluidized Bed Combustion of High-Volatile Solid Fuels: an Assessment of Char Attrition and Volatile Matter Segregation, the 15th international conference on FBC, ASME.

Chua KJ, Yang WM, Er SS, Ho CA. Sustainable energy systems for a remote island community. Applied Energy 2014;113:1752–63.

Cipollina, A., Micale, G., Rizzuti, L., 2009. Seawater Desalination: Conventional and Renewable Energy Processes. Springer.

Colpan, C.O., Dincer, I., Hamdullahpur, F., 2007. Thermodynamic modeling of direct internal reforming solid oxide fuel cells operating with syngas. International Journal of Hydrogen Energy 32, 787-795.

Conn, R.W., Kuo, S.C., 1976. An advanced conceptual tokamak fusion power reactor utilizing closed cycle helium gas turbines. Nuclear Engineering and Design 39, 45-72.

Costamagna, P., Honegger, K., 1998. Modeling of Solid Oxide Heat Exchanger Integrated Stacks and Simulation at High Fuel utilization. Journal of The Electrochemical Society 145, 3995-4007.

Criscuoli, A., Drioli, E., 1999. Energetic and exergetic analysis of an integrated membrane desalination system, Proceedings of the 1999 European Conference on Desalination and the Environment, November 9, 1999 - November 12, 1999, 1-3 ed. Elsevier, Las Palmas, Spain, pp. 243-249.

Croper, M., 2004. Fuel Cell Market Survey: Niche Transport, Fuel Cell Today.

Crowder, M.L., Gooding, C.H., 1997. Spiral wound, hollow fiber membrane modules: A new approach to higher mass transfer efficiency. Journal of Membrane Science 137, 17-29.

Davidson, J.F., Harrison, O., 1963. Fluidized Particles. Cambridge Univ. Press.

De Simon, G., Parodi, F., Fermeglia, M., Taccani, R., 2003. Simulation of process for electrical energy production based on molten carbonate fuel cells. Journal of Power Sources 115, 210-218.

Dicks, A.L., 2004. Molten carbonate fuel cells. Current Opinion in Solid State and Materials Science 8, 379-383.

Dincer, I., Rosen, M.A., 2004. Exergy as a driver for achieving sustainability. International Journal of Green Energy 1, 1-19.

Dincer, I., Rosen, M.A., 2013. Exergy : energy, environment, and sustainable development. 2th ed. Elsevier.

DOE, 2003. Cogeneration or Combined Heat and Power. Office of Energy Efficiency and Renewable Energy: US Department of Energy.

Drioli, E., Curcio, E., Di Profio, G., Macedonio, F., Criscuoli, A., 2006. Integrating membrane contactors technology and pressure-driven membrane operations for seawater desalination - energy, exergy and costs analysis. Chemical Engineering Research & Design 84, 209-220.

Dryer, F.L., Glassman, I., 1973. High-temperature oxidation of CO and CH4. Symposium (International) on Combustion 14, 987-1003.

EIA, 2014. International Energy Outlook 2014. US Energy Administration Information, US DOE.

El-Dessouky, H.T., Ettouny, H.M., 2002. Fundamentals of Salt Water Desalination. Elsevier.

El-Emam, R.S., Dincer, I., 2014a. Performance Assessment of a Recuperative Helium Gas Turbine System, in: Dincer, I., Midilli, A., Kucuk, H. (Eds.), Progress in Exergy, Energy, and the Environment. Springer International Publishing, pp. 251-266.

El-Emam, R.S., Dincer, I., 2011. Energy and exergy analyses of a combined molten carbonate fuel cell – Gas turbine system. International Journal of Hydrogen Energy 36, 8927-8935.

El-Emam, R.S., Dincer, I., 2013. Exergy and exergoeconomic analyses and optimization of geothermal organic Rankine cycle. Applied Thermal Engineering 59, 435-444.

El-Emam, R.S., Dincer, I., 2014b. Thermodynamic and thermoeconomic analyses of seawater reverse osmosis desalination plant with energy recovery. Energy 64, 154-163.

El-Emam, R.S., Dincer, I., Naterer, G.F., 2012. Energy and exergy analyses of an integrated SOFC and coal gasification system. International Journal of Hydrogen Energy 37, 1689-1697.

Fanchi, J.R., 2004. Energy: Technology and Directions for the Future. Elsevier.

Fiorentino, M., Marzocchella, A., Salatino, P., 1997. Segregation of fuel particles and volatile matter during devolatilization in a fluidized bed reactor—I. Model development. Chemical Engineering Science 52, 1893-1908.

Fiorenza, G., Sharma, V.K., Braccio, G., 2003. Techno-economic evaluation of a solar powered water desalination plant. Energy Conversion and Management 44, 2217-2240.

Franco, A., Villani, M., 2009. Optimal design of binary cycle power plants for water-dominated, medium-temperature geothermal fields. Geothermics 38, 379-391.

Frutschi, H.U., 2005. Closed-Cycle Gas Turbines. ASME.

Fryda, L., Panopoulos, K.D., Karl, J., Kakaras, E., 2008. Exergetic analysis of solid oxide fuel cell and biomass gasification integration with heat pipes. Energy 33, 292-299.

Gandhidasan, P., 1993. Thermodynamic Analysis of a Closed-Cycle, Solar Gas-Turbine Plant. Energy Conversion and Management 34, 657-661.

Genç, G., Çelik, M., Serdar Genç, M., 2012. Cost analysis of wind-electrolyzer-fuel cell system for energy demand in Pınarbaşı-Kayseri. International Journal of Hydrogen Energy 37, 12158-12166.

Goldberg D. E., Genetic algorithms in search, optimization, and machine learning. 1989.

Gómez-Barea, A., Leckner, B., 2010. Modeling of biomass gasification in fluidized bed. Progress in Energy and Combustion Science 36, 444-509.

Gong, S, Goni Boulama, K, Parametric study of an absorption refrigeration machine using advanced exergy analysis, Energy, Volume 76, 1 November 2014, Pages 453-467.

Gool, W., 1997. Energy Policy: Fairy Tales and Factualities, in: Soares, O.D., Cruz, A.M., Pereira, G.C., Soares, I.R.T., Reis, A.P.S. (Eds.), Innovation and Technology — Strategies and Policies. Springer Netherlands, pp. 93-105.

Hance, C., 2005. Factors Affecting Costs of Geothermal Power Development. Geothermal Energy Association, Department of Energy, USA.

Haseli, Y., Dincer, I., Naterer, G.F., 2008. Thermodynamic analysis of a combined gas turbine power system with a solid oxide fuel cell through exergy. Thermochimica Acta 480, 1-9.

Hawlader, M.N.A., Ho, J.C., Malek, A., 1994. An experimental and analytical study of Permasep B10 separation characteristics. Journal of Membrane Science 87, 1-21.

Heberle, F., Bassermann, P., Preiinger, M., Bruggemann, D., 2012. Exergoeconomic optimization of an organic rankine cycle for low-temperature geothermal heat sources. International Journal of Thermodynamics 15, 119-126.

Helal, A.M., Al-Malek, S.A., Al-Katheeri, E.S., 2008. Economic feasibility of alternative designs of a PV-RO desalination unit for remote areas in the United Arab Emirates. Desalination 221, 1-16.

Henriknen, D.L., Macjay, D.B., Anderson, V.R., 1979. Prototype Hydrogen Automobile Using a Metal Hydride, 1st World Hydrogen Energy Conference.

Hocevar, S., 2007. Hydrogen Production and Cleaning from Renewable Feedstock, in: Graziani, M., Fornasiero, P. (Eds.), Renewable Resources and Renewable Energy: A Global Challenge. CRC Press, Boca Raton.

Hoogers, G., 2003. Portable Applications, in: Hoogers, G. (Ed.), Fuel Cell Technology Handbook. CRC Press, Boca Raton.

Horlock, J.H., 2002. Combined Power Plants. Krieger.

Hosseini, M., Dincer, I., Rosen, M.A., 2012. Steam and air fed biomass gasification: Comparisons based on energy and exergy. International Journal of Hydrogen Energy 37, 16446-16452.

Hosseini, M., Dincer, I., Rosen, M.A., 2013. Integrated Renewable Energy-Based Systems for Reduced Greenhouse Gas Emissions in: Dincer. I, C.C.O., Kadioglu F. (Ed.), Causes, Impacts and Solutions to Global Warming.

Howard, J.B., Williams, G.C., Fine, D.H., 1973. Kinetics of carbon monoxide oxidation in postflame gases. Symposium (International) on Combustion 14, 975-986.

Huangfu, Y., Wu, J.Y., Wang, R.Z., Kong, X.Q., Wei, B.H., 2007a. Evaluation and analysis of novel micro-scale combined cooling, heating and power (MCCHP) system. Energy Conversion and Management 48, 1703-1709.

Huangfu, Y., Wu, J.Y., Wang, R.Z., Xia, Z.Z., 2007b. Experimental investigation of adsorption chiller for Micro-scale BCHP system application. Energy and Buildings 39, 120-127.

Jaaskelainen, H.E., Wallace, J.S., 2009. Operating experience with a 240 kW microturbine combined heating, cooling and power system, 2008 2nd International Conference on Energy Sustainability, ES 2008, August 10, 2008 - August 14, 2008. ASME, Jacksonville, FL, United states, pp. 809-820.

Jenkins, B.M., 1989. Physical properties of biomass, in: Kitani, O., Hall, C.W. (Eds.), Biomass Handbook. Gordon & Breach Science, Amsterdam.

Justi, E.W., Bockris, J.O.M., 1987. A Solar-Hydrogen Energy System. Plenum Press, New York.

Kalogirou, S.A., 2004. Solar thermal collectors and applications. Progress in Energy and Combustion Science 30, 231-295.

Karabulut, H., Yucesu, H.S., Cinar, C., Aksoy, F., 2009. Construction and testing of a dish/Stirling solar energy unit. Journal of the Energy Institute 82, 228-232.

Karamarkovic, R., Karamarkovic, V., 2010. Energy and exergy analysis of biomass gasification at different temperatures. Energy 35, 537-549.

Karellas, S., Schuster, A., 2008. Supercritical fluid parameters in organic rankine cycle applications. International Journal of Thermodynamics 11, 101-108.

Kaushal, P., Abedi, J., Mahinpey, N., 2010. A comprehensive mathematical model for biomass gasification in a bubbling fluidized bed reactor. Fuel 89, 3650-3661.

Kemp, W.H., 2005. The renewable energy handbook: a guide to rural energy independence, off-grid and sustainable living. Aztext Press, ON, Canada.

Kerr, T., 2008a. Combined Heat and Power and Emissions Trading: Options for Policy makers. International Energy Agency, France.

Kerr, T., 2008b. Combined Heat and Power: Evaluating the Benefits of Greater Global Investment. International Energy Agency, France.

Khaliq, A., 2009. Exergy analysis of gas turbine trigeneration system for combined production of power heat and refrigeration. International Journal of Refrigeration 32, 534-545.

Khaliq, A., Kumar, R., 2008. Thermodynamic Performance Assessment of Gas Turbine Trigeneration System for Combined Heat Cold and Power Production. Journal of Engineering for Gas Turbines and Power 130, 024501-024501.

Kishore, V.V.N., 2009. Renewable energy engineering and technology: principles and practice. Earthscan, London, UK.

Koh, J.-H., Kang, B.S., Lim, H.C., 2000. Effect of various stack parameters on temperature rise in molten carbonate fuel cell stack operation. Journal of Power Sources 91, 161-171.

Kolb, G. J., Jones, S. A., Donnelly, M. W., Gorman, D., Thomas, R., Davenport, R., and Lumia, R., 2007, Heliostat Cost Reduction Study. Technical Report June, Sandia National Laboratories, Albuquerque, New Mexico 87185 and Livermore, California 94550

Koroneos, C., Dompros, A., Roumbas, G., 2008. Hydrogen production via biomass gasification—A life cycle assessment approach. Chemical Engineering and Processing: Process Intensification 47, 1261-1268.

Kotas, T.J., 1995. The Exergy Method of Thermal Plant Analysis. Exergon Publishing Company, UK.

Kranz, S., 2007. Market survey - Germany, GFZ Potsdam, http://www.lowbin.eu/public/GFZ-LowBin_marketsituation.pdf.

Krishnamurthy, P., Mishra, S., Banerjee, R., 2012. An analysis of costs of parabolic trough technology in India. Energy Policy 48, 407-419.

Kunii, D., Levenspiel, O., 1991. Fluidization Engineering. Butterworth Heinemann, Elsevier.

Leckner, B., Palchonok, G.I., Andersson, B.A., 1992. Representation of heat and mass transfer of active particles, the IEA-FBC, Mathematical Modelling Meeting, Turku, Finland.

Lecomte, E.L., Pang, A.W., Russell, J.W.R., 1998. Ice Storm 98. Institute for Catastrophic Loss Reduction, ICLR Research Paper Series 1.

Levy, C.J., Zernike, K., August 16, 2003. The Blackout: Hospitals; Lessons Learned on 9/11 Help Hospitals Respond, The New York Times.

Li, X., 2006. Principles of fuel cells. Taylor & Francis, New York.

Li, C.-H., Zhu, X.-J., Cao, G.-Y., Sui, S., Hu, M.-R., 2009. Dynamic modeling and sizing optimization of stand-alone photovoltaic power systems using hybrid energy storage technology. Renewable Energy 34, 815-826.

Liang, H.X., Wang, Q.W., 2007. Evaluation of energy efficiency for a CCHP system with available microturbine, 2007 ASME Turbo Expo, May 14, 2007 - May 17, 2007. American Society of Mechanical Engineers, Montreal, Que., Canada, pp. 969-975.

Luecke, K., Hartge, E., Werther, J., 2004. A 3D Model of Combustion in Large-Scale Circulating Fluidized Bed Boilers. International Journal of Chemical Reactor Engineering 2, 1542-6580.

Lynn, P.A., 2010. Electricity from Sunlight: An Introduction to Photovoltaics. John Wiley and Sons.

Madhawa Hettiarachchi, H.D., Golubovic, M., Worek, W.M., Ikegami, Y., 2007. Optimum design criteria for an Organic Rankine cycle using low-temperature geothermal heat sources. Energy 32, 1698-1706.

Maidment, G.G., Tozer, R.M., 2002. Combined cooling heat and power in supermarkets. Applied Thermal Engineering 22, 653-665.

Malek, A., Hawlader, M.N.A., Ho, J.C., 1996. Design and economics of RO seawater desalination. Desalination 105, 245-261.

Mann, M.K., Spath, P.L., 1997. Life cycle assessment of a biomass gasification combined-cycle power system. National Renewable Energy Laboratory, Golden, CO, USA.

Marcovecchio, M.G., Aguirre, P.A., Scenna, N.J., 2005. Global optimal design of reverse osmosis networks for seawater desalination: modeling and algorithm. Desalination 184, 259-271.

Marriott, J., Sørensen, E., 2003. A general approach to modelling membrane modules. Chemical Engineering Science 58, 4975-4990.

Matsoukas, T., 2013. Fundamentals of Chemical Engineering Thermodynamics. Prentice Hall.

McDonald, C.F., 2012. Helium turbomachinery operating experience from gas turbine power plants and test facilities. Applied Thermal Engineering 44, 108-142.

McDonald, C.F., Orlando, R.J., Cotzas, G.M., 1994. Helium Turbomachine Design for GT-MHR Power Plant, International Joint Power Generation Conference. ASME, Phoenix, Arizona, pp. 1-11.

Medrano, M., Castell, A., Fontanals, G., Castellón, C., Cabeza, L.F., 2008. Economics and climate change emissions analysis of a bioclimatic institutional building with trigeneration and solar support. Applied Thermal Engineering 28, 2227-2235.

Medrano, M., Mauzey, J., McDonell, V., Samuelsen, S., Boer, D., 2006. Theoretical analysis of a novel integrated energy system formed by a microturbine and an exhaust fired single-double effect absorption chiller. International Journal of Thermodynamics 9, 29-36.

Meng X, Yang F, Bao Z, Deng J, Serge NN, Zhang Z. Theoretical study of a novel solar trigeneration system based on metal hydrides. Applied Energy, 2010;87:2050–2061.

Míguez, J.L., Murillo, S., Porteiro, J., López, L.M., 2004. Feasibility of a new domestic CHP trigeneration with heat pump: I. Design and development. Applied Thermal Engineering 24, 1409-1419.

Milioli, F.E., Foster, P.J., 1995. Entrainment and elutriation modelling in bubbling fluidized beds. Powder Technology 83, 233-244.

Miller, J.E., 2004. Review of Water Resources and Desalination Technologies. Sandia National Laboratories, Materials Chemistry Department.

Moran, M.J., Shapiro, H.N., Boettner, D.D., Bailey, M.B., 2011. Fundamentals of Engineering Thermodynamics, 7 ed. Wiely.

Mostoufi, N., Cui, H., Chaouki, J., 2001. A Comparison of Two- and Single-Phase Models for Fluidized-Bed Reactors. Industrial & Engineering Chemistry Research 40, 5526-5532.

Nafey, A.S., Sharaf, M.A., García-Rodríguez, L., 2010. Thermo-economic analysis of a combined solar organic Rankine cycle-reverse osmosis desalination process with different energy recovery configurations. Desalination 261, 138-147.

Nakaoka, T., Uehara, H., 1988a. Performance test of a shell-and-plate type condenser for OTEC. Experimental Thermal and Fluid Science 1, 275-281.

Nakaoka, T., Uehara, H., 1988b. Performance test of a shell-and-plate type evaporator for OTEC. Experimental Thermal and Fluid Science 1, 283-291.

Nemtsov, D.A., Zabaniotou, A., 2008. Mathematical modelling and simulation approaches of agricultural residues air gasification in a bubbling fluidized bed reactor. Chemical Engineering Journal 143, 10-31.

Ni, M., Leung, M.K.H., Leung, D.Y.C., 2008. Energy and exergy analysis of hydrogen production by a proton exchange membrane (PEM) electrolyzer plant. Energy Conversion and Management 49, 2748-2756.

Nicolin, F., Verda, V., 2011. Lifetime optimization of a molten carbonate fuel cell power system coupled with hydrogen production. Energy 36, 2235-2241.

No, H.C., Kim, J.H., Kim, H.M., 2007. A Review of Helium Gas Turbine Technology for High-Temperature Gas-Cooled Reactors. Nuclear Engineering and Technology 39, 21-30.

Okasha, F., 2007. Modeling combustion of straw–bitumen pellets in a fluidized bed. Fuel Processing Technology 88, 281-293.

Okasha, F.M., El-Emam, S.H., Zaatar, G., 2005. Fluidized Bed Combustion of an Agriculture Waste, Case Study: Combustion of Rice Straw. Mansoura Engineering Journal 30.

Ozcan H, Dincer I., 2013. Thermodynamic analysis of an integrated SOFC, solar ORC and absorption chiller for tri-generation applications. Fuel Cells, 13 (5), 781-793.

Patel, M.R., 1999. Wind and Solar Power Systems. CRC Press, FL, USA.

Patro, T.N., 1993. Combustion study of hydrogen fueled DI diesel engine: simplified heat release analysis. International Journal of Hydrogen Energy 18, 231-241.

Pemberton, S.T., Davidson, J.F., 1984. Turbulence in the freeboard of a gas-fluidised bed: The significance of ghost bubbles. Chemical Engineering Science 39, 829-840.

Petela, R., 2005. Exergy analysis of the solar cylindrical-parabolic cooker. Solar Energy, 79, 221-233.

Petersen, I., Werther, J., 2005. Experimental investigation and modeling of gasification of sewage sludge in the circulating fluidized bed. Chemical Engineering and Processing: Process Intensification 44, 717-736.

Philippek, C., Knobig, T., Schnfelder, H., Werther, J., 1997. NOx formation and reduction during combustion of wet sewage sludge in the circulating fluidized bed—measurement and simulation, 14th International Conference on FBC.

Porteiro, J., Míguez, J.L., Murillo, S., López, L.M., 2004. Feasibility of a new domestic CHP trigeneration with heat pump: II. Availability analysis. Applied Thermal Engineering 24, 1421-1429.

Prins, M.J., Ptasinski, K.J., Janssen, F.J.J.G., 2003. Thermodynamics of gas-char reactions: first and second law analysis. Chemical Engineering Science 58, 1003-1011.

Qin, J., Zhou, W., Bao, W., Yu, D., 2010. Thermodynamic analysis and parametric study of a closed Brayton cycle thermal management system for scramjet. International Journal of Hydrogen Energy 35, 356-364.

Quaschning, V., 2005. Understanding renewable energy systems. Earthscan, London, UK.

Quoilin, S., Declaye, S., Tchanche, B.F., Lemort, V., 2011. Thermo-economic optimization of waste heat recovery Organic Rankine Cycles. Applied Thermal Engineering 31, 2885-2893.

Radmanesh, R., Chaouki, J., Guy, C., 2006. Biomass gasification in a bubbling fluidized bed reactor: Experiments and modeling. AIChE Journal 52, 4258-4272.

Rashidi, R., Berg, P., Dincer, I., 2009. Performance investigation of a combined MCFC system. International Journal of Hydrogen Energy 34, 4395-4405.

Rashidi, R., Dincer, I., Berg, P., 2008. Energy and exergy analyses of a hybrid molten carbonate fuel cell system. Journal of Power Sources 185, 1107-1114.

Rawlings, R., 2009. Capturing Solar Energy, CIBSE Knowledge series, The Chartered Institution of Building Services Engineers, London, UK.

Romero-Ternero, V., García-Rodríguez, L., Gómez-Camacho, C., 2005a. Thermoeconomic analysis of a seawater reverse osmosis plant. Desalination 181, 43-59.

Romero-Ternero, V., García-Rodríguez, L., Gómez-Camacho, C., 2005b. Thermoeconomic analysis of wind powered seawater reverse osmosis desalination in the Canary Islands. Desalination 186, 291-298.

Rosen, M.A., Dimitriu, J., 1993. Potential benefits of utility-based cogeneration in Ontario, The International Symposium on CO2 Fixation and Efficient Utilization of Energy, pp. 147-156.

Rosiek S, Batlles FJ. Renewable energy solutions for building cooling, heating and power system installed in an institutional building: case study insouthern Spain. Renew Sustain Energy Rev 2013;26:147–68.

Roy, J.P., Mishra, M.K., Misra, A., 2011. Performance analysis of an Organic Rankine Cycle with superheating under different heat source temperature conditions. Applied Energy 88, 2995-3004.

Saidur, R., BoroumandJazi, G., Mekhilef, S., Mohammed, H.A., 2012. A review on exergy analysis of biomass based fuels. Renewable and Sustainable Energy Reviews 16, 1217-1222.

Salatino, P., Scala, F., Chirone, R., 1998. Fluidized-bed Combustion of a Biomass Char: The Influence of Carbon Attrition and Fines Postcombustion on Fixed Carbon Conversion, 27th Symposium on Combustion, The Combustion Institute, pp. 3103-3110.

Scala, F., Chirone, R., 2006. Combustion and Attrition of Biomass Chars in a Fluidized Bed. Energy and Fuels 20, 91-102.

Schaffer J.D., Multiple objective optimization with vector evaluated genetic algorithms. In Proceedings of the 1st international Conference on Genetic Algorithms. L. Erlbaum Associates Inc.; 1985: 93-100.

Schuster, G., Loffler, G., Weigl, K., Hofbauer, H., 2001. Biomass steam gasification - an extensive parametric modeling study. Bioresource Technology 77, 71-79.

Scott, W.G., 1998. Microturbine generators for distribution systems. IEEE Industry Applications 4, 57-62.

Segal, A., Epstein, M., 2000. The optics of the solar tower reflector. Solar Energy 69, 229-241.

Segal, A., Epstein, M., Yogev, A., 2004. Hybrid concentrated photovoltaic and thermal power conversion at different spectral bands. Solar Energy 76, 591-601.

Sen, Z., 2004. Solar energy in progress and future research trends. Progress in energy and combustion science 30, 367-416.

Shaaban, W., 2010. Fluidized Bed Combustion of Rice Straw and Bitumen Pellets, Mechanical Engineering. Mansoura university, Egypt.

Shengjun, Z., Huaixin, W., Tao, G., 2011. Performance comparison and parametric optimization of subcritical Organic Rankine Cycle (ORC) and transcritical power cycle system for low-temperature geothermal power generation. Applied Energy 88, 2740-2754.

Simoes, M.G., Farret, F.A., 2004. Renewable Energy Systems: Design and Analysis with Induction Generators. CRC Press, New York, USA.

Song, G., Chen, L., Xiao, J., Shen, L., 2013. Exergy evaluation of biomass steam gasification via interconnected fluidized beds. International Journal of Energy Research 37, 1743-1751.

Sorensen, B., 2011. Renewable Energy: Physics, Engineering, Impacts, Economics and Planning, 4th ed. Elsevier.

Specchia, S., Saracco, G., Specchia, V., 2008. Modeling of an APU system based on MCFC. International Journal of Hydrogen Energy 33, 3393-3401.

Stefansson, V., 2001. Investment cost for geothermal power plants, Proceeding of The 5th INAGA Annual Scientific Conference & Exhibitions, Indonesia

Szargut, J., Morris, D.R., Steward, F.R., 1988. Exergy analysis of thermal, chemical and metallurgical processes. Hemisphere Publishing Co., New York.

Szargut, J., Styrylska, T., 1964. Approximate evaluation of the exergy of fuels. Brennst.Wärme Kraft 16, 589-596.

Szokolay, S.V., 2004. Introduction to Architectural Science: The Basis of Sustainable Design. Elsevier.

Tao, G., Armstrong, T., Virkar, A., 2005. Intermediate temperature solid oxide fuel cell (IT-SOFC) research and development activities at MSRI, 9th annual ACERC & ICES conference, Utah.

Tchanche, B.F., Lambrinos, G., Frangoudakis, A., Papadakis, G., 2010. Exergy analysis of micro-organic Rankine power cycles for a small scale solar driven reverse osmosis desalination system. Applied Energy 87, 1295-1306.

Toonssen, R., Woudstra, N., Verkooijen, A.H.M., 2008. Exergy analysis of hydrogen production plants based on biomass gasification. International Journal of Hydrogen Energy 33, 4074-4082.

Tracy, T., Ordonez, J.C., Vargas, J.V.C., 2007. First and second law thermodynamic analysis of a domestic scale trigeneration system, 2007 Energy Sustainability Conference, June 27, 2007 - June 30, 2007. American Society of Mechanical Engineers, Long Beach, CA, United states, pp. 759-766.

Tse, L.K.C., Wilkins, S., McGlashan, N., Urban, B., Martinez-Botas, R., 2011. Solid oxide fuel cell/gas turbine trigeneration system for marine applications. Journal of Power Sources 196, 3149-3162.

Turton, R., Bailie, R., Whiting, W.B., Shaeiwitz, J., Bhattacharyya, D., 2012. Analysis, Synthesis and Design of Chemical Processes, 4 ed. Pearson.

Uehara, H., Dilao, C.O., Nakaoka, T., 1988. Conceptual design of ocean thermal energy conversion (OTEC) power plants in the Philippines. Solar Energy 41, 431-441.

Uehara, H., Ikegami, Y., 1990. Optimization of a closed-cycle OTEC system. Transactions of the ASME. Journal of Solar Energy Engineering 112, 247-256.

Uehara, H., Kusuda, H., Monde, M., Nakaoka, T., Sumitomo, H., 1984. Shell-and-plate-type heat exchangers for OTEC plants. Transactions of the ASME. Journal of Solar Energy Engineering 106, 286-290.

Uehara, H., Miyara, A., Ikegami, Y., Nakaoka, T., 1996. Performance analysis of an OTEC plant and a desalination plant using an integrated hybrid cycle. Journal of Solar Energy Engineering, Transactions of the ASME 118, 115-118.

Uehara, H., Nakaoka, T., Nakashima, S., 1985. Heat transfer coefficients for a vertical fluted-plate condenser with R113 and 114. International Journal of Refrigeration 8, 22-28.

Uehara, H., Stuhltrager, E., Miyara, A., Murakami, H., Miyazaki, K., 1997. Heat transfer and flow resistance of a shell and plate-type evaporator. Transactions of the ASME. Journal of Solar Energy Engineering 119, 160-164.

Valenzuela, L., Zarza, E., Berenguel, M., Camacho, E.F., 2005. Control concepts for direct steam generation in parabolic troughs. Solar Energy 78, 301-311.

Valero, A., Serra, L., Lozano, M.A., 1993. Structural theory of thermoeconomics, Proceedings of the 1993 ASME Winter Annual Meeting, November 28, 1993 - December 3, 1993. Publ by ASME, New Orleans, LA, USA, pp. 189-198.

Varbanov, P., Klemeš, J., Shah, R.K., Shihn, H., 2005. Power Cycle Integration and Efficiency Increase of Molten Carbonate Fuel Cell Systems. Journal of Fuel Cell Science and Technology 3, 375-383.

Velumani, S., Guzma, C.E., Peniche, R., Vega, R., 2010. Proposal of a hybrid CHP system: OFC/microturbine/absorption chiller. International Journal of Energy Research 34, 1088–1095.

Verda, V., Nicolin, F., 2010. Thermodynamic and economic optimization of a MCFC-based hybrid system for the combined production of electricity and hydrogen. International Journal of Hydrogen Energy 35, 794-806.

Voros, N.G., Kiranoudis, C.T., Maroulis, Z.B., 1998. Solar energy exploitation for reverse osmosis desalination plants. Desalination 115, 83-101.

Wade, N.M., 1993. Technical and economic evaluation of distillation and reverse osmosis desalination processes. Desalination 93, 343-363.

Wade, N.M., 2001. Distillation plant development and cost update. Desalination 136, 3-12.

Wang J, Zhao P, Niu X, Dai Y. Parametric analysis of a new combined cooling,heating and power system with transcritical CO2 driven by solar energy. Applied Energy 2012;94:58–64.

Wei, D., Lu, X., Lu, Z., Gu, J., 2007. Performance analysis and optimization of organic Rankine cycle (ORC) for waste heat recovery. Energy Conversion and Management 48, 1113-1119.

Weizsacker, V., Lovins, A.B., Lovins, L.H., 1998. Factor Four: doubling wealth – halving resource use, a report to the club of Rome. London, UK.

Wenlong, L., Heng, X., Zuoyi, Z., Yujie, D., 2012. Development and primary verification of a transient analysis software for high temperature gas-cooled reactor helium turbine power system. Nuclear Engineering and Design 250, 219-228.

White, C.M., Steeper, R.R., Lutz, A.E., 2006. The hydrogen-fueled internal combustion engine: a technical review. International Journal of Hydrogen Energy 31, 1292-1305.

Wichert, B., Nayar, C.V., Lawrance, W.B., 1999. Photovoltaic-Diesel hybrid energy systems for off-grid rural electrification. International Journal of Renewable Energy Engineering 1, 7-17.

Wilf, M., Klinko, K., 1994. Performance of commercial seawater membranes. Desalination 96, 465-478.

Wilf, M., Klinko, K., 1999. Effective new pretreatment for seawater reverse osmosis systems. Water Supply 17, 117-125.

Wilf, M., Klinko, K., 2001. Optimization of seawater RO systems design. Desalination 138, 299-306.

Williams, M.C., 2011. Fuel Cells, in: Shekhawat, D., Spivey, J.J., Berry, D.A. (Eds.), Fuel Cells: Technologies for Fuel Processing. Elsevier.

Wongchanapai, S., Iwai, H., Saito, M., Yoshida, H., 2012a. Performance evaluation of an integrated small-scale SOFC-biomass gasification power generation system. Journal of Power Sources 216, 314-322.

Wongchanapai, S., Iwai, H., Saito, M., Yoshida, H., 2012b. Selection of suitable operating conditions for planar anode-supported direct-internal-reforming solid-oxide fuel cell. Journal of Power Sources 204, 14-24.

Xu, C., Wang, Z., Li, X., Sun, F., Energy and exergy analysis of solar power tower plants, Applied thermal engineering, 31, 2011; 3904-3913.

Yoshiba, F., Izaki, Y., Watanabe, T., 2004. Wide range load controllable MCFC cycle with pressure swing operation. Journal of Power Sources 137, 196-205.

Zhao, H., Peterson, P.F., 2008. Multiple reheat helium Brayton cycles for sodium cooled fast reactors. Nuclear Engineering and Design 238, 1535-1546.

Zhou, W., Song, L., Guan, T.K., 2006. A numerical study on concentration polarization and system performance of spiral wound RO membrane modules. Journal of Membrane Science 271, 38-46.

Ziher, D., Poredos, A., 2006. Economics of a trigeneration system in a hospital. Applied Thermal Engineering 26, 680-687.